



HAL
open science

Indoor localization system for telemonitoring

Rupesch Kumar

► **To cite this version:**

Rupesch Kumar. Indoor localization system for telemonitoring. Signal and Image processing. Télécom ParisTech, 2014. English. NNT : 2014ENST0086 . tel-01380232

HAL Id: tel-01380232

<https://pastel.hal.science/tel-01380232>

Submitted on 12 Oct 2016

HAL is a multi-disciplinary open access archive for the deposit and dissemination of scientific research documents, whether they are published or not. The documents may come from teaching and research institutions in France or abroad, or from public or private research centers.

L'archive ouverte pluridisciplinaire **HAL**, est destinée au dépôt et à la diffusion de documents scientifiques de niveau recherche, publiés ou non, émanant des établissements d'enseignement et de recherche français ou étrangers, des laboratoires publics ou privés.



EDITE ED 130

Doctorat ParisTech

THÈSE

pour obtenir le grade de docteur délivré par

Télécom ParisTech

Spécialité “ Electronique et Communications ”

présentée et soutenue publiquement par

Rupesh KUMAR

le 17 décembre 2014

Indoor Localisation pour Telemonitoring

Directeur de thèse : **Bernard HUYART**

Co-encadrement de la thèse : **Jean-Christophe COUSIN**

Jury

M. Cyril DECROZE, Professeur, UPMC

M. Marc HEDDEBAUT, Professeur, TELECOM Sud Paris

M. Aziz BENLARBI, Professeur, UPMC

M. Nel SAMAMA, Professeur, TELECOM Sud Paris

M. Benoit DENIS, Ingénieur de Recherche, CEA-Leti Minatec

M. Bernard HUYART, Professeur, TELECOM ParisTech

M. Jean-Christophe COUSIN, Maître de Conférences, TELECOM ParisTech

M. Jean-Baptiste POTHIN, Ingénieur de Recherche, DataHertz SA

Rapporteur

Rapporteur

Examineur

Examineur

Examineur

Directeur de thèse

Directeur de thèse

Invité

T
H
È
S
E

Télécom ParisTech

école de l'Institut Mines Télécom – membre de ParisTech

46, rue Barrault – 75634 Paris Cedex 13 – Tél. + 33 (0)1 45 81 77 77 – www.telecom-paristech.fr

I dedicate this thesis to
my teachers and my family
for their kind support.

ACKNOLEGMENT

It is my pleasure to thank my supervisors, Prof. Bernard HUYART and Dr. Jean-Christophe COUSIN, who have offered me the opportunity to work on a very interesting subject-Indoor Localization System. I acknowledge with deepest gratitude for their guidance and help throughout my PhD.

Many thanks go to committee members, Prof. Aziz BENLARBI, the jury president, Prof. Mohamed HIMDI, Dr. Cyril DECROZE, Prof. Marc HEDDEBAUT, Prof. Nel SAMAMA, Ing. Benoit DENIS, and Ing. Jean-Baptiste POTHIN, for serving as my jury, and for your important comments and suggestions.

I would like to thank Mr. Karim BENKALAIA, and Mr. Antoine KHY. I am extremely grateful to them for helping me over the past three years. I sincerely wish to thank the members of the COMELEC department at Telecom ParisTech.

I am also thankful to all my teachers who taught me throughout the schooldays.

I thank all Doctors and PhD students in the COMELEC, Christopher, Lana, Lila, Reda, José, Taghrid, Nga, Mark, Abdou, Mohammad, Chetan, Yunfei, and Elie. I am always indebted to all my friends in France and India.

Special recognition goes to Prem, Archana, Chadi, Asma and Shivam for their support and friendship that helped me in difficult time.

A special thanks to almighty and my family. Words cannot express how grateful I am to my mother, father, brother and sisters' families for all the sacrifices that they have made on my behalf. Their prayer for me was what sustained me thus far. I would also like to thank all nieces and nephews for theirs unconditional love and support.

The list of the people I wish to thank cannot fit in a page. Indeed, thanks to all!! ☺

Rupesh KUMAR

RESUME

Introduction :

La faible pénétration des signaux GPS (Global Positioning System) à l'intérieur des bâtiments a favorisé la conception de systèmes de localisation dédiés aux environnements indoor. Différentes approches sont exploitées pour estimer la position d'un utilisateur. Généralement, elles sont basées sur des méthodes de triangulation par la mesure de puissance entre différents émetteurs (dont la position est connue) et un récepteur à localiser, sur des méthodes de caractérisation en puissance de l'environnement ou encore exploite des techniques radar.

L'objectif principal de cette thèse est de réaliser un système compact permettant la localisation 3D de badges actifs (ou transpondeurs) avec une précision submétrique dans un environnement indoor. La méthode utilisée s'appuie sur la mesure conjointe de distance et d'angles d'arrivée à l'aide d'un système basée sur l'architecture d'un radar monopulse à 4 canaux exploitant des signaux radar FMCW (Frequency Modulation Continuous Wave).

Cette thèse est composée de quatre chapitres. Le premier chapitre est dédié à l'analyse critique des différents systèmes ou méthodes de localisation indoor. Le second chapitre concerne l'analyse théorique de la méthode proposée. Dans le troisième chapitre, nous détaillons l'architecture du système développé et le quatrième chapitre est consacrée à l'analyse des performances les performances obtenues dans des cas réels. Les conclusions sont présentées dans le cinquième chapitre.

Chapitre 1. Systèmes de Localisation Indoor:

De nos jours, de nombreuses applications nécessitant la localisation en temps réel sont en développement. Le principal système est le GPS (Global Positioning System) développé, initialement, pour les applications militaires. Depuis quelques années, les applications dites civiles se sont démocratisées avec, en premier lieu, l'aide à la conduite automobile. D'autres applications peuvent concerner la sécurité lorsqu'il s'agit de repérer et identifier une présence humaine si le sujet est équipé d'un système de signature par technologie RFID. En milieu indoor, le GPS seul ne fournit pas actuellement une localisation précise à cause des niveaux de puissance très faibles des signaux GPS à l'intérieur de bâtiments ainsi que l'influence des effets des multitrajets affectant ces signaux. Aussi la localisation indoor est devenue un enjeu important pour des applications aussi bien militaires, commerciales ou de santé publique. Pour l'aspect santé publique, les conclusions extraites d'une étude menée en 2008 par l'Organisation Mondiale de la Santé mettent en avant l'idée d'une vie meilleure et plus longue à domicile. Dans ce cadre, la télésurveillance permet de rester chez soi sans que cela devienne une contrainte pour l'accès aux soins. Les moyens d'accès sont assurément les réseaux de communications (satellite, fibre optique, réseaux de téléphone fixes et mobiles) couvrant une grande partie du globe et pouvant permettre de mettre en liaison un patient avec un professionnel de la santé partout dans le monde. Des techniques doivent être mises en œuvre pour permettre à ces professionnels d'avoir accès à la télésurveillance des patients. La localisation indoor est une des applications apportant une solution dans le domaine de l'e-santé et la surveillance de personnes âgées, atteintes de maladie telle que celle d'Alzheimer.

Le développement des systèmes de localisation indoor est actuellement mené suivant deux classes. La première classe exploite l'infrastructure déjà existante des réseaux sans fil couramment rencontrés dans les bâtiments (WiFi par exemple). La technique principale est basée sur la méthode de localisation par trilatération exploitant le RSSI (Received Signal Strength Indicator), qui est le niveau de puissance d'un signal provenant d'une station WLAN située à proximité du récepteur à localiser. Ce type de système nécessite conjointement l'utilisation minimale de 3 stations de base. Si cette méthode paraît efficace en intérieur dans des espaces vides ou homogènes, la précision se dégrade rapidement lorsque le milieu devient inhomogène avec la présence de murs, mobiliers etc. Des méthodes ont été développées pour appréhender ce problème. Pour améliorer la précision, une première technique connue est le

“fingerprinting” qui consiste à discrétiser la surface de localisation par une maille et de mesurer la puissance des signaux provenant de chaque station sur chaque nœud de la maille. Les valeurs obtenues sont stockées dans une matrice où les lignes et les colonnes correspondent aux coordonnées cartésiennes des nœuds de la maille. Cette méthode semble efficace mais la précision sur la localisation augmente avec le nombre de nœuds et donc le pas de grille pour la maille. Dans le cas où la surface couverte est de grande taille, la base de données de référence augmente considérablement. Un second inconvénient est que la surface de localisation doit répondre aux contraintes de canal de propagation radio stationnaire. L’environnement doit être statique (mobilier, murs etc) sous peine de devoir recréer une nouvelle base de données. De plus les méthodes évoquées s’appuient sur le fait que la surface de localisation est couverte par au moins 3 émetteurs WLAN (Wifi ou UWB), cette architecture est rarement rencontrée chez un particulier.

La seconde classe de systèmes utilise ses propres infrastructures. Les méthodes alors couramment utilisées exploitent la différence de temps d’arrivée (TDOA), de phase d’arrivée (PDOA) ou de fréquence d’arrivée (FDOA). Elles ont prouvées leur fonctionnement en espace libre mais pour des applications en milieu indoor et pour des courtes distances, la précision sur la position se dégrade par rapport à la surface de localisation envisagée. Les erreurs sont alors principalement dues soit aux trajets multiples générés par le milieu de propagation rencontré (technique PDOA), soit, pour les applications dites « courtes distances », à la gestion des horloges de synchronisation entre les émetteurs utilisés notamment pour les systèmes basés sur une technique TDOA. Ce problème peut être contourné dans les systèmes exploitant la PDOA ou FDOA. Outre les problèmes de trajets multiples, la technique basée sur la PDOA rencontre aussi la contrainte d’ambiguïté sur la mesure de phase. Dans ce cas une technique multi-fréquentielle peut être utilisée qui peut s’apparenter à une technique FDOA. Les problèmes de gestion d’ambiguïtés et de multi trajets sont résolus en associant une méthode PDOA et FDOA ou une modélisation de canal au préalable dans le cadre d’un canal radio dit LOS (Line of Sight) présentant un trajet direct entre un récepteur à localiser et la base de localisation.

Chapitre 2. Méthode de localisation indoor développée:

La méthode proposée permet la localisation en 3 dimensions, dans un environnement indoor, d'un badge transpondeur dédié. Cette méthode est basée sur l'exploitation des techniques du radar monopulse utilisant 1 canal d'émission et 4 canaux de réception colocalisés et utilise des signaux du type FMCW (Frequency Modulation Continuous Wave). Cette base de localisation radar (ILS) est aussi appelée ancre. Les canaux de propagation indoor exploités sont obligatoirement des canaux LOS (Line of Sight) où il existe un trajet optique direct entre le badge à localiser et la station de localisation avec ou non la présence de trajets multiples.

Contrairement aux méthodes traditionnelles proposées où il faut obligatoirement l'utilisation d'au moins 3 ancres distinctes pour une estimation par triangulation ou trilateration, une seule suffit. Cette allègement d'architecture permet de s'affranchir de la contrainte de synchronisation temporelle entre les différentes ancres. Cette synchronisation devient délicate à réaliser dès lors que les zones ou volumes sous investigation pour la localisation 3D sont petits.

Les paramètres de localisation 3D à estimer sont présentés en coordonnées polaires. Il s'agit de déterminer dans ce cas la distance radiale d et les angles d'azimut β et d'élévation α du badge (AT) par rapport au plan d'antennes de la station de localisation. La méthode de mesure est une technique hybride basée sur la FDoA (la différence de fréquence d'arrivée) et PDoA (la différence de phase d'arrivée) entre le signal émis de l'antenne A_0 et les signaux reçus sur les 4 canaux de réception associées aux antennes $A_{1..4}$ comme illustré dans la **Fig. 1**.

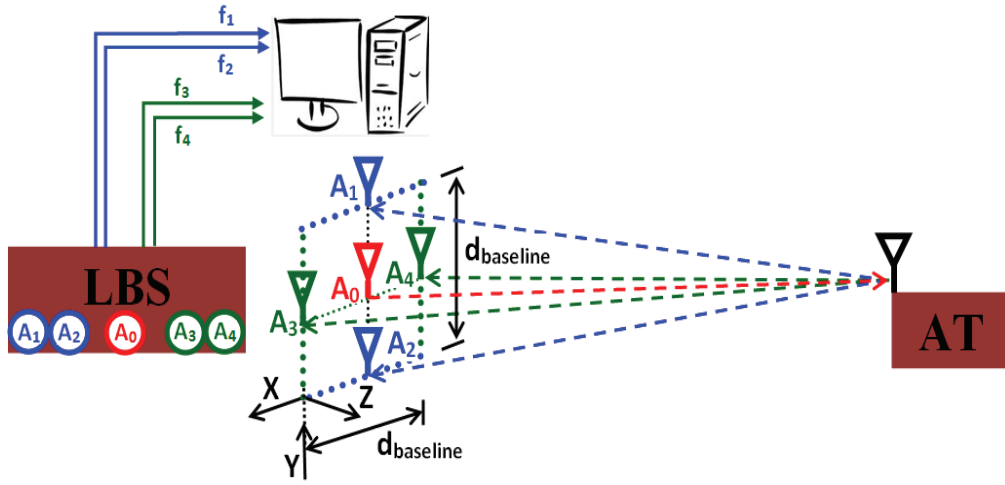


Fig. 1: Diagramme du système de localisation intérieure(ILS).

De manière générale, dans le cas d'une mesure radar monocanal, la distance radiale d est proportionnelle au temps de vol aller-retour (T_{ToF}) entre la station de base et le badge et déterminée par la relation

$$d = \frac{c * T_{ToF}}{2} \quad 1$$

Où c est la vitesse de lumière.

Dans le cas de l'utilisation de signaux FMCW, nous pouvons exprimer la distance radiale d en fonction du décalage fréquentiel instantané f_B entre le signal à l'émission et sa réplique sur l'un des canaux de réception comme

$$f_B = \frac{BW}{T_m} \frac{2d}{c} \quad 2$$

où BW (f_1-f_0) est la bande passante exploitée et T_m le temps de cycle pour la modulation comme illustré dans la **Fig. 2**.

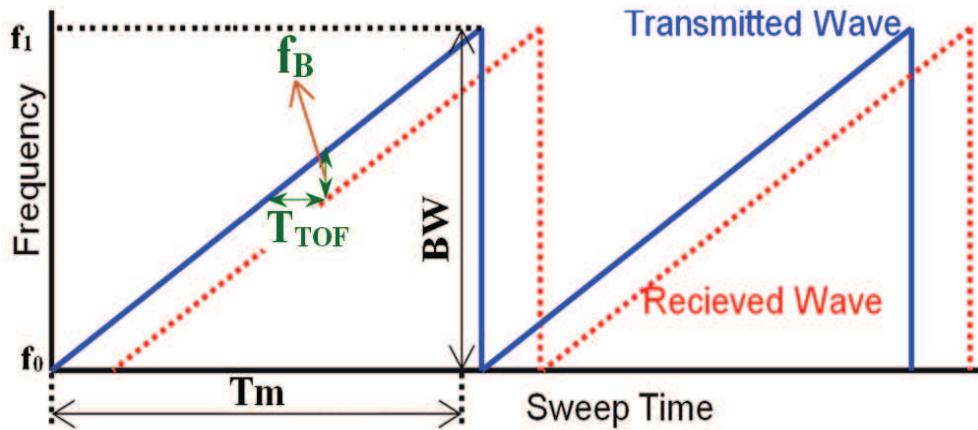


Fig. 2: Diagramme du FMCW.

Dans le cadre de notre application de localisation, nous adaptons cette méthode pour le cas d'une réception multicanaux.

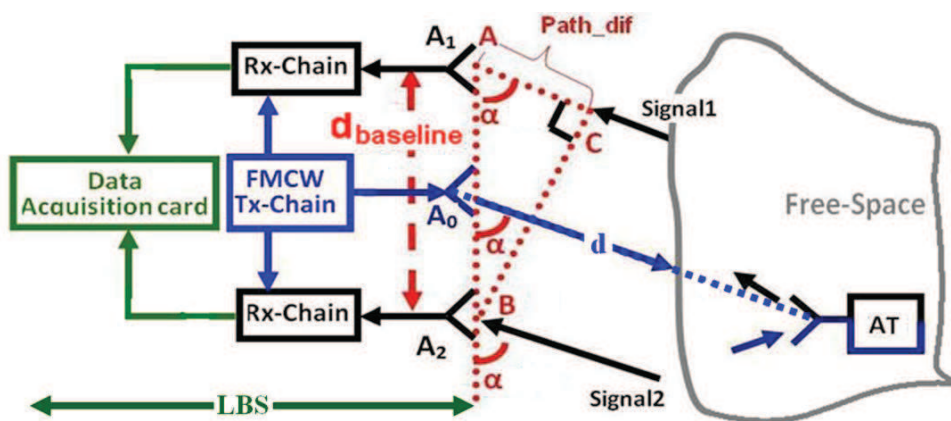


Fig. 3: Configuration pour la localisation systématique 2D.

La Fig.3 présente le schéma synoptique du principe pour une localisation en 2D où la distance radiale d et l'angle d'élévation α sont à estimer. Un générateur FMCW (Tx-Chain) fournit un signal FMCW de largeur fréquentielle BW avec un temps de cycle de modulation T_m . Ce signal est émis par A_0 et sert aussi de référence pour les 2 canaux de réception Rx-Chain associés aux antennes de réception A_1 et A_2 . Ces 2 antennes sont placées, de manière symétrique à l'antenne A_0 , sur un axe passant par l'antenne A_0 . La distance entre les antenne est appelée $d_{baseline}$ qui est, par hypothèse, beaucoup plus petite que les distances radiales d à mesurer. Le badge AT reçoit le signal émis et le retransmet vers la station de localisation. Le signal est reçu par les antennes A_1 et A_2 et chaque chaîne de réception fournit en bande de

base un signal sinusoïdal dont la fréquence F_{S1} ou F_{S2} dépend de l'écart fréquentiel instantané entre le signal de référence et ceux reçus sur les chaînes de réception. En exploitant la relation 1, nous déterminons 2 distances radiales d_1 et d_2 de la manière suivante:

$$\left. \begin{aligned} T_{TOF1} &= \frac{F_{S1} * T_m}{BW}; & d_1 &= \frac{c * T_m * F_{S1}}{2BW} \\ T_{TOF2} &= \frac{F_{S2} * T_m}{BW}; & d_2 &= \frac{c * T_m * F_{S2}}{2BW} \end{aligned} \right\} \quad 3$$

La détermination de la distance radiale d est déterminée à partir de la moyenne de d_1 et d_2 comme suit

$$d = \frac{d_1 + d_2}{2} \quad 4$$

La mesure de l'angle α dépend de la différence de marche au niveau des antennes A1 et A2, appelée ici $Path_dif$. Suivant l'hypothèse sur le paramètre $d_{baseline}$ présentée ci dessus, nous pouvons écrire que :

$$Path_dif = d_{baseline} * \cos\alpha \quad 5$$

De part leur définition, les fréquences F_{S1} et F_{S2} peuvent s'écrire :

$$F_{S1} = \frac{d\phi_1(t)/dt}{2\pi}; F_{S2} = \frac{d\phi_2(t)/dt}{2\pi}$$

où $d\phi_1(t)$ et $d\phi_2(t)$ représentent la dérivée de la phase des signaux en bande de bande en sortie des chaîne de réception en fonction du temps.

Sur un durée T_m , cette variation de phase correspond à la valeur de la phase des signaux en bande de base au temps T_m , notée $\phi_{1,2}(T_m)$ avec l'hypothèse que $\phi_{1,2}(0) = 0$. Dans ce cas la valeur de l'angle α peut s'écrire:

$$\alpha = \cos^{-1} \left\{ \frac{\Delta\phi_{21} * c}{4\pi * BW * d_{baseline}} \right\} \quad 6$$

Où, $\Delta\phi_{21} = \phi_2(T_m) - \phi_1(T_m)$.

La position du badge à localiser est ainsi déterminée en coordonnées polaires.

L'obtention de la localisation en 3D peut se faire en ajoutant un axe de localisation 2D orthogonalement au précédent comme illustré dans la **Fig. 4**.

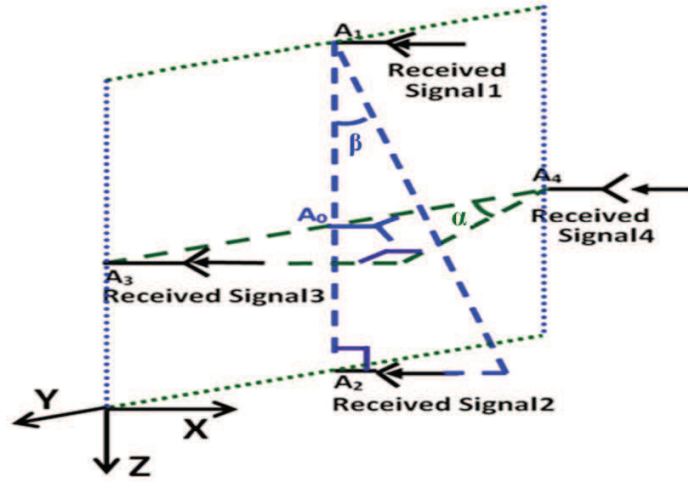


Fig. 4: Structure orthogonale d'antennes de récepteur pour les mesures 3D.

Les coordonnées pour une localisation 3D s'écrivent alors

$$\begin{cases} d = \frac{d_1 + d_2 + d_3 + d_4}{4} \\ \alpha = \cos^{-1} \left\{ \frac{\Delta\phi_{34} * c}{4\pi * BW * d_{baseline}} \right\} \\ \beta = \cos^{-1} \left\{ \frac{\Delta\phi_{21} * c}{4\pi * BW * d_{baseline}} \right\} \end{cases} \quad 7$$

où $d_{1..4}$ représentent les trajets des signaux reçus sur les antennes $A_{1..4}$, $\Delta\phi_{34}$.

Le système de localisation intérieure se compose de deux parties : une Station de Base de localisation (LBS) et un Tag actif (AT) comme illustré dans la **Fig. 5**. La LBS agit comme une station de base fixe pour la localisation. Elle contient une chaîne de transmission RF et deux chaînes de réception RF. Chacune d'elles est connectée séparément à une antenne. Par conséquent, la LBS dispose de trois antennes individuelles (A_0 , A_1 et A_2) placées toutes sur un même axe nommé ligne de base ($d_{baseline}$). L'antenne A_0 est utilisée pour l'émission et les deux autres antennes, A_1 et A_2 , sont utilisées pour la réception. L'antenne émettrice A_0 est placée au centre de la ligne de base $d_{baseline}$. Ici, les deux oscillateurs locaux à 1.5 GHz (LO1 et LO2) sont considérés comme synchronisés en phase.

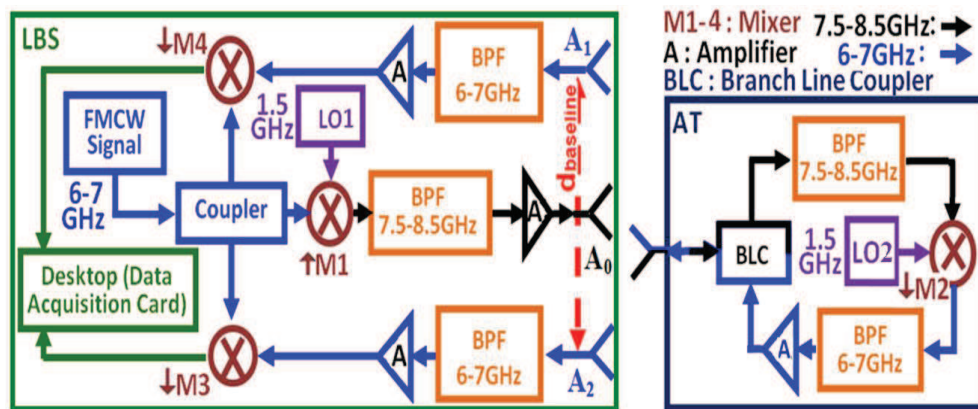


Fig. 5: Architecture pour la localisation 2D.

Un signal sinusoïdal FMCW dont la fréquence varie linéairement dans le temps entre 6 et 7 GHz sur une période de 10 ms est utilisé. Une partie de ce signal FMCW est prélevé par un coupleur (Coupler) afin de servir de référence dans les chaînes de réception. En sortie de la voie principale du coupleur, le signal est transposé en fréquence (M1) vers la bande [7.5-8.5 GHz] puis filtré par un filtre passe bande (BPF 7.5-8.5 GHz). Après amplification (A), le signal obtenu est transmis par l'antenne A0.

Ici, le tag AT est utilisé comme un transpondeur. Sa fonction principale est de convertir en fréquence (via le mixeur M2) le signal FMCW provenant de la LBS et couvrant la bande [7.5-8.5 GHz] vers la bande [6-7 GHz]. Cette transposition de fréquence permet de réduire/d'annuler le phénomène de feedback au niveau du transpondeur, de séparer bien distinctement le canal LBS/tag du canal tag/LBS et de réduire les phénomènes de rétrodiffusion passive de l'environnement. L'architecture du tag utilisée est de type full duplex.

Enfin, le signal FMCW converti est retransmis vers la LBS où il est reçu par les deux antennes (A₁ & A₂) associées aux canaux de réception. Sur chaque canaux de réception, les signaux reçus sont filtrés par un filtre passe bande BPF (6-7 GHz) puis amplifiés par un amplificateur. Les signaux obtenus sont mélangés avec le signal de référence par les mélangeurs (M3-ou M4). Le signal en sortie de chaque mélangeur est sinusoïdal avec une fréquence dite de battement égale à la différence de fréquence instantanée entre le signal de référence et le signal reçu sur chaque canal de réception. Les signaux sont numérisés par la carte d'acquisition de données (SECTRUM, M3I. 2132) qui permet ainsi le traitement de

signal par un PC afin d'obtenir les grandeurs métriques (distance radial et angles d'arrivée) à partir des différentes fréquences de battement obtenues.

En outre, le traitement du signal est réalisé par la technique DMTD (Dual-Mixer Time-Difference) pour la position des estimations.

La méthode DMTD est considérée comme l'une des méthodes les plus précises pour mesurer une différence de fréquence faible entre deux signaux sinusoïdaux. Cette méthode est principalement basée sur le calcul du nombre de passage par "0" d'un signal sinusoïdal à moyenne nulle. Toutefois, la précision à obtenir une valeur de fréquence précise dépend essentiellement du bruit de numérisation de la carte d'acquisition permettant de d'acquérir le signal à traiter. En présence bruit, le signal peut présenter plusieurs passages par "0" au lieu d'un seul. On peut s'affranchir de ce problème en appliquant une technique de double seuillage pour éviter les problèmes de redondance non voulues des passages par "0". La Transformée de Fourier (FFT) est également la méthode la plus connue pour l'estimation de fréquence. Toutefois, une bonne résolution sur la détermination de fréquence est dépendante de la durée du signal étudié associé au nombre de points d'acquisition sur cette durée.. Naturellement le temps de traitement devient beaucoup plus long. De telles limitations ne se produisent pas avec le DMTD qui fournit également une bonne résolution tout en considérant un nombre de points beaucoup plus faible par rapport à la FFT.

Chapitre 3. Réalisation de système de localisation intérieure:

Ce chapitre de thèse est consacré à la mise en œuvre pratique du système de localisation 3D à partir de composants connectés commerciaux dont la présentation est faite dans la thèse. Deux types d'antennes spécifiques à polarisation circulaire couvrant la bande UWB européenne ont été étudiées et réalisées pendant cette thèse. Nous présentons ici le développement et les performances de ces antennes.

La transmission et la réception des ondes radio sont dépendantes des antennes utilisées en terme de polarisation.. La polarisation d'une onde est classée en deux catégories : Polarisation Linéaire (LP) et polarisation elliptique où la polarisation circulaire (CP) est un cas particulier. Dans le cas de notre application nous avons choisi d'utiliser deux types

d'antennes à polarisation circulaire couvrant la bande UWB européenne [6-8.5 GHz] et présentant un volume le plus faible possible. LA première antenne utilisée sur la LBS est à simple polarisation circulaire (droite ou gauche). La seconde antenne est utilisée sur le badge et exploite une double polarisation circulaire droite et gauche pour séparer les canaux descendants et montant dans le cas d'un fonctionnement de type full duplex . Les antennes traditionnelles permettant d'obtenir une polarisation circulaire sur une telle bandesont de forme spirale (Archimède...) . La difficulté est que ces antennes ont besoin d'un circuit d'alimentation spécifique ou balun qui les rendent incompatibles avec les contraintes de dimension dans notre cas. En outre, la double polarisation circulaire nécessite deux circuits d'alimentation ce qui rend impossible l'utilisation sur un badge. Toutefois, une double polarisation circulaire peut être obtenue avec une structure d'antenne réalisées à partir de 2 dipôles placés orthogonalement et alimentés en quadrature de phase.

Du côté de la station LBS, cinq antennes à simple polarisation circulaire sont nécessaires pour faire une localisation en 3D. Les antennes sont adaptées pour fonctionner sur la bande de fréquence [6- 8,5 GHz]. Les antennes réalisées sont présentées Fig.6. Shen & Law ont réalisé une antenne planaire quasi-spirale bidimensionnelle très compacte adaptée pour la bande de fréquence [6-10 GHz]. Nous avons adapté cette antenne pour notre système fonctionnant dans la bande [6-8.5 GHz]. Deux bras quasi spirales sont imprimés sur les 2 faces d'un substrat de type sur DuroidRT 5880-substrat avec permittivité relative, $\epsilon_r=2,2$, épaisseur= 1,575mm présentant une tangente de pertes $\tan\delta = 0,0009$. Ces 2 bars sont alimentés par un balun en microstrip en forme de "taper". Sur les 5 antennes , l'une , en mode de fonctionnement à polarisation circulaire droite, est liée à la chaîne d'émission, les 4 autres, en mode de fonctionnement à polarisation circulaire gauche, sont associées chacune à une chaîne de réception,

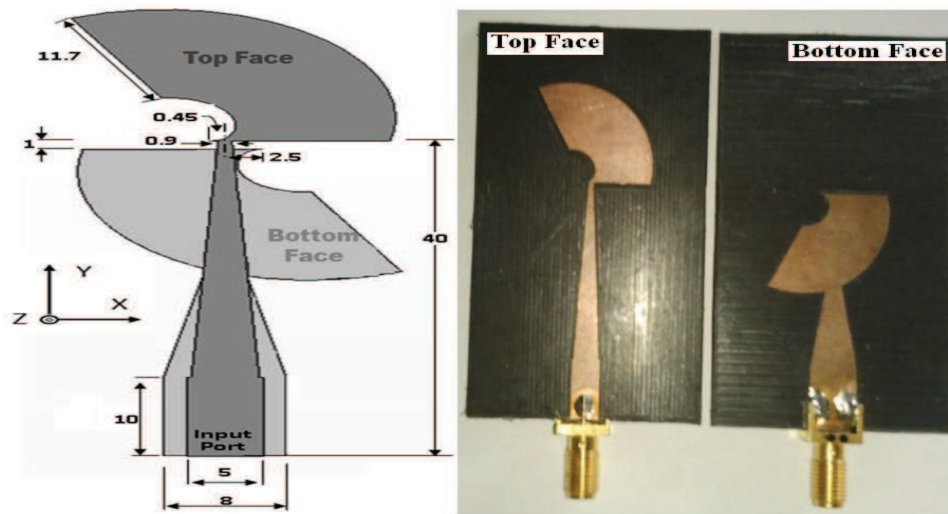


Fig. 6: Polarisation circulaire planaire pour le LBS.

Pour le badge, la réalisation de l'antenne à double polarisation circulaire est présentée Fig.7. Cette antenne est réalisée à partir de 2 dipôles placées orthogonalement sur chacun une face d'un substrat (CuClad250 permittivité relative $\epsilon_r=2,5$, épaisseur= 1,575mm et tangente de pertes $\tan\delta = 0,0018$). Chaque dipôle est fermé aux 2 extrémités par des disques optimisés pour obtenir la bande passante voulue. Les 2 dipôles sont alimentés par la même source mais déphasée de 90° entre les 2 accès Port11 et Port22. La contrainte de déphasage est réalisée grâce à un coupleur 3dB 90° (BLC). Cette structure permet de recevoir les signaux issus de la LBS en mode de polarisation circulaire droite et de réémettre en polarisation circulaire gauche dans le cadre d'une communication "full-duplex".

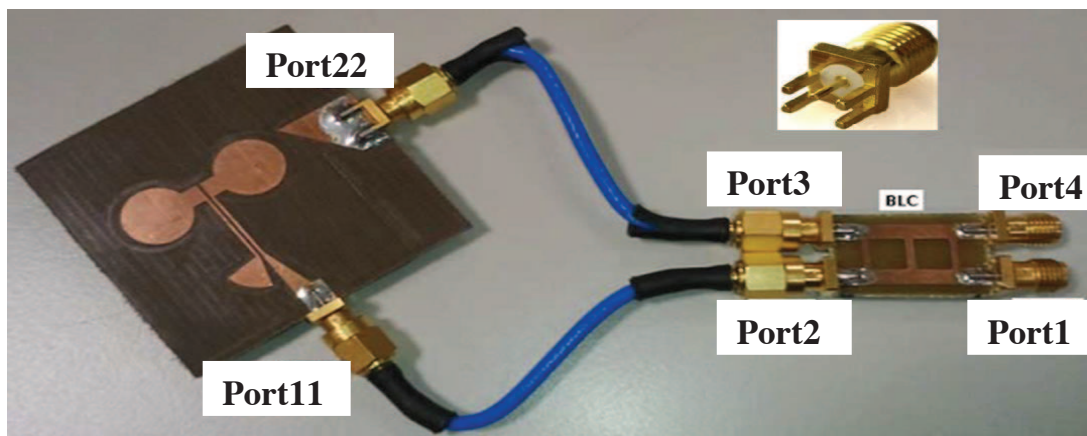


Fig. 7: Schéma de la double CP en introduisant déphasage de 90° .

Les longueurs des dipôles sont égaux à un quart de longueur d'onde ($\lambda/4$) à 7,25 GHz (fréquence centrale de bande), ce qui correspond à 1cm. L'adaptation des dipôles est faite par un balun présent sur chaque face du substrat. Les performances des antennes sont détaillées dans la thèse.

Chapitre 4. Performances et Analyses du système de localisation développé:

Dans ce chapitre, nous évaluons les performances du système de localisation (ILS) développé dans différentes conditions en milieu indoor. La station ILS est maintenue à une position fixe et connue. Le badge (Active-Tag) est positionné sur différentes positions connues que nous cherchons à déterminer.

Les estimations des différentes fréquences de battement à obtenir sont déterminées à partir de la méthode DMDT présenté dans le paragraphe 2. Les paramètres du signal FMCW utilisé sont : Bande de fréquence initiale = 1GHz [6-8.5 GHz], Temps de cycle de modulation = 10 ms, la puissance de signal émis =7dBm. Le baseline entre les antennes de réception = 30 cm. Pour l'acquisition des signaux de battement, la fréquence d'échantillonnage de la carte d'acquisition = 22,5 MHz,

Une description synoptique des paramètres physiques à estimer (distance radial entre la LBS et le Tag, les angles α et β correspondent aux angles d'azimut et d'élévation entre les signaux entrants reçus par A_1-A_2 et A_3-A_4) est reportée Fig.8 .

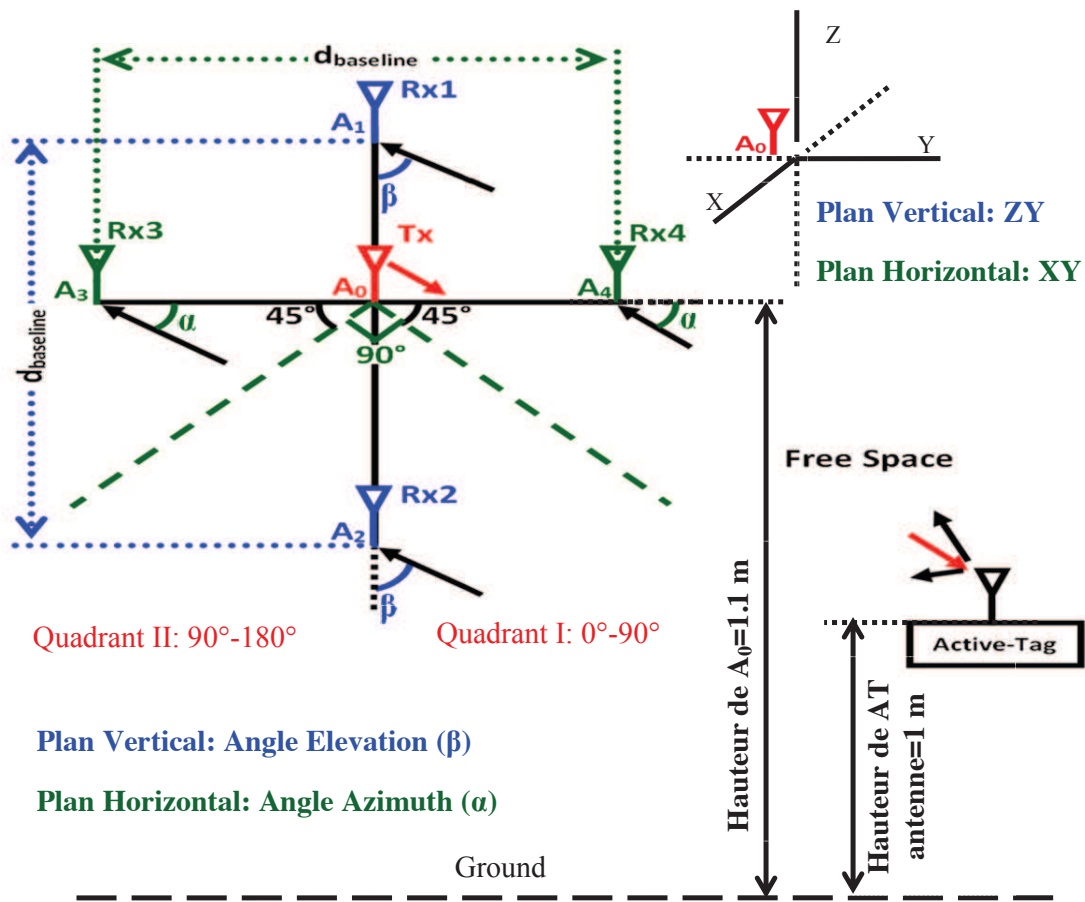


Fig. 8: Paramètres physiques à estimer pour une mesure 3D.

Afin de connaître les performances en terme d'erreur, nous avons cherché à estimer, grâce à la méthode développée, 19 positions différentes connues d'un badge (Active Tag) vis à vis de la LBS dans le cas d'une situation LOS avec un nombre de trajets multiples faibles. Les distances radiales des 19 positions sont comprises dans l'intervalle $[0,9 \text{ m} - 1,25 \text{ m}]$. Les angles d'azimut (α) relevés pour les 19 positions sont compris dans l'intervalle $[45^\circ - 90^\circ]$. Les angles d'élévation (β) pour les 19 positions sont compris dans l'intervalle $[97^\circ - 101^\circ]$. Les mesures sont effectuées dans le Quadrant I (Fig.8) du fait de la structure symétrique du réseau d'antennes de réception.

Sur la Fig.9, nous présentons les résultats de mesure en terme de distance radiale et d'angle d'azimut (α) pour la mesure effectuée sur le plan horizontal (Rx3 Tx Rx4). Ces mesures (en rouge) sont comparées aux valeurs réelles (en bleu).

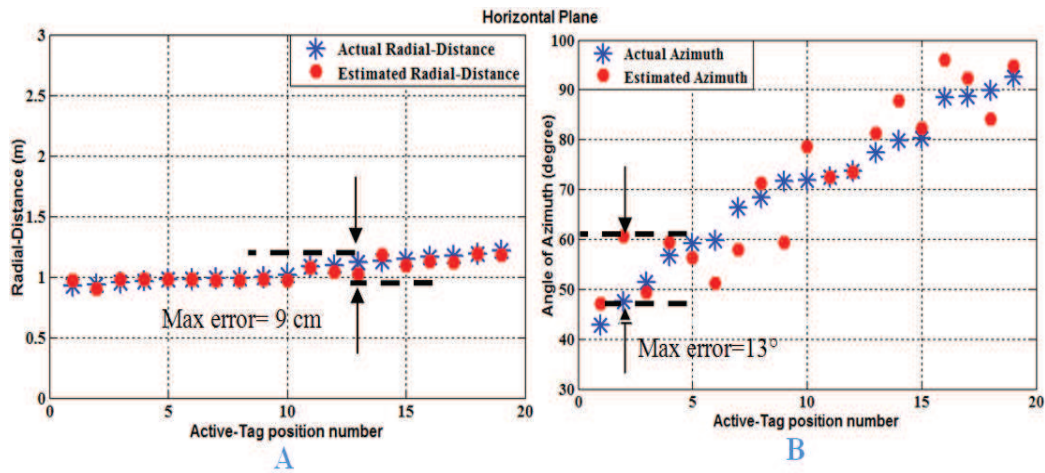


Fig. 9: 3D Distance radiale (A) et angle d'azimut (B) sur le plan horizontal.

Pour la distance radiale, l'erreur maximale est de 9 cm autour de 1,03 m Pour l'angle d'azimut, l'erreur maximale est de 13° pour les valeurs estimées de 60° . L'erreur quadratique moyenne sur l'angle d'azimut est de 5° .

Sur la Fig.10, nous présentons les résultats de mesure pour les distances radiales et les angles d'élévation (β) pour les 19 positions relevés sur le plan verticale (Rx1 Tx Rx2). Ces mesures (en rouge) sont comparées aux valeurs réelles (en bleu).

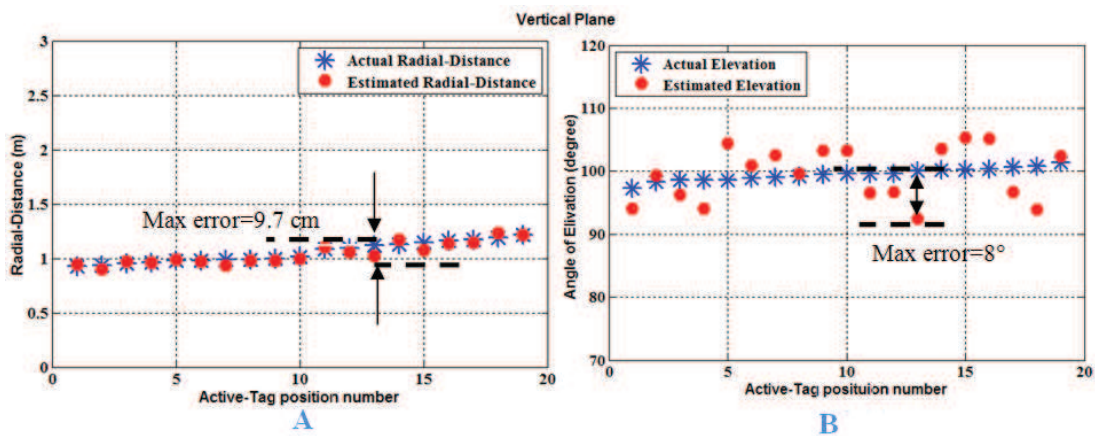


Fig. 10: Distance Radiale (A) et Angle d'élévation (B) sur le plan vertical.

Pour la distance radiale, l'erreur maximale est de 9.7 cm autour de 1,02 m Pour l'angle d'élévation, l'erreur maximale est de 8° pour les valeurs estimées de 92°. L'erreur quadratique moyenne sur l'angle d'élévation est de 4°.

Une campagne de mesure a aussi été effectuée afin de connaître la distance radiale maximale (ou portée) qui peut être mesurée par le système. La distance maximale mesurée est de 6,7 m. Sur ce champ de mesure, l'erreur quadratique moyenne est de 18,2 cm avec un erreur maximale observée de 36 cm à 5,1 m.

Dans un second temps nous avons introduit un réflecteur important ajoutant un trajet indirect superposé aux trajets directs décrits dans la situation précédente. En association avec la bande de fréquence utilisée, l'influence du réflecteur devient faible lorsque celui-ci propose un écart de trajet entre le trajet direct (tag antenne de réception du récepteur) et un trajet réfléchi (par le réflecteur) supérieur à 30 cm.

Une analyse permettant d'estimer l'impact de la largeur de la bande de fréquences sur les performances du système a été entreprise. Nous avons comparé, dans un premier temps, les résultats obtenus dans la même situation pour une bande de fréquences utilisée de 1 GHz et une bande de fréquences de 500 MHz. Dans les 2 cas et pour une position fixe et prise aléatoirement, le nombre N de cycles complets des signaux de battement en bande de base sur les 4 chaînes de réception pour 1GHz et 500 MHz sont 27 et 13 respectivement. L'erreur quadratique moyenne sur la distance radiale reste quasi identique. En théorie, l'estimation de la position du badge peut être effectuée avec N=1. A partir de cette valeur nous pouvons calculer la bande de fréquences minimale pour le signal FMCW. Le rapport (bande passante/N) reste le même et ne varie pas une distance radiale fixée. Elle s'écrit comme

$$\left. \begin{array}{l} \frac{Bandwidth}{N} = \frac{1GHz}{27} = 37MHz / cycle \\ \frac{Bandwidth}{N} = \frac{500MHz}{13} = 38MHz / cycle \end{array} \right\} Constant = \frac{(37 + 38)}{2} = 37.5MHz / cycle \quad 8$$

Par conséquent, la bande passante minimale requise par le système pour un cycle complet est de 37,5 MHz. Toutefois, avec le bruit du à la carte d'acquisition, la méthode DMDT n'apparaît plus très fiable du aux nombreux passages par 0 pour un seul cycle. Pour la suite de ce travail, une étude plus complète devra être menée pour estimer la bande de fréquences minimales pour une configuration donnée.

L'une des hypothèses de base de ce système est l'utilisation sous contrainte d'onde plane (PWC). Sur la Fig.11, nous présentons ce problème pour une localisation à 2 dimensions (distance radiale et azimut α).

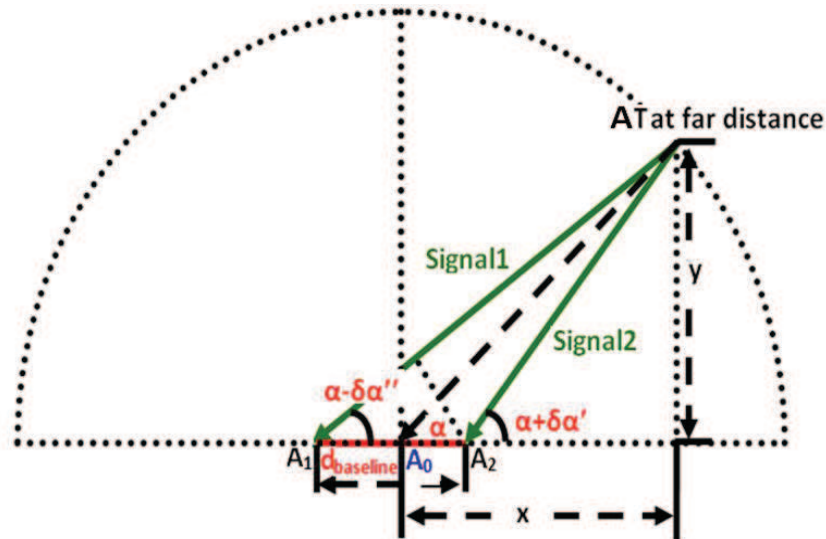


Fig. 11: Déviation angulaire et onde plane.

On suppose dans ce cas que les trajets des signaux issus du badge (AT) arrivent sur les 2 antennes de réception (A_1 et A_2) de manière parallèle. Ceci n'est vérifiée que pour une distance radiale assez grande par rapport à d_{Baseline} . En pratique, on admet une tolérance ($\delta\alpha$) définie par un cahier des charges et qui peut s'écrire:.

$$\delta\alpha = \frac{\delta\alpha' + \delta\alpha''}{2} = \frac{1}{2} \left(\tan^{-1} \frac{\tan \alpha}{1 - \left(\frac{1}{B_f \cos \alpha} \right)} - \tan^{-1} \frac{\tan \alpha}{1 + \left(\frac{1}{B_f \cos \alpha} \right)} \right) \quad 9$$

Où, B_f est le facteur de base (B_f), définie comme le rapport entre la distance radiale et la demi-longueur de ligne de base ($d_{baseline}$). La condition d'onde plane peut être vérifiée pour une petite valeur de $\delta\alpha$. Ceci peut être obtenu soit en augmentant la distance radiale soit en diminuant $d_{baseline}$. Par conséquent, l'analyse de la déviation angulaire porte sur les effets des paramètres B_f et $d_{baseline}$.

Un compromis est aussi à prendre ne compte, plus la ligne de base $d_{baseline}$ est petite plus les déviations angulaires sont faibles mais l'erreur sur la mesure angulaire sera grande. grande ligne de base permet une grande précision sur la mesure angulaire mais impose une distance radiale minimale importante.

Sur la **Fig.12**, nous avons reporté l'estimation des erreurs quadratiques moyennes pour la distance radiale et la mesure d'angle en fonction de la longueur de ligne de base (Baseline length) pour une distance radiale donnée. Les courbes bleue, rouge représentent les erreurs quadratiques moyennes pour la mesure d'angle, de distance radial respectivement. La courbe noire représente l'évolution de la déviation angulaire $\delta\alpha$.

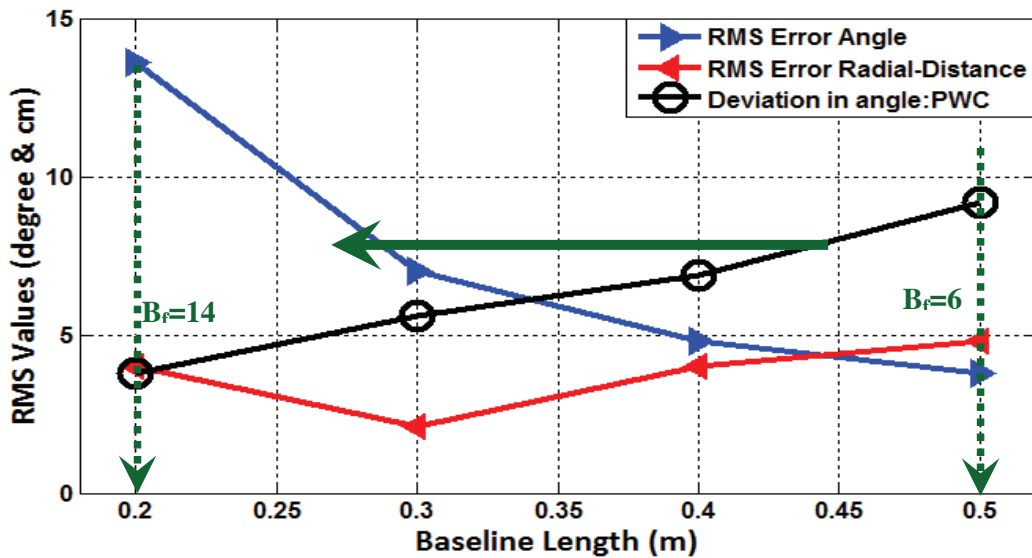


Fig. 12: Erreur quadratique moyenne (RMS) pour la distance radiale et la mesure d'angle, évolution de la déviation angulaire $\delta\alpha$.

Nous remarquons que l'erreur quadratique moyenne (rms) l'estimation de la distance radiale ne dépend pas de la longueur de ligne de base. Seul la mesure d'angle est affectée en

relation avec la déviation angulaire constatée. Nous pouvons donc conclure ici que les conditions d'onde planes (PWC) auront une réelle influence que sur la mesure angulaire.

Chapitre 5. Conclusion

Dans cette thèse, nous avons démontré la faisabilité d'un système de localisation 3D (ILS), ne nécessitant qu'une station de base, de badges actifs pour des environnements indoor présentant un milieu de propagation LOS incluant des trajets multiples. L'originalité de ce système est que, contrairement aux systèmes généralement rencontrés, un seul point d'ancrage connu est nécessaire. L'avantage de cette structure est qu'il n'est pas obligatoire de gérer une horloge de synchronisation précise entre les différents ancres permettant la localisation. Le système développé est basé sur la structure d'un système radar monopulse multistatique utilisant typiquement un signal FMCW et permet de connaître l'estimation de la position relative, par rapport à la station de base en terme de distance radiale, azimuth, et élévation, d'un badge dédié. La bande totale de fréquences exploitées est la bande UWB européenne [6-8.5 GHz] divisée en 2 canaux, le premier couvrant [6-7 GHz] et le second [7.5-8.5GHz] afin de réaliser une communication de type "full duplex" entre la station de base et le badge à localiser en limitant les problèmes d'interférences entre le canal montant et le canal descendant. Afin d'augmenter la robustesse du système vis à vis des trajets multiples et du fouillis générés naturellement par le milieu de propagation indoor, 2 types d'antennes à polarisation circulaire compactes adaptées pour fonctionner dans la bande [6-8.5 GHz] ont été développées. Le premier modèle exploite une polarisation circulaire simple (droite ou gauche) et est utilisé par la station de base de localisation. Le second modèle est à double polarisation circulaire et est utilisé sur le badge. Pour valider le principe, nous avons effectuées l'estimation de position en 3 dimensions du badge sur 19 positions préalablement déterminées. Les erreurs quadratiques moyennes sur les 3 paramètres (distance radiale, azimuth, élévation) sont de 4 cm , 5° et 6° respectivement.

ABSTRACT

Regular and accurate position monitoring of elderly patients suffering from dementia related problems (Alzheimer) is always required. To assist their monitoring a compact and a less complex indoor localization system is required. This thesis is dedicated towards this noble task of continuous position monitoring.

The thesis aims to develop an Indoor Localization System (ILS) for three-dimensional position estimates with respect to single Localization Base Station as an anchor. The designed ILS uses an Active-Tag (AT) as remote target. The system uses the monopulse multistatic FMCW radar principle and operates in the European UWB (6-8.5 GHz) frequency band. The designed ILS uses the frequency-difference of arrival (FDoA) and the phase-difference-of-arrival (PDoA) techniques for the radial-distance and the angles (azimuth and elevation) estimates. In order to validate this system, a prototype of the ILS is built at Telecom ParisTech, France.

The two main units of the ILS are: Localization Base Station (LBS) and Active-Tag (AT). The LBS acts as a monopulse radar system, a 6-7 GHz FMCW signal is used as the reference signal which is subsequently up-converted to 7.5-8.5 GHz and then is transmitted towards the AT. Here, AT acts as an active-transponder for duplex communication and the received signal (7.5-8.5 GHz) is again retransmitted towards the LBS in 6-7 GHz frequency bandwidth after frequency transposition. The retransmitted signal (6-7 GHz) is received by the four receiver antennas of the LBS which are placed spatially on an orthogonal base centered about the transmitter antenna which forms two orthogonal planes.

The LBS measures the frequencies of sinusoidal baseband signals between transmitted and received signals via the AT. The beat frequency data give the range/radial-distance between LBS and AT using classical FMCW radar approach. The azimuth and elevation angles are determined from the PDoA between baseband signals.

The *objective of designed ILS* is to have a localization system with accuracy in few centimetres in Line-of-Sight condition. The system is designed to use a single anchor, and simultaneously addressing the indoor challenges such as multipaths, strong signal attenuations, reflections, etc.

LIST OF CONTENTS

ACKNOLEGMENT	5
RESUME	7
ABSTRACT	27
LIST OF CONTENTS	29
LIST OF ABBREVIATIONS.....	34
INTRODUCTION	37
Chapter 1. Indoor Localization System	42
1.1 Introduction	42
1.2 Indoor Localization System	42
1.2.1 Classification of Wireless Network Used Localization System	44
1.2.1.1 Available Wireless Communication Network (AWCN).....	44
1.2.1.2 Own Wireless Network (OWN).....	44
1.3 Algoritm	44
1.3.1 Triangulation.....	44
1.3.1.1 Time-Difference-of-Arrival (TDoA).....	46
1.3.1.2 Angle-of-Arrival (AoA).....	48
1.3.1.3 Received Signal Strength Indicator (RSSI).....	49
1.3.2 Scene Analysis.....	50
1.3.3 Proximity.....	50
1.4 Performnce Matrics	50
1.5 Indoor Localization System and Solutions.....	51
1.5.1 Survey of Localization System	51
1.5.2 Proposed Solution for Indoor Localization System.....	53
1.6 Conclusion.....	56

REFERENCES	58
Chapter 2. Developed Method	69
2.1 Introduction	69
2.2 FMCW Radar Basics.....	70
2.2.1 Dual-Mixer Time-Difference Technique	74
2.3 Architecture of ILS.....	77
2.4 Developed Localization Method	80
2.4.1 2D Measurements	81
2.4.2 3D Measurements	84
2.4.3 Concept Validation	86
2.4.4 Constraints	89
2.4.4.1 Parallel Wave Condition	89
2.4.4.2 Mapping of Baseline into AoA: Least Count.....	94
2.4.4.3 Far-Field Approximation.....	95
1.6 Conclusion.....	96
REFERENCES	98
Chapter 3. Realization of Indoor Localization System	103
3.1 Introduction	103
3.1.1 System Integration and Management.....	103
3.1.1.1 Equal-Split Divider.....	105
3.1.1.2 Mixer	106
3.1.1.3 Filter	109
3.1.1.4 Amplifier	110
3.2 Circular Polarization Antenna.....	112
3.2.1 Circular Polarised Planar Antenna-Single Port.....	115

3.2.1.1	Return Loss.....	117
3.2.1.2	Axial Ratio	118
3.2.1.3	Gain & Radiation Pattern	119
3.2.1.4	Conclusion.....	121
3.2.2	Dual Circular Polarised Planar Antenna-Double Ports.....	121
3.2.2.1	Return Loss & Crosstalk	129
3.2.2.2	Axial Ratio	131
3.2.2.3	Gain & Radiation Pattern	131
3.2.2.4	Conclusion.....	134
3.3	Realized 3D ILS	134
3.4	Conclusion.....	138
	REFERENCES	141
Chapter 4.	ILS Performance and Analysis.....	146
4.1	Introduction	146
4.2	Field-Measurements	146
4.2.1	Signal Computation	148
4.2.2	System Calibration.....	157
4.3	Performance in Line-of-Sight Case.....	161
4.3.1	2D Field-Measurements	161
4.3.2	3D Field-Measurements	165
4.3.3	Maximum Radial-Distance	170
4.3.4	Performance in Presence of strong Scatter (Multipath Effects).....	175
4.4	Performance in Non-Line-of-Sight Case.....	187
4.5	Impact of Bandwidth.....	189
4.6	ILS Constraints.....	193
4.6.1	Plane Wave Condition	193

4.6.2	Coupling Effects	203
4.7	Conclusion.....	205
	REFERENCES	208
Chapter 5.	Conclusions and Perspectives	210
5.1	Conclusions.....	210
5.2	Possible Upgradation and Otimization.....	211
5.2.1	Architectural Level: 3D positioning with three antenna structure.....	211
5.2.2	Improvement in Non-Line-of-Sight Condition.....	212
5.2.3	Multiple Active-Tag Detection Scheme	214
5.2.4	Synchronization between Active-Tag and LBS.....	215
5.2.5	Integration of system in MMIC Technology	217
	REFERENCES	220
	LIST OF PUBLICATIONS	225
	ANNEXURE A.....	228
	ANNEXURE B.....	230
	ANNEXURE C	241
	ANNEXURE D.....	243
	ANNEXURE E	244
	ANNEXURE F	245
	LIST OF FIGURES	247
	LIST OF TABLES.....	252
	REFERENCES	254

LIST OF ABBREVIATIONS

AoA	Angle-of-Arrival
APR	Active Pulse Reflector
AR	Axial Ratio
AT	Active-Tag
AWCN	Available Wireless Communication Network
Bf	Baseline-Factor
BLC	Branch Line Coupler
BW	Bandwidth
CP	Circular Polarization
DMTD	Dual Mixer Time Difference
DoA	Direction of Arrival
FMCW	Frequency Modulated Continuous Wave
FDoA	Frequency-Difference-of-Arrival
FSPL	Free Space Path Loss
GaN	Gallium Nitride
GaAs	Gallium Arsenide
GPS	Global Positioning System
HP	Horizontal Polarization
HBLC	Hybrid Branch Line Coupler
ILS	Indoor Localization System
LP	Linear Polarization
LHCP	Left Hand Circular Polarization
LBS	Localization Base Station
LO	Local Oscillator
LoS	Line-of-Sight
LNA	Low Noise Amplifier
MMIC	Monolithic Microwave Integrated Circuit
NFA	Near-Field Approximation
NLoS	Non-Line-of-Sight
OWN	Own Wireless Network
PDoA	Phase Difference of Arrival
PWC	Plane Wave Condition

RF	Radio Frequency
RHCP	Right Hand Circular Polarization
RLB	Return Loss Bandwidth
RMS	Root-Mean-Square
RSSI	Received Signal Strength Index
RTID	Radio Triggered ID
RToF	Round Time of Flight
SAW Filter	Surface Acoustic Wave Filter
SiGe	Silicon Germanium
SMAA	Successive Mean Approach Algorithm
SNR	Signal-to-Noise Ratio
SQNR	Signal-to-Quantization-Noise Ratio
TDoA	Time Difference of Arrival
TSoA	Time Sum of Arrival
ToA	Time of Arrival
ToF	Time-of-Flight
UWB	Ultra-Wide Band
VNA	Vector Network Analyzer
VP	Vertical Polarization
2D	Two-Dimension
3D	Three-Dimension



INTRODUCTION

Low penetration of GPS (Global Positioning Signal) in indoor has put a challenge to design an accurate indoor localization or navigation system. Additionally, the growing demand of accuracy (in few centimeters) has also influenced the architectural design including measurement methods. Different approaches of the navigation systems are used for estimating the position close to actual one, particularly in robotic industries. This leads to the use of UWB (ultra wideband) technology which makes possible to achieve a high accuracy by the virtue of its very fine time-based signal which also helps in resolving the extra delays due to multipaths [1].

A typical Indoor-Localization-System (ILS) uses at least three anchors to estimate the position of remote target. However, the number of anchors could be reduced to two with the use of Direction-of-Arrival [2] technique which requires at least two interrogators. Furthermore, a single anchor point with four interrogators can also be used for the three-dimensional localization [3]. Additionally, the localization system can be implemented through the FMCW Radar systems which would give accuracy in few centimeters [4].

In addition the use of active-tag [5] as a remote target could also help in reducing the backscatter signals through the use of frequency transposition so that the intended signals are easily filter-out from the backscattered signals. Hence, this helps in improving the performance of the system in Line-of-Sight (LoS) case.

The main objective of this thesis is to develop a compact Indoor Localization System with accuracy in centimeters through a single anchor which has four interrogators. This thesis is composed of four chapters.

Chapter 1 is dedicated to the state of the art design of indoor localization systems. Brief introduction about the ILS is discussed in this chapter. Some algorithms such as trilateration related to the position estimates are presented here along with the different measurement methods such as time of arrival (ToA). A survey on the currently available system are performed which gives a fair knowledge about the advantages of the various indoor localization systems. After that, the features and techniques about the proposed ILS are highlighted in this chapter.

In **chapter 2**, the mathematical expressions of proposed localization system are derived and explained here. The architecture of Indoor Localization System for 3D positioning is outlined in this chapter. This positioning requires an orthogonal antenna structure which consists of four identical but separate interrogators (receivers) as a single anchor. Hence, this approach reduces the necessary requirement of three or four anchors to one. Initially, the system concept is validated by performing some experiments under controlled environment. Additionally, the constraints related to the proposed design such as parallel wave conditions are mathematically validated for the better understanding of system performance.

Next, a built prototype of the ILS is presented in **Chapter 3**. The prototype is completely based on the architecture discussed in the second chapter. The characterization of different RF components such as antennas, mixers are presented and explained here. For the use of circular polarization diversity, two compact patch antenna designs are presented and discussed in this chapter. Then, the management of the system is outlined, and further the power consumptions by the built prototype are also discussed and explained.

The performance analysis of the ILS is presented in **Chapter 4**. The built prototype of the proposed Indoor Localization System is used for the field-measurements in a real indoor environment. The 2D and 3D positions can be estimated by the prototype. The results are discussed and explained while considering the different indoor conditions such as line-of-sight. Experiments are also carried out for estimating the maximum range that could be achieved by the system. Besides these, some constraints such as plane wave condition are also tested through the field measurements for comparative analysis with the theoretical concepts and are presented in the second chapter.

Finally, the conclusion of thesis work is presented along with some future work plans. For example, the implementation of multiple tags is proposed. Also, the developed system can be used for the Received Signal Strength measurements which would facilitate the implementation of Scene Analysis algorithm such as Fingerprinting for the better position estimation in non-line-of-sight case. Hence, the developed system may be used for hybrid measurement technique as time-based and received- signal-strength based methods.



Reference

- [1] I. Guvenc, C. C. Chong, and F. Watanable, "NLOS identification and mitigation for UWB localization systems," Proc. Of Wireless Communication and Networking Conf., pp. 1571-1576, 2007.
- [2] V. Y. Vu, and A. B. Delai, "Digital Solution for inter-vehicle localization system by means of Direction-Of-Arrival," Int. Symp. on Intelligent Signal Processing and Communication Systems (ISPACS 2006), pp; 875-878, 2006.
- [3] A. B-Delai, J. C. Cousin, R. Ringot, Ahmed Mamouni, and Y. Leroy, " Microwave Short Baseline Interferometers for Localization Systems," IEEE Trans. On Instrumentation and Measurement, vol; 50, no; 1, pp. 32-39, Feb 2001.
- [4] B. Waldmann, R. Weigel, R. Ebel, and M. Vossiek, "An ultra-wideband local positioning system for highly complex indoor environments," Int. Conf. On Localization and GNSS, ICL-GNSS 2012, pp. 1-5.
- [5] M. Vossiek, and P. Guldenl, "The Switched Injection-Locked Oscillator: A Novel Versatile Concept for Wireless Transponder and Localization Systems", IEEE Transactions on Microwave Theory & Technique, vol. 56, no. 4, 2008, pp. 859-866.

Chapter 1. Indoor Localization System

1.1 Introduction

A better and meaningful wireless communication have pushed the human race into an advance stage of social-secure, and the desire of seamless wireless connectivity has given birth to the localization/navigation of person or different useful items. For example, people who are suffering from dementia (Alzheimer) need continuous monitoring and a localization-system can play an important role in this regard. The localization also helps in economy growth such as automation industry, tourism, and safety (during natural or man-made hazards), and in defence (positioning of soldiers in a battle-field). Some applications based on localization are reported in [1-6] which explain the importance of an indoor localization system.

One can define the localization system (LS) as a system which assists us in estimating the position of a remote target under scan, and the target could be an object or a person. The LS tells the target position with respect to the known anchor/s. If the localization system is designed to operate in a confined area then this is known as **Indoor Localization System (ILS)**. The ILS has numerous applications. It can only be realized if it utilizes a low cost technology with acceptable accuracy according to requirement.

This chapter describes the overall information about the indoor localization system. **Section 1.2** presents the basic concepts behind the system and the different algorithms are discussed in **Section 1.3**. The performance metrics and some solutions are discussed in **Section 1.4-1.5**. Finally, the chapter ends with the conclusion in **Section1.6**.

1.2 Indoor Localization System

Today, Global Positioning System (GPS) is a well known buzz-word for navigation in outside environment and almost all smart phones have this service [7-9]. The received GPS signals are not strong enough, especially inside a building. Because of the very weak signal reception from the GPS network within an indoor environment, it is ruled out for the indoor applications. The reason behind such weak signal is the strong attenuation which is introduced by the concrete-buildings and signal becomes almost unreadable by the GPS-receiver such as phones inside a building. For outdoor navigation, the GPS needs at least four

satellites for the position estimation of a target through the trilateration method. Here, the target's distances are measured through each satellite and these distance informations are used for target's position estimate; this has been illustrated in **Fig 1.1** [10].

The distance informations obtained through four satellites are used by the target which in this case is happened to be a man having a GPS-receiver for position estimation by the trilateration method [11].

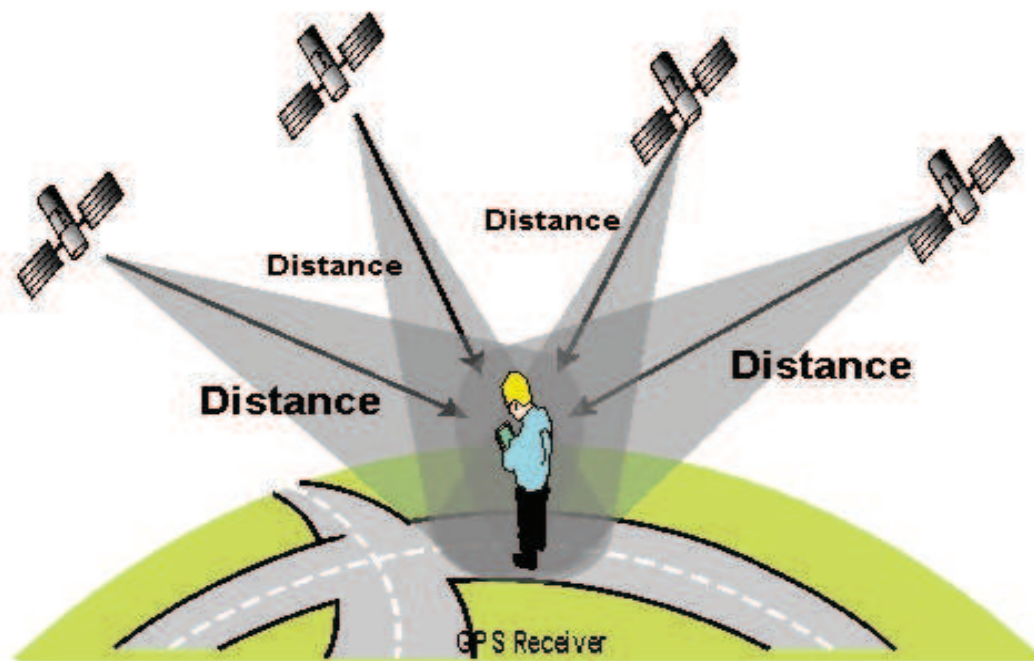


Fig 1.1: GPS methodology for position estimate [10].

This concept of position estimation, trilateration method, can be used in indoor positioning by replacing the satellites with the anchors and the GPS-receiver can be replaced by a system which can perform the necessary computations related to trilateration method. Some application of such system systems are reported in [12-15].

Although, the direct use of GPS signal is not a viable option but through the use of GPS-Repeaters, it can be used as presented in [16]; here, the repeaters collect the best available GPS signal and then signal is retransmitted without any further treatment other than amplification. To do a partial conclusion, the case of the well known GPS system is a good example: four anchors are required. Hence, the important issue for localization is the

availability of continuous wireless network to perform the necessary estimations such as distance. Therefore based on the use of various known wireless network by the Indoor Localization System [1-6], the localization system can be broadly classified into two main groups [12-21]: one which uses the available wireless communication network (AWCN) and second which uses own wireless network (OWN).

1.2.1 Classification of Wireless Network Used by Localization System

1.2.1.1 Available Wireless Communication Network (AWCN)

This class of systems are those which mainly use the freely available wireless communication networks such as GPS, WiFi, and Cellular-Network [21-25]. The AWCN based systems are commonly utilized for the services related to the public navigation inside a museum or big shopping-mall. These kinds of systems do not require initial investment but generally they suffer of a low precision in distance.

1.2.1.2 Own Wireless Network (OWN)

These systems use their own wireless sensor network for the localization and are mainly based on the radar principle [26-29]. This type of system generally has good precision and is commonly deployed for the industrial purpose. It often shows precision within meter, but it requires initial investment in network infrastructure building. Moreover, the deployed Indoor Localization System uses different algorithm such as triangulation for the position estimates. Some of the well known algorithms are presented in next section.

1.3 Algorithm

The algorithm consists of a number of procedures to estimate the position of a target. Some known algorithms are Triangulation, Scene Analysis, and Proximity. These algorithms are developed for better estimation of a target location by reducing the measurement errors through signal processing. Brief information about these algorithms is presented in this section.

1.3.1 Triangulation

Triangulation uses the geometric properties of triangles to estimate the remote position of the target. It has two derivations: *Angulation* and *Lateralation*. Angulation locates the target

by the intersection of several pairs of angle direction lines, each formed by the circular radius from an anchor. Lateration estimates the position target by measuring distances (radial-distances) with respect to different anchors. Sometimes, it is also called as range measurement techniques. The measurement of radial-distance is usually done through different approaches such as received signal strength (RSS) or time based approach, ToA/TDoA (Time-of-Arrival/Time-Difference-of-Arrival). After knowing three distance informations, the position of the remote target is located through the intersection of radial-distance. For the position estimates often three anchors are used and hence it is called as triangulation. The triangulation is illustrated in **Fig 1.2**.

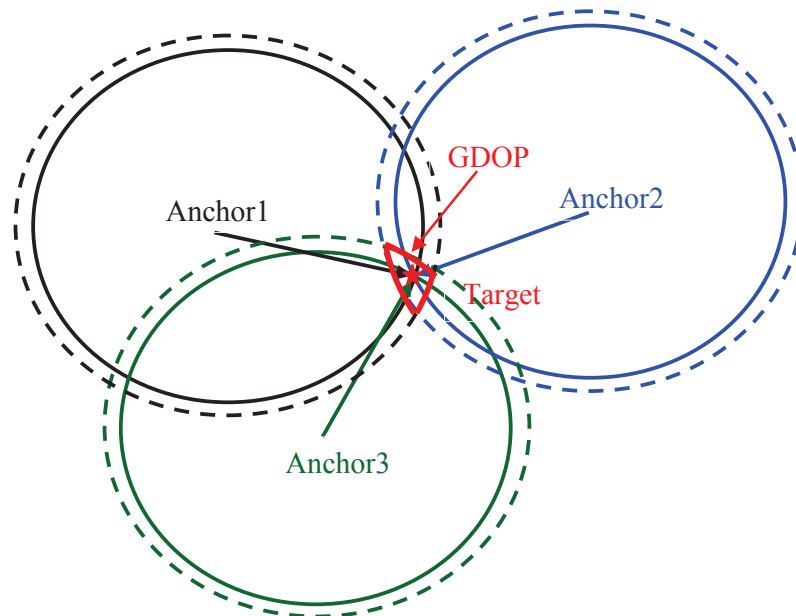


Fig 1.2: Triangulation algorithm.

The three different anchors are noted as Anchor1-3 in the above figure. The intersection obtained by the estimated radial-distances by the three nodes is the location of target. The estimated position is marked by a red-star. However, because of the error in estimated radial-distance the intersection between circles does not intersect at a single point and it forms an area which is known as Geometric-Dilution-of-Precision (GDOP) [30].

These radial-distances are often obtained through different measurement techniques such as time-based or received signal strength based measurement techniques. Some commonly used measurements techniques are angle-of-arrival (AoA), time-of-arrival (ToA), and Received Signal Strength (RSS). These techniques are explained below.

1.3.1.1 Time-Difference-of-Arrival (TDoA)

This is a time based approach which uses the information about the travel time of a radio signal from a signal transmitter to a remote receiver. This is based on the fact that the time taken by a signal to travel from point A to point B (often known as time-of-flight) is directly proportional to the distance between the two points, $d=c\tau$, where c is the speed of light 2.98×10^8 m/s and τ is the time-of-flight (ToF). There are three general ways of using the time of flight as Time-of-Arrival (ToA), Time-Difference-of-Arrival (TDoA), and Time-Sum-of-Arrival (TSoA). TSoA is similar to TDoA and is not so common. The only difference is that the TDoA uses several hyperbolas (position obtained by 1.3 is an equation of hyperbola) to determine the position of target while the TSoA uses several ellipses (obtained position when plotted form ellipse) as mentioned in [31]. Therefore, we only discuss about the TDoA and ToA.

Assume that we can measure the ToA of a signal transmitted by the remote target at N_A number of anchors with their prior knowledge of positions. This measurement is typically considered the synchronization between N_A anchors and target. Let τ_i be the time of flight between the target position (x, y) and the i -th anchor position (x_i, y_i) . Assume that the signal was transmitted at time t_m and it reaches to i -th anchor at t_i . Therefore, the measured τ_i value can be translated with the target position as

$$t_i = \left. \begin{array}{l} t_i = \tau_i + t_m \\ \sqrt{(x_i - x)^2 + (y_i - y)^2} \\ c \end{array} \right\} + t_m \quad 1.1$$

The above relationship cannot be solved because it has three unknowns (x , y , and t_m). However, we can eliminate one of these unknowns (t_m) by taking the difference between two arrival time measurements at two anchors ($i \neq j$)

$$t_i - t_j = \left. \begin{array}{l} t_i - t_j = (\tau_i + t_m) - (\tau_j + t_m) = (\tau_i - \tau_j) \\ \sqrt{(x_i - x)^2 + (y_i - y)^2} - \sqrt{(x_j - x)^2 + (y_j - y)^2} \\ c \end{array} \right\} \quad 1.2$$

Now, we have one relationship but still two unknowns (x , and y) which still cannot be solved. But, one more relationship can be obtained with respect to another anchor (x_k, y_k) . Therefore, we can define two relationships as

$$\left. \begin{aligned} t_i - t_j &= \frac{\sqrt{(x_i - x)^2 + (y_i - y)^2} - \sqrt{(x_j - x)^2 + (y_j - y)^2}}{c} \\ t_i - t_k &= \frac{\sqrt{(x_i - x)^2 + (y_i - y)^2} - \sqrt{(x_k - x)^2 + (y_k - y)^2}}{c} \end{aligned} \right\} \quad 1.3$$

We now have two nonlinear relationships and two unknowns. The two nonlinear relationships provide one or two solutions (positions), but in practice only one position is possible. So, in order to confirm a particular position we need one measurement at fourth anchor position. This method is known as TDoA. Sometimes, it is also known as hyperbolic positioning because the position (x, y) obtained from 1.3 follows the hyperbola locus.

In fact, the position of remote target can also be obtained with three anchors by considering only three measurements if we have the prior knowledge of starting time (t_m). This can be expressed as

$$\left. \begin{aligned} t_i - t_m &= \frac{\sqrt{(x_i - x)^2 + (y_i - y)^2}}{c} \\ t_j - t_m &= \frac{\sqrt{(x_j - x)^2 + (y_j - y)^2}}{c} \end{aligned} \right\} \quad 1.4$$

Thus, the prior knowledge of t_m will require two measurements and for the confirmation of position we need one more measurement at third anchor. This approach is known as the ToA. Since it uses extra information, prior information about t_m , compared to the TDoA it requires one less anchor than TDoA. Additionally, the locus of ToA estimated position follows (1.4 is an equation of circle) a circular curve unlike the hyperbola in TDoA [32]. The time of flights can be estimated by different ToA estimation techniques such as correlation-based approach, deconvolution methods, maximum likelihood (ML)-based methods.

Furthermore, the number of anchors can be reduced to two if the angle-of-arrival technique is used. The position of the remote target is estimated by coupling the ToA technique and the angle-of-arrival (AoA) technique. The AoA technique and its application in localization are explained in the subsequent section.

1.3.1.2 Angle-of-Arrival (AoA)

The angle-of-arrival (AoA), also known as Direction-of-Arrival (DoA), locates the angle of target position by determining the angle of incidence at which signals arrive at the receiving antenna array. However, for positioning it requires at least three anchors (having antenna array) and locates the target by the intersection of angle direction lines using triangulation algorithm. The commonly used configuration of AoA is illustrated in **Fig 1.3**.

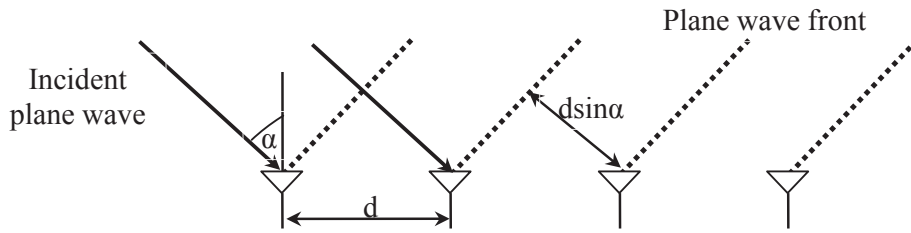


Fig 1.3: Angle-of-Arrival technique.

The AoA (α) can be expressed as the function of signals phase difference between two consecutive antenna elements which is estimated from signal complex envelopes or correlation products between receivers attached to antenna elements. The phase difference between signals are expressed as

$$\Delta\phi = \frac{2\pi d}{\lambda} \sin \alpha \quad 1.5$$

Where, $\Delta\phi$ is the measured phase-difference-of-arrival (PDoA) between two adjacent antenna elements, λ is the wavelength of signal carrier, and d is the separation between two antenna elements. Hence, knowing the measured value of PDoA leads to the determination of angle-of-arrival (α). MUSIC (multiple signal classification) algorithm is a well known application of AoA technique [33]. A lot more direct application of AoA technique in localization is reported in different works [34-38]. However, compared to ToA estimation techniques, the AoA implementation needs the antenna arrays and each antenna element needs to be connected to a receiver chain which is a costly affair. Moreover, the power consumptions of these receiver chains are relatively high. Thus, its implementation expects higher design complexity and power consumption.

Typically, the PDoA can be measured with the two antenna elements and these two antennas can also be used for the ToA measurements, too. A fine example of localization system based on AoA and ToA techniques are reported in [39-40]. Hence, it is possible to locate the remote target with two anchors. This gives a higher flexibility to AoA compared to ToA/TDoA which needs at least three anchors. But, in Non-Line-of-Sight (NLoS) condition, the ToA based system estimates positive-biased error because the first arriving multipath component travels a distance that is more than the actual Line-of-Sight (LoS) distance as explained in the second chapter of [32]. This (NLoS case) is also a measure drawback in AoA implementation. However, another approach based on the received signal strength (RSS) technique can be used for the position estimates. The use of RSS technique is explained in the next section.

1.3.1.3 Received Signal Strength Indicator (RSSI)

In this approach, the power level of a received radio signal is used to estimate the position of a remote target and the measured power is denoted as Received Signal Strength Indicator (RSSI). The RSSI measurements are translated into distance estimations either by the theoretical radio propagation modelling or by the radio fingerprinting [41]. Typically, the modelling of theoretical radio propagation channel is not an easy task as the received signals are continuously affected by the complex nature of indoor environment such as distance from the transmitter, multipath, and reflection from walls, buildings, floors. Hence, it is difficult to model such a complex environment which could present the characteristics of the signal in reality. But, the radio fingerprinting relies on the principle that the location of a target can be determined by correlating the current RSSI values to a Radio Map. The radio map is a data bank that contains the measured RSSI values from different anchor points which is built during an offline training phase. In this way the characteristics of the signal propagation in an indoor environment is saved in a data bank and the modelling of complex signal propagation is avoided. However, the training phase is quite time consuming process. Additionally, the dynamic nature of indoor environment demands continuous update of the radio map which jeopardizes the system performance [42]. However, fingerprinting is capable of alleviating some of the problems related to multipath and non-line-of-sight condition as mentioned in [41].

1.3.2 Scene Analysis

This algorithm utilizes the prior information about the power of radio signal for online comparison with the received power. In this case the RSSI is not used to estimate the value of the distance. Instead, the vicinity of the RSSI value with the preregistered RSSI values are compared, and a close comparison determines the position of the remote targets. Fingerprinting is a fine example of Scene Analysis algorithm. At least five algorithms are known so far using pattern recognition technique: probabilistic methods [43], k -nearest-neighbour (k NN) [44], neural networks [45], support vector machine (SVM) [46], and smallest M-vertex polygon (SMP) [47].

1.3.3 Proximity [48]

Proximity localization senses the close presence of target to well-known location information. Usually, it relies upon a dense grid of antennas (each linked to a receiver and its accuracy depends upon the grid density), each having a well-known position. When a mobile target is detected by a single antenna (with receivers), it is considered to be collocated with it but when more than one antenna detects the mobile target, it is considered to be collocated with the one that receives the strongest signal. This relatively simple method can be implemented by different types of physical media. In particular, the systems using infrared radiation (IR) and radio frequency identification (RFID) [48, 49] are often based on this method. Another example is the cell identification (Cell-ID) or cell of origin (COO) method. This method relies on the fact that mobile cellular networks can identify the approximate position of a mobile handset by knowing which cell site the device is using at a given time. The main benefit of Cell-ID is that it is already in use today and can be supported by all mobile handsets.

1.4 Performance Metrics

It gives the benchmark parameters upon which system performance can be observed [21]. The following performance benchmarks for an indoor localization system are considered: accuracy, complexity, scalability, robustness, and cost. These metrics are defined in **Table 1.1**.

Table 1.1
PERFORMANCE METRICS

Metrics	Definition
Accuracy	Degree of closeness of the measured value (in quantity) to that of actual (true) value
Complexity	Can be attributed to system architecture, computing complexity of localization algorithm, and rate of location update with the target
Scalability	Positioning scope, in terms of distance over which a system can perform under acceptable value of error
Robustness	Estimation of position under uncertainty conditions
Cost	Money, time (installation and maintenance), measurement units, weight, and energy

Accuracy (or location error) is the most important performance benchmark for a positioning system. Usually, mean distance error is considered as the performance metric, which is the average Euclidean distance between the estimated location and the actual location. The higher the accuracy, the better the system; however, there is often a tradeoff between accuracy and other characteristics. Most often higher accuracy comes with the complexity of system-design and high cost. To guaranty the robustness of the system in a harsh environment (indoor), it requires the increase in the number of anchors and the cost as well. Usually, the positioning performance degrades with the increase in distance between the anchor nodes and the target and becomes worst in the NLoS condition.

1.5 Indoor Localization System and Solutions

This section presents the analysis of different ILS in use. Later, some solutions for the thesis work are also discussed.

1.5.1 Survey of Indoor Localization System

The knowledge of the different algorithms and performance metrics help in understanding the different systems in use. There are two basic approaches for designing a wireless positioning system either develop a new wireless-network for locating a remote target/tag or use the existing wireless communication network such as cellular network, WiFi. Different types of wireless positioning systems are mentioned in [15-21]. Fig 1.4 illustrates the overview of different technologies in use which is a modified form of [21, 50].

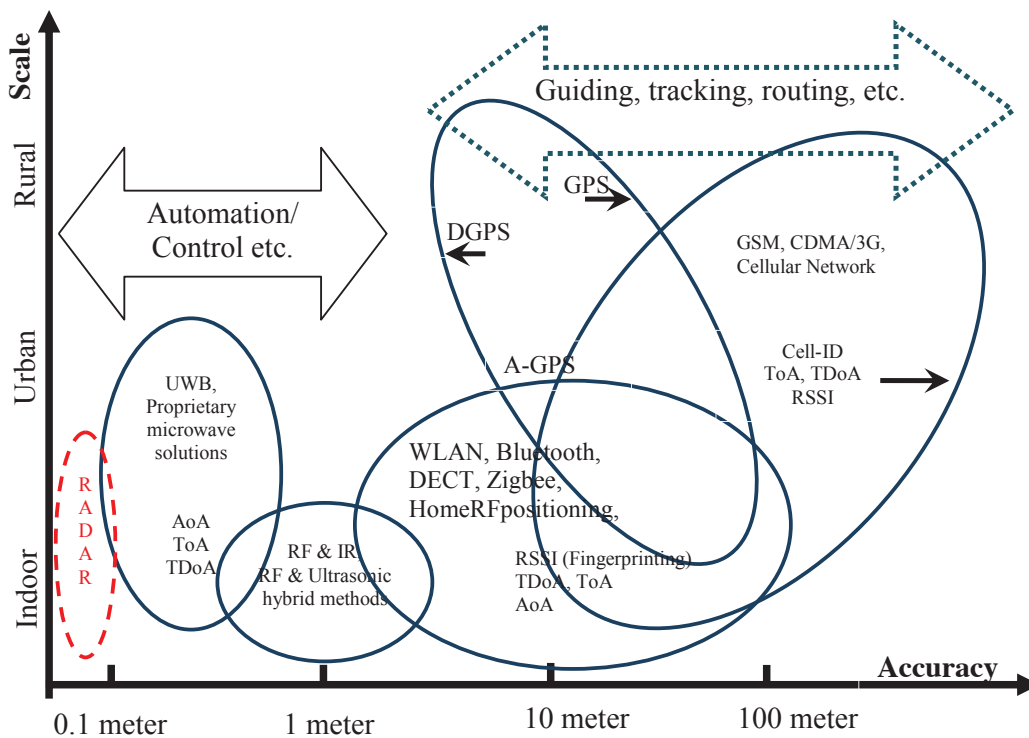


Fig 1.4: Outline of current wireless-base positioning system.

Fig 1.4 represents the different technology scales (defined as Indoor, Urban) versus the accuracy in meter expressed by a logarithmic scale. Only few systems are available in the centimeter accuracy. However, localization system based on the FMCW radar principle with UWB bandwidth has accuracy in few centimeters, more specifically <0.1 m as mentioned in [27]. The system which has used the UWB characteristics for time synchronization has achieved high accuracy (20cm). The UbiSence Company [51] has designed the UWB positioning system using AoA and TDoA. Siemens LPR design [50] uses RToF (Round Time of Flight) system with the help of FMCW radar principle, but this is only applicable in LoS case. These systems are mainly used in automation applications where high precision is required often in few centimeters.

The GPS (or its differential complement DGPS) [52] is widely used positioning system has low performance in dense urban areas compared to rural areas. Especially, the poor coverage of satellite signal in indoor environment decreases its accuracy and makes it unsuitable. SnapTrack, a Qualcomm company, has used assisted-GPS (A-GPS) technology for indoor localization with an average accuracy of 5-50 m. Effectively, the accuracy is better in

rural environment than in indoor which is marked by the left-tilted ellipse block. On the contrary, the right-tilted ellipse represents the systems based on cell-ID generally have low accuracy (20-200m) in rural environment than the densely covered urban environment.

There are several positioning systems available using WLAN technology [53-56]. These mainly use RSSI for positioning. SpotON [49] is a very well-known location sensing system and is based on RFID technology. Typical range of the RFID based system is very low, just between 1-2 m, and its implementation cost is quite high due to costly reference point. Besides, the positioning systems based on Bluetooth, Zigbee, Cell-ID or Cellular Network also have accuracy in meters [57-59].

There are lots of indoor positioning systems available and a brief idea can be drawn regarding system functionalities and its challenges. The study of different systems shows that the performance in centimeters from an indoor localization system in an indoor environment is a real challenge. The future trends of the positioning system will incorporate more complex and multiple positioning systems that is hybrid system like TIX [60]. A hybrid algorithm is presented in [61] using Propagation loss method and fingerprinting method. One example is the selective fusion estimation, SELELOC [62]. Other technologies such as optical (e.g., IR) inertial, and ultrasonic are latest trend in positioning system and its integration with the available system is a topic of sensor fusion. Localization based on UWB technology is also a promising research topic [63]. And the last thing, how to integrate indoor and outdoor positioning system is an interesting field for research.

1.5.2 Proposed Solution for Indoor Localization System

A number of wireless technologies are available for indoor positioning as mentioned in the previous **Section 1.5.1**. Depending upon the technology and the system designs, the performance of the systems are different. For example, ToA or TDoA has better performance in LoS compared to NLoS, however, the fingerprinting has better performance in NLoS condition compared to ToA or TDoA but not so in LoS. Additionally, a number of anchors are required for the target position estimate. For example, TDoA needs at least four anchors. Fingerprinting also needs a number of anchors for better offline processing that is for making Radio Map [64]. However, the use of single anchor carrying four antennas for indoor positioning is reported in [65, 66]. The proposed architecture is quite compact and uses array antenna receivers by a single anchor and has utilized the concept of AoA as mentioned in

Section 1.3.1.2. The AoA is computed by the virtue of antenna positions as reported in [34-38, 67-68]. Similar approach has also been reported in [69-70]. This brings the number of different anchors, located at different positions in ToA/TDoA, to one position as a single anchor. Thus, this architectural design is good for reducing the number of anchors. The mentioned architectural design has used two separate units that is a transmitter unit and a receiver unit. If the mentioned design [67-68] is used on the principle of mono-pulse radar principle then it will further combined the separate transmitter and receiver units into a single unit whereas the target can be tagged with an active-transponder [71]. A fine example of such a design is reported in [72-73, 29] which use ultra wideband short range radar (UWB-SRR). Furthermore, [29] has successfully demonstrated the use of UWB bandwidth and has achieved accuracy < 10 cm upto 10 m of range as UWB signal posses higher temporal resolution and robustness to multipath fading than narrowband and wideband signals. However, for time-based localization, NLoS propagation induces extra delay to the ToA measurement which results in location errors. In [74], Cramer-Rao bound (CRB) analysis indicates that if the statistical information of NLoS error is unknown then only the LoS ToA estimates contribute to the location estimates, but if the knowledge of NLoS is available then both LoS and NLoS ToA estimates contribute to the estimation. Therefore, the NLoS ToA estimates need to be identified and should be discarded before the position estimation. More details on NLoS identification techniques are mentioned in [32, 75-76].

The radio propagation faces multiple reflections because of the crowded indoor environment with furniture, walls, floors, and doors which attribute multiple reflections as well as attenuation. The unwanted reflected signals are also mixed-up with the desired signals. These backscattered signals can be filtered-out by performing carrier frequency transposition; the desired signals are shifted to another frequency-carrier through active-tag so that the separation between the desired signals and the backscattered signals can be easily done as mentioned in [71]. Besides signal separation, the desired signals can also be amplified which will compensate the strong attenuation because of multiple reflections. The polarization diversity can also be used for the better reception such as Circular Polarized (CP) or Linear Polarized (LP) signals. The influence of signal polarization under different conditions are analysed in [77] and the influence of antenna characteristics on accuracy are mentioned in [78]. For NLoS, the absence of LoS can be compensated with the use of Anchor-cum-Relay (AcR) nodes as mentioned in [79] or by exploring dedicated technique

such as Fingerprinting method [80] based on received signal strength indicator (RSSI). Here, each AcR should estimate the position independently from each other and for higher accuracy the estimations from all nodes should be merged in a cooperative way to have more precision through data fusion. An interesting methodology has also been reported by *Arumugam et al* [81-82] that is by the use of quasistatic field for the robust wireless connectivity such as magnetoquasistatic field. The quasistatic fields are not as fragile as the RF signals and hence the propagation signals suffer less attenuation.

Mainly, the localization systems are based on time- (ToA, TDoA) or RSSI-based techniques. But, the phase-difference-of-arrival (PDoA) [83] or frequency-difference (FD) [84-89] properties of radar technology in LoS condition can be a good prospect for indoor localization system. A direct implementation of this concept is reported in [90]. By using the antenna structure as mentioned in [65-66] and applying FD-PDoA to each receiver, one can locate the remote target in three-dimensions, like it is done in [65-66, 91] because FD-PDoA technique has a similar approach as of FMCW radar.

Proposed ILS: Based on the knowledge gained from the above study, the proposed Indoor Localization System (ILS) is based on multistatic FMCW radars in the European UWB band [6-8.5] GHz. An active-tag can be used as a remote target and will get located through the trilateration technique. The radial-distance can be estimated through the measurement of FD and the angle can also be computed by PDoA according to the concept of angle-of-arrival method. The proposed ILS can utilize the similar antenna setup as mentioned in [65] so that only one anchor point will be needed for three-dimension estimates. In addition, the transmitter antenna can be kept at the centre of the receiver antennas. So that it will have a compact design and the signal will be reflected back by the Active-Tag which will act as a locatable target.

The **working principle** of the proposed system can be summed up as: the proposed Indoor Localization System will consist of two main units- first one will have a transceiver station as Localization Base Station (LBS) with antenna setup similar to [65] and second will have an active-tag (AT) unit. The LBS will have one transmitter chain and four identical & independent receiver chains. A 6-7 GHz Frequency Modulation Continuous Wave signal will be generated by the signal generator and then up-converted to 7.5-8.5 GHz and then will be transmitted towards the AT. The 7.5-8.5 GHz frequency band is used as the up-link

communication channel from LBS to AT. The active-tag should be a loop-system fitted as a duplex communication (received and retransmitted signals simultaneously communicate). The received frequency bandwidth (7.5-8.5 GHz as uplink channel) will be retransmitted towards the LBS in 6-7 GHz frequency bandwidth after one more frequency transposition as a down-link channel. This signal would be finally received by the receiver antennas and then is mixed with the reference signal for frequency-difference (FD) analysis. Finally, the position will be estimated as an application of FD and PDoA. The *objective of the proposed solution* is to have precision in <10 cm in LoS condition with simple architectural design with the use of a single known anchor point. Here, the performance in NLoS is not expected much. Also, the coherent synchronization between tag-unit and the main anchor-unit will be required.

1.6 Conclusion

The information about the indoor localization system has been presented in this chapter. The use of different algorithm and the measurement techniques have been discussed. The analyses of various available indoor systems are also presented. The knowledge gained from the study conducted on various techniques and systems is used in proposing our Indoor Localization System. The rest of the thesis has been designed into four more chapters.

The proposed Indoor Localization System is presented in **Chapter 2**. The developed method for three-dimension position estimates is presented and is explained with the help of mathematical relationships. The architectures of Indoor Localization System (LBS & AT) are also presented in this chapter, and initial results based on the proposed system are also completely discussed. Besides this, the constraints related to the proposed design are fully demonstrated through the developed mathematical relationships.

As per the proposed ILS system, a prototype is built for the three-dimension positioning. Some necessary components such as antennas are designed and characterized in the anechoic chamber. The characteristics of the designed and some purchased components such as filters are also presented in **Chapter 3**. The underline steps for the indoor navigation are also outlined in this chapter.

Chapter 4 represents the performance of the built prototype in a real indoor environment. The performance has been checked under different situations like LoS and

NLoS conditions. The presence of multipaths and its influence on the ILS performance are also verified through the field-measurements. Some constraints such as plane wave condition are also verified through the field-measurements in an indoor environment. The mentioned performances have considered only one anchor point in the form of fixed LBS unit.

Finally, the conclusion is presented in **Chapter 5**. Some future works related to system upgradation have been proposed and its implementations are explained in the end.

Reference

- [1] S. Buyukcorak, T. Erbas, G. K. Kurt, and A. Yongacoglu, "Indoor localization applications," Signal Processing and Communication Applications Conference, SIU 2014, pp. 1239-1242.
- [2] B. Jensen, R. Kruse, and B. Wendholt, "Application of indoor navigation technologies under practical conditions," Workshop on Positioning, Navigation and Communication, WPNC 2009, pp 267-273.
- [3] D. J. Seo, and J. Kim, "Development of autonomous navigation system for an indoor service robot application," Int. Conf. On Control, Automation and Systems, ICCAS 2013, pp. 204-206.
- [4] J. A. F. Marigal, E. C. Martin, J. Gonzalez, C. Galindo, and J. L. Blanco, "Application of UWB and GPS technologies for vehicle localization in combined indoor-outdoor environments," Int. Conf. On Signal Processing and Its Applications, ISSPA 2007, pp. 1-4.
- [5] E. Lohnert, W. Bar, E. Gohler, and J. Mollmer, "Galileo/GPS indoor navigation & positioning for SAR and tracking applications," Int. Conf. On Indoor Positioning and Indoor Navigation, IPIN 2010, pp. 1-6.
- [6] U. Yayan, B. Akar, F. Inan, and A. Yazici, "Development of indoor navigation software for intelligent wheelchair," IEEE Int. Sympo. On Innovations in Intelligent Systems and Applications, INISTA 2014, pp. 325-329.
- [7] http://www.phonearena.com/phones/Samsung-Galaxy-Note-3_id7984
- [8] http://www.phonearena.com/phones/Apple-iPhone-6-Plus_id8908
- [9] http://www.phonearena.com/phones/Google-Nexus-5_id8148
- [10] <http://copter.ardupilot.com/wiki/common-gps-how-it-works/>
- [11] <http://en.wikipedia.org/wiki/Trilateration>

-
- [12] A. E. C. Redondi, and E. Amaldi, "Optimizing the placement of anchor nodes in RSS-based indoor localization systems," Ann. Mediterranean Ad Hoc netw. Workshop, MED-HOC-Net 2013, pp. 8-13.
- [13] J. N. Ash, and R. L. Moses, "On optimal anchor node placement in sensor localization by optimization of subspace principal angles," in ICASSP, 2008, pp. 2289-2292.
- [14] S. Hara, and T. Fukumura, "Determination of the placement of anchor nodes satisfying a required localization accuracy," in Wireless Communication Systems. 2008. ISWCS '08. IEEE International Symposium on, oct. 2008, pp. 128 -132.
- [15] G. Yanying, A. Lo, L. Niemegeers, "A survey of indoor positioning systems for wireless personal networks", IEEE Communications Surveys & Tutorials, vol. 11, no. 1, 2009, pp. 13 – 32.
- [16] N. Jardak, and N. Semama, "Indoor Positioning Based on GPS-Repeaters: Performance Enhancement using an Open Code Loop Architecture," IEEE Transactions on Aerospace and Electronic Systems, vol. 45, no. 1, 2007, pp. 347 – 359.
- [17] P. Gulden, S. Roehr, M. Christmann, "An overview of wireless local positioning system configurations", IEEE Int. Microwave Workshop on Wireless Sensing, Local Positioning, and RFID, Sept. 2009, pp. 1 – 4.
- [18] K. Pahlavan, L. Xinrong J. P. Makela, "Indoor geolocation science and technology", IEEE Communications Magazine, vol. 40, no. 2, Feb. 2002, pp. 112 – 118.
- [19] H. Yucel, A. Yazici, and R. Edizkan, "A survey of indoor localization systems," Signal Processing and Communication Applications Conference, SIU 2014, pp. 1267-1270.
- [20] F. Li, C. Zhao, G. Ding, J. Gong, C. Liu, and F. Zhao, "A Reliable and Accurate Indoor Localization Method Using Phone inertial Sensors," in ACM UbiComp, 2012, pp. 421-430.
- [21] Hui Liu, Houshang Darabi, Pat Banerjee, and Jing Liu, "Survey of Wireless Indoor Positioning Techniques and Systems," in *IEEE Trans. on systems, man, and cybernetics-PartC*, Nov. 2007, vil. 37, pp. 1067–1080.

-
- [22] I. Lee, G. Yoon, and D. Han, "Nerimi: WiFi-based subway navigation system," IEEE MTT-S Int. Micro. Workshop Series on Intelligent Radio for Future Personal Terminals, IMWS-IRFPT 2011, pp. 1-2.
- [23] A. Fluerasu, A. Vervisch-Picois, G. Boiero, G. Ghinamo, P. Lovisolo, and N. Samama, "Indoor positioning using GPS transmitter: Experimental results," Int. Conf; on Indoor Positioning and Indoor Navigation, IPIN 2010, pp. 1-9.
- [24] F. L; Piccolo, "A new cooperative localization method for UMTS cellular networks," IEEE Global Telecommunications Conference, GLOBECOM 2008, pp. 1-5.
- [25] G. Heinrichs, "Using of Rake receiver architecture for combining GNSS and CDMA cellular wireless location," IEEE 7th Int. Sympo. On Spread Spectrum Techniques and Applications, pp. 787-791, 2002.
- [26] M. Brugger, T. Christ, F. Kemeth, S. Nagy, M. Schaefer, and M. M. Pietrzyk, "The FMCW Technology-Based Indoor Localization System," Ubiquitous Positioning Indoor Navigation and Location Based Service, UPINLBS 2010, pp. 1-6.
- [27] B. Waldmann, R. Weigel, R. Ebel, and M. Vossiek, "An ultra-wideband local positioning system for highly complex indoor environments," Int. Conf. On Localization and GNSS, ICL-GNSS 2012, pp. 1-5.
- [28] T. Ussmueller, M. Jung and R. Weigel, "Synthesizer concepts for FMCW based locatable wireless sensor nodes," IEEE MTT-S International Microwave Workshop on Wireless Sensing , Local Positioning, and RFID, IMWS 2009, pp. 1-4.
- [29] N. Obeid, M. Heddebaut, F. Boukour, C Loyez, and N. Rolland, "Millimeter Wave Ultra Wide Band Short range Radar Localization Accuracy," IEEE Vehicular technology Conference, VTC Spring 2009, pp. 1-5.
- [30] N. Patwari, A. O. Hero III, M. Perkins, N. S. Correal, and R. J. O'Dea, "Relative location estimation in wireless sensor networks," IEEE Trans. Signal Process., vol 51, no. 8, pp. 2137-2148, 2003.

-
- [31] Z. Zheng, J. Hua, Y. W, H. Wen, and L. Meng, "Time of arrival and Time Sum of arrival based NLOS identification and Localization," *Int. Conf. Communication Technology, ICCT 2014*, pp. 1129-113.
- [32] Seyed A. (Reza) zekavat, and R. Michael Buehrer, "Handbook of positioning Location: Theory, Practice and Advances," John Wiley & Sons, Inc. 2012.
- [33] L. Kumar, A. Tripathy, and R. M. Hegde, "Robust Multi-source Localization Over Planar arrays Using MUSIC-group Delay Spectrum," *IEEE Trans. Sig. Pro.* 2014.
- [34] B. D. Van Veen and K. M. Buckley, "Beamforming: A versatile approach to spatial filtering," *IEEE ASSP Mag.*, vol. 5, no. 2, pp. 4–24, Apr. 1988.
- [35] P. Stoica and R. L. Moses, *Introduction to Spectral Analysis*. Englewood Cliffs, NJ: Prentice-Hall, 1997.
- [36] B. Ottersten, M. Viberg, P. Stoica, and A. Nehorai, "Exact and large sample ML techniques for parameter estimation and detection in array processing," in *Radar Array Processing*, S. S. Haykin, J. Litva, and T. J. Shepherd, Eds. New York: Springer-Verlag, 1993, pp. 99–151.
- [37] T. Huang, and A. S. Mohan, "Effect of array mutual coupling on near-field DOA estimation," *IEEE CCECE 2003 Canadian Conf. On elect; and Computer Engineering*, pp. 1881-1884.
- [38] D. S. Yang, J. Shil, and B. S. Liu, "Adaptive target tracking for wideband sources in near field," *Int; Conf; on Informtion Fusion, FUSION 2009*, pp. 315-318.
- [39] W. Wang, and S. A. Zekavat, "A novel semi-distributed localization via multi-node TOA-DOA fusion," *IEEE Trans. Veh. Technol*, vol. 58, no; 7, pp. 3426-3435, 2009.
- [40] W. Wang, and S. A. Zekavat, "Comparison of semi-distributed multi-node TOA-DOA fusion localization and GPS-aided TOA (DOA) fusion localization for manets," *EURASIP J; Adv. Signal process.*, vol. 2008, Article ID 439523, 16 pages, 2008. Doi: 10.1155/2008/439523, 2008.

-
- [41] B. Li, "Terrestrial mobile user positioning using TDOA and fingerprinting techniques," PhD thesis, School of Surveying & Spatial Information Systems, University of New South Wales, Sydney, Australia, 2006.
- [42] V. A. Papapostolou, X. Wendong, and H. Chaouchi, "Cooperative fingerprint-based indoor localization using Self-Organizing Maps," *Int. Wireless Communications and Mobile Computing Conference, IWCMC 2011*, p.p. 1814-1819.
- [43] S.A.P. Kontkanen, P. Myllymäki, T. Roos, H. Tirri, K. Valtonen, and H. Wetteg, "Topics in probabilistic location estimation in wireless networks," in *Proc. 15th IEEE Symp. Pers., Indoor, Mobile Radio Commun.*, Barcelona, Spain, Sep. 2004, vol. 2, pp. 1052–1056.
- [44] P. Torteeka, and Xiu Chundi, "Indoor positioning based on Wi-Fi Fingerprinting Technique using Fuzzy K-Nearest Neighbor," *Int. Burban Conf; on Applied Ascienes and Technology, IBCAST 2014*, pp. 461-465.
- [45] B; Kachimczyk, D. Dzaik, and J. W. Kulesza, "RFID-Hybrid Scene Analysis-Neural Network system for 3D Indoor Positioning optimal system arrangement approach," *IEEE Int. Instrument and Measurement Technology Conf. Proc., I2MTC 2014*, pp. 191-196.
- [46] V. Vapnik, *The Nature of Statistical Learning Theory*. New York: Springer, 1995.
- [47] P. Prasithsangaree, P. Krishnamurthi, and P. K. Chrysanthis, "On indoor position with wireless LANs," in *Proc. IEEE Int. Symp. Pers. Indoor, Mobile Radio Commun.*, Sep. 2002, vol. 2, pp. 720–724.
- [48] D. Macii, F. Trenti, and P. Pivato, "A robust wireless proximity detection technique based on RSS and ToF measurements," *IEEE Int. Workshop on Measurements and Networking Proc. M&N 2011*, pp. 31-36.
- [49] J. Hightower, R. Want, and G. Borriello, "SpotON: An indoor 3D location sensing technology based on RF signal strength," *Univ. Washington, Seattle, Tech. Rep. UW CSE 2000-02-02*, Feb. 2000.

-
- [50] M. Vossiek, M. Wiebking, L. Gulden, P. Weighardt, and J. Hoffmann, "Wireless local positioning—Concepts, solutions, applications," in Proc. IEEE Wireless Commun. Netw. Conf., Aug. 2003, pp. 219–224.
- [51] UbiSense Company. <http://www.ubisense.net>
- [52] P. K. Enge, "The global positioning system: Signals, measurements and performance," *Int. J. Wireless Inf. Netw.*, vol. 1, no. 2, pp. 83–105, 1994.
- [53] S. Manapure, H. Darabi, V. Patel, and P. Banerjee, "A comparative study of radio frequency-based indoor location systems," in Proc. IEEE Int. Conf. Netw., Sens. Control, 2004, vol. 2, pp. 1265–1270.
- [54] P. Krishnan, A. S. Krishnakumar, W.-H. Ju, C. Mallows, and S. Ganu, "A system for LEASE: Location estimation assisted by stationary emitters for indoor RF wireless networks," in Proc. IEEE INFOCOM, Mar. 2004, pp. 21–32.
- [55] M. Eallbaum, "Wheremops: An indoor geolocation system," in Proc. IEEE Int. Symp. Pers., Indoor, Mobile Radio Commun., Sep. 2002, vol. 4, pp. 1967–1971.
- [56] A. Smailagic, D. P. Siewiorek, J. Anhalt, D. Kogan, and Y. Wang, "Location sensing and privacy in a context aware computing environment," in Proc. Int. Conf. Pervasive Comput., May 2001, pp. 10–17.
- [57] A. Kotanen, M. Hannikainen, H. Leppakoski, and T. D. Hamalainen, "Experiments on local positioning with Bluetooth," in *Proc. IEEE Int. Conf. Inf. Technol.: Comput. Commun.*, Apr. 2003, pp. 297–303.
- [58] J. J. Caffery and G. L. Stuber, "Overview of radiolocation in CDMA cellular system," *IEEE Commun. Mag.*, vol. 36, no. 4, pp. 38–45, Apr. 1998.
- [59] P. Cherntanomwong, and D. J. Suroso, "Indoor Localization System using Wireless Sensor Networks for Stationary and Moving Target," *Inte. Conf. On Information, Communication and Signal Processing, ICICS 2011*, pp. 1-5.

-
- [60] Y. Gwon and R. Jain, "Error characteristic and calibration-free techniques for wireless LAN-based location estimation," in *Proc. Mobi- Wac'04*, Philadelphia, PA, Oct. 1, 2004, pp. 2–9.
- [61] J. Kwon, B. Dunder, and P. Varaiya, "Hybrid algorithm for indoor positioning using wirelessLAN," *IEEE Veh. Technol. Conf.*, vol. 7, pp. 4625–4629, Sep. 2004.
- [62] Y. Gwon, R. Jain, and T. Kawahara, "Robust indoor location estimation of stationary and mobile users," in *Proc. IEEE INFOCOM*, Mar. 2004, vol. 2, pp. 1032–1043.
- [63] V. Otsason, A. Varshavsky, A. LaMarca, and E. de Lara, "Accurate GSM indoor localization," *UbiComp 2005, Lecture Notes Computer Science*, Springer-Verlag, vol. 3660, pp. 141–158, 2005.
- [64] Y. Cho, J. Kim, M. J. Y. Lee, and S. Park, "GPRS based Wi-Fi radio map construction from real/virtual indoor dynamic surveying data," *Int. Conf. on Control, Automation and Systems*, ICCAS 2013, pp. 712-714.
- [65] A. B-Delai, J. C. Cousin, R. Ringot, Ahmed Mamouni, and Y. Leroy, "Microwave Short Baseline Interferometers for Localization Systems," *IEEE Trans. On Instrumentation and Measurement*, vol; 50, no; 1, pp. 32-39, Feb 2001.
- [66] A. Bocquet, C. Loyez, and A. B-Delai, "Using Enhanced-TDOA Measurement for Indoor Positioning," *IEEE Microwave and Wireless Components Letters*, vol; 15, no; 10, pp; 612-614, Oct 2005.
- [67] V. Y. Vu, and A. B. Delai, "A New Digital Receiver Architecture for Direction Finding Systems," *Int. Conf. on Communication and Electronics (ICC 2006)*, pp; 430-433, 2006.
- [68] V. Y. Vu, and A. B. Delai, "Digital Solution for inter-vehicle localization system by means of Direction-Of-Arrival," *Int. Symp. on Intelligent Signal Processing and Communication Systems (ISPACS 2006)*, pp; 875-878, 2006.
- [69] S. Galler, W. Geork, J. Schroeder, K. Kyamakya, and T. Kaiser, "Combined AOA/TOA UWB localization," *Int. Symp. On Communications and information Technologies*, ISCIT 2007, pp. 1049-1053.

-
- [70] I. B. Shirokov, G. V. Jandieri, D. V. Sinitsyn, and D. I. Martynjuk, "Multipath Angle-Of-Arrival And Phase Progression Measurements On Microwave Line-Of-Sight links," *Ant. and Prog. Proc, EuCAP 2006*, pp. 1-6.
- [71] M. Vossiek, and P. Guldenl, "The Switched Injection-Locked Oscillator: A Novel Versatile Concept for Wireless Transponder and Localization Systems", *IEEE Transactions on Microwave Theory & Technique*, vol. 56, no. 4, 2008, pp. 859-866.
- [72] D. Boontrai, T. Jingwangsa, and P. Cherntanomwong, "Indoor Localization Technique using Passive RFID Tags," *ISCIT 2009*, pp. 922-926.
- [73] S. Wehrli, R. Gierlich, J. Huttner, D. Barras, F. Ellinger, and H. Jackel, "Integrated Active Pulsed Reflector for an Indoor Local Positioning System", *IEEE Transactions on Microwave Theory & Technique*, vol. 58, no. 2, 2010, pp. 267-276.
- [74] Y. Qi, H. Kobayashi, and H. Suda, "Analysis of wireless geolocation in a non-line-of-sight environment," *IEEE Trans. Wireless Commun.*, vol. 5, no. 3, pp. 672-681, 2006.
- [75] I. Guvenc, C. C. Chong, and F. Watanable, "NLOS identification and mitigation for UWB localization systems," *Proc. Of Wireless Communication and Networking Conf.*, pp. 1571-1576, 2007.
- [76] J. Khodjaev, Y. Park, and A. S. Malik, "Survey of NLoS identification and error mitigation problems in UWB-based positioning algorithms for dense environments," *Ann. Telecommun.*, vol. 65, no. 5-6, pp. 301-311, 2010.
- [77] C. P. Vega, and G. Garcia, "Polarisation behaviour in the indoor propagation channel," *IEE, electronics Letters*, pp. 898-899, March 1997.
- [78] R. Szumny, K. Kurek, S. Kozlowski, and J. Modelski, "Influence of antennas characteristics on accuracy of TOA indoor positioning systems," *Microwave, Radar and Wireless Communications, MIKON 2008*, pp. 1-4.
- [79] J P Ramirez, and D K Borah, "Anchor-cum-Relay Nodes for Localizing a mobile Source and Relaying Source Signals," *Vehicular Technology Conference (VTC Fall), 2013 IEEE 78th* DOI:10.1109/VTCFall.2013.6692107.

-
- [80] C. Stenir, and A. Wittneben, "Low Complexity Location Fingerprinting With Generalized UWB Energy Detection Receivers," *IEEE Trans. Signal. Proc.*, vol. 58, no. 03, pp. 1756–1767, March. 2010.
- [81] D.D. Arumugam, J. D. Griffin, D. D. Stancil, and D. S. Ricketts, "Two-dimensional position measurement using magnetoquasistatic fields," *IEEE-APS Tropical Conference on Antenna and Propagation in Wireless Communication 2011*, pp. 1193-1196.
- [82] D.D. Arumugam, D. D. Stancil, and D. S. Ricketts, "Proximity and orientation sensing using magnetoquasistatic fields and complex image theory," *IEEE Vehicular Technology Conference (VTC 2011)*, pp. 1-5.
- [83] J P. Nikitin, R. Martinez, S. Ramamurthy, H. Leland, G. Spiess, and K. Rao, "Phase based spatial identification of UHF RFID Tags," *Intermec Technol. Corp., Everett, WA, USA, 2010 IEEE International Conference on RFID, 2010*.
- [84] H. Griffiths, "New ideas in FM radar", *Electronics & Communication Engineering Journal*, vol. 2, no. 5, Oct. 1990, pp. 185 – 194.
- [85] M.Vossiek et al., "Inverse Synthetic Aperture Secondary Radar Concept for Precise Wireless Positioning", *IEEE Transactions on Microwave Theory and Techniques*, vol. 55, no. 11, Nov. 2007, pp. 2447 – 2453.
- [86] J. Shefer, R. Klensch, "Harmonic radar helps autos avoid collisions", *IEEE Spectrum*, vol. 10, no. 5, May 1973, pp. 38 – 45.
- [87] B. Colpitts, G. Boiteau, "Harmonic radar transceiver design: miniature tags for insect tracking", *IEEE Transactions on Antennas and Propagation*, vol. 52, no. 11, Nov. 2004, pp. 2825 – 2832.
- [88] D. Psychoudakis et al., "A Portable Low-Power Harmonic Radar System and Conformal Tag for Insect Tracking", *IEEE Antennas and Wireless Propagation Letters*, vol. 7, 2008, pp. 444 – 447.

-
- [89] E. de Moura Presa, et al., “A new microwave harmonic direction-finding system for localization of small mobile targets using passive tags”, *Microw. and Opt. Techn. Letters*, vol. 47, no. 2, Oct. 2005, pp. 134-137.
- [90] J. Cousin, “Radar multistatique d’aide la conduite pour le positionnement 2D de cible à courtes distances par la technique FMCW associe l’interférométrie”, 15^{mes} Journées Nationales Microondes, 2007.
- [91] M. Vossiek at al., “Inverse Synthetic Aperture Secondary Radar Concept for Precise Wireless Positioning”, *IEEE Transactions on Microwave Theory and Techniques*, vol. 55, no. 11, Nov. 2007, pp. 2447 – 2453.

Chapter 2. Developed Method

2.1 Introduction

Currently radio frequency systems used for the indoor localization can be classified into two main groups according to the use of wireless network:

- a. Wireless Sensor Network (WSN) based on RSSI (Received Signal Strength Indicator) data [1-6].
- b. Radar using ToA (Time-of-Arrival) or TDoA (Time Difference of Arrival) data [7-11].

Systems based on sensor networks mainly used the available wireless infrastructure for the measurement of received radio-signal-strength (RSS) from a number of anchors. Some reported systems are good example of RSS technique [12-15]. This technique uses the prior knowledge of the signal's radio wave signatures which is used to compare with the real-time signals for the position estimations. The precision of this kind of system mostly depends on the radio-signature gradient, that is, precised prior knowledge of radio-signature [16, 17]. Generally, the accuracy achieved by these systems is in meters and is advised for the Non-Line-of-Sight (NLoS) case where signals are recovered after some reflections from the surrounding environment as such conditions are quite common in an indoor environment. Fingerprinting [17] is a well known method for the computation of radio-signature.

The radar based systems such as FMCW (Frequency-Modulation Continuous Wave) [8-9] use its own wireless infrastructure and are commonly known for precised estimation of radial-distance. Generally, the radar based system uses the time-stamp (ToA or TDoA) for the radial-distance estimation. However, these systems also need the prior knowledge of at least three anchors [18] for localization. Apart from this, it also requires a good synchronization between different anchors. Therefore, it needs a high precised clock for synchronization. But, achieving an accurate synchronization is not an easy task because of the clock-drift & clock initialization issues [19]; for an example a mismatch of 1ns in synchronization can introduce 30cm of error in radial-distance estimation. Moreover, the performance of this kind of system in the NLoS is not as good as in the LoS (Line-of-Sight)

due to the large variation of time-stamp values in the NLoS as the time taken by the signals are completely different from the actual condition, that is, LoS.

Each one has its own pros and cons in terms of performance and complexity. However, the Indoor Localization System (ILS) developed by the RFM team of Télécom ParisTech is not bounded by such needs and is based on the mono-pulse radar system. The developed ILS facilitates the 3D localization of a remote target through a multistatic FMCW Radars system. It uses a hybrid technique based on FoA (Frequency-of-Arrival) and PDoA (Phase-Difference-of-Arrival) which will lead to a less complex system in comparison with the existing ones and will lead to accuracy in centimetres. The FoA will provide the radial-distance of the tag from the LBS (Localization Base Station) and the angle-of-arrival of the waves coming from the Tag will be computed from the PDoA.

The basic principle of FMCW radar is presented in [Section 2.3](#). The complete information about the architectures and its functions are presented in [Section 2.3](#), and the developed method for the position estimations is presented in [Section 2.4](#). It is presented in three parts: [Section 2.4.1](#) gives the details about the 2D measurements, and the 3D measurements method is presented in [Section 2.4.2](#). The initial validation of the developed method is presented in [Section 2.4.3](#) through experimental results. The constraints related to the developed system are also discussed in [Section 2.4.4](#). Finally, the conclusion about the ILS is presented in [Section 2.5](#).

2.2 FMCW Radar Basics

RADAR is defined as “Radio Detection And Ranging” system which uses the radio waves for determining the radial-distance of a remote target by measuring the round-trip time, i.e., Time-of-Flight (ToF) [20]. The fundamental relationship between the two-way round-trip time and the radial-distance is given as

$$d = \frac{c * T_{ToF}}{2} \tag{2.1}$$

Where c is the speed of light, d is the radial-distance between the target and the radar, and T_{ToF} is ToF. Here, the radial-distance is considered as the direct path between the radar and the remote target which represents the LoS case.

The maximum radial-distance depends upon the signal repetition time while the radial-distance resolution, the minimum distance required to distinguish one target from another, depends on the bandwidth of the radio waves

$$\delta d = \frac{c}{2 * BW} \quad 2.2$$

Where δd is the radial-distance resolution and BW is the frequency bandwidth of radio signal.

However, the exact measurement of ToF is not an easy task as it requires a very high sampling rate for the correct assessment of received signals. For example, 1ns ToF will require sampling with few hundreds of picoseconds (as per Nyquist principle it should be 500 picoseconds) and hence, this will require a really high precised clock. But, the measurement of frequency-shift as a representation of the ToF is possible with the FMCW principle. The FMCW radar transmits a linearly swept sinusoidal signal over a certain period of time often known as Chirp. The reflected signal or echo from a remote target is mixed with a copy of the transmitted signal for the radial-distance determination. The transmitted time varying frequency $f(t)$ is given by

$$f(t) = f_0 + kt \quad \forall \quad t \leq T_m \quad 2.3$$

Where f_0 is the starting frequency, k is the rate of change of frequency over T_m and T_m is the sweep time (also known as modulation time).

The linearly increasing frequency sweep is shown in [Fig 2.1](#). The starting frequency is f_0 at the start of the sweep and increases to f_1 at the end of the sweep, that is, after T_m . The bandwidth (BW) is the difference between f_1 and f_0 .

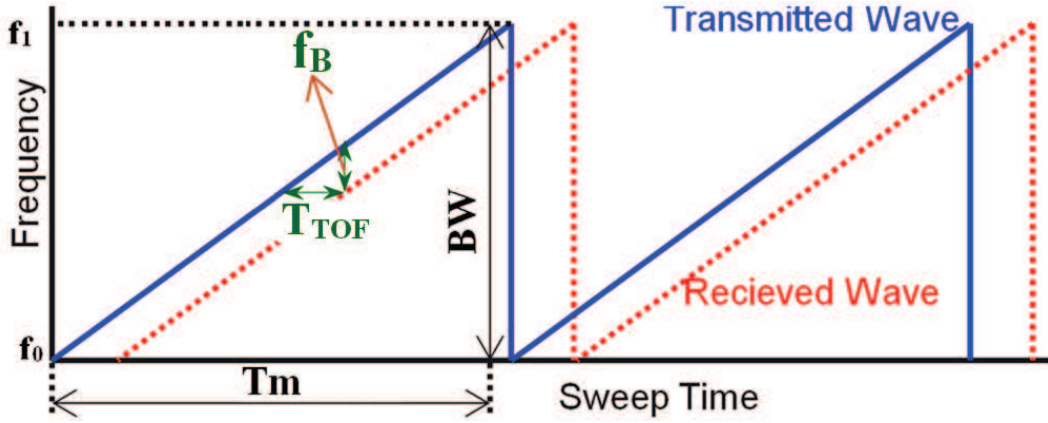


Fig 2.1: FMCW concept: transmitted modulation patterns vs. time-delayed received modulation patterns from a remote target.

The rate of linearly varying frequency is

$$k = \frac{BW}{T_m} \quad 2.4$$

Due to the property of frequency as phase derivative, the phase represented by the $f(t)$ is expressed as

$$\phi(t) = 2\pi \int f(t) dt = 2\pi \left(f_0 t + \frac{1}{2} k t^2 \right) \quad 2.5$$

The transmitted and its delay version as the received signal frequencies are expressed as

$$\begin{aligned} f_T(t) &= f_0 + kt & \forall & 0 < t < T_m \\ f_R(t) &= f_0 + k(t - T_{TOF}) & \forall & T_{TOF} < t \leq T_m \end{aligned} \quad 2.6$$

Mixing of these two signals produces the sum ($f_T + f_R$) and the difference ($f_T - f_R$) frequencies, and filtering of these mixed signals with a low-pass filter will give the beat frequency as

$$f_B = f_T - f_R \quad 2.7$$

The radial-distance covered by the radio waves after a delay equivalent to ToF can be defined with the relationship 2.1. Therefore, using relationships 2.6 & 2.1 in 2.7

$$\begin{aligned} f_B &= k T_{TOF} \\ &= \frac{BW}{T_m} \frac{2d}{c} \end{aligned} \quad 2.8$$

Thus knowing the beat frequency and other FMCW radar parameters (BW & T_m) can determine the radial-distance or range information. The beat frequency is commonly computed using Fourier Transform technique. The frequency resolution of the Fourier Transform is related to the sampling period (T_{sample}) and the number of samples (N_p) considered for the processing as [21]

$$f_{\text{res}} = \frac{1}{T_{\text{samp}} * N_p} \quad 2.9$$

Therefore, using relationships 2.8 & 2.9 the radial-distance resolution can be written as

$$\delta d = \frac{T_m c}{2BW T_{\text{samp}} N_p} \quad 2.10$$

Thus, the resolution of radial-distance is dependent on the number of sampling points. Therefore a large number of sample points or conversely a high sampling frequency is always desired for better resolution. Therefore, a large number of sampling points will need longer time for signal processing. Besides, the ToF can also be determined in terms of phase-difference by evaluating relationship 2.5 as

$$\left. \begin{aligned} \phi(t) = 2\pi \int f(t) dt &\Leftrightarrow f(t) = \frac{1}{2\pi} \frac{\Delta\phi}{\Delta t} \\ f_{\text{TOF}} &= \frac{1}{2\pi} \frac{\phi_{\text{TOF}}}{T_{\text{TOF}}} \end{aligned} \right\} \quad 2.11$$

Knowing the phase-difference over T_m in the received beat frequency between the transmitter and the receiver can determine the radial-distance

$$d = \frac{c}{2} * T_{\text{ToF}} = \frac{c}{f_{\text{TOF}}} * \frac{\phi_{\text{TOF}}}{4\pi} \quad 2.12$$

Moreover, the radial-distance resolution (δd) depends upon the phase resolution as

$$\delta d = \frac{\lambda}{4\pi} \delta\phi \quad 2.13$$

Where, λ is the wavelength and $\delta\phi$ is the instantaneous phase-difference. The phase-difference information can be precisely determined using well known DMTD (Dual-Mixer Time-Difference) technique [22].

2.2.1 Dual-Mixer Time-Difference Technique

The Dual-Mixer Time-Difference (DMTD) is considered as one of the most precise ways of measuring frequency difference which is based on the principle that phase information is preserved in a mixing process. However, the ability of measuring frequency depends on the accuracy of Zero-Crossing counter. In presence of jitter-noise, the signal may cross the zero-reference level for a number of times which will lead to false computation of frequency-difference and hence it could cause error in computations. Therefore, a precised zero-crossing decision is required for correct computations.

Fourier Transform (FT) is also a widely used method for the frequency determination. However, the resolution of the frequency spectrum spacing is given by the time duration of the signal under consideration and a good frequency resolution can only be traded with a large number of points/samples taken for consideration and hence, it will require a large amount of time. Such limitations do not occur with the DMTD and it also provides a good resolution while considering fewer numbers of points compared to FT.

In this work, the analysis has been only done for the frequency counter (Zero-Crossing level because of jitter-noise effects).

The difference between frequency-shifts, f_1 & f_2 , can be considered as the phase difference between two incoming signals versus a reference signal (here, it is sinusoidal FMCW signal from 6-7 GHz) over the sweep time. Let assume this difference be Δf_{12} and phase comparison is performed using DMDT method.

The 2D measurement scheme is presented in **Fig 2.2**, and the same concept can be easily utilized for the 3D measurements without any further modifications.

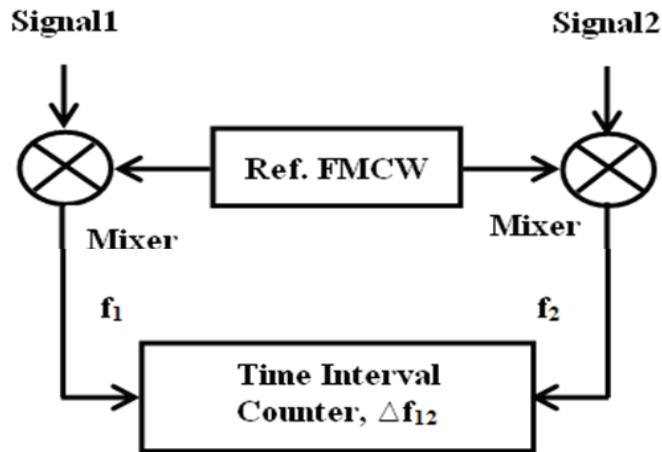


Fig 2.2: DMTD-Time delay measurement scheme.

Assume that Signal1 and Signal2 are two delayed signals, arriving from the AT, of the reference FMCW signal and are received by the two receiver chains connected to A_1 & A_2 , respectively. At the output of each mixer, f_1 & f_2 are the frequency-shifts (baseband signals shown in Fig 2.2) obtained after the down conversion of the two delayed signals (Signal1 & Signal2) as depicted in Fig 2.3. The difference between f_1 & f_2 , denoted as Δf_{21} , is computed by the Time Interval counter and is expressed as

$$f_2 - f_1 = \Delta f_{21} \quad 2.14$$

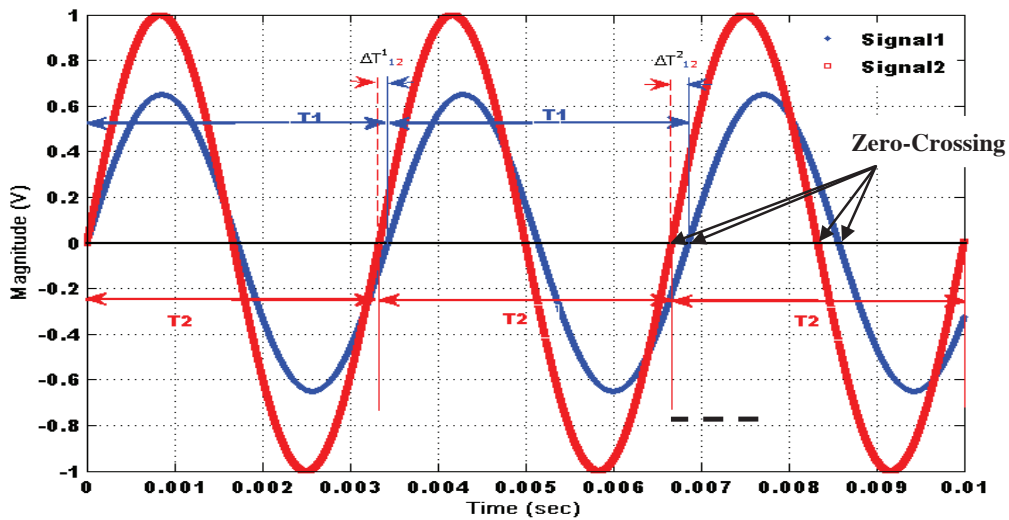


Fig 2.3: Simulated Signals- Signal1 & Signal2.

The time-periods corresponding to f_1 & f_2 are given by

$$T_1 = 1/f_1 \quad T_2 = 1/f_2 \quad 2.15$$

The difference in time-period can be expressed as

$$\Delta T = T_1 - T_2 = \Delta T_{12}^{2nd} - \Delta T_{12}^{1st} = \dots = \Delta T_{12}^N - \Delta T_{12}^{N-1} \quad 2.16$$

Where ΔT_{12}^{N-th} is the N^{th} difference in time-period between the N^{th} cycle of f_1 & f_2 , respectively, and ΔT is the constant successive difference between two consecutive cycles.

Now, the average value of the N cycles can be written as

$$\frac{\sum_{i=1}^N \Delta T^i}{N} = \frac{(\Delta T_{12}^{2nd} - \Delta T_{12}^{1st}) + \dots + (\Delta T_{12}^N - \Delta T_{12}^{N-1})}{N} \quad 2.17$$

Further, the average time-period of the two signals for N number of cycles can be written as

$$\left. \begin{aligned} \frac{\sum_{i=1}^N T_1^i}{N} &= \frac{T_1^{1st} + T_1^{2nd} \dots + T_1^{N-th}}{N} \\ \frac{\sum_{i=1}^N T_2^i}{N} &= \frac{T_2^{1st} + T_2^{2nd} \dots + T_2^{N-th}}{N} \end{aligned} \right\} \quad 2.18$$

Also, Δf_{21} can be expressed in terms of T_1 & T_2 as

$$\Delta f_{21} = \frac{1}{T_2 \left(1 + \frac{T_2}{\Delta T} \right)} \quad 2.19$$

Where, ΔT is given by the relationship 2.16.

Finally, the above expression can be generalized for N , the number of cycles as

$$\left. \begin{aligned} \frac{\sum_{i=1}^N f_{21}^i}{N} &= \frac{1}{\frac{\sum_{i=1}^N T_2^i}{N} \left(1 + \frac{\frac{\sum_{i=1}^N T_2^i}{N}}{\frac{\sum_{i=1}^N \Delta T^i}{N}} \right)} \\ &= \frac{1}{\frac{\sum_{i=1}^N T_2^i}{N} \left(1 + \frac{\sum_{i=1}^N T_2^i}{\sum_{i=1}^N \Delta T^i} \right)} \end{aligned} \right\} \quad 2.20$$

Thus, the average value of the frequency difference for N cycles between Signal1 & Signal2 is expressed by 2.20. Using relationship 2.11, the relative phase-difference between Signal1 & Signal2 can be easily determined.

It is important to reemphasize that the advantages of the FMCW radar system has been used for the estimations of radial-distance and angle-of-arrival information.

2.3 Architecture of ILS

An indoor localization's architecture has two main components, a *base station* which is used to locate the position of objects or people with the help of a *tag* attached to objects or worn by people [23]. Cellular (Mobile Network) based localization system is also based on the same concept where the mobile unit acts as a *tag* and the Mobile Base Station as a *base station*. Indoor localization system is commonly used in a confined area such as within a building. Therefore, such system must be designed to address the harsh conditions of indoor environment such as reflection, multipath, backscattering, diffraction and etc, which leads to signal attenuation. The harsh indoor conditions can be reduced to some extent by providing some proper adaptation to the radio signal like the use of circular polarized waveform which provides a better chance of signal reception [24]. Although, this is not a perfect solution but it helps in reducing the harsh effects. The signal polarization will be discussed in Chapter 3. Also, some interesting works have been reported by [25] for avoiding the backscattering effects in an indoor environment by intentionally shifting the radio frequency spectrum with the use of an active-Tag [26].

The presented Indoor Localization System (ILS) has two main components, a Localization Base Station (LBS) and an Active-Tag (AT).

The architecture for the 2D localization is shown in Fig 2.4. The Localization Base Station (LBS) acts as a fixed base station for locating the AT. The 2D LBS architecture has one RF transmitter chain and two RF receiver chains, and each one is separately connected to an antenna. Therefore, it (2D LBS) has three separate individual antennas (A_0 , A_1 & A_2) and all of them are placed on a collinear line. The collinear line is named as Baseline and is denoted as d_{baseline} . Out of three antennas, A_0 is used as a transmitter and the rest two, A_1 & A_2 , are used as receivers. The transmitter antenna is kept at the middle position of d_{baseline} and the rest two receiver antennas are kept at each end. Here, the two local oscillators (LO1 & LO2) are considered as coherently connected.

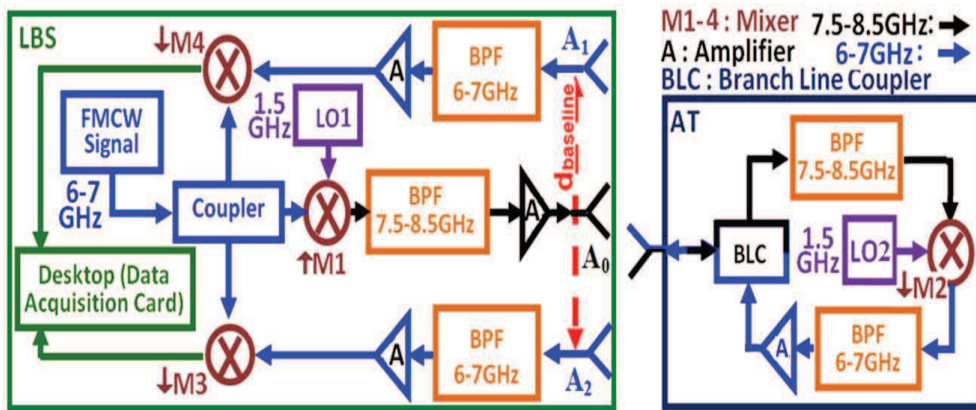


Fig 2.4: Architecture for the 2D localization.

The architecture of the ILS is explained in sequence with the RF-path of the FMCW signal that starts from the transmitter chain of the LBS then goes to AT and then finally returned to receiver chains of the LBS.

A 6-7 GHz linearly frequency swept sinusoidal signal has been used as the fundamental FMCW chirp signal for the ILS. The time duration of each sweep is considered as 10 ms. The FMCW signal passes through a coupler for later mixing with the received signal for obtaining the beat frequency, as a reference signal. Before transmitting the 6-to-7GHz FMCW signal via A_0 , first it is up-shifted to 7.5-to-8.5 GHz by the mixer (M1) and the local oscillator (LO1, 1.5GHz), and finally the up-shifted signal is filtered with the filter (BPF, 7.5-8.5 GHz)

and then amplified by the amplifier (A). Thus the up-converted, 7.5-to-8.5 GHz, FMCW signal is transmitted towards the AT via A_0 .

Here, the AT is used as a transponder [26] so that the backscattering effects can be avoided. The main objective behind the use of AT is to shift the carrier frequency of the received signals to a predetermined carrier frequency in the range 6-7 GHz; this will help in segregating the intended signal at the LBS from the backscattered signals of an indoor environment because the intended signal will have different and distinct carrier frequency from the scattered ones. Indeed in our case the backscattered signals will remain between 7.5 GHz and 8.5 GHz. Further, the intended carrier frequency can be easily selected with the use of a passband RF filter, specifically. The AT architecture has used similar approach as mentioned in [26], but the presented architecture has simple design as no switch has been used for the duplex communications. This considerably reduces the complexity of the AT design.

Meanwhile, the incoming signal (from the LBS, 7.5-to-8.5 GHz) is received by the AT. The received signal is first filtered out with a bandpass filter (BPF, 7.5-8.5 GHz) and then is down-shifted to 6-7 GHz by the local oscillator (LO2, 1.5GHz) with the help of the mixer (M2). Finally, the amplified down-shifted FMCW signal (6-to-7 GHz) is retransmitted towards the LBS. Thus, the frequency shift of 1.5GHz helps in cancelling as well as suppressing the backscattering effects produced by the radio propagation channel. Additionally, this also helps in reducing the coupling effects between the LBS antennas (A_0 , A_1 , & A_2) as well as in avoiding the feedback effects at the AT with the help of two bandpass filters (BPF6-7 GHz and BPF7.5-8.5 GHz). Here, the AT antenna is used for the duplex communication mode. The AT antenna has two ports and each port is connected to a 3dB 90°-Hybrid Branch Line Coupler for the segregation between the receiver and the transmitter paths.

Finally, the down-converted FMCW signal retransmitted from the AT reaches the LBS where it is received by the two receiver chains' antennas (A_1 & A_2). The received signals are filtered by BPF (6-7 GHz) and then amplified by A (amplifier). Now, the amplified signals are mixed with the reference signal, earlier separated by the coupler, by the mixers (M3-4) which produce the beat frequencies. After that, the beat frequencies are collected by the Data Acquisition Card (SECTRUM, M3I.2132) [27] in digital form; this works as an Analog-to-

Digital converter. Further, the signal processing is done by the DMTD technique for the position estimations. The detailed information about the characteristic of different used components such as amplifier is presented in [Chapter 3](#).

In this section, the architecture of the designed ILS has been explained and the main functionalities of the ILS's components are mentioned in [Table 2.1](#). In the next section, the developed method is explained which is used for the position estimation of the AT in an indoor environment.

Table 2.1
ILS: LBS AND ACTIVE-TAG

Components	Functions
LBS	a) As a fixed known reference position/anchor b) Acts as a transceiver station c) Has only one transmitter chain, but has two identical, independent & separate receiver chains which help in reducing the known number of reference/anchor position to one (explained in section 2.3)
Active-Tag	a) Used to shift the radio spectrum for avoiding backscattering effect b) Act as a signal booster for long range coverage

2.4 Developed Localization Method

Generally, the Frequency-Modulation Continuous-Wave radar is known for the good radial-distance resolution for localization [9], and further use of an ultra-wide bandwidth helps in attaining precision in centimetres [28]. Although, there are a number of wireless technologies have been reported [1][2][3], such as UWB, Ultrasound, RFID, Bluetooth, Wireless Sensor Network, etc, but these are not as good as the precision given by a radar based method, for example FMCW [8][9]. Recently, mobile based sensor (like gyroscope, accelerometer and so) technology has also been reported [29] but it is quite difficult to have reliable and accurate positions out of it because it uses the RSSI based technique which is not robust in nature.

In order to have good resolution; the developed method is basically used the principle of FMCW radar for the radial-distance estimation. Further, this (radial-distance) information has been used to compute the Angle-of-Arrival (AoA). Therefore, the developed method is a hybrid technique which is based on the multistatic FMCW radar systems. This facilitates the

2D/3D location information of the Active-Tag in polar form, that is, radial-distance and angle-of-arrival/s.

In this section, the developed method is presented for the position estimation. The fundamental information about the 2D/3D measurements is presented with the help of developed mathematical expressions and the diagrams.

2.4.1 2D Measurements

Radial-distance of the remote Active-Tag can be computed with the help of the FMCW radar principle by computing the Time-of-Flight between the LBS and the AT. The angle-of-arrival can also be calculated by computing the relative phase-shift between two incoming parallel signals from the AT. The proposed technique requires the measurements of Frequency-of-Arrival (FoA) & Frequency-Difference-of-Arrival (FDoA) in terms of phase-shift as explained earlier in the introduction of the chapter. Therefore, the 2D information about the AT is given by the radial-distance (d) and the angle-of-arrival (α), simultaneously.

A systemic configuration of the 2D architecture for the localization technique is shown in Fig 2.5.

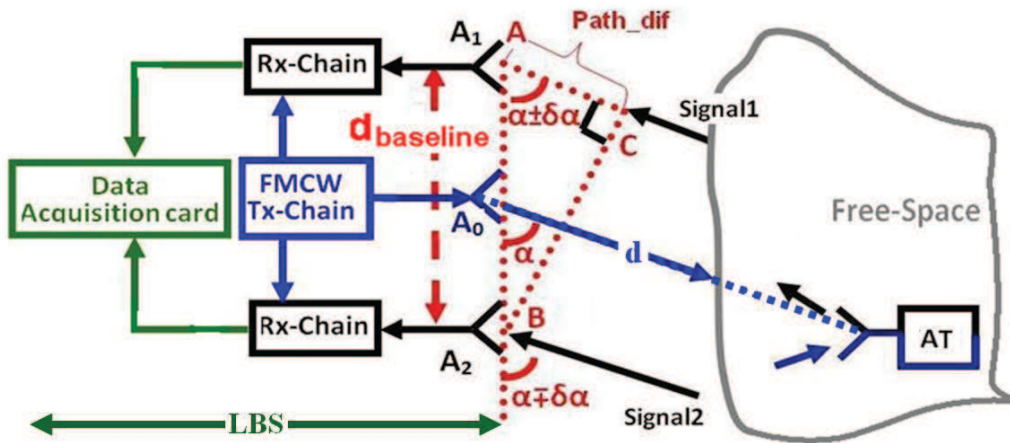


Fig 2.5: Systemic Configuration for the 2D localization.

The linearly swept sinusoidal FMCW signal, 7.5-8.5 GHz, is transmitted through the front end antenna A_0 and each receiving chain receives the reflected signal from the AT. Let, the transmitted signal, which is retransmitted by the remote AT, reaches A_1 & A_2 with time-of-flight equal to T_{TOF1} & T_{TOF2} , respectively.

The computation of the radial-distance between the LBS and the AT can be obtained by measuring the beat frequency which leads to the time-of-flight. Using relationship 2.1 & 2.8, the radial-distances are

$$\left. \begin{aligned} T_{TOF1} &= \frac{F_{S1} * T_m}{BW}; & d_1 &= \frac{c * T_m * F_{S1}}{2BW} \\ T_{TOF2} &= \frac{F_{S2} * T_m}{BW}; & d_2 &= \frac{c * T_m * F_{S2}}{2BW} \end{aligned} \right\} \quad 2.21$$

Where d_1 and d_2 are the radial-distances measured through A_1 & A_2 for two different paths, that is, A_0 -AT- A_1 and A_0 -AT- A_2 , and F_{S1} & F_{S2} are their beat-frequencies (frequency-shifts).

The radial distance (d), between A_0 and AT, is calculated as the average value of d_1 & d_2 (this would be same distance if the receiver is supposed to be connected to A_0).

$$d = \frac{d_1 + d_2}{2} \quad 2.22$$

Now, the AoA computation is based on AoA algorithm. As the two receiving antennas (A_1 and A_2 as presented in Fig 2.5) are separated by $d_{baseline}$, the FMCW radar principle gives the frequency difference ($F_{S2}-F_{S1}$) between two independent incoming signals (Signal 1 & 2). The data ($F_{S2}-F_{S1}$) will give the path difference (Path_dif) [30]. This assumption is valid for a plane waves if the radial-distance remains relatively larger than the $d_{baseline}$. Let, the signals, signal1 & signal2, have a small deviation $\delta\alpha$ (Fig 2.4) from α at A_1 & A_2 , respectively. This deviation will only appear if the assumption of Plane Wave Condition (PWC) between two incoming signals is not satisfied, that is, $\delta\alpha \neq 0$. The PWC and its effects are explained in the Section 2.4.4. So, let Signal1 & Signal2 represent two plane waves and the Path_dif is given by the base-length (AC) of the right-angle triangle ABC, Fig 2.5-Fig 2.6. Hence, the Path_dif between these two parallel independent incoming signals at an angle α to the baseline can be expressed as

$$Path_dif = d_{baseline} * \cos\alpha \quad 2.23$$

Where α is AoA as azimuth angle at A_1 .

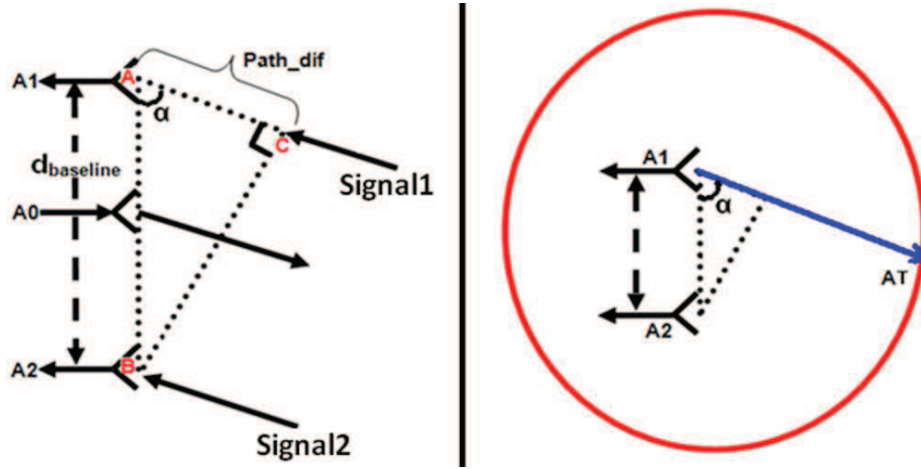


Fig 2.6: Scheme for signal measurement: right angle triangle ABC is shown on the left side while whole scenario of the system is depicted on the right side.

Now, using the relationships 2.21 in 2.23, the path difference between Signal1 and Signal2, for locating the AT can be expressed as

$$Path_dif = (F_{S2} - F_{S1}) * c * T_m / 2 * BW \quad 2.24$$

From, the relationships 2.23 and 2.24, the α is obtained as

$$\alpha = \cos^{-1} \left\{ \frac{(F_{S2} - F_{S1}) * c * T_m / 2 * BW * d_{baseline}}{d_{baseline}} \right\} \quad 2.25$$

As explained earlier, the beat frequency can be precisely evaluated as a phase-shifts. Therefore, the relationship 2.11 helps in expressing the beat frequencies as phase-shifts

$$F_{S1} = \frac{d\phi_1(t)/dt}{2\pi}; F_{S2} = \frac{d\phi_2(t)/dt}{2\pi} \quad 2.26$$

The relative frequency-shifts between signals may be written as

$$F_{S21} = F_{S2} - F_{S1} \quad 2.27$$

$$F_{S21} = \frac{d\phi_2(t)/dt - d\phi_1(t)/dt}{2\pi} \quad 2.28$$

We took into account the initial phase value and then subtracted it to obtain an initial value equals to zero. Therefore, we can assume that $\phi_{1,2}(t)$ has zero initial value ($\phi_{1,2}(0) = 0$). Using 2.11 over the time T_m , F_{S21} can be expressed as

$$\left. \begin{aligned} F_{S21} &= \frac{\phi_2(T_m) - \phi_1(T_m)}{2\pi * T_m} \\ F_{S21} &= \frac{\phi_{21}(T_m)}{2\pi * T_m} \end{aligned} \right\} \quad 2.29$$

Therefore, the AoA given by 2.25 can be expressed as

$$\alpha = \cos^{-1} \left\{ \frac{\Delta\phi_{21} * c}{4\pi * BW * d_{baseline}} \right\} \quad 2.30$$

Where $\Delta\phi_{21} = \phi_2(T_m) - \phi_1(T_m)$ over T_m .

Thus, the relationships 2.21 and 2.30 can be used for the 2D measurements in the polar form with-‘d’ and ‘ α ’ as radial-distance and angle parameters with the prior knowledge of only one reference position as fixed position of the LBS.

Furthermore, the developed 2D measurements technique can also be used for the 3D measurements with the addition of two more receiver chains at the LBS for the computation of angle-of-elevation. The 3D measurements technique is explained in the subsequent section.

2.4.2 3D Measurements

In the previous section, the Optics interferometry concept has been used for the extraction of angle information with the help of two receiver chains. The computed angle actually confined within the plane formed by the two receivers’ antennas. Hence, if we consider one more plane then it will provide one more angle and this additional data helps in obtaining 3D in polar form as radial-distance, angle of azimuth & angle of elevation, provided the second plane must remain orthogonal to the previous one.

Thus, the 3D measurement is possible with the addition of two more receiver chains orthogonal to the previous receiver chains at the LBS. Therefore, the 3D measurement is achieved by the use of one transmitter and four receiver antennas. The front end antennas’ structure of the LBS is shown in Fig 2.7. The transmitter chain and the four receiver chains are linked to the antennas, A_0 and A_i ($i=1-4$), respectively. All antennas (Fig 2.7) are circularly polarized and are placed on the same plane. A_0 is kept at the origin of the orthogonal axis formed by the blue and green dot lines. For both axes, the distance between the receiver antennas are identical and is equal to $d_{baseline}$.

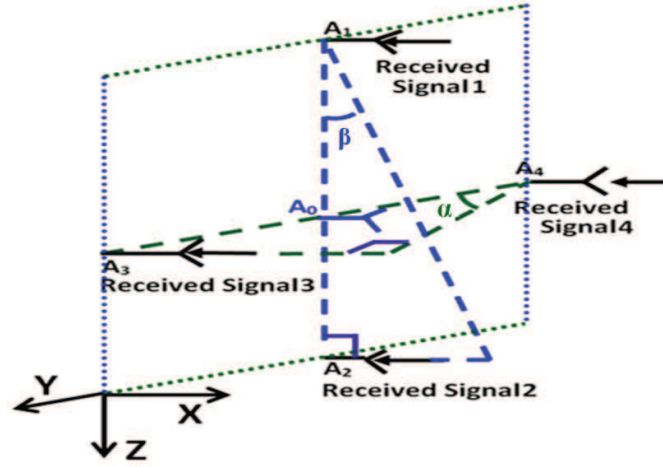


Fig 2.7: Orthogonal structure of receiver antennas for 3D measurements.

Using the developed relationships 2.2 and 2.10, the mathematical expressions for the 3D measurements are expressed as follow:

$$\text{Y-X Plane: } \left\{ \begin{array}{l} d_{34} = \frac{c * T_{delay34}}{2} \\ \alpha = \cos^{-1} \left\{ \frac{\Delta\phi_{34} * c}{4\pi * BW * d_{baseline}} \right\} \end{array} \right. \quad 2.31$$

$$\text{Z-X Plane: } \left\{ \begin{array}{l} d_{21} = \frac{c * T_{delay21}}{2} \\ \beta = \cos^{-1} \left\{ \frac{\Delta\phi_{21} * c}{4\pi * BW * d_{baseline}} \right\} \end{array} \right. \quad 2.32$$

Further, the radial-distance can be considered as the average values of d_{34} & d_{21} , and the 3D parameters in polar form is written as

$$\text{Polar form (d, } \alpha, \beta): \left\{ \begin{array}{l} d = \frac{d_{34} + d_{21}}{2} \\ \alpha = \cos^{-1} \left\{ \frac{\Delta\phi_{34} * c}{4\pi * BW * d_{baseline}} \right\} \\ \beta = \cos^{-1} \left\{ \frac{\Delta\phi_{21} * c}{4\pi * BW * d_{baseline}} \right\} \end{array} \right. \quad 2.33$$

Compared to other systems [1-11], the main advantages are:

- ⌘ Single reference position/anchor (as the fixed known position of the LBS) is needed for 3D position estimation and also the synchronization not required between four receiver chains.
- ⌘ Use of two different radio frequency bands (7.5-to-8.5 GHz & 6-to-7 GHz) does the separation between up-link and down-link channels for strong reduction of the backscattering effects in an indoor environment.

Before the realization of the ILS, the defined method is tested under a control environment for the concept validation. The measurement setup for this test is presented in the following section.

2.4.3 Concept Validation

The defined 2D architecture of [Section 2.3](#) is initially realized using available equipment at Télécom ParisTech such as signal generator, vector network analyser. The free-space has been replaced with Delay-Lines of different lengths. The experimental setup used for the LBS is shown in [Fig 2.8](#). In proposed architecture, the local oscillators (LO) have been assumed as coherent between LBS and AT as mentioned in [Section 2.3](#), therefore, during measurement the two local oscillators (LO1 & LO2) are also considered as coherent-connected.

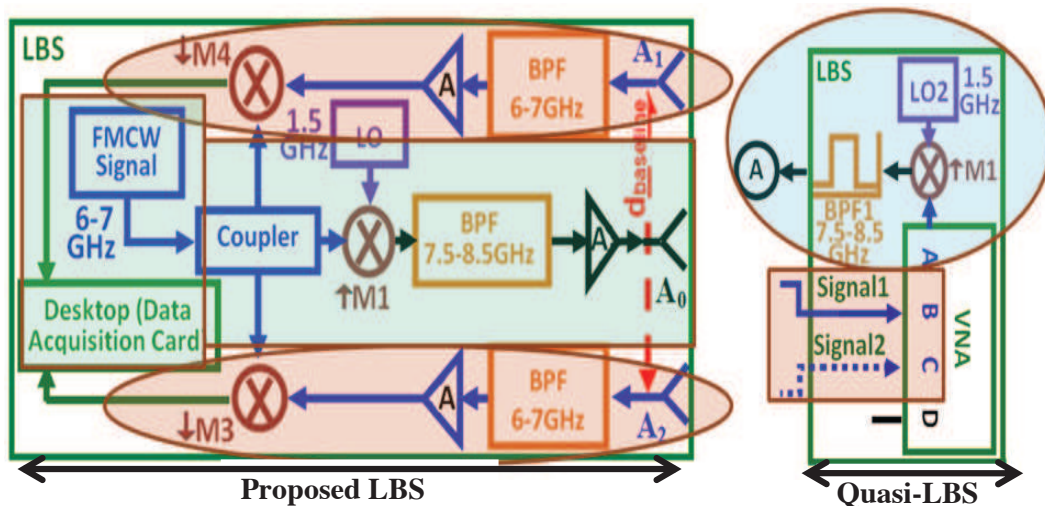


Fig 2.8: Representation of LBS for Initial Test.

The Quasi-LBS is represented by a 4-port Vector Network Analyzer, VNA- Agilent's E5071C. Port A generates the fundamental linearly swept over 10ms from 6 GHz to 7 GHz in continuous mode. This output signal looks like FMCW signal. The 6-to-7 GHz signal is up-shifted by 1.5 GHz with the local oscillator (LO2) through the mixer (M1, Marki M3-0309) and subsequently the up-shifted signal is filtered with the bandpass filter (BPF1, REACTEL Inc. for 7.5-8.5 GHz). This represents the transmitter chain of the LBS as marked by the light green colour. The receiver chains are represented by the PortB & PortC.

Next, the setup of AT is shown in Fig 2.9. Circle with letter 'A' shows the cable connection between Quasi-LBS and Quasi-AT.

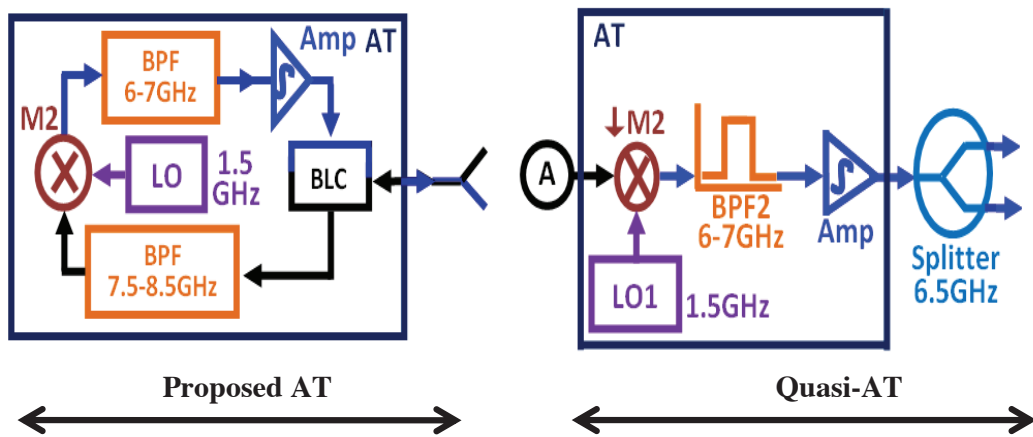


Fig 2.9: Representation of AT for Initial Test.

The emitted signal of frequency 7.5-8.5 GHz is down-shifted in frequency by the mixer (M2, Marki M3-0309) and the local oscillator (LO1, Agilent's Signal Generator E8267D). The mixer output is connected to a chain of bandpass filter (BPF2, REACTEL Inc. for 7.5-8.5 GHz), amplifier Amp1 (HWLF6090-30-10) and one splitter. With the application of splitter, there are two distinct outputs that will be connected to coaxial cables of different lengths to simulate the paths of the RF signal from the Quasi-AT to the A₁ and A₂ of the proposed LBS. The different time-of-flights of the signals will be measured by the VNA.

Down-shift in frequency is introduced by the mixer (M2, Marki M3-0309) and the local oscillator (LO1, Agilent's Signal Generator E8267D) which is then connected to the bandpass filter (BPF2, REACTEL Inc. for 7.5-8.5 GHz) and then to the amplifier Amp1 (HWLF6090-30-10). The amplified signal is connected to a splitter for the representation of

two distinct paths followed by the signals. The down-link uses different Delay-lines so that it becomes analogous to the different time-of-flights covered by the signals.

The complete experimental setup is shown in Fig 2.10. The outputs of splitter are connected to a Ref line (signal 1) and to a variable Delay-line (signal 2). The variable delay line has been used for the representation of the path difference. The Ref line is plugged to the port B of VNA and the Delay-line channel is plugged to Port C. This setup is used for the phase measurement analysis.

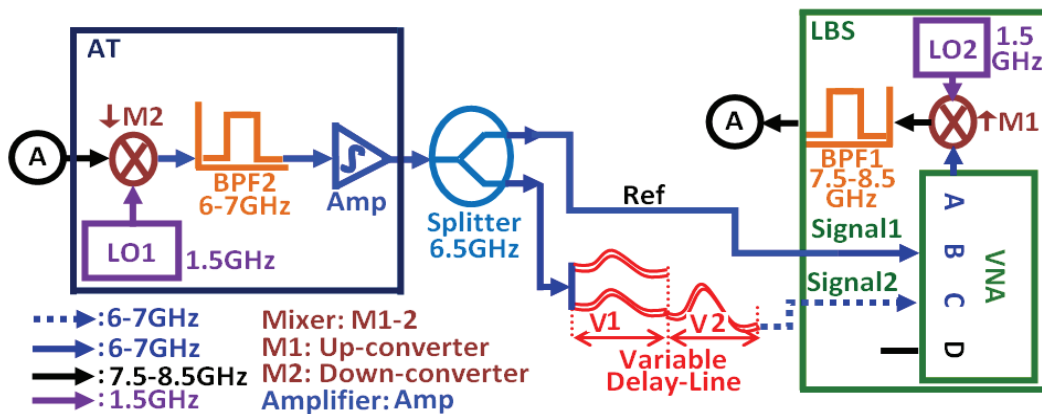


Fig 2.10: Initial Measurement Setup under Controlled Environment.

Two coaxial cables of 20 cm and 40 cm are used as the variable delay lines as V1 & V2 marked in Fig 2.10. The data collected by VNA are further processed in MATLAB for computation.

The path difference between two incoming signals (Signal1 and Signal2) is used for the AoA computation for a given value of d_{baseline} (0.96cm, assumed for the validation of the measurements) and then it is compared with the theoretical results obtained through MATLAB. The results are mentioned in Table 2.2.

Table 2.2
PATH-DIFFERENCE & AoA COMPUTATION

Delay-line (m)	Phase (degree) $\phi_2(Tm)$	Phase shift(degree) $\Delta\phi_{21}$	Path_dif (in m)	AoA (degree)	MATLAB AoA
0.20	322°	32	0.17	79.2°	77.6°
0.40	359°	69	0.38	66.5°	64.7°

The phase, $\phi_1(Tm)$, measured for the Ref line is 290° . The relationships, 2.24 & 2.30, have been used for the Path_dif and the AoA computations, respectively.

The difference between the measured and the theoretical values of AoA and Path_dif are under 1.8° and 3cm, respectively. The developed method and the system architecture have shown insignificant error on the measured results, although, the shift in frequency spectrum has been deliberately introduced by the AT. The computed Path_dif can be assumed as the phase difference between Signal1 and for Signal2.

This initial measurement results gives a good insight of the performances of the proposed system for further development of Indoor Localization System. However, this setup does not take into account of a real localization system such as plane wave conditions between two incoming signals. Therefore, the next section presents the detail information about constraints related to the ILS.

2.4.4 Constraints

For a successful ILS design, it is quite important to outline all possible constraints /limitations related to the system's performance in terms of accuracy, complexity, scalability, robustness, and cost. The main constraint of the proposed ILS for 2D/3D measurements is the plane wave conditions between incoming signals at the LBS. The other constraints, for example Near-Field Approximation are also covered in this section.

The constraints are presented with the help of mathematical expressions and the models based on those expressions are used to analyze the behaviour of 2D method in MATLAB through simulation.

2.4.4.1 Parallel Wave Condition

The proposed 2D/3D measurements method is based on radar interferometry technique for the angle-of-arrival computation which assumes the plane wave condition is fulfilled between incoming signals at the LBS. Therefore, the Plane Wave Condition (PWC) between two incoming signals needs to be verified for close proximity which will be the most likely condition in an indoor environment. A general situation of 2D measurements for AoA calculation is shown in Fig 2.11.

Ideally, two incoming signals can be assumed parallel if the angle of intersection between them remains zero. However, in real world, this condition is impossible to achieve if the signal's source remains at a finite distance from the point of observation. In our case, the AT acts as a source and the receivers' antennas at the LBS represent the points of observations where the PWC between two incoming signals must satisfy, or if not, then an acceptable level of tolerance, in the form of deviation in AoA, must be provided so that the incoming signals can be considered as parallel to each other.

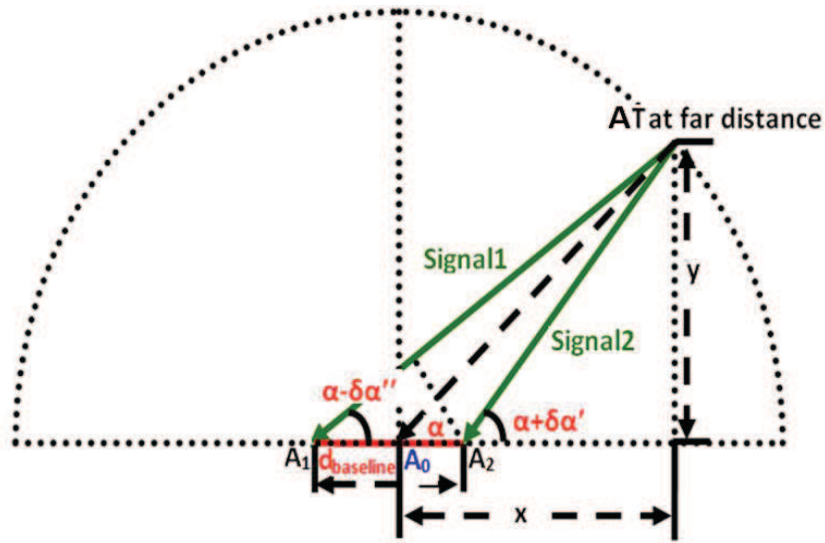


Fig 2.11: Optics Interferometry Technique

Let, the AT be at an arbitrary position and its coordinate be (x, y) , i.e., at a finite range (far-distance) from the LBS. The baseline ($d_{baseline}$) is considered along the x-axis with its ends coordinate at $(\pm d_{baseline}/2, 0)$, respectively. The two receiver antennas (A_1 & A_2) are positioned at each end of the baseline while the transmitter antenna (A_0) is positioned at $(0, 0)$ coordinate.

The transmitted signal from A_0 is reflected back by the AT and reaches to receiver antennas (A_1 & A_2). Let α , the angle of direction of departure of the output signal from A_0 to AT and the incoming signals at A_1 & A_2 with deviations $\delta\alpha'$ and $\delta\alpha''$.

If the deviations become zero, we can say that the two incoming signals are parallel to each other. Otherwise, we can define $\delta\alpha'$ and $\delta\alpha''$ as

$$\left. \begin{aligned} \alpha + \delta\alpha' &= \tan^{-1} \frac{y}{x - 0.5 * d_{baseline}} \\ \alpha - \delta\alpha'' &= \tan^{-1} \frac{y}{x + 0.5 * d_{baseline}} \end{aligned} \right\} \quad 2.34$$

The relationship 2.34 is rearranged in terms of radial-distance, $d = \sqrt{x^2 + y^2}$, angle-of-arrival, α as $\tan \alpha = \frac{y}{x}$, and $x = d \cos \alpha$

$$\left. \begin{aligned} \alpha + \delta\alpha' &= \tan^{-1} \frac{\tan \alpha}{1 - \left(0.5 * d_{baseline} / d \cos \alpha\right)} \\ \alpha - \delta\alpha'' &= \tan^{-1} \frac{\tan \alpha}{1 + \left(0.5 * d_{baseline} / d \cos \alpha\right)} \end{aligned} \right\} \quad 2.35$$

The ratio of the radial-distance over the half of the baseline is considered as Baseline-Factor as B_f . This will help in reducing the number independent parameters (d & $d_{baseline}$) to one (B_f) as

$$\text{Baseline-Factor, } B_f = \frac{d}{0.5 * d_{baseline}} \quad 2.36$$

This will further simplify the 2.35 as

$$\left. \begin{aligned} \alpha + \delta\alpha' &= \tan^{-1} \frac{\tan \alpha}{1 - \left(1 / B_f \cos \alpha\right)} \\ \alpha - \delta\alpha'' &= \tan^{-1} \frac{\tan \alpha}{1 + \left(1 / B_f \cos \alpha\right)} \end{aligned} \right\} \quad 2.37$$

The sum of difference in magnitude of $\delta\alpha'$ and $\delta\alpha''$ is expressed as

$$|\delta\alpha' + \delta\alpha''| = \left| \tan^{-1} \frac{\tan \alpha}{1 - \left(1 / B_f \cos \alpha\right)} - \tan^{-1} \frac{\tan \alpha}{1 + \left(1 / B_f \cos \alpha\right)} \right| \quad 2.38$$

From the simulation of relationship 2.38, the difference in deviations has a steep fall (Fig 2.12) and it reduces to 0.5° from 29° over B_f from 1 to 10. Further, it continues to decay and becomes comparable to zero. This shows that the deviations $\delta\alpha'$ and $\delta\alpha''$ are comparable to each other in term of magnitude for $B_f > 10$. The differential value is marked by the red-

curve in Fig 2.12 at α equal to 60° (an arbitrary value considered). Therefore, the $\delta\alpha'$ and $\delta\alpha''$ can be assumed as equal for $B_f > 10$.

At this point, $\delta\alpha'$ and $\delta\alpha''$ are considered as $|\delta\alpha'| \approx |\delta\alpha''|$ for $B_f > 10$, therefore, the $\delta\alpha$ can be written as $\delta\alpha' + \delta\alpha'' = 2*\delta\alpha$. Hence, $\delta\alpha$ is expressed

$$\delta\alpha = \frac{\delta\alpha' + \delta\alpha''}{2} = \frac{1}{2} \left(\tan^{-1} \frac{\tan \alpha}{1 - \left(\frac{1}{B_f} \cos \alpha \right)} - \tan^{-1} \frac{\tan \alpha}{1 + \left(\frac{1}{B_f} \cos \alpha \right)} \right) \quad 2.39$$

With the help of relationship 2.39, the behaviour of $\delta\alpha$ can be analysed for any given value of α by varying B_f ; this behaviour is plotted in Fig 2.12.

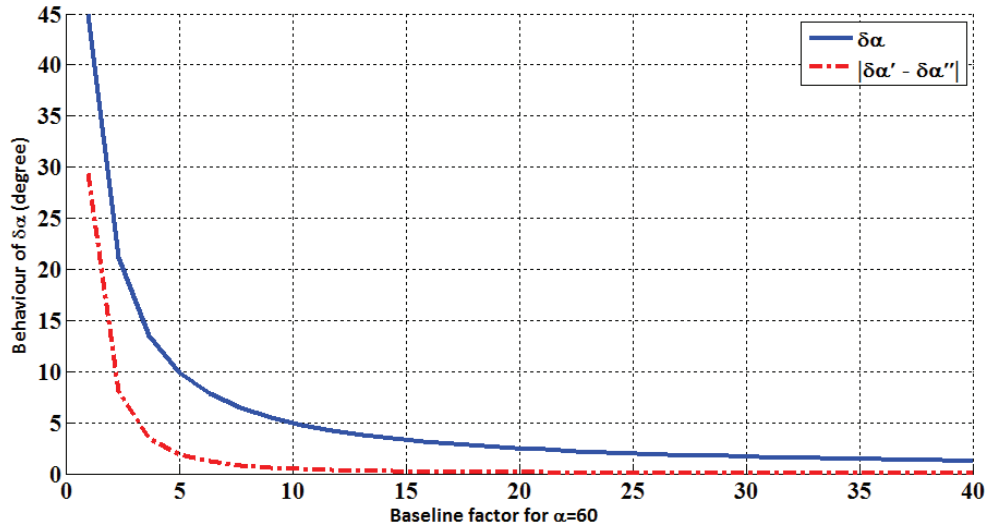


Fig 2.12: Deviation in AoA ($\delta\alpha$) at $\alpha=60^\circ$.

The steep fall is also noticed in $\delta\alpha$ upto B_f equal to 10 and it becomes almost constant after $B_f=30$. Moreover, it remains under 1° for $B_f > 30$ as shown in Fig 2.12. The decrease in $\delta\alpha$ leads the signals close to PWC.

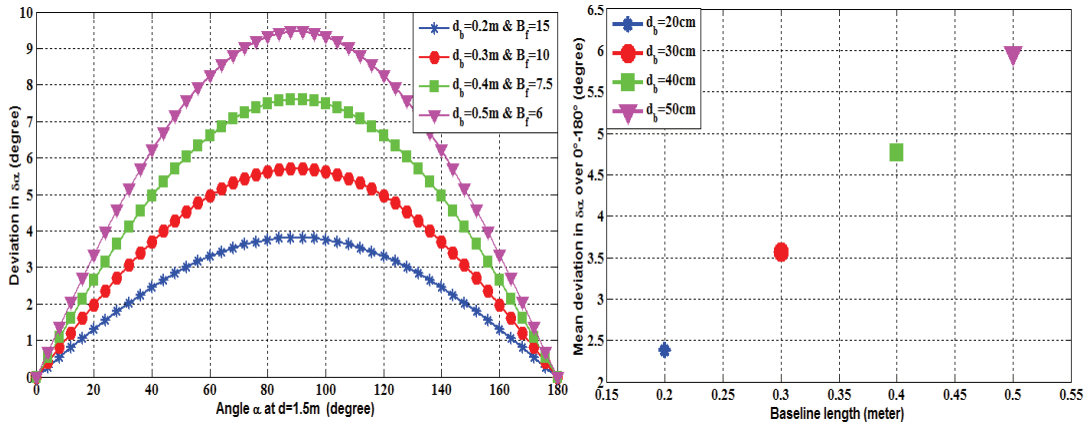


Fig 2.13: Deviation in AoA ($\delta\alpha$) and its mean value over (0° - 180°).

Furthermore, the behaviour of $\delta\alpha$ is analysed for different values of the baseline $\{20, 30, 40, 50\}$ cm by varying α from 0° to 180° ; these are shown on the left side of Fig 2.13, and its mean values on the right side. The $\delta\alpha$ reaches the maximum value at the orthogonal position to the baseline. For B_f equals to $\{15, 10, 7.5, 6\}$, the simulated mean values of $\delta\alpha$ are $\{2.4^\circ, 3.6^\circ, 4.8^\circ, 5.9^\circ\}$, respectively. The PWC condition completely fails at α equal to 90° and the maximum values of $\delta\alpha$ are $\{3.8^\circ, 5.7^\circ, 7.6^\circ, 9.5^\circ\}$. This also shows that the $\delta\alpha$ decreases with the increase of B_f . This implies that the smaller baseline will hold the PWC better than the larger one as the B_f increases. So it looks viable to use a smaller baseline length for AoA computation.

The behaviour of α with respect to the range is also plotted in Fig 2.14 for different values of the baseline. The B_f is marked with the black coloured dash-line. Its value increases with the vertical axis and remains constant across the horizontal axis for all baselines.

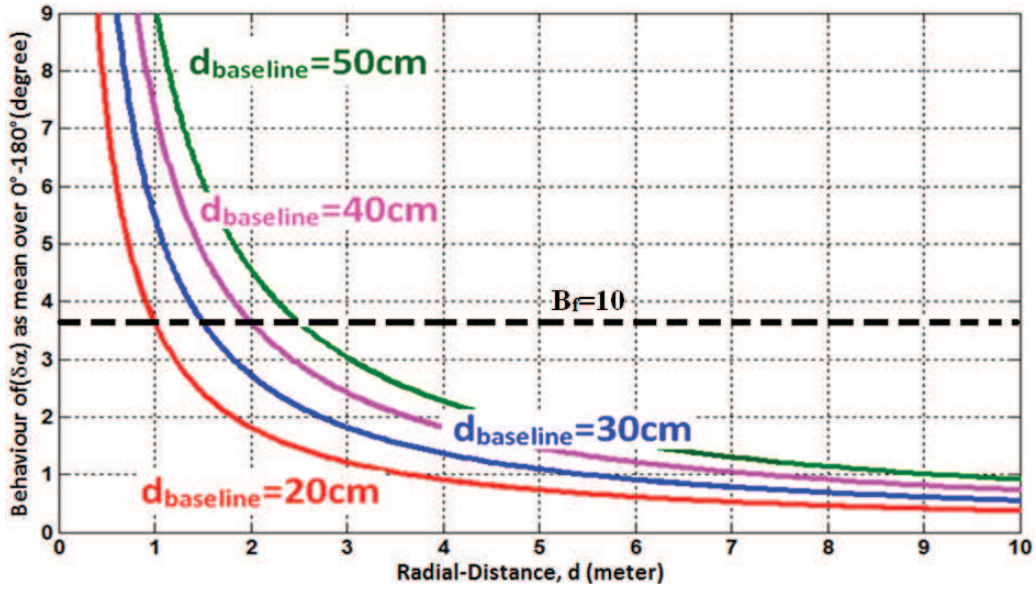


Fig 2.14: Mean deviation in AoA ($\delta\alpha$).

This shows that the overall deviation decreases with the increase of the radial-distance. As long as deviation remains zero or close to it, we can assume that the two incoming signals are parallel to each others. As the mean value $\delta\alpha$ is under 3.5° for $B_f=10$; it can be assumed as threshold value for the PWC. If the $\delta\alpha$ remains less than 3.5° then the incoming signals can be considered as parallel. The measurements have been performed in order to validate this condition and it is presented in [Chapter 4](#).

The smaller baseline appears to be good for AoA computation. However, this is not the correct perception in real situations and the reason is explained in the subsequent section.

2.4.4.2 Mapping of Baseline into AoA: Least Count

The relationship [2.30](#) computes the Angle-of-Arrival from the relative phase-shift ($\Delta\phi_{21}$) over the sweep time (T_m). However, this relative phase-shift has been derived for the path difference (Path_dif) via the relationships from [2.23](#) to [2.29](#). Therefore, the AoA is derived from the relative Path_dif over the sweep time. With the relationship [2.23](#), Path_dif is associated with the length of baseline as a scaling factor

$$\frac{Path_dif}{d_{baseline}} \leq |1| \Leftrightarrow \cos \alpha \leq |1| \quad 2.40$$

Thus, the path difference always remain less than or equal to the baseline for an angle estimation, otherwise it will lead to an absurd error. For simplicity, if we consider a linear relationship between the path-difference and the AoA; each value of the path-difference has a distinct value in AoA as appears from the relationship 2.40. As, α varies from 0°-to-90°, the path-difference also varies from 0-to- d_{baseline} . Therefore, if a baseline of 30cm is used to scale-down the AoA (a span of 90°) then each centimetre of the baseline presents a scale division of 3°, or conversely, each degree in AoA represents a path-difference of 0.33cm.

Hence, a larger value of the baseline will give a better resolution as a least count but at the same time PWC condition must be checked for the trade-off between PWC and angle resolution. This is contradictory to the conclusion of the previous investigation in Section 2.4.4.1. Therefore, the length of the baseline acts as a balance between the resolution and the PWC; an optimum length must be determined for the optimum performance of the system. The optimum length has been proposed in Chapter 4.

2.4.4.3 Far-Field Approximation

The physical dimension of an antenna plays an important role in a Near-Field Approximation (NFA) and hence it can also affect the PWC in close proximity between the LBS and the AT. The NFA can be defined as a distance where the PWC breaks down as [31]: the crossover distance (D_{ff}) between near and far-fields is taken to be where the phase error is 1/16 of a wavelength, or about 22.5°, and its expression is written as

$$D_{\text{ff}} = 2 * \left(\frac{D^2}{\lambda} \right) \quad 2.41$$

Where, λ is the wavelength, D is the largest dimension of the antenna in use and D_{ff} represents the distance for NFA. Generally, an antenna is designed with D as a function of λ . The various values of D_{ff} are mentioned in Table 2.3 for two antennas used in ILS; the antennas are presented in Chapter 3. The computation has been done for a factor of 5 instead of 2 for strict performance check-up. The edge frequencies of both channels, up-link (7.5-8.5 GHz) & down-link (6-7 GHz), are considered for the calculation, according to the ILS working principle defined in Section 2.3.

Table 2.3
NFA COMPUTATION

Frequency (GHz)	λ (cm)	Tag-Antenna		LBS-Antenna	
		D (cm)	$D_{ff}=5*D^2/\lambda$ (cm)	D (cm)	$D_{ff}=5*D^2/\lambda$ (cm)
6	5.0	6.4	41	7.6	58
7	4.3	6.4	48	7.6	67
7.5	4.0	6.4	51	7.6	72
8.5	3.5	6.4	58	7.6	82

The maximum values of D_{ff} are 58cm & 82cm for the two antennas used in ILS. If the radial-distance is considered as D_{ff} then it represents the minimum distance between the LBS and the active-Tag for which NFA condition must hold true.

Besides near-field approximation, the influence of receiver antennas on each other because of close-proximity in space, antenna factor, is discussed in **Chapter 4** by performing measurements.

2.5 Conclusion

In this chapter, the architecture of the developed ILS is presented. The evolved methods for the position estimation are also described. The 2D and 3D methods have been presented as a hybrid method by combining the radial-distance and angles in the polar-form. The developed methodology has been successfully verified through the experimental results under controlled condition. Initial result has shown a good sign for the further development of the ILS.

The main advantage of the ILS is the reduction of the known reference/anchor positions to one; this will give the freedom from the synchronization management between different reference positions as required in other positioning systems. Also, the frequency shifting methodology in AT will help in reducing the indoor's constraints such as backscattering effect. The other possible constraints such as PWC, NFA are also discussed and analyzed in order to understand their influence on the designed ILS performance.

The ILS system will have a less complex architectural design with low realization cost. The next chapter presents the realization of the ILS and its various components in order to achieve the objective, ILS.

References

- [1] R. Al Alwai, "RSSI based location estimation in wireless sensors networks," IEEE International Conference on Networks (ICON) 2011, pp. 118-122.
- [2] X. Xiao, X. Jing, S. You, and J. Zeng, "An environmental-adaptive RSSI based indoor positioning approach using RFID," International Conference on Advanced Intelligence and Awareness Internet (AIAI 2010), pp. 127-130.
- [3] U. Grossmann, M. Schauch, and S. Hakobyan, "RSSI based WLAN Indoor Positioning with Personal Digital Assistants," Intelligent Data Acquisition and Advanced Computing Systems: Technology and Applications, IDAACS 2007, pp. 653-656.
- [4] K. Wen-Hsing, C. Yun-Shen, J. Gwei-Tai, and L. Tai-Wei, "An intelligent position approach: RSSI-based indoor and outdoor localization scheme in Zigbee networks," International Conference on Machine Learning and Cybernetics (ICMLC 2010), pp. 2754-2759.
- [5] A. Narzullaev, P. YongWang, and J. Hoyoul, "Accurate signal strength prediction based positioning for indoor WLAN systems," Position, Location and Navigation Symposium 2008, Monterey pp. 127-130.
- [6] Widawan, M. Klepal, and D. Pesch, "Influence of Predicted and Measured Fingerprint on the Accuracy of RSSI-based Indoor Location Systems," Position, Navigation and Communication 2007, Hannover, pp. 145-151.
- [7] L. Ruey-Hsuan, W. Jen-Chieh, C. Shao-Hsuan Chang, and C. Sheng-Fuh, "Radar design for wireless indoor positioning applications," European Microwave Conference (2013), Nuremberg, pp. 846-849.
- [8] M. Brugger, T. Christ, F. Kemeth, and S. Nagy, "The FMCW technology-based indoor localization system," Ubiquitous positioning Indoor Navigation and Localization Based Service (UPINLBS 2010), Kirkkonummi, pp. 1-6.

-
- [9] T. Ussmuller, M. Jung, and R. Weigel, "Synthesizer concepts for FMCW based locatable wireless sensor nodes," IEEE MTT-S International Microwave Workshop, IMWS 2009, Cavtat, pp. 1-4.
- [10] S. Junyang, and A. F. Molisch, "Passive location estimation using TOA measurements," International Conference on Ultra-Wideband (Microwave Workshop, ICUWB 2011, Bolonga, pp. 253-257.
- [11] A. Gholoobi, and S. Stavrou, "A hybrid TDoA-ToA localization method," International Conference on Telecommunications, ICT 2013, Casablanca, pp. 1-4.
- [12] Y. Gu, A. Lo, and I. Niemegeer, "A survey of indoor positioning systems for wireless personal networks," IEEE Communications Survey & Tutorials, vol.11, NO. 1, First Quarter 2009, pp. 13-32.
- [13] S. Manapure, H. Darabi, V. Patel, and P. Banerjee, "A comparative study of radio frequency-based indoor location systems," in Proc. IEEE Int. Conf. Netw., Sens. Control, 2004, vol. 2, pp. 1265-1270.
- [14] Hui Liu, Houshang Darabi, Pat Banerjee, and Jing Liu, "Survey of Wireless Indoor Positioning Techniques and Systems," in IEEE Trans. on systems, man, and cybernetics-PartC, Nov. 2007, vil. 37, pp. 1067-1080.
- [15] F. Tappero, B. Merminod, and M. Ciurana, "IEEE 802.11 ranging and multi-lateration for software-defined positioning receiver," in Indoor positioning and Indoor Navigation (IPIN), 2010, pp. 1-6.
- [16] W. Vinichayakul, and S. Promwong, "Improvement of fingerprinting technique for UWB indoor localization," Information and Communication Technology, Electronic and Electrical Engineering (JICTEE), 2014, pp. 1-5.
- [17] M. Vuckovic, I. Petrovic, D. Vidovic, Z. Kostovic, S. Pletl, and D. Kukulj, "Space grid resolution impact on accuracy of the indoor localization fingerprinting," Telecommunications Forum (TELEFOR), 2011 19th, pp. 321-324.

-
- [18] Y. Gu, A. Lo, and I. Niemegeer, "A survey of indoor positioning systems for wireless personal networks," *IEEE Communications Survey & Tutorials*, vol.11, NO. 1, First Quarter 2009, pp. 13-32.
- [19] S. el Khediri. A. Kachouri, and N. Nasri, "Diverse synchronization issues in wireless sensor networks," *International Conference on Microelectronics, ICM 2011*, pp. 1-6.
- [20] Bassem R.Mahafza, *Introduction to RADAR ANALYSIS*, Chapter-5, "Continuous Wave and Pulsed Radar", Page-117.
- [21] B. Lathi, "Modern digital and analog communication systems," *The Oxford series in electrical and computer engineering*, Oxford University Press, 1998.
- [22] R. Barillet, J. Y. Richard, J. Cermak, and L. Sojdr, "Application of dual-mixer-time-difference multiplication in accurate time-delay measurements," *Frequency Control Symposium and Exposition, 2004*, pp. 729-733.
- [23] Y. Zhang, M. G. Amin, and S. Kaushik, "Localization and Tracking of Passive RFID Tags Based on Direction Estimation," *International Journal of Antenna and Propagation Hindwai Publishing Corporation*, vol 2007, ID 17426, doi. 10.1155/2007/17426.
- [24] R.Szumny, K.Kurek, and J.Modelski, "Attenuation of multipath components using directional antennas and circular polarization for indoor wireless positioning systems," *Radar Conference, EuRAD*, pp. 401-404, 2007.
- [25] S. Wehrli. R. Gierlich, J. Huttner, D. Barras, F. Ellinger, and H. Jackel, "Integrated Active Pulsed Reflector for an Indoor Local Positioning System", *IEEE Transactions on Microwave Theory & Technique*, vol. 58, no. 2, 2010, pp. 267-276.
- [26] M. Vossiek, and P. Guldenl, "The Switched Injection-Locked Oscillator: A Novel Versatile Concept for Wireless Transponder and Localization Systems", *IEEE Transactions on Microwave Theory & Technique*, vol. 56, no. 4, 2008, pp. 859-866.
- [27] "<http://spectrum-instrumentation.com/en/products/m3i2132>".

-
- [28] B. Waldmann, R. Weigel, R. Ebel, and M. Vossiek, "An Ultra-Wideband Local Positioning System for Highly Complex Indoor Environments," Localization and GNSS (ICL-GNSS 2012), Starnberg, pp. 1-5.
- [29] Z. Ma, Y. Qiao, B. Lee, and E. Fallon, "Experimental Evaluation of Mobile Phone Sensors," Signals and Systems Conference (ISSSC 2013), LYIT Letterkenny, pp. 1-8.
- [30] J. Cousin, "Radar multistatique d'aide la conduite pour le positionnement 2D de cible à courtes distances par la technique FMCW associé l'interférométrie," 15^{es} Journées Nationales Microondes, 2007 (in french).
- [31] Constantine A. Balanis, "Antenna Theory: Analysis and Design," 3rd ed (2005), Ch. 2, USA Wiley, pp. 32-34.

Chapter 3. Realization of Indoor Localization System

3.1 Introduction

Most of the localization systems based on the triangulation method [1, 2] need a prior knowledge of at least three references/anchors for the position estimation. Apart from the prior knowledge of anchors position; these anchors also need to be tightly synchronised. However, the developed architecture and the method for 3D-Indoor Localization System (ILS) will not require such needs because it utilises the concept of mono-pulse radar system. The developed ILS will provide 3D location of a remote tag with the prior knowledge of single reference/anchor point.

The complete integrated system and its managements are presented in [Section 3.2](#) for 3D position estimations. The scheme used for the data collection and its processing for the position estimations are explained in this chapter. The various designed components and their performances are also presented in this chapter. The antenna design and their characterizations are presented in [Section 3.2](#). Finally, the chapter ends with the realized ILS and its conclusion in [Section 3.4-3.5](#), respectively.

3.1.1 System Integration and Management

A schematic diagram of the 3D Indoor Localization System is depicted in [Fig 3.1](#). The integrated ILS system is solely based on the architecture presented in [Section 2.3- 2.4.3](#). The FMCW signal is generated by the Agilent's signal generator-Agilent (E8267D) with a sweep time equal to 10ms. The transmitted signal from the Localization Base Station (LBS) is marked in red arrow towards the active-Tag (AT). The reflected signals from AT are marked in blue and green arrows.

These coloured arrows represent the four radio waves picked by the four receivers' antennas placed in xy- and zx-plane. Then the output voltages resulting from the mixing of emitted and received signals by the four receivers are collected by the data acquisition card and provide the beat frequencies (f_{1-4}) for the signal processing. The card is installed in a remote desktop as shown in the schematic diagram of the complete ILS. The necessary signal processing is carried out through MATLAB.

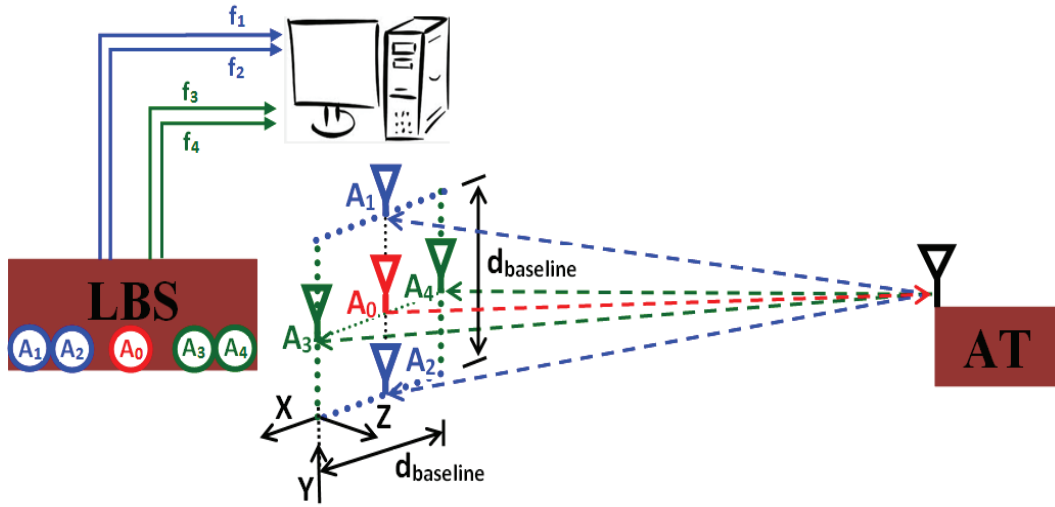


Fig 3.1: Schematic diagram of complete ILS.

Here, Spectrum-M3I.2132 is used as the data acquisition card. Its main purpose is to collect the beat frequencies. The acquisition card acts as an Analog-to-Digital Converter which converts the analog baseband signals, beat frequencies, into the digital form. The data have been collected with a sampling rate equals to 22.5MHz. The received signal and its processing is discussed in [Chapter 3](#). Input range of the voltage that the card can measure is between ± 50 mV and ± 500 mV. It has root-mean-square noise near zero level is < 0.5 dB. Its SNR (Signal to Noise Ratio) is between 44.6 dB and 45.1 dB, and the corresponding ENOB (Effective Number of Bits) are between 7.1 and 7.2. Therefore, the Signal-to-Quantization-Noise ratio (SQNR) is given by the expression mentioned in [\[3\]](#)

$$SQNR = 20 \log_{10}(2^Q) \approx 6.02 \cdot Q \text{ dB} \quad 3.1$$

Where Q is the number of quantization bits. Therefore, the 7.2 ENOB has a maximum SNR of $6.02 \times 7.2 = 43.34$ dB, and hence the quantization error is 43.34 dB below the maximum level. Besides, more information about the data acquisition card can be obtained from the data sheet [\[4\]](#).

The various components used in the ILS are: passband filter, amplifier, mixer, equal-split divider, 90° hybrid-branch line coupler, and circular polarized antennas. The characterization of these components is presented in this section.

3.1.1.1 Equal-Split Divider

An equal-split divider [5] has been used for the division of reference FMCW signal, 6-7 GHz. The split part of the signal is used for mixing with the received signals coming from Active-Tag for the extraction of beat frequencies. The layout of the designed is presented in Fig 3.2 and its simulated and measured results are in Fig 3.3. The CST Studio Suit has been used for the design.

The dimension size of the designed splitter is 31mmx26mm and FR4 substrate (FR4, $\epsilon_r=4.2$, thickness=1.575mm, $\tan\delta = 0.01$) is used for the design realization.

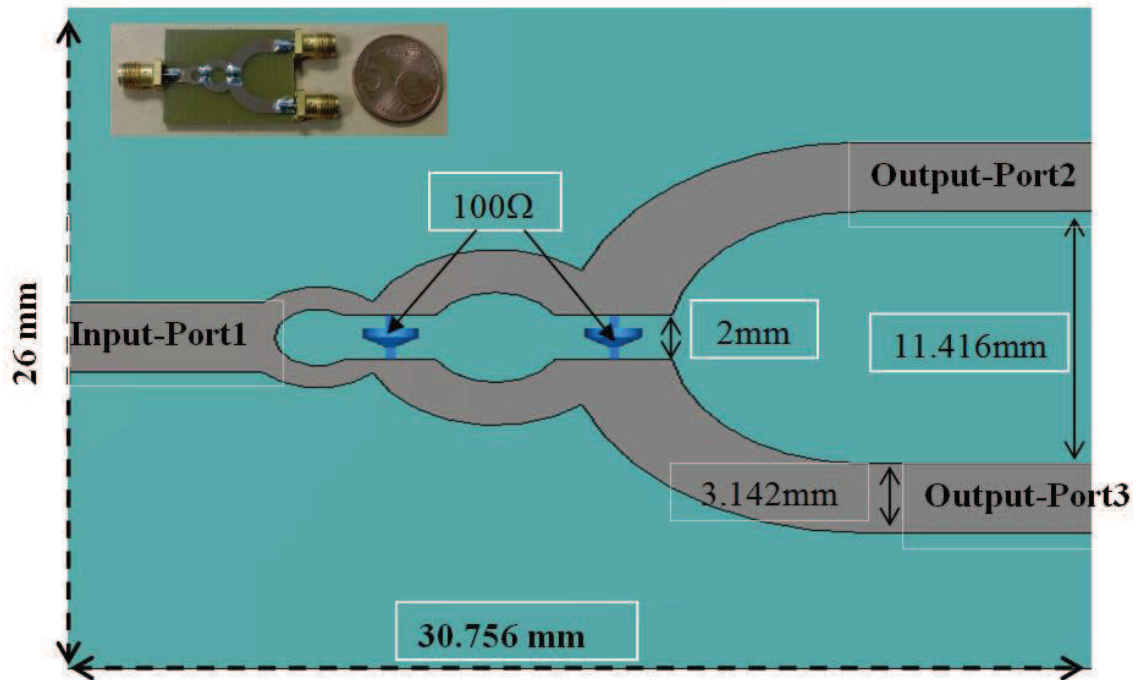


Fig 3.2: Layout of Equal Split-Divider.

The characterization has been done by connecting the three ports of the splitter to Vector Network Analyser (VNA). The return losses are less than 20 dB between 6 GHz and 7 GHz. The insertion loss is equal to 4.3 dB, measured values marked in green (Port21) and black (Port31), between 6-7 GHz. The extra 1.3 dB loss can be assumed because of the fabrication error. However, the out-put signals from the output-ports (Output-Port2 and Output-Port2) are of almost same power.

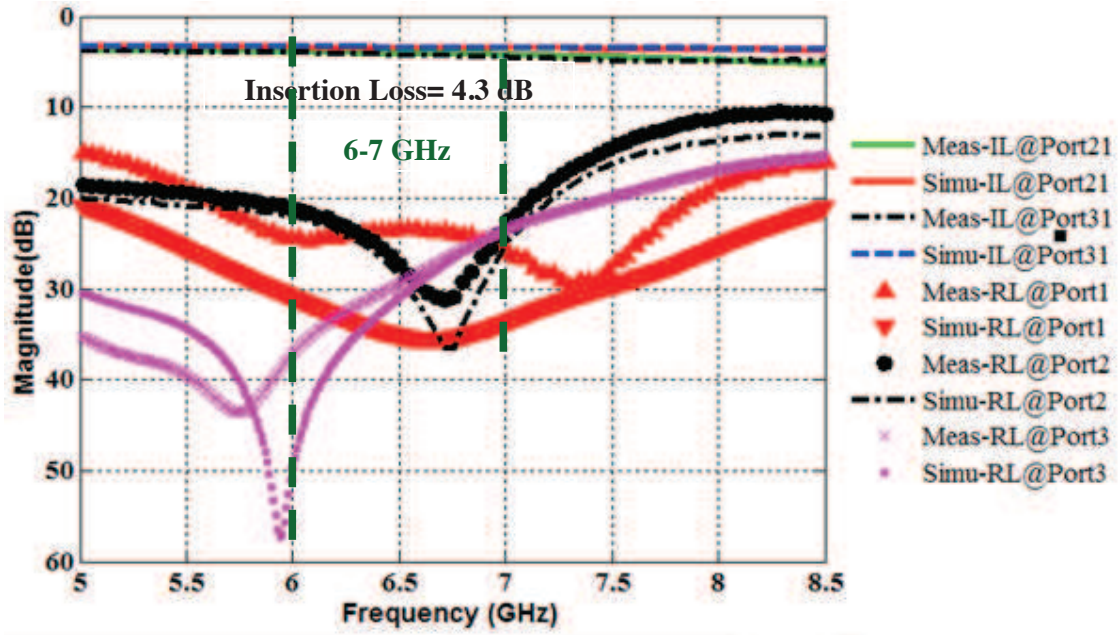


Fig 3.3: Measured and Simulated results.

The characteristics of the above design are mentioned in **Table 3.1**.

Table 3.1
EQUAL-SPLIT DIVIDER: FABRICATED

Specification	Characteristics
Frequency Band	2-9.75 GHz
Return Loss	≥ 23 dB @ 6-7 GHz
Isolation	≥ 21 dB @ 6-7 GHz, between outputs
Insertion Loss	4.3dB @ 6-7 GHz
Substrate	FR4, $\epsilon_r=4.2$, thickness=1.575mm, $\tan\delta = 0.01$

3.1.1.2 Mixer

The ILS uses two dedicated channels, up-link and down-link, over 7.5-8.5 GHz and 6-7 GHz, respectively. The frequency band 6-7 GHz is up-converted for the uplink and for the downlink is down-converted to produce the beat frequencies with the help of mixer. The mixers from Marki Microwave have been used in the ILS design which is shown in **Fig 3.4** and its data sheet is presented in [6].



Fig 3.4: Mixer- Marki Microwave.

The different frequency transposes by the mixer are presented in **Table 3.2**. These configurations are considered according to the architecture define in **Section 2.3**. Configurations, A & C, represent the first and the last frequency transpose by the transmitter and the receiver sections of Localization Base Station, whereas B corresponds to the frequency transpose by the active-Tag.

Table 3.2
MIXER: MARKI M30309LP

Configuration	Inputs		Outputs
A (transmitter)	LO: 6-7 GHz	IF: 1.5GHz	RF: 7.5-8.5 GHz
B (active-Tag)	LO: 7.5-8.5 GHz	IF: 1.5GHz	RF: 6-7 GHz
C (receiver)	LO: 6-7 GHz	RF: 6-7 GHz	IF: 0-1 GHz (beat frequency)

The functionality of the mixers are verified by feeding two signals to the mixer from two RF signal generators and one spectrum analyser for observing the resulting output signal, that is, the resultant mixed signal. The same mixer will be tested for the up-and-down conversions and no filter has been used, therefore, for each configuration the spectrum analyser has been set as per the expected signal output. The main interest lies in knowing the output power of the desired signal. A common expression for the output signals can be expressed as

$$f_{out} = (f_{LO} + f_{IF}), (f_{LO} - f_{IF}), f_{LO}, f_{IF} \quad 3.2$$

The first two signals represent the mixed signals, up-and-down converted signals that is $f_{LO}+f_{IF}$ and $f_{LO}-f_{IF}$, whereas the rest two are leaked/parasitic signals, f_{LO} and f_{IF} . The observed results are mentioned in **Table 3.3**. The local oscillator port of the mixer is

represented by the LO and likewise RF and IF represent the radio-frequency and intermediate-frequency ports.

Table 3.3
MIXER: CONVERSION LOSS

Configuration	Inputs		Outputs	Conversion Loss
	LO (5dBm)	IF (3.5dBm)	RF	
A (transmitter)	6 GHz	1.5 GHz	-8.3dBm@7.5 GHz	13.3 dB
	6.5 GHz	1.5 GHz	-6.8 dBm @ 8 GHz	11.8 dB
	7 GHz	1.5 GHz	-6.4 dBm @ 8.5 GHz	11.4 dB
B (active-Tag)	7.5 GHz	1.5 GHz	-4.8 dBm @ 6 GHz	9.4 dB
	8 GHz	1.5 GHz	-4.7 dBm @ 6.5 GHz	9.7 dB
	8.5 GHz	1.5 GHz	-7.7 dBm @ 7 GHz	12.7 dB
C (receiver)	RF(5dBm)	LO (3.5dBm)	IF	
	6 GHz	6.1 GHz	-3.6 dBm @ 100 MHz	7.1 dB
	6.5 GHz	6.6 GHz	-3.5 dBm @ 100 MHz	6.9 dB
	6.9 GHz	7 GHz	-3.4 dBm @ 100 MHz	6.9 dB

The conversion losses, difference between input and output power levels, are between 9.4-13.3 dB when the mixer uses the RF port for signal output instead of IF port. However, the conversion losses are between 6.9-7.1 dB when IF is used as the output port which comply with the values mentioned in the data sheet. The variation of the RF output power levels of the transmitter or the active-Tag is almost 2 dB and 3 dB, respectively. But, such strong variation is not observed for the IF power output level of the receiver which almost remains stable around 3.5 dBm. Furthermore the power levels of the leakage signals resulting from the input signals are mentioned in [Table 3.4](#).

Table 3.4
MIXER: LEAKAGE POWER

LO (5dBm)	IF (3.5dBm)	RF (LO Leakage)	RF (IF Leakage)
6GHz	1.5GHz	-20.3dBm @ 1.5GHz	-31dBm @ 6GHz
6.5GHz	1.5GHz	-23.9dBm @ 1.5GHz	-37dBm @ 6.5GHz
7GHz	1.5GHz	-24.8dBm @ 1.5GHz	-32dBm @ 7GHz
7.5GHz	1.5GHz	-25.3dBm @ 1.5GHz	-33dBm @ 7.5GHz
8GHz	1.5GHz	-23.1dBm @ 1.5GHz	-36dBm @ 8GHz
8.5GHz	1.5GHz	-24.2dBm @ 1.5GHz	-38dBm @ 8.5GHz

The power levels of the 1.5 GHz IF signal are between -31 dBm and -38 dBm at the output port (RF), and the power levels of the 6-8.5 GHz LO signal are between -20 dBm and -25 dBm. The mixer has better isolation for the IF signals compared to the LO ones. These leakage signals must be suppressed with the use of filters for reaching a better performance for the ILS. This can be done with two passband filters (6-7 GHz and 7.5-8.5 GHz) with attenuation higher than 40 dB in the stop bands.

3.1.1.3 Filter

Two types of the passband filters, 6-7GHz and 7.5-8.5 GHz, from REACTEL have been selected for suppressing those leakages/parasitic signals observed in the previous section. The characterization of the filter has been done by connecting the two ports of the filter to VNA. The performances of the filters are mentioned in **Table 3.5** and the filters are shown in **Fig 3.5**.

Table 3.5
PASSBAND FILTER: REACTEL, INC

Specification	Characteristic
Passband	6-7 & 7.5-8.5 GHz's
Insertion Loss	0.5dB @ Passband
Return Loss	≥15B @ Passband



Fig 3.5: Filters.

The measurement results of two filters are plotted in **Fig 3.6**.

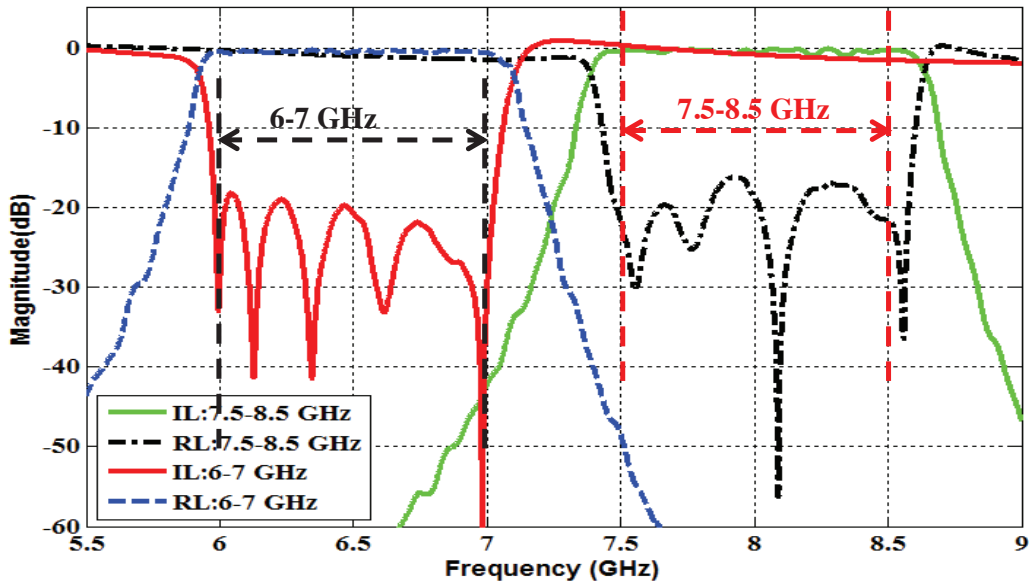


Fig 3.6: Filter characterization.

The insertion losses (IL) are less than 0.5 dB between 6-7 GHz (blue curve) and 7.5-8.5 GHz (green curve), respectively. Both filters have almost flat response in passband frequency for two channels. The measured return loss is more than 20 dB for the first filter between 6-7 GHz (red curve) whereas it is 15 dB for the second filter between 7.5-8.5 GHz (black curve).

Additionally, these filters will help in filtering out the backscattered (7.5-8.5 GHz, reflected from the indoor clutter) RF signals by separating the retransmitted signal (6-7 GHz). The use of filters will also help in reducing the feedback effects in the Active-Tag.

3.1.1.4 Amplifier

For RF signal boosting, the amplifier from HengWei Microwave Electronic is used in the ILS which is shown in Fig 3.7.



Fig 3.7: Amplifier-HWLF6090-30-10.

The characterization of the amplifier is carried out at two frequencies, 8GHz and 6.5GHz, which represent the central frequencies of the uplink and the downlink channels. The signal is connected to the input port of the amplifier and then its corresponding output signal is observed in the spectrum analyser (at one frequency) for gain measurement. The output power level versus the input power level is plotted in Fig 3.8. The measurements are done for two frequencies, 6.5 GHz and 8 GHz. The amplifier requires a 12V/130mA DC source supply.

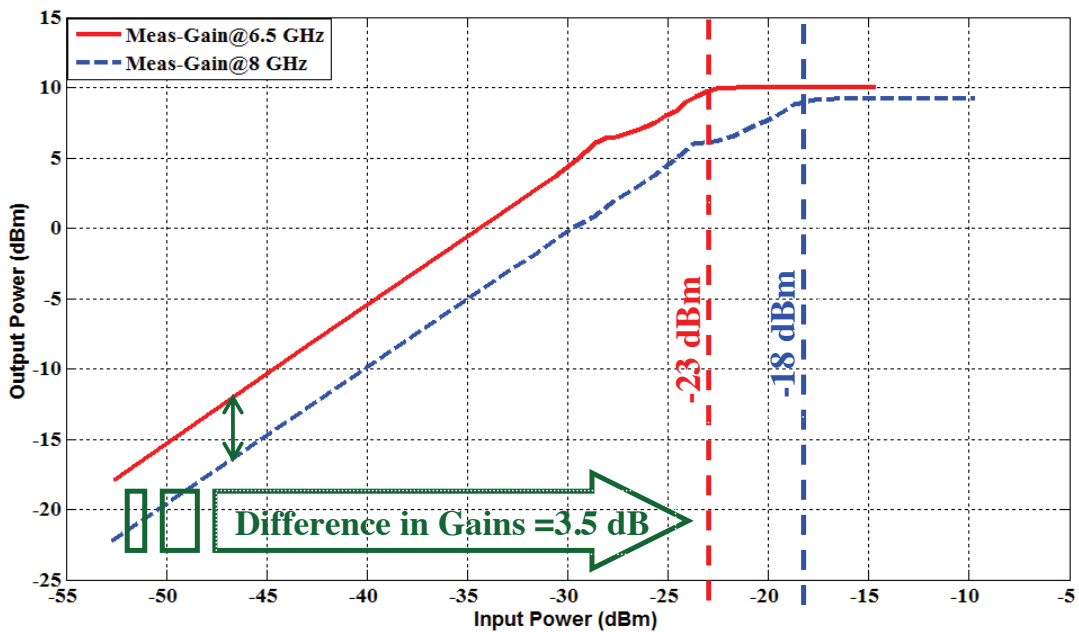


Fig 3.8: Amplifier characterization.

The maximum observed gains at 6.5GHz and 8GHz are 33.5 dB and 30 dB. The observed gain at 6.5GHz is same as mentioned in the data sheet [7] but at 8GHz its gain is 3dB less. The input saturation (the maximum input power level of signal for which the output power level of signal remains constant) levels at 6.5GHz and 8GHz are -23dBm and -22dBm, respectively. The noise factor of the used amplifier is 2.6 dB [7]. Its performances are mentioned in Table 3.6.

Table 3.6
AMPLIFIER: HWLF6090-30-10

Specification	Characteristic
Passband	6.5GHz & 8GHz
Gain	33.5dB @ 6.5GHz, 30dB @ 8GHz
RF Saturation Level	-23dBm @ 6.5GHz, -22dBm @ 8GHz

The design of antennas and their feeding circuit are presented in the next section.

3.2 Circular Polarized Antenna

The transmission and the reception of radio signals are mainly characterized through the antenna in terms of signal polarization and the radiation pattern. Broadly, the polarization is classified into two categories: Linear Polarization (LP) and Circular Polarization (CP). These are special case of elliptical polarization. Furthermore, LP is sub-classified as horizontal & vertical polarizations. Likewise, CP is also sub-classified as Right Hand Circular Polarization (RHCP) and Left Hand Circular Polarization (LHCP).

The difference between LP & CP comes from the orientation of electric field. In case of LP, the electric field vector always remains confined within a single plane. But in case of CP, rather confining in a single plane the electric field vector remains rotating in 360°-plane. This gives, CP, a better chance of penetrating an indoor environment as it has less chance of depolarization because it has less chance of impact by obstructions in comparison of linear polarization. Although, the reflection, diffraction all such phenomena are responsible for the depolarization. However, the use of CP radio waveform gives a better chance of good receptions of the transmitted signal. Thus, it provides an increased likelihood of good reception in an indoor environment. Additionally, the use of different polarizations scheme will reduce the chances of signal interference because either the LHCP can be used as the uplink and the RHCP as the downlink in inverse manner. Moreover, the CP provides an upper hand compared to the linearly polarized antenna in reducing the harsh indoor conditions, like reflectivity, absorption, phasing issues, multipath, etc [8-9].

However, it is not so easy to obtain a CP because its antenna designs are more complex than the linear ones. There are two common ways for producing CP [10]: one way is the use of traditional antenna which produces CP by virtue of their physical structure [11-12] such as Archimedean, Sinuous, Spiral, and another way is through the dual-feeding technique [13-15] that is by introducing two identical orthogonal electric field vectors with a separation of 90° in phase.

The traditional antennas such as Sinuous [16] have symmetric design and hence antennas have ultra-wideband frequency response. Since these antennas are symmetric

therefore it requires a balance feeding circuit which is known as balun; however, this makes the antennas quite heavy in weight as well as big in size. For example, a sinuous antenna along with balun is shown in [Fig 3.9](#).

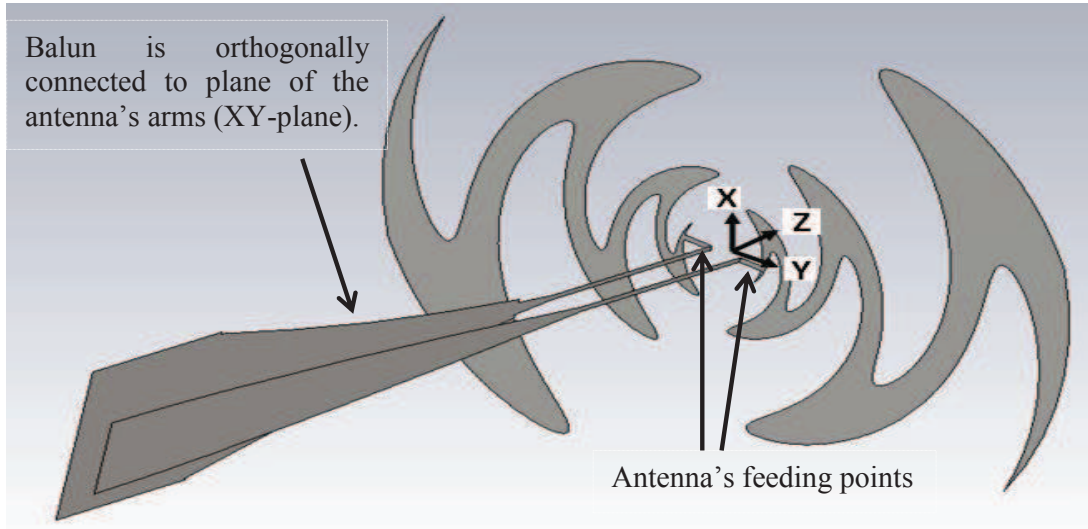


Fig 3.9: Sinuous antenna with balun in orthogonal position.

Balun is orthogonally connected to the plane of antenna structure (arms, xy-plane). But dual CP requires two feeding circuit [17-19], and it is difficult to feed two signals at the same feeding position to two traditional antennas. Hence, the dual CP is difficult to achieve with the traditionally antennas and can only produce one CP, either LHCP or RHCP, in a given space and time. That is, if LHCP is produced in positive direction of z-axis then the RHCP will be produce in negative direction of z-axis. And the dual polarization will only be achieved if the antenna produces both polarizations (LHCP & RHCP) simultaneously in a given direction of z-axis. This can be stated as the dual polarization is only achieved if the two orthogonal polarizations are simultaneously exist in a given space and time.

However, the dual polarization can be achieved with antenna based on orthogonal elements structure with a quadrature phase dual feeding. An example of such antenna is the crossed-dipole connected with a 90° -hybrid coupler which is illustrated in [Fig 3.10](#).

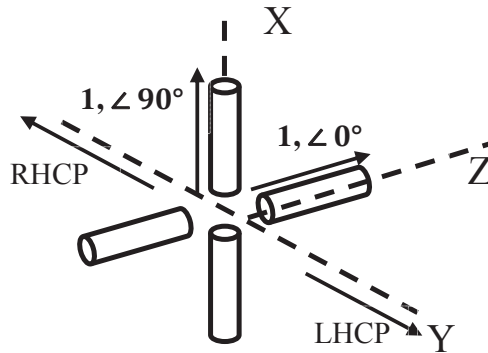


Fig 3.10: Crossed-dipole with quadrature phase.

This type of antennas is capable of producing right-hand and left-hand circular polarization simultaneously, and is usually based on the dual feeding technique. In dual-feeding technique, two orthogonal elements are simultaneously excited by the equal-amplitude electric field in a quarter phase relation at a given frequency. In this case, the CP can be easily reversed by the reversing the quadrature phase feeding, that is, LHCP becomes RHCP and vice-versa.

Nevertheless, the combination of traditional CP antenna and Dual-CP antenna can be used for the polarization diversity (use of LHCP and RHCP simultaneously) scheme between any two wireless units which is depicted in Fig 3.11. Suppose, two wireless units be Unit1 and Unit2. Also, assume that the Unit1 has separate antennas for transmission (A_Tx) and reception (B_Rx) of RF signals whereas the Unit2 acts as a reflector (transceiver) and uses same antenna (AB) for transmission and reception.

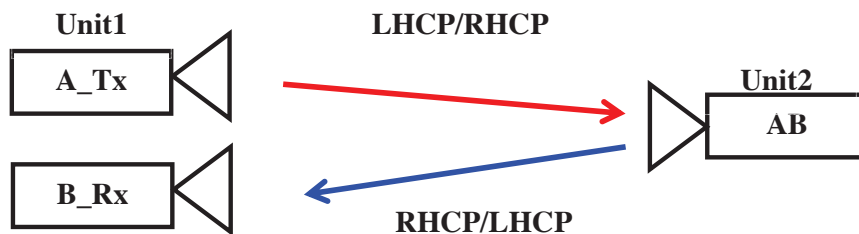


Fig 3.11: Circular Polarization diversity scheme.

Let, Unit1 transmits to as well as receives from the Unit2, simultaneously and they use two different CP. Therefore, Unit1 can use the traditional CP antenna with a desired CP

(either LHCP or RHCP) towards the Unit2 as it uses two separate antennas for transmitting (A_Tx) and receiving (B_Rx). But, the traditional antenna does not produce dual CP therefore it cannot be used. However, the antennas based on dual-feeding technique can be used by the Unit2 because such antenna supports the dual-CP. Hence, the CP diversity can be exploited by the system similar to one presented in [Fig 3.11](#). In fact, the proposed ILS is based on the similar system and the Unit1 can be replaced by the LBS which has one transmitter antenna and four receiver antennas ([Section 2.3-2.4](#)) and the Unit2 by the AT. This facilitates the use of CP diversity by the proposed ILS explained in [Chapter 2](#).

Moreover, the orthogonal feeding structure ([Fig 3.9](#)) to traditional antenna can be easily modified to two-dimensional planar structure such as [\[20-21\]](#). Such modification will provide a simple and compact antenna design. This modification has been used for the realization of LBS antenna and the designed antenna is presented in [Section 3.3.1](#) whereas the designed dual CP antenna using the dual-feeding technique is presented in [Section 3.3.2](#).

Both antennas are designed in CST Microwave Studio using Transient Solver and later the fabricated antennas are characterized in an anechoic chamber. The performances of the antennas are presented through the measured and the simulated results.

3.2.1 Circular Polarized Planar Antenna-Single Port

The LBS requires five CP antennas as the architecture shown in [Section 2.3](#) for 3D measurements and the antennas must operate between 6-8.5 GHz.

The CP antennas such as Spiral, Sinuous are known for ultra-wideband CP functionality and its performances are well proven in European UWB band, 6-8.5 GHz [\[22-24\]](#). This type of antenna produces the CP by virtue of its structural design and has only one input port. Normally, these antennas come in bulky size because of the commonly used feeding circuit that is balun [\[21, 25\]](#). In traditional CP antenna, the microstrip-to-coplanar stripline (CPS) balun is orthogonally connected to the plane of antenna's arms. However, Shen & Law presented a quasi-spiral two-dimensional planar antenna design [\[20\]](#) which is remarkably compact and has good performance between 6-to-10 GHz. Instead of feeding orthogonally they used a simple Microstrip tapered line in the same plane as one of its arms while keeping another arm as a partial ground. One arm is printed on the bottom face of the substrate and second arm on the top face, hence it has asymmetric structure. Since it is a two-

dimensional planar antenna and has good circular performance so this type of antenna is considered for the LBS.

Out of five antennas, one will be used as a transmitter whereas rest four will be used as receivers. The transmitter can either use the LHCP or the RHCP signal waveforms, and the receivers will use the opposite sense of polarization, either RHCP or LHCP, to the transmitted one.

The designed antenna is based on [20]; the reported antenna operates at the upper UWB frequency range between 7 GHz and 10 GHz. The [20] has used Rogers RO₄₀₀₃C (relative permittivity=3.38 and loss tangent=0.0027) substrate with thickness 0.508 mm in order to hold the symmetric feeding structure of the antenna. The width (Fig 3.12) of the antenna can be varied for the change in frequency. The wider width leads to better axial-ratio but the width is limited by the feeding point. Also, the higher substrate thickness leads to poor performance by the design.

The optimized design is shown on the right side of Fig 3.12 and its geometry on the left side. The return loss has good matching at 125 Ω which is less than 15dB between 6-to-8.5 GHz. A microstrip balun has been designed for the impedance transformation from 50 Ω to 125 Ω between 6-to-8.5 GHz frequency bandwidth. The simulated design is printed on DuroidRT 5880-substrate with relative permittivity, $\epsilon_r=2.2$, thickness=1.575mm and the tangent loss, $\tan\delta = 0.0009$.

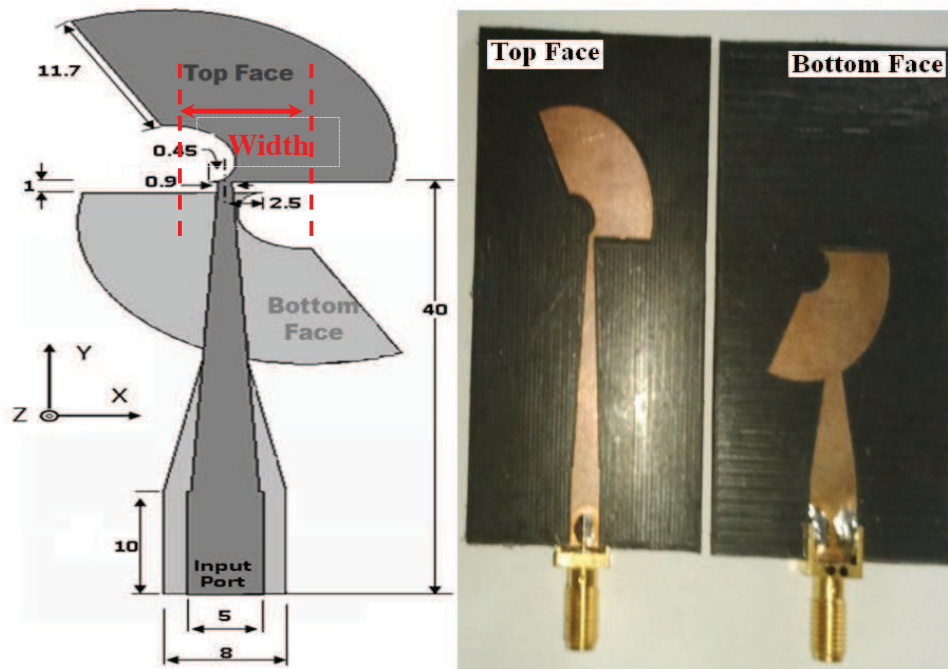


Fig 3.12: Circular Polarized Planar Antenna-Single Port.

3.2.1.1 Return Loss

The simulated and measured return losses are shown in Fig 3.13.

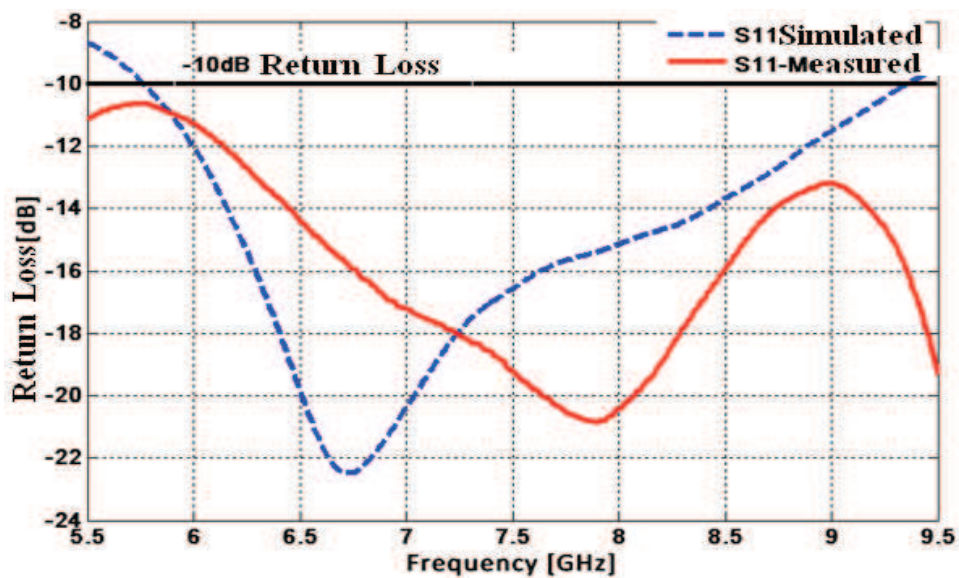


Fig 3.13: Return Loss results.

The simulated return loss is plotted in blue-dashed curved and the measured one is in red. The measured return loss is more than 10dB between 6-8.5 GHz frequency band. The observed maximum value is 21dB at 7.9GHz whereas in simulation it is a little over than 22dB at 6.7GHz. The difference between the simulated and the measured values may be due to the transition between the coaxial and the microstrip line. Nevertheless, the obtained results has good return loss value over the desired, 6-8.5 GHz, frequency band.

3.2.1.2 Axial Ratio

The 3dB boundary is the standard maximum value defined for the axial ratio of a radio wave as a circular polarized. Since the designed antenna is asymmetric therefore it is necessary that the axial ratio must remain with 3dB boundary throughout the working frequency range, 6-8.5 GHz.

The axial ratio is given by the expression [26]

$$AxialRatio = 20 \log \left(\frac{|E_{co}| + |E_{xp}|}{|E_{co}| - |E_{xp}|} \right) \quad 3.3$$

Where E_{co} is the co-polar electric field and E_{xp} is the cross-polar electric field. These electric fields are measured in the anechoic chamber with reference to LINDGREN 3117 Horn Antenna [29]. The ferrite material has been used to reduce the effects of coaxial cable and Fig 3.14.

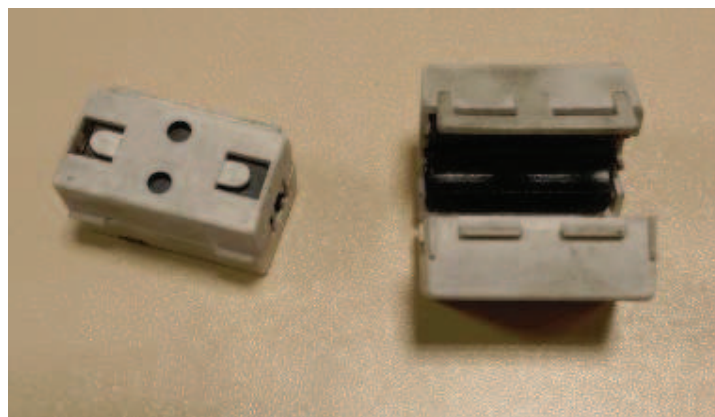


Fig 3.14: Ferrite materials used during measurement.

Fig 3.15 shows the measured and the simulated axial ratios of the designed antenna.

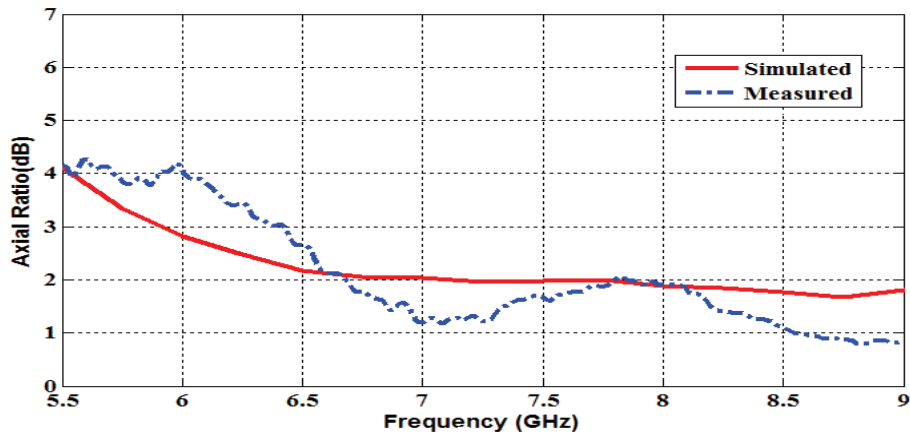


Fig 3.15: Simulated and Measured Axial ratio.

The measured axial ratio plotted in blue coloured dashed line is under 3dB standard boundary throughout the frequency (6-8.5GHz). The measured curve breaks through the 3dB boundary between 6-6.4 GHz by 1dB. Therefore, the design antenna will produce an elliptical polarized waveform. But, the measured axial ratio is close to the 3dB mark so it is an acceptable value.

3.2.1.3 Gain & Radiation Pattern

The simulated and the measured gains are shown in Fig 3.16. The LHCP and the RHCP curves are plotted in blue and red colours. The simulated gains for LHCP and RHCP are between 3-4.2 dBi over 6-8.5 GHz and the measured gains of the fabricated antenna are between 1.8-4.3 & 4.2 dBi, respectively. The RHCP has maximum gain of 4.2dBi whereas the LHCP has 4dBi. The realized antenna performance curves are close to the simulated ones.

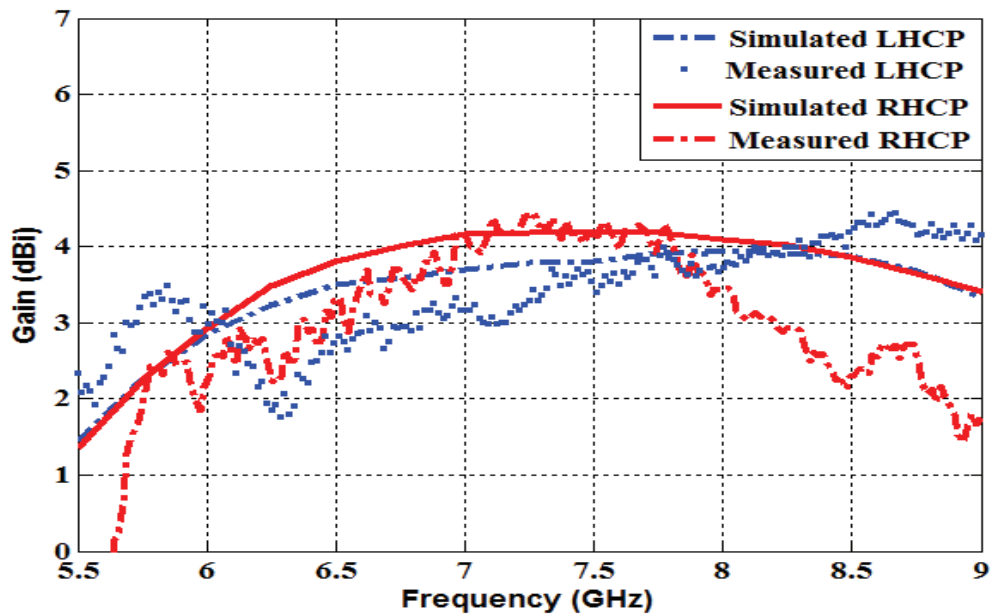


Fig 3.16: Simulated and Measured Gains (LBS-antenna).

The radiation patterns are presented in two planes, i.e., z-x and x-y planes. The z-x plane is shown in **Fig 3.17**. The simulated and the measured results are presented for the two frequencies: 6.5GHz and 8GHz. The radiation patterns at these two frequencies are shown on left and right side of the figure. The red curves represent the simulated results and the measured radiation patterns are represented by the blue curves. The measured curves are in good agreement with the simulated ones.

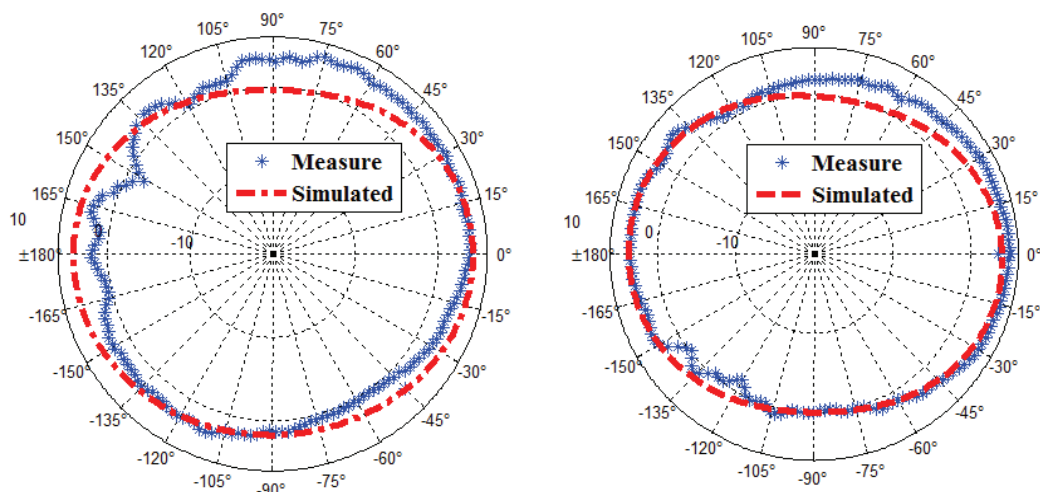


Fig 3.17: Left & Right side show the radiation pattern in z-x plane at 6.5 & 8 GHz (LBS-antenna).

Likewise, the x-y plane is shown in **Fig 3.18**; the left side and the right side show the radiation pattern at 6.5GHz and 8GHz, respectively.

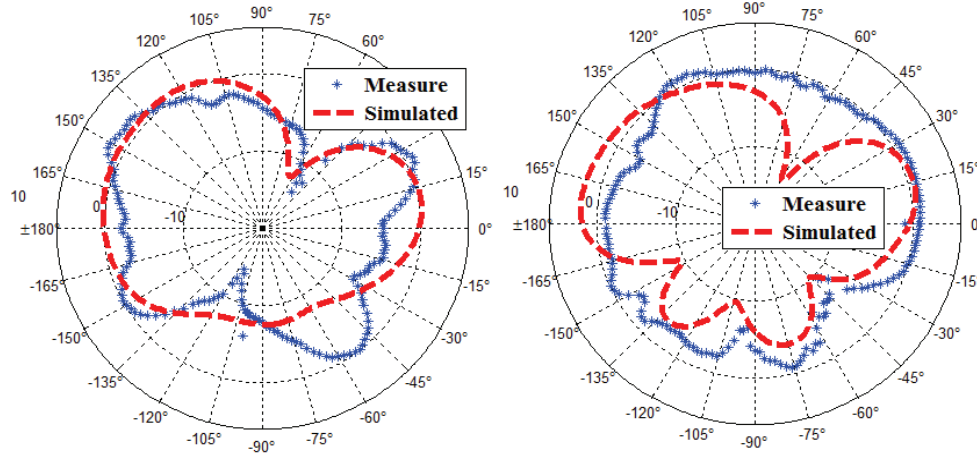


Fig 3.18: Left & Right side show the radiation pattern in x-y plane at 6.5 & 8 GHz.

The difference between the radiation patterns can be accounted because of the blockage from the SMA connector shown in **Fig 3.12**. A similar effect has also been reported by Shen & Law in their design [20]. As the simulated and the measure results have deep-cuts around 60° and -105° at 6.5 GHz, and similarly two more deep-cuts are present around -100° and -45° at 8 GHz. These directions will lead to wrong estimation of AT position.

3.2.1.4 Conclusion

The designed CP antenna has two-dimensional planar structure which is an acceptable and desirable structure for the LBS. The fabrication process is simple compared to the traditional designs because of its simple feeding method. The designed antenna is asymmetric which can be accounted for break-away of the 3dB axial-ratio boundary around 6 GHz. But, the designed antenna has an acceptable performance for the LBS. Hence, the designed CP antenna is suitable for the ILS.

3.2.2 Dual Circular Polarized Planar Antenna-Double Ports

The circular polarization can be produced with the use of dual feeding technique [24, 28]. In dual-feeding technique, two orthogonal electric fields are simultaneously used with a phase difference of 90°. This technique has been reported in some works [13-15]. These reported works mainly provide the performance over a narrow bandwidth such as for few

MHz frequencies [26]. Some work has also performances in term of bandwidth upto 1GHz [28]. Typically, it is always difficult to achieve ultra-wideband performance for CP. Some well known designs such as Spiral, Sinuous are known for good performance over ultra-wideband. But from the architectural point of our ILS design, we need an antenna for dual-CP and should have two ports.

The dual-CP can be achieved by using dual-feeding technique; one of the necessary conditions is 90° phase shift between two input signals which can be provided through the 90° -hybrid branch line coupler (BLC). At the same time BLC also facilitates equal power splits and isolation between receiver and emitter of the Active-Tag and quadrature signals required for the CP of the wave. The circuit connection between 90° -BLC and two-port antenna is depicted in Fig 3.19.

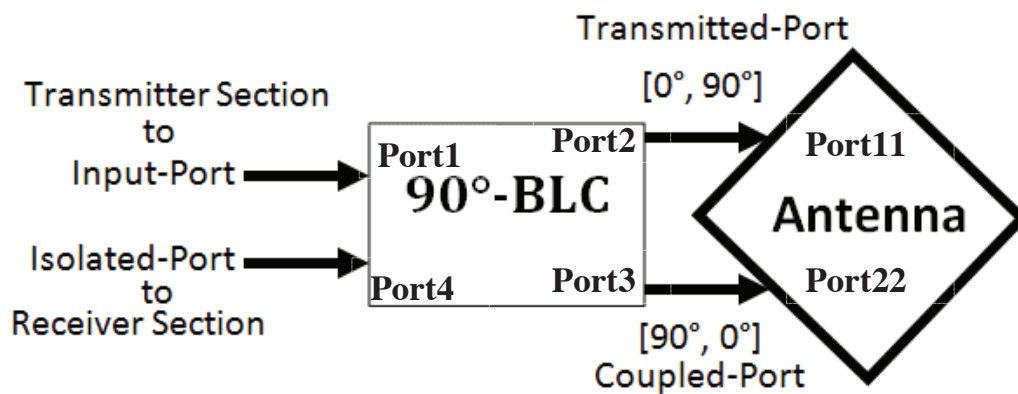


Fig 3.19: Connection between 90° -BLC and Antenna.

The above arrangement will provide the 90° phase difference and the phase lags or advances will remain opposite for the transmitter or the receiver sections. Hence, this will provide a way to connect the RF chains with opposite sense of CP that is LHCP or RHCP.

A cross-structure has been used for producing CP while utilizing dual-feeding technique as mentioned in some works [14, 28]. Two orthogonal dipoles like cross-structure have been used in the beginning of simulation in CST MWS under Transient Solver mood. (The transient solver delivers broadband frequency domain results like S-parameters and the simulation can be performed with an arbitrary fine frequency resolution without extra computational cost. Moreover, the field results for many frequencies can be obtained from a single simulation.)

The lengths of the dipole arms are considered as equal to quarter-wavelength ($\lambda/4$) at 7.25GHz (resonance frequency) that is equal to 1cm.

The orthogonal dipoles and its s-parameter responses are shown in **Fig 3.20**. The dipoles are designed on each face of the substrate. The 10 dB Return Loss Bandwidth (RLB), bandwidth over which return loss remains greater than 10 dB, response obtained with the wider arms is around 2 GHz as shown by blue curve on the right side of **Fig 3.20**. In simulation, the wider dipoles have better RLB performance compared to narrower ones.

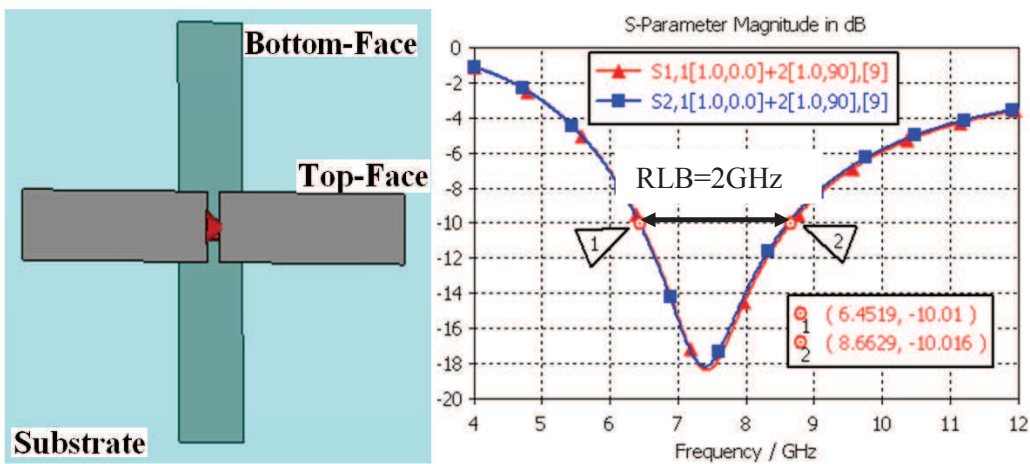


Fig 3.20: Return Loss performance of cross diode.

Although the wider dipoles help in attaining better RLB but it also increases the crosstalk effects because the effective mutual area of interaction becomes large. This effect becomes more dominating once the feeding circuit such as balun was integrated with the dipoles.

Some circular microstrip patch designs have been reported for ultra-wideband applications [29-31]. When a circular patch of quarter wavelength ($\lambda/4 \cong 1\text{cm}$ at 7.25GHz) is added at the end of each dipole's arm then the RLB response becomes double compared to the previous case (without circular patch) as plotted by blue-curve on the right side of **Fig 3.21** whereas the attached circular patches are shown on the left side of the figure.

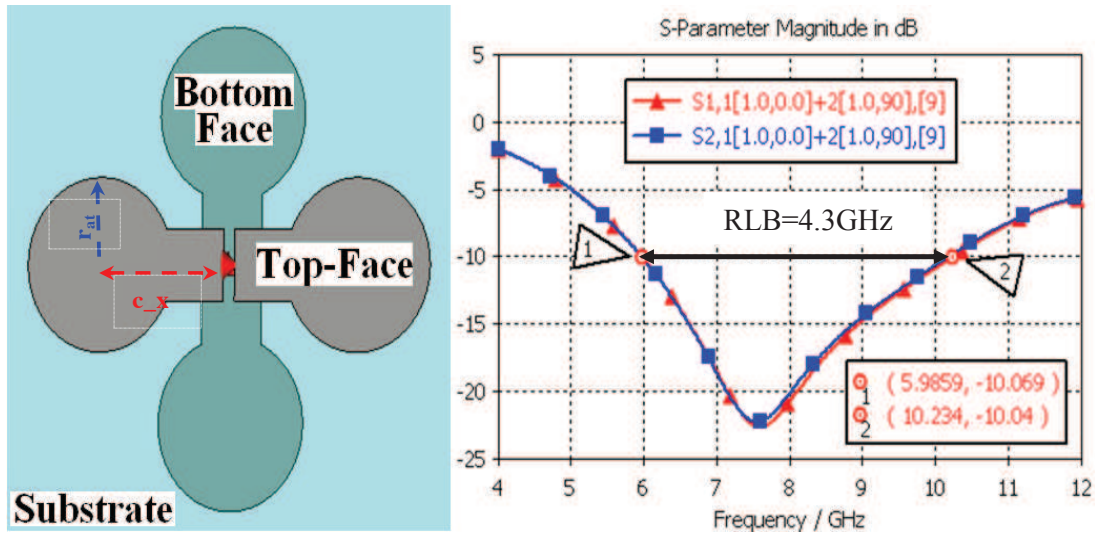


Fig 3.21: Improved 10 dB Return Loss Bandwidth.

The increased RLB response covers almost the whole upper UWB frequency spectrum (6-10.6 GHz). This clearly shows the improvement of the RLB response because of the addition of microstrip circular patch at the end of dipoles' arms. In above design, the two parameters (c_x and r_{at}) are very important in terms of antenna's return loss performance. The c_x represents the distance between circular patch and the input feed point as marked in **Fig 3.21** whereas the r_{at} represents radius of the circular patch. The 10 dB return loss bandwidth can be easily shifted by varying c_x , while keeping the r_{at} (4 mm) as constant. The return loss response for different values of c_x is plotted in **Fig 3.22**.

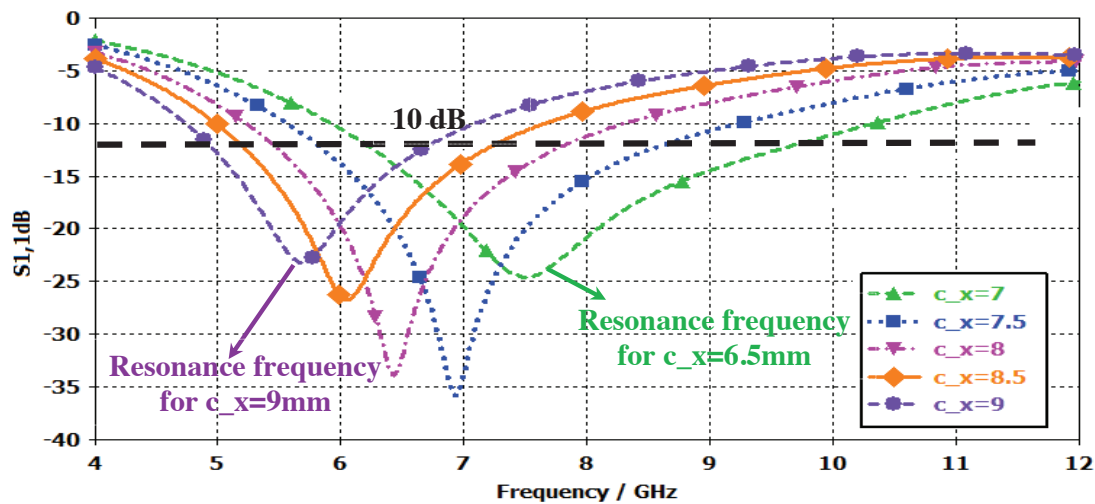


Fig 3.22: Shift in resonance frequency (c_x is in mm).

The resonance frequency for $c_x=7$ mm is at 9 GHz (green curve) whereas the resonance frequency shifted to 5.8 GHz for $c_x=9$ mm (magenta curve). Likewise, the bandwidth can be easily increased for a given resonance frequency by increasing r_{at} . The effect of r_{at} over 10 dB return loss bandwidth is plotted in Fig 3.23. The c_x (7 mm) parameter was kept constant for this analysis.

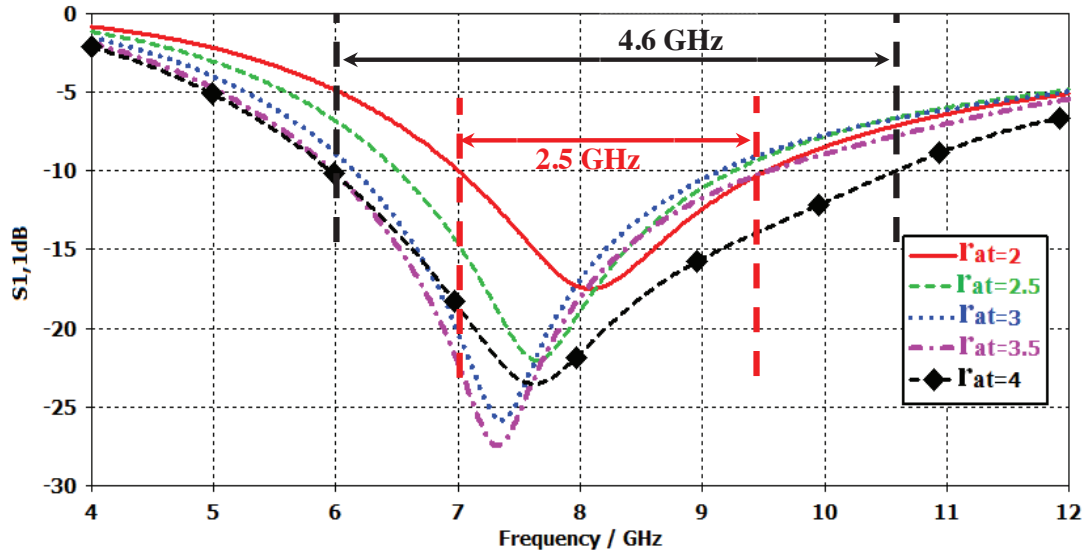


Fig 3.23: Widening of the bandwidth (r_{at} is in mm).

The bandwidth of the design is 2.5 GHz for $r_{at}=2$ mm (red curve) whereas it becomes 4.6 GHz for $r_{at}=4$ mm (black curve). The best performance can be obtained by first defining the resonance frequency by c_x and then the bandwidth can be enhanced by the r_{at} .

The shifting and the widening of the 10 dB return loss bandwidth are limited by the circular patch size which can be used without overlapping circular patches between top and bottom faces. The overlapping gives poor performance in terms of RLB. Therefore, for better performance overlapping should be avoided. However, it has good performance between 5 GHz and 12 GHz. In comparison with [24, 28], the 10 dB RLB of the designs is better.

The RLB performance was good for the input impedance equal to 160Ω . Generally, the co-axial port (SMA connector) has input impedance equal to 50Ω . Therefore, an input impedance transformation circuit is required. The simulated orthogonal dipole has a symmetric structure but the co-axial port has an asymmetric structure. Therefore, the input transformation circuit must transform the co-axial port input impedance to the antenna's

balanced feeding point. Such transformation circuit can be easily implemented with the design of a microstrip coplanar balun design which is also known for good performance over ultra-wide band (>1GHz) [25].

The designed orthogonal dipoles and the integrated baluns are shown in Fig 3.24.

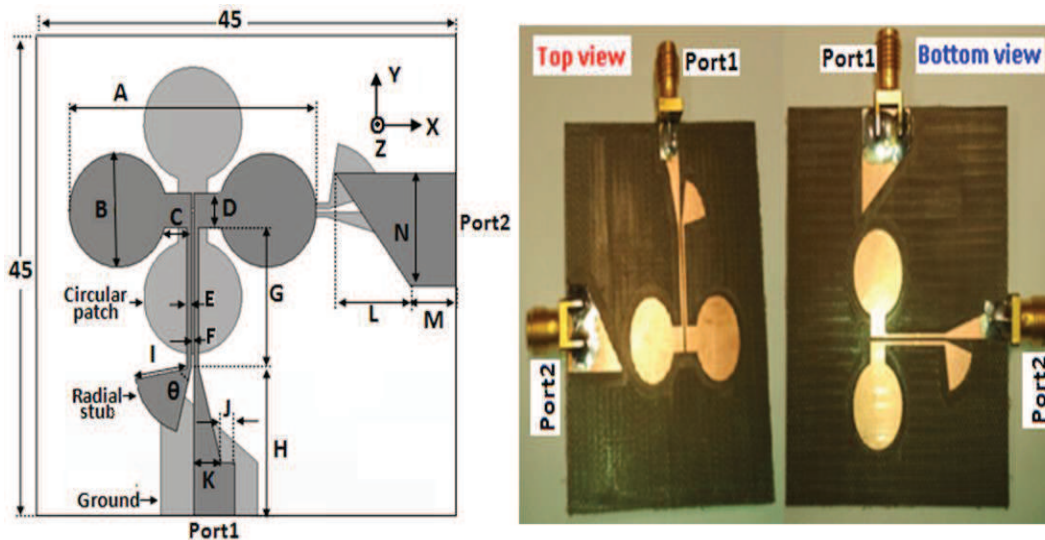


Fig 3.24: Left- antenna configuration; Right-fabricated antenna.

The left side of Fig 3.24 shows the geometry & all necessary parameters of the simulated antenna while the fabricated antenna is presented on the right side. Each face of the substrate has a dipole with circular patch and balun is placed between each of the antennas' feeding points and the co-axial ports (Port1 and Port2). The resonating frequency of the balun depends on the radial stub geometry, that is, radius (I) & angle (θ). The better trade-off between return loss and crosstalk of the design is obtained at θ equal to 65° . In this case, the input impedance is transformed from 50Ω to 160Ω over the frequency range (6GHz - 8.5GHz).

The optimized parameters are tabulated in the Table 3.7; the dimensions are in mm.

Table 3.7
OPTIMISED PARAMETERS OF DESIGNED ANTENNA (ACTIVE-TAG)

A	B	C	D	E	F	G	H	I	J	K	L	M	N
27.18	12.2	2.39	3.2	0.5	0.3	13.25	13.75	5.7	1.5	3	8.25	5	5.7

Because of the unavailability of the previous substrate, DuroidRT 5880, in our laboratory, another substrate (CuClad250) is used for antenna fabrication. Its features are: relative permittivity $\epsilon_r=2.5$, thickness=1.575mm and tangent loss $\tan\delta = 0.0018$.

The dipoles are simultaneously excited by two identical signals with a phase difference of 90° based on the dual feeding technique. The required 90° phase difference between Port 1 & Port 2 can be easily obtained from a 90° -Hybrid Branch Line Coupler (HBLC) [32]. The layout obtained from the ADS of the designed BLC is shown in Fig 3.25 whereas the fabricated one is in Fig 3.28. All dimensions are used in millimetre. The low cost FR4 substrate (relative permittivity $\epsilon_r=4.2$, thickness=1.575mm and tangent loss $\tan\delta = 0.01$) has been used for the fabrication.

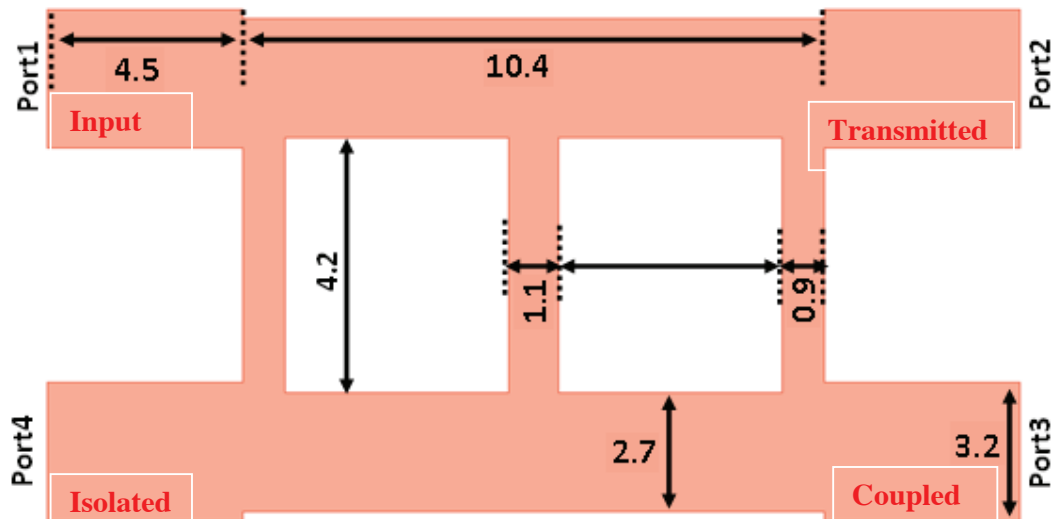


Fig 3.25: Layout of designed 90° -Hybrid Branch Line Coupler (dimensions are in mm).

The simulated and measure S-parameters are plotted in Fig 3.26 and Fig 3.27.

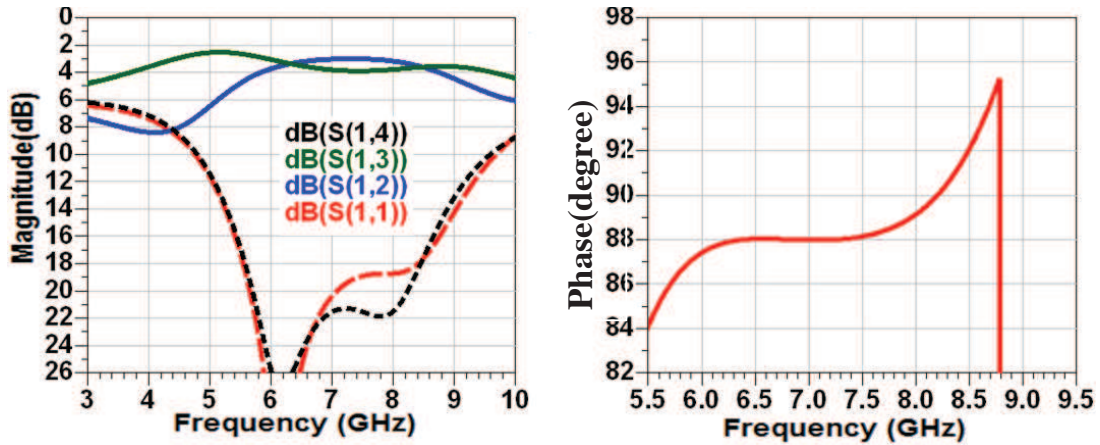


Fig 3.26: Simulated S-parameters of the designed 90°-Hybrid Branch Line Coupler.

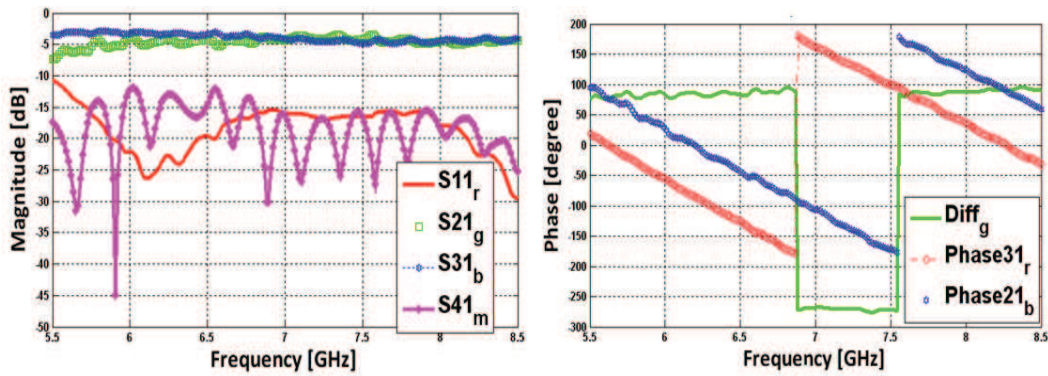


Fig 3.27: Measured values of the fabricated 90°-Hybrid Branch Line Coupler.

The maximum simulated and measured insertion losses are 4 dB (S(1,3)) and 4.8 dB (marker, S21g), respectively. The measured return loss (marker, S11r) is less than 15 dB between 6 GHz and 8.5 GHz, and same observation was also made in simulation (marker, S(1,1)). Likewise, the isolation level is also less than 15 dB in measurement (marker, S41m) as well as in simulation (marker, S(1,4)). In simulation, the observed phase-difference is 90° ($\pm 2^\circ$) that is between 88° and 92° over the desired 6-8.5 GHz frequency band. However, the measured phase-difference is 90 ($\pm 9^\circ$) and the maximum deviation is observed at 6 GHz that is 81° whereas the deviation over rest of the frequency band was less than 6°. These differences can be assumed as the influence of soldering. These results were obtained after removing the SMA support as shown in Fig 3.28; the performances were not good at all with the support.

The complete setup for the production of dual circular polarization is shown in [Fig 3.28](#).

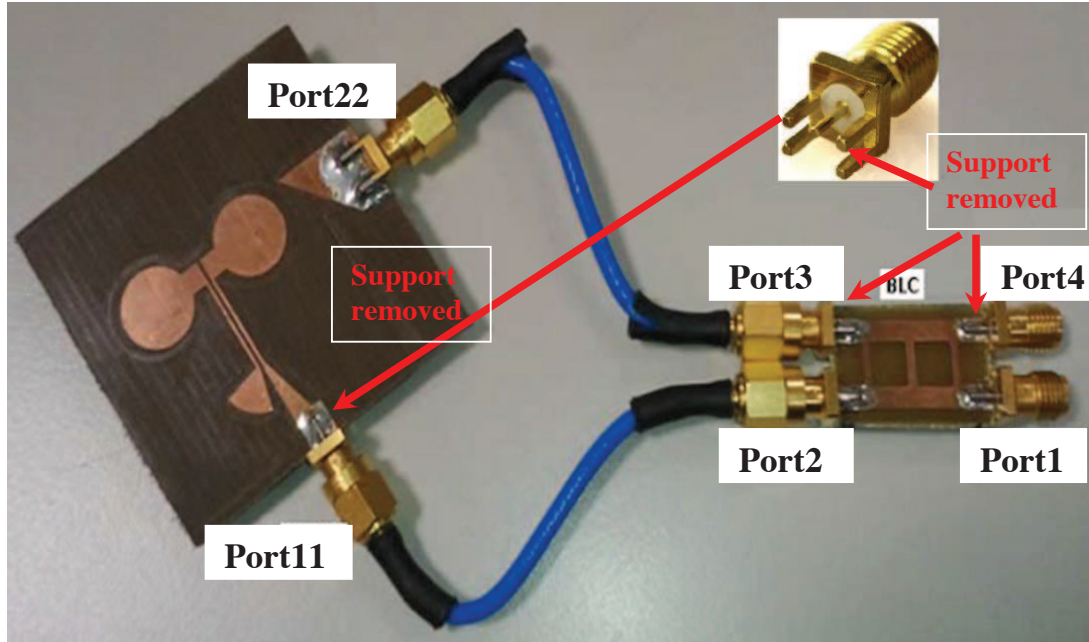


Fig 3.28: Scheme for dual CP by introducing 90° phase shift.

The 90°-BLC will provide the necessary 90° phase difference between Port2 & Port3. Meanwhile the receiver and the transmitter chains of the active-Tag can be connected to Port1 & Port2 as presented in [Fig 3.19](#).

The described setup, antenna & BLC, has been used for the antenna characterization in the anechoic chamber, similar to the previously mentioned in [Section 3.3.1](#). The measured results are compared with the simulated ones. The detail performance analyses are presented next.

3.2.2.1 Return Loss & Crosstalk

The fabricated antenna is directly connected to the VNA without BLC. The simulated results, the return loss and the crosstalks, are obtained without the BLC. Therefore, the measured results are obtained from the antenna only. The observed return loss bandwidth and the crosstalk are plotted in [Fig 3.29](#).

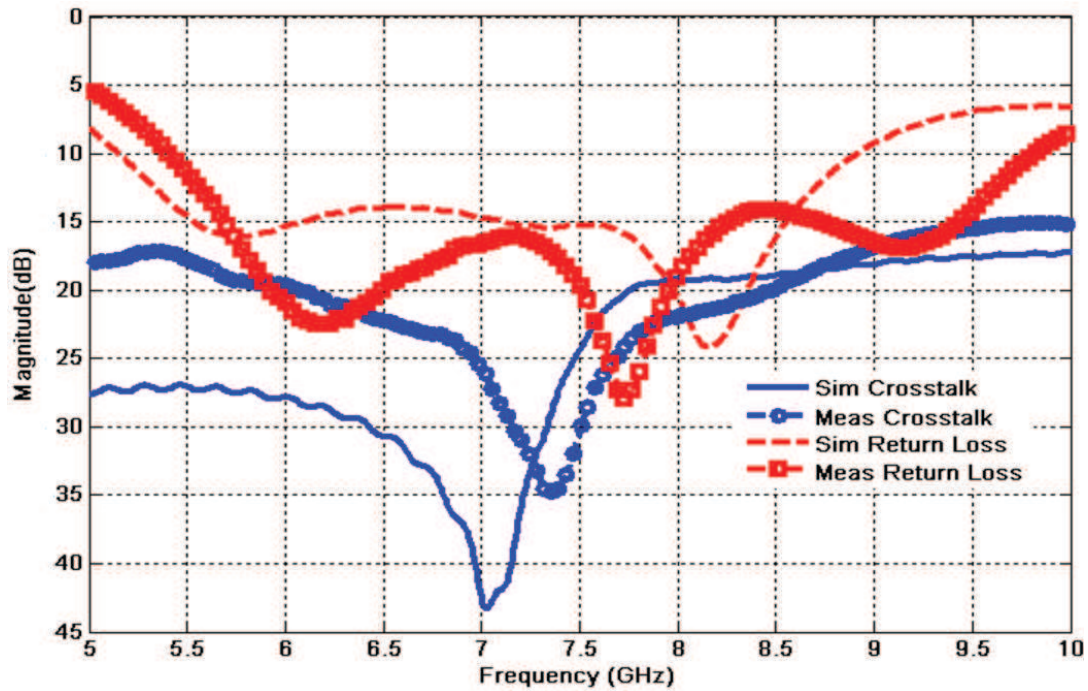


Fig 3.29: Simulated and Measured: Return Loss & Crosstalk (AT-antenna).

The measured and the simulated Return Loss Bandwidth are shown in red plots. The dashed red plot represents the simulated result and the square-marked represents the measured. The measured RLB has -10 dB response between 5.5-to-9.7 GHz which is a slightly better than the simulated. The measured results also show good impedance matching between 6-to-8.5 GHz frequency. The measured result has best resonance at 7.68 GHz whereas the simulated one is at 8.15 GHz. The difference between the measured and the simulated results may be due to fabrication as the presented results are obtained after the removal of the support which was not good earlier, see [Fig 3.28](#).

Similarly, the measured and the simulated crosstalks are presented in blue circular-marked and blue solid lines. Here, the crosstalk is considered as the leakage of signals between Port1 and Port2. The measured and the simulated curves are less than -15 dB between 5-to-10 GHz. The measured crosstalk over the desired band (6-8.5 GHz) is under -20 dB which can be further isolated with the use of fitted filters as proposed in the architecture, [Section 2.3](#). The minimum simulated value is observed at 7 GHz while the measured is at 7.4 GHz. Such shift was also considered for the return loss. The difference in the depth can be

assumed as the low sensitivity of the VNA compared to the simulated one. Nevertheless, the measured results are acceptable for the use in ILS.

3.2.2.2 Axial Ratio

The setup shown in Fig 3.28 has been used for the computation of Axial Ratio (AR). The co-polar (E_{co}) & cross-polar (E_{xp}) electric fields are measured in the anechoic chamber with respect to the reference antenna, LINDGREN 3117 Horn Antenna. The relationship 3.1 has been used for the AR computation. The measured and the simulated value are represented by the dashed-blue and solid-red curves in Fig 3.30.

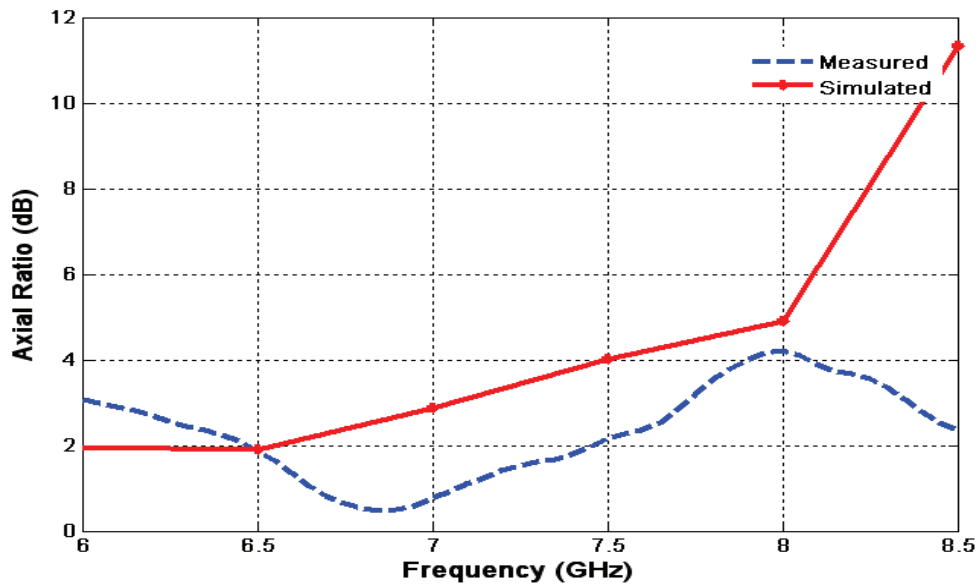


Fig 3.30: Simulated and Measured Axial ratio (AT-antenna).

The measured value is within 4 dB over the range 6 GHz-to 8.5 GHz while the simulated axial ratio is less than 5 dB from 6 GHz to 8 GHz, respectively. Generally 3 dB is considered as the benchmark for the circular polarization, therefore we can say that it has elliptical wave form between 7.5-to-8.5 GHz rather than circular polarization. The AR has better performance than the simulated one as it was observed for the return loss case.

3.2.2.3 Gain & Radiation Pattern

The simulated and the measured gains are shown in Fig 3.31 with respect to frequency.

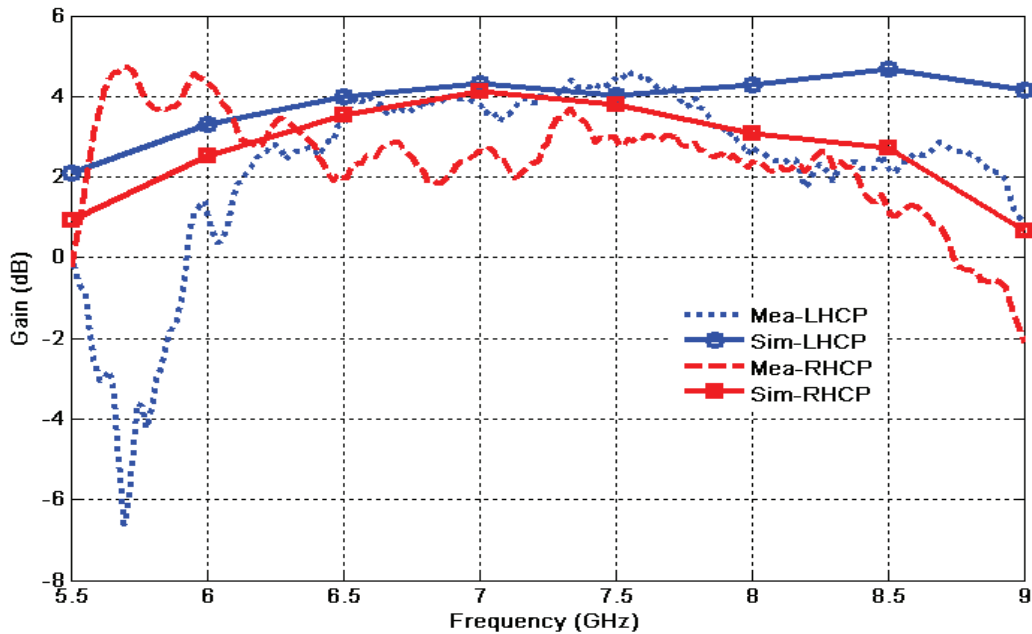


Fig 3.31: Simulated and Measured Antenna gains (AT-antenna).

The maximum gain observed in simulation for the LHCP and the RHCP waveforms are 4.6 dB and 4.1 dB, respectively and the maximum measured gain for the LHCP and the RHCP waveforms are found to be 4.3 dB and 5.1 dB, respectively. The measured gain is slightly lower than the simulated one; this can be accounted because of the insertion loss introduced by the 90°-BLC.

Next, the radiation patterns are presented in two planes, i.e., z-x and x-y planes. The z-x plane is shown in Fig 3.32. The simulated and the measured radiation patterns are shown at two frequencies, 6.5 GHz on the left side & 8 GHz on the right side, respectively (these are centre frequencies for the up-link and the down-link channels as described in Section 2.3). The red plot represents the simulated result and the measured radiation pattern is represented by the blue plot. This represents the copolar plane for the antenna.

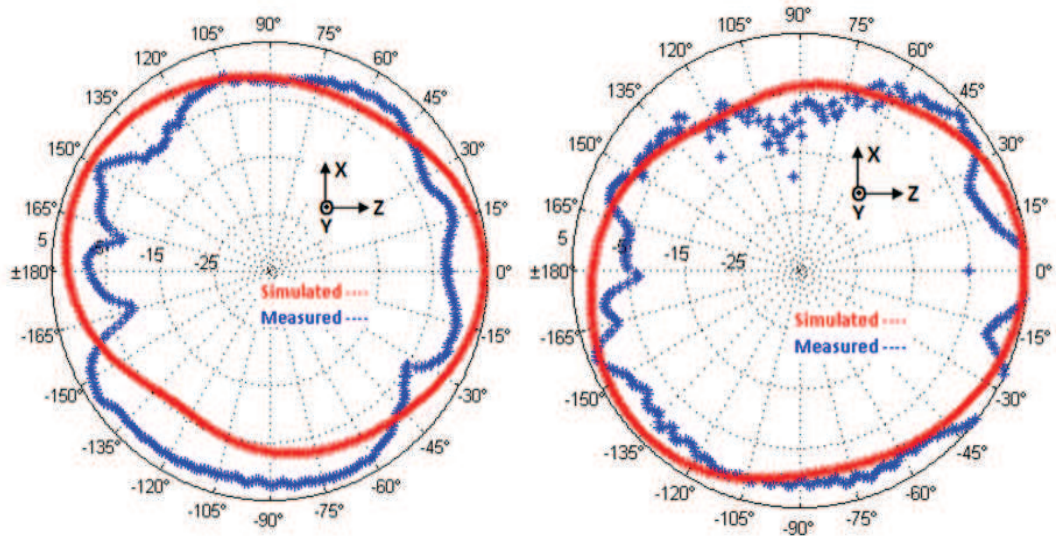


Fig 3.32: Left and Right side show the radiation pattern in z-x plane at 6.5 & 8 GHz (AT-antenna).

The measured and the simulated radiation patterns in x-y plane are shown in **Fig 3.33**.

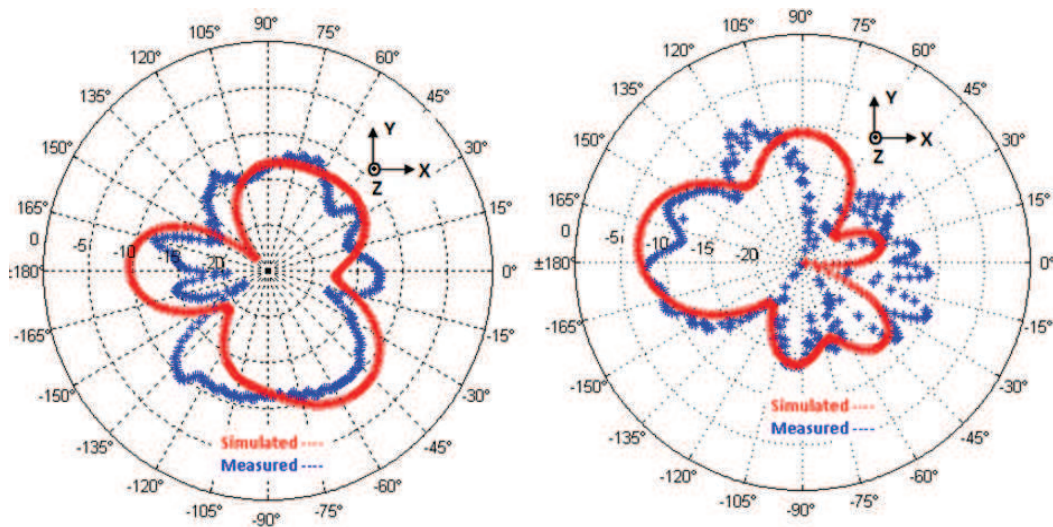


Fig 3.33: Left and Right side show the radiation pattern in x-y plane at 6.5 & 8 GHz (AT-antenna).

The observed gains are less than -13 dB and -10 dB which represent the cross-polar plane for the antenna. The differences between the co-polar and cross-polar gains are more than 16 dB and 14 dB for the LHCP and the RHCP, respectively. The radiation patterns are shown at 6.5 GHz and 8 GHz, respectively. The holes around 120°, -150° and 0° are

observed at 6.5 GHz and in these directions the AT positions will be not correctly observed. Similarly, the 30°, -15° and -135° directions have error in position estimates.

The differences in the plots can be assumed because of the blockage by the SMA connector and the feeding circuit as presented in **Fig 3.28**.

3.2.2.4 Conclusion

Similar to the LBS antenna, the designed dual CP antenna also has two-dimensional planar structure. The designed antenna will be used for the active-Tag. The designed antenna has acceptable performance between 6-to-8.5 GHz. Besides, this is the first time such structure has been reported for the dual circular polarization in European UWB band, 6-to-8.5 GHz. To the best of author knowledge, this is the first time such a design has been reported for the dual circular polarization.

3.3 Realized 3D ILS

The realized Active-Tag and LBS are shown in **Fig 3.34** and **Fig 3.35**. The LBS will locate the remote active-Tag [33-34] in an indoor environment. This presents the 3D-Indoor Localization System.

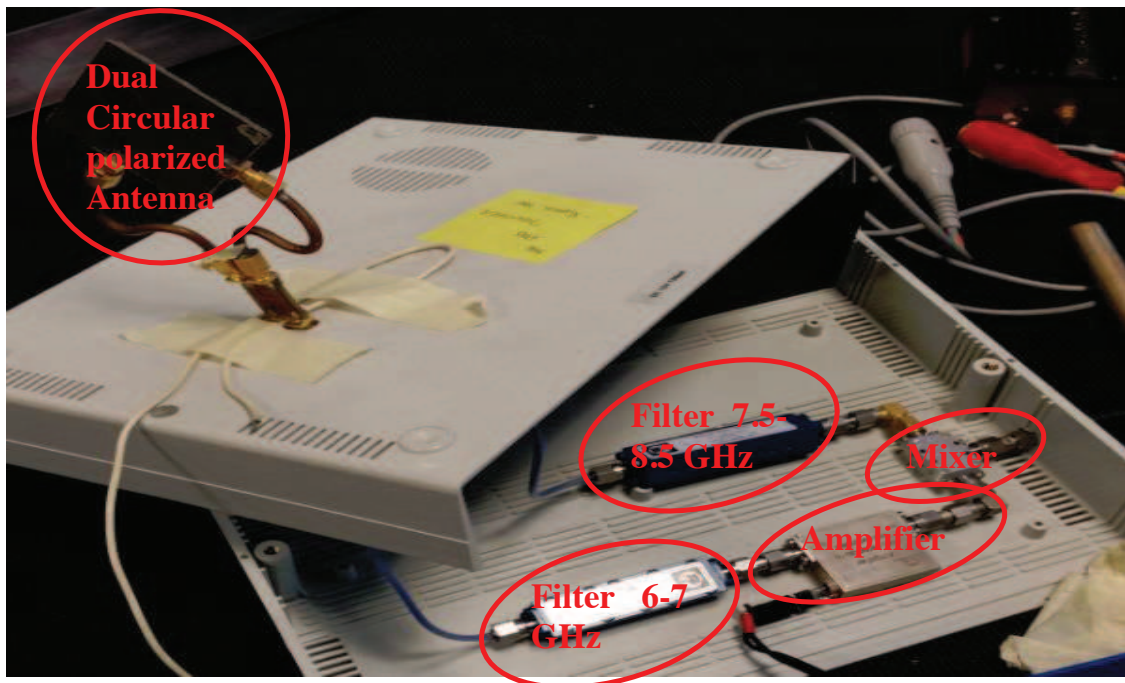


Fig 3.34: Realized Active-Tag (Indoor Localization System).

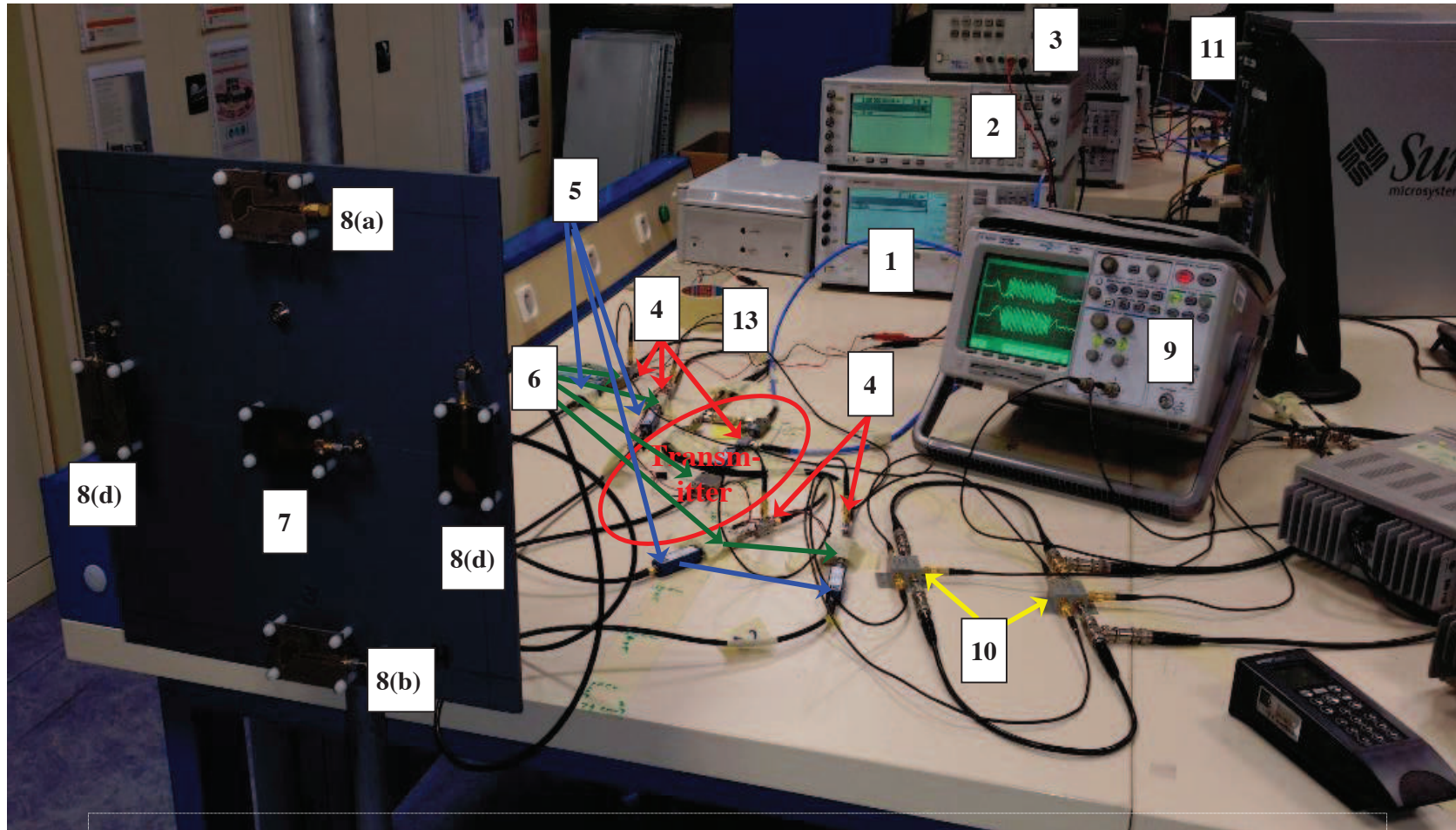


Fig 3.35: Realized LBS (Indoor Localization System) for 3D Measurements.

1. Agilent E8267D, 2. Agilent E4431B, 3. DC-Supply, 4. Mixers, 5. Filters, 6. Amplifiers, 7. Transmitter Antenna, 8 (a-d). Receiver Antennas, 9. Oscilloscope, 10. RF Switches, 11. Data Acquisition Card (Desk-Top), 13. Splitter

The power losses at different stages of the LBS and the Active-Tag are depicted in three parts: transmitter chain, active-Tag, and receiver chain.

Power levels at different stages of the transmitter chain are shown in Fig 3.36. Here, ‘P’ is assumed as the power generated by the FMCW signal generator. All powers are presented in dBm unit. Loss introduced by the connecting cables or SMA connectors are considered as 1dB.

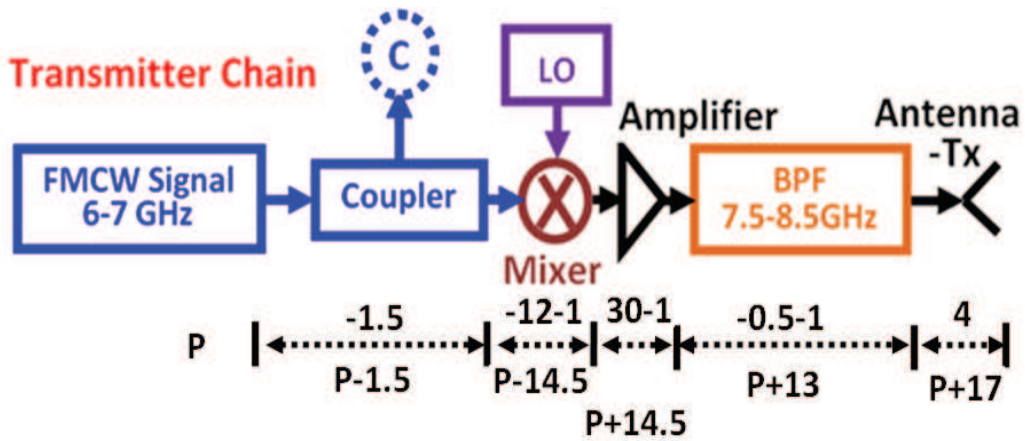


Fig 3.36: Power losses in transmitter section.

The losses at various stages are considered according to the components specification presented in this chapter. The signal transmitted by the antenna is ‘P+17’ dB. The power lost by the transmitted signal in free space can be presented by the expression [35]

$$FSPL(dB) = 20 \log(len) + 20 \log(freq) + 32.44 \quad 3.4$$

Where ‘FSPL’ is free-space-path-loss, ‘len’ is distance travelled by the signal in Km, and ‘freq’ is the transmitted signal’s frequency in MHz.

If the active-Tag is at a radial-distance of ‘len’ from the transmitter antenna then the signal approaches the active-Tag with power equal to ‘P+17-FSPL’ dB. The power losses at the various stages of the active-Tag are presented in Fig 3.37.

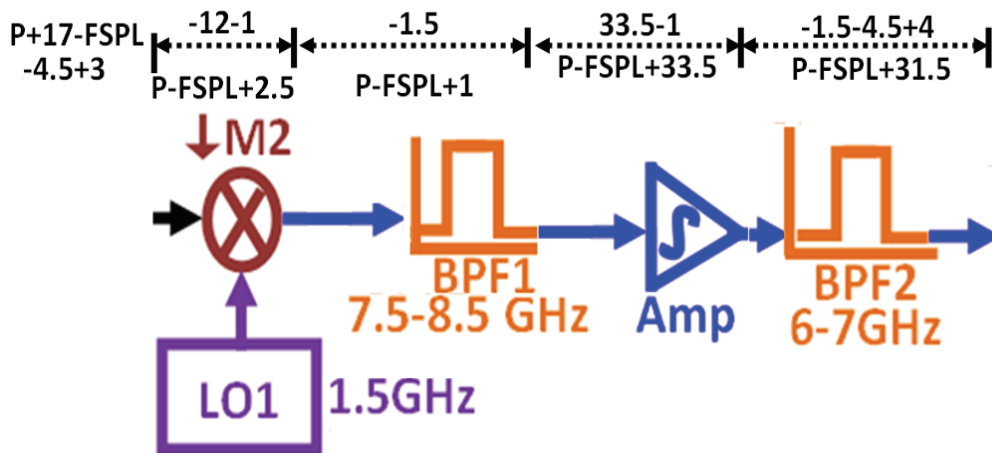


Fig 3.37: Power losses in the Active-Tag.

The signal retransmitted from the active-Tag with power equal to ‘P-FSPL+31.5’ dB. This signal will again travel through the free space and then reaches to the LBS antenna. For simplicity, this travelled distance is considered as same that is equal to ‘len’. The power losses for the receiver section are mentioned in Fig 3.38.

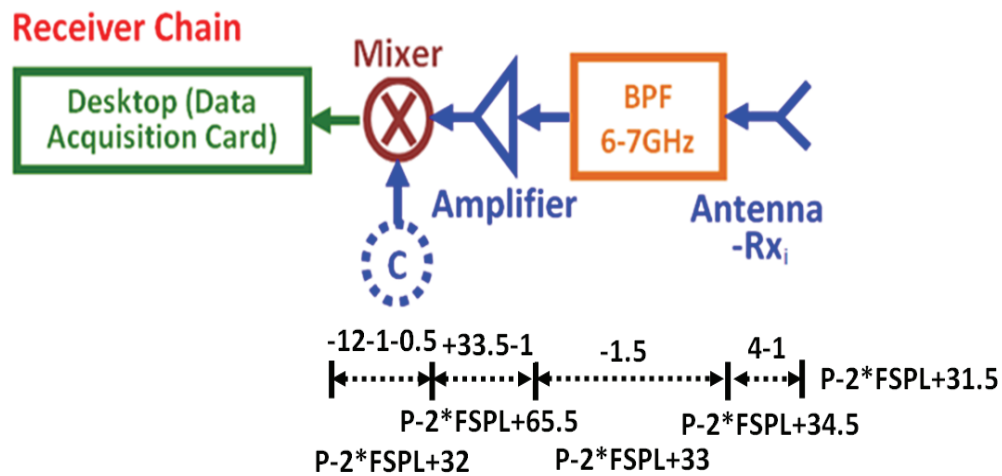


Fig 3.38: Power losses in the receiver section.

The signal reaches the receiver’s antenna with power equal to ‘P-2*FSPL+31.5’ dB. Table 3.8 shows the losses because of different free space distances: 1m, 10m and 20m. Initial power generated by the FMCW generator is considered as P=0dBm in the above table.

The relationship 3.3 has been used for the FSPL computation while considering the central frequencies, 8 GHz & 6.5 GHz, of the uplink and the downlink channels.

Table 3.8
RECEIVED POWER BY RECEIVER ANTENNA

Free Space distance (len) Km	FSPL (dB)		Total Loss (dB)	Signal reaches the receiver's antenna with power (dBm)
	Uplink [7.5-8.5]GHz	Downlink [6-7]GHz		
	Freq=8GHz	Freq=6.5GHz		
1e-3	50.5 dB	48.7 dB	99.2 dB	-67.7 dBm
10e-3	70.5 dB	68.7 dB	139.2 dB	-107.7 dBm
20e-3	76.5 dB	74.7 dB	151.2 dB	-119.7 dBm

As evident from the table, the received power varies from -67.7dBm to -119.7dBm between 1-to-20 meters of free space. The sensitivity of the receivers should be enhanced by decreasing the noise figure of the receiver. The use of LNA close to the receiving antenna will help in reducing the noise figure. Additionally, if two or more amplifiers are in cascaded form, then, the first amplifier should have lowest noise figure because the first amplifier will have greatest influence upon the SNR as the noise floor is lowest at its input. Apart from this, a better mixer is also advised for the sensitivity increment because the used mixer has 12 dB of conversion loss (Table 3.3) which is not a good value.

3.4 Conclusion

In this chapter, the realized ILS is presented which includes the Localization Base Station and the Active-Tag. Some required components such as CP antennas have been designed and fabricated for LBS and AT realizations, Section 3.2-3.3. The performance analysis of these components is presented in terms of measured and simulated results, and their roles with respect to the LBS are also explained. The realized 3D-Indoor Localization System is presented in Section 3.4. The receiver sensitivity is also discussed for the better range coverage. The designed LBS will also helps in reducing the minimum number of reference/anchor points to one. Moreover, it will also remove the synchronization issue which is commonly required between different reference positions.

The realized LBS incorporates architectural as well as modular innovations in design as per Henderson-Clark Model [36]. Hence, it can be asserted that the developed 3D-LBS provides a radical innovation in the field of indoor localization.

The performance of the LBS is presented in the next chapter. Some common situations of an indoor environment such as line-of-sight have been are considered for this purpose.

References

- [1] Y. Gu, A. Lo, and I. Niemegeer, "A survey of indoor positioning systems for wireless personal networks," IEEE Communications Survey & Tutorials, vol.11, NO. 1, pp. 13-32, First Quarter 2009.
- [2] B. Waldmann, R. Weigel, R. Ebel, and M. Vossiek, " An ultra-wideband local positioning system for highly complex indoor environments," International Conference on Localization and GNSS 2012, pp. 1-5.
- [3] [H1] http://en.wikipedia.org/wiki/Analog-to-digital_converter
- [4] <http://spectrum-instrumentation.com/en/products/m3i2132>.
- [5] Daniel D. Harty, "Novel Design of a wideband Ribcage-Dipole Array and its feeding," Master's Degree Thesis, Worcester Polytechnic Institute. ECE Dept. 2010.
- [6] Annexure C
- [7] Annexure D
- [8] Warren L. Stutzman, "Polarization in Electromagnetic Systems," Ch. 4 & 8, Artech House Boston-London, pp. 96-98 & 183-216.
- [9] <http://www.astronwireless.com/topic-archives-antennas-polarization.asp>.
- [10] J. E. Hill, "Antenna Polarization," Watkins-Johnson Tech-notes, Aug. 1979.
- [11] Constantine A. Balanis. Antenna theory analysis and design, 3rd ed., USA: A John Wiley & Sons, INC, 2005.
- [12] Z. Chen, and Q. Cao, "Study of a two-arm sinuous antenna and the relevant wideband balun," International Conference on Microwave and Millimeter Wave Technology, ICMMT2008, pp. 1837-1840.
- [13] J. R. James and P. S. Hall, "Handbook of Microstrip Antennas, London, U.K.," Peter Peregrinus, 1989.

-
- [14] R. Moini, M. Samiee, A. Tavakoli, and G.Z. Rafi, "A dual-feed dual-excitation mode circularly-polarized crossed-slot antenna," Antennas and Propagation Society International Symposium, APS Digest 1996, pp. 58-61.
- [15] J. Huang, "A technique for an array to generate circular polarization with linearly polarized elements," IEEE Transaction on Antennas and Propagation, 1986, pp. 1113-1124.
- [16] A. Manna, P. Baldonero, and F. Trotta, "Novel UWB Low-Profile Sinuous Slot Antenna," Proceedings of 5th European Conference on Antennas and Propagation, EuCAP 2011.
- [17] J. Edwards, and G. Rebeiz, "Dual-Polarized Sinuous Antennas on Silicon Dielectric Lenses," Antennas and Propagation Society International Symposium, APSURSI 2010, pp. 1-4.
- [18] L. Liu, H. Xu, R. R. Percy, D. L. Herald, a. W. Lichtenberger, J. L. Hesler, and R. M. Weikle, "Development of Integrated Terahertz Broadband Detectors Utilizing Superconducting Hot-Electron Bolometers," IEEE Transaction on Applied Superconductivity, 2009, pp. 282-286.
- [19] M. C. Buck, and D. S. Filipović, "Split-Beam Mode Four-Arm Slot Sinuous Antenna," IEEE Antennas And Wireless Propagation Letter, 2004, pp. 83-87.
- [20] Y. Shen, C.L. Law, "A microstrip-fed quasi spiral circularly polarized ultra-wideband antenna," Antennas and Propagation Society International Symposium, APSURSI 2011.
- [21] M. Vahdani, and X. Begaud, "Sinuous Antenna fed by a Microstrip to CPS Balun," Proceedings of 3rd European Conference on Antennas and Propagation, EuCAP 2009, pp. 1622-1626.
- [22] S. G. Mao, J. C. Yeh, and S. L. Chen, "Ultra wideband circularly polarized spiral antenna using integrated balun with application to time domain target detection," IEEE Trans. Antennas Propag., vol. 57, no. 7, pp. 1914-1919, Jul. 2009.

-
- [23] K. M. Mak, K. M. Luk, "A Circularly Polarized Antenna With Wide Axial Ratio Beamwidth", IEEE Trans. on Ant. And Prop., vol. 57, No. 10, Oct 2009.
- [24] X. L. Bao, and M. J. Ammann, "A printed dipole antenna for wideband circular polarization operation," Antennas and Propagation, EuCAP, pp.2367-2370, 2009.
- [25] Y. H. Suh, and K. Chang, "A wideband coplanar stripline to microstrip transition," Microwave and Wireless Components Letters, IEEE, vol. 11, pp. 28-29, 2001.
- [26] Per-Simon Kildal, Foundation of Antenna- A Unified Approach, 1st ed., Studentlitteratur AB, 2000, Chapter 2, pp. 30.
- [27] Annexure E
- [28] K. M; Mac, and K. M. Luk, "A shorted cross bowtie patch antenna with a cross dipole for circular polarization," Antennas and Propagation Society International Symposium 2007, pp. 2702-2705.
- [29] C. C. Chiaw, and M. R. Kamarudin, "Novel Design of Circular UWB Antenna," Asia Pacific Microwave Conference, APMC 2009, pp. 1977-1979.
- [30] X. Chen, J. Liang, P. Li, L. Guo and C. C. Chiau, "Planar UWB Monopole Antennas," IEEE Transaction on Asia-Pacific Conference Proceedings 2005, pp. 1-4.
- [31] L. Guo, S. Wang, Y. Gao, X. Chen, and C. Parini, "Miniaturization of Printed Disc UWB Monopoles," IEEE Transaction on Antenna Technology: Smart Antennas and Novel Metamaterials 2008, pp. 95-98.
- [32] C. L. Hsu, "Design of quadrature hybrid with closely separated dual passband using three-branch line coupler," Microwave proceedings (AMC), pp. 1232-1235, 2010.
- [33] Zhang, M. G. Amin, and S. Kaushik, "Localization and Tracking of Passive RFID Tags Based on Direction Estimation," International Journal of Antenna and Propagation Hindwai Publishing Corporation, vol 2007, ID 17426, doi. 10.1155/2007/17426.

-
- [34] M. Vossiek, and P. Guldenl, “The Switched Injection-Locked Oscillator: A Novel Versatile Concept for Wireless Transponder and Localization Systems”, IEEE Transactions on Microwave Theory & Technique, vol. 56, no. 4, 2008, pp. 859-866.
- [35] I. Glover and P. Grant, Digital Communications. Prentice Hall, 2009.
- [36] A. Afuah, Innovation Management: Strategies, Implementation and Profits, Oxford Univ. Press, 2003.

Chapter 4. ILS Performance and Analysis

4.1 Introduction

The prototype of the Indoor Localization System is built and has been used for estimating the 3D position via the Active-Tag. In this chapter, the performance of the ILS is presented through the field-measurement performed under different conditions such as Line-of-Sight case. Besides the performance analysis, some constraints related with the designed ILS such as Plane Wave Condition are also presented through the field measurements.

Before the field measurements, the system has been calibrated and the involved signal process is presented in [Section 4.2](#). After calibration, the system is used for the field measurements. The field measurements primarily cover the line-of-sight (LoS) conditions for the system's performance analysis and later the non-line-of-sight (NLoS) conditions. The 2D field measurements are presented in [Section 4.3.1](#) and the 3D results are mentioned in [Section 4.3.2](#). The NLoS and the influence of multipaths because of the presence of strong scatter in the environment has also been analysed and presented in [Section 4.4.2](#). Also, the use of signal's bandwidth for the location estimation has been investigated and presented in [Section 4.5](#). The developed mathematical relationship such as plane wave condition and other constrains reported in [Chapter 2](#) have been verified through the field measurements and the observed performances are outlined in [Section 4.6](#) and the chapter is concluded in [Section 4.7](#).

4.2 Field Measurements

The performance of the designed Indoor Localization System is tested through the field measurements under different conditions of a real indoor environment. The localization base station has been kept at a fixed point which represents the known reference position and Active-Tag has been kept at arbitrary different positions. The different positions of AT are estimated with respect to the fixed LBS known position. Initially, 2D localization is performed in terms of radial-distance and azimuth angle in polar form. Later, the system has been used for the 3D localization by estimating angle of elevation. Therefore, the 3D localization is presented by the radial-distance, angle of azimuth and angle of elevation in polar coordinate. Each operation of the ILS is presented in [Fig 4.1](#).

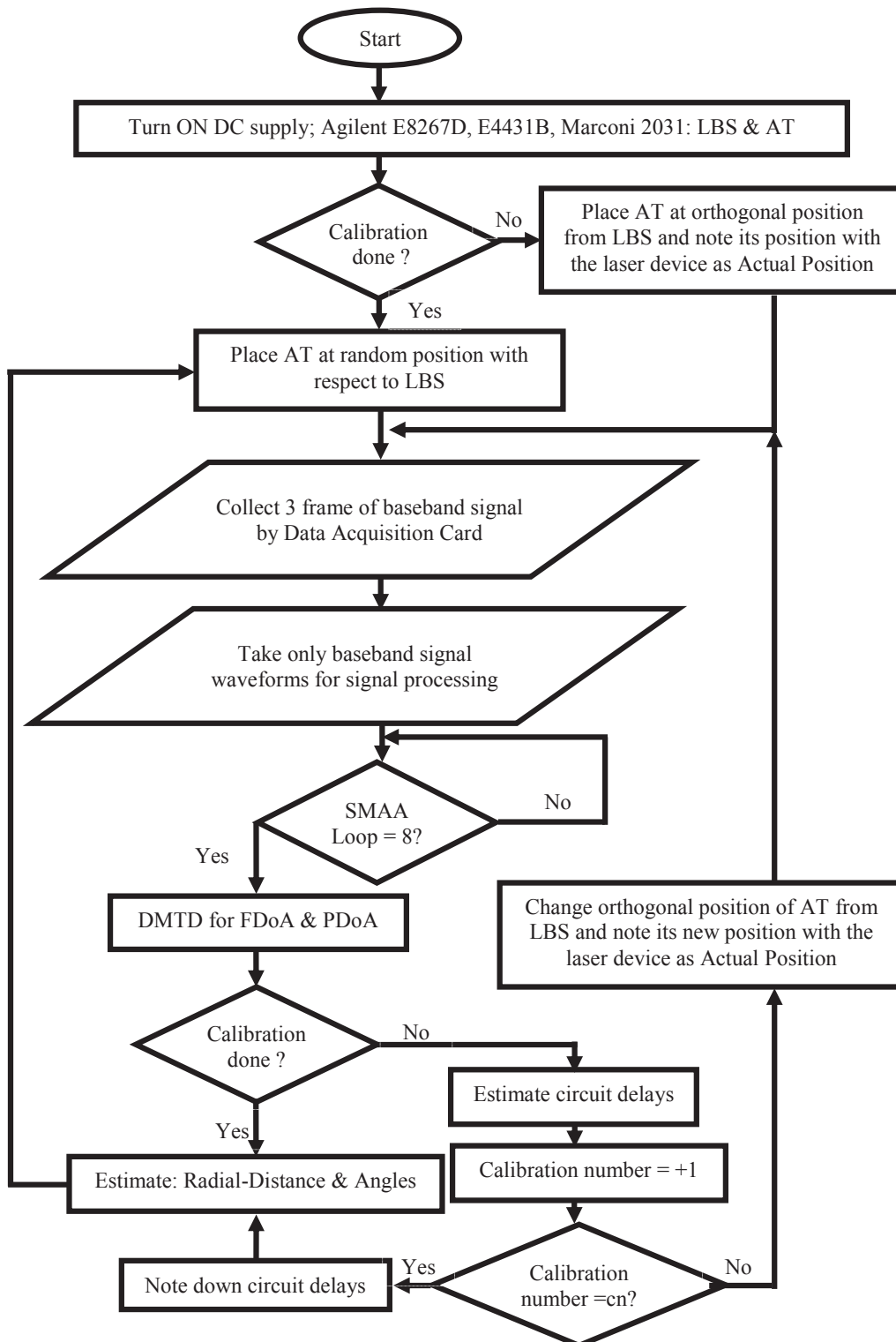


Fig 4.1: Flow chart of Indoor Localization System.

The prototype (LBS & AT) can be put in running condition by switching-ON the signal generators and necessary DC supply sources required by the circuits (mainly amplifiers). The localization process of the designed ILS can be broadly segregated into two parts: first is the calibration of ILS and second is the localization process. First of all, the calibration process is performed for determining the signal delays within the circuit so that the position of Active-Tag would be correctly approximated. The delays are estimated with different known radial-distances of the AT and this is repeated for at least 10 times (marked by variable, cn) for the better estimation of circuit-delays (LBS & AT). Three frames of the incoming signals (one frame of baseband signal is being produced by each cycle (30 ms) of the FMCW signal which is generated by the E8267D, see [Fig 4.2](#)) are collected by the data acquisition card and further a complete frame of baseband signal is considered for the signal processing. The signal is sent into the SMAA (Successive Mean Approximation Algorithm, [Section 4.1](#)) loop for eight times and then DMTD method is applied for the FDoA and PDoA computation which leads to the position estimation of the remote Active-Tag. But before the AT position estimation, the calibration process should be performed for the operation of the ILS-prototype.

Each step of flow-chart is presented in the following sub-section.

4.2.1 Signal Computation

The signal generator produces the reference sinusoidal FMCW signal (6-7 GHz) with sweep time of 10 ms and with a cycle of 30 ms in continuous mode. The beat frequencies (baseband data) are used for radial-distance as well as angle computations as described in [Chapter 2](#).

The baseband data, Signal1 and Signal2, are respectively the beat signals of the RF signal picked by the antennas A_1 (Rx1-f1) and A_2 (Rx2-f2) with reference signal. They are converted by the data acquisition card [1] which acts as an analog-to-digital convertor (ADC). The data acquisition is triggered by the *Prog1.m* [2], using MATLAB software installed in the desktop, [Fig 3.1](#). The beat signals are shown in [Fig 4.2](#).

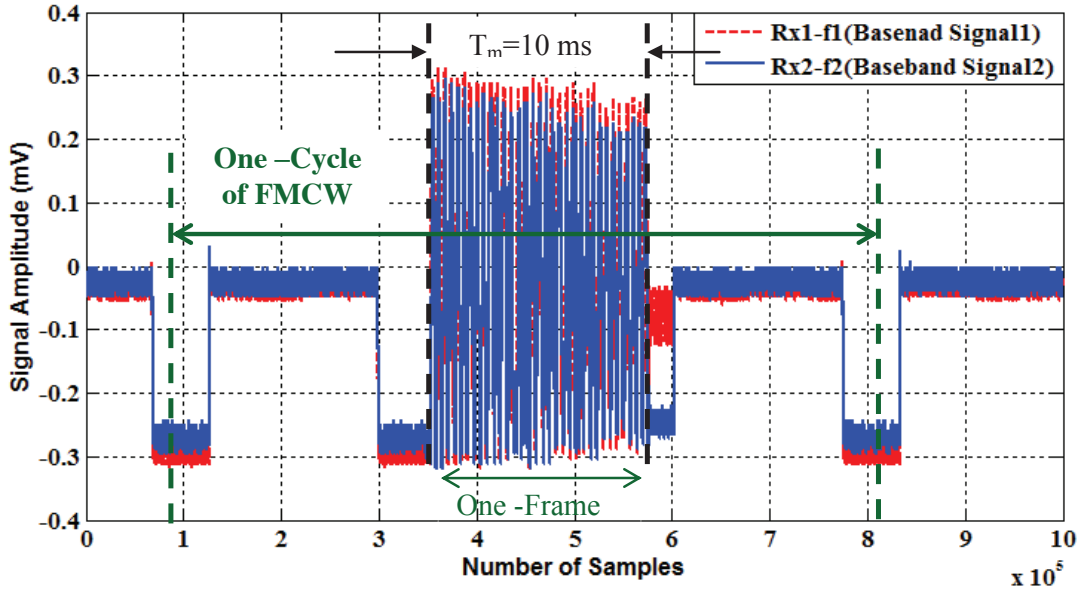


Fig 4.2: Baseband signals acquired by the Data Acquisition Card.

The two baseband data obtained over sweeping time ($T_m=10$ ms) are shown in red (received with antenna A_1) and blue (received with antenna A_2) colours. Fig 4.2 contains 1.5×10^6 samples over 66.7 ms acquired by 22.5 MHz sampling rate of the data acquisition card.

The duration between two successive sampled points can be obtained by the sampling frequency of the data acquisition card. Time period (T_{sample}) between any two continuous sample points are given by the expression

$$T_{sample} = \frac{1}{f_{SF}} \quad 4.1$$

Where, f_{SF} is the sampling frequency of acquisition card.

The number of samples collected over $T_m=10$ ms with the sampling frequency $f_{SF}=22.5$ MHz is given by

$$N_{sample} = \frac{T_m}{T_{sample}} = T_m f_{SF} = 225000 \quad 4.2$$

Where, N_{sample} and T_{sample} are the total number of samples and the sampling period, respectively.

In order to understand the influence of sampling frequency on the precision of the received beat frequency computations, let assume two extreme cases of the tag's position that is the distance between Active-Tag and Localization Base Station be 1m and 7 m, respectively. Therefore, the beat frequency of the baseband signal obtained by the use of FMCW principle will be 666.7 Hz and 4.6667 Hz, respectively with $T_m=10$ ms, $BW=1$ GHz using relationship 2.8.

Hence, the time period of each cycle of the baseband signal will be 1.5 ms and 0.21 ms based on the relationship 2.15-2.18. These time periods of data represent 6 and 46 complete sinusoidal cycles (λ in terms of wavelength or 2π as phase) over 10 ms. Typically, the number of samples in each cycle can be expressed as

$$N_{sample} = \frac{T_m}{T_{sample}} = T_m f_{SF} \Leftrightarrow (Nt_{sample}N + N_{fraction}) = T_m f_{SF} \quad 4.3$$

$$N_{fraction} = N_{sample} - Nt_{sample}N$$

Where, Nt_{sample} is the total number of samples in one complete sinusoidal signal, N is the number of complete sinusoidal cycle over T_m (10 ms), and $N_{fraction}$ is the uncompleted cycle. Thus, the computation is performed only on complete cycles.

This gives us

$$Nt_{sample} = \begin{cases} 33750; & N = 6 \\ 4891; & N = 46 \end{cases} \quad 4.4$$

Therefore, the 33750 samples will provide a precision of 0.01° ($360^\circ/33750$, resolution of one sample can be expressed as the total phase change over total number of samples for a given time period of sinusoidal signal). Similarly, the 4891 samples will give a precision of the 0.07° . Hence, the difference in frequency shifts (between two arriving signals) can be expressed in terms of phase change over T_m as earlier mentioned through the relationships 2.11-2.13

$$\Delta f_{21} = \frac{1}{2\pi} \left(\frac{\Delta\phi_2 - \Delta\phi_1}{T_m} \right) \quad 4.5$$

Where, Δf_{21} is difference in frequency shifts, and $\Delta\phi_1$ and $\Delta\phi_2$ are total change in phase shifts between transmitted and received signals.

With increase in distance, the N also increases over T_m and hence it will help in attaining better estimate of Δf_{2l} by taking the average value as explained through the relationships 2.14-2.20 in Chapter 2. Also, the increment in N from 6 to 50 between 1 m and 7 m means that the resolution in terms of phase decreases from 0.01° to 0.07° . But the absolute change is just 0.06° ($0.07^\circ - 0.01^\circ$) which can be accepted while considering the range of radial-distance, that is, from 1 m to 7 m.

Fig 4.3 represents the two incoming baseband signals ($Rx1-f_1$ & $Rx2-f_2$) acquired by the data acquisition card over sweep time ($T_m=10$ ms) of the FMCW signal when the AT is at 0.82 m (546 Hz theoretical value in terms of beat frequency) of radial-distance. Fig 4.3 also includes the extra time delay introduced by the circuits (LBS and AT) which must be compensated out as discuss in Section 4.2.2. Therefore, Fig 4.3 represents the beat frequencies because of 0.82 m plus the delay in ILS circuit.

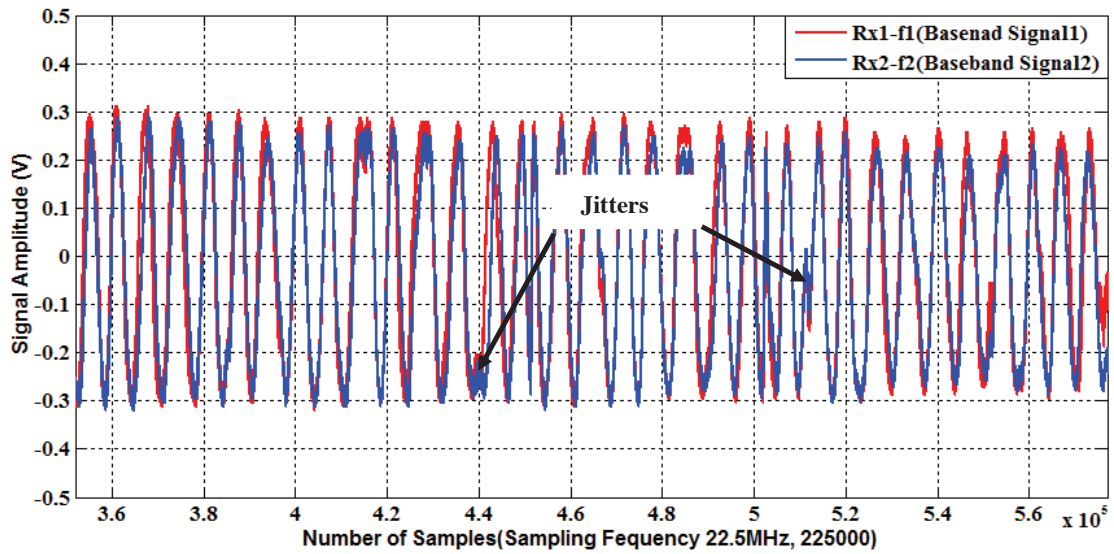


Fig 4.3: Baseband signals over $T_m=10$ ms.

Fig 4.4 shows the estimated frequencies of the baseband signals after minimizing the jitters by the successive mean approach algorithm (SMAA, explained later in this section) and applying the DMTD technique as presented in Section 2.2.1.

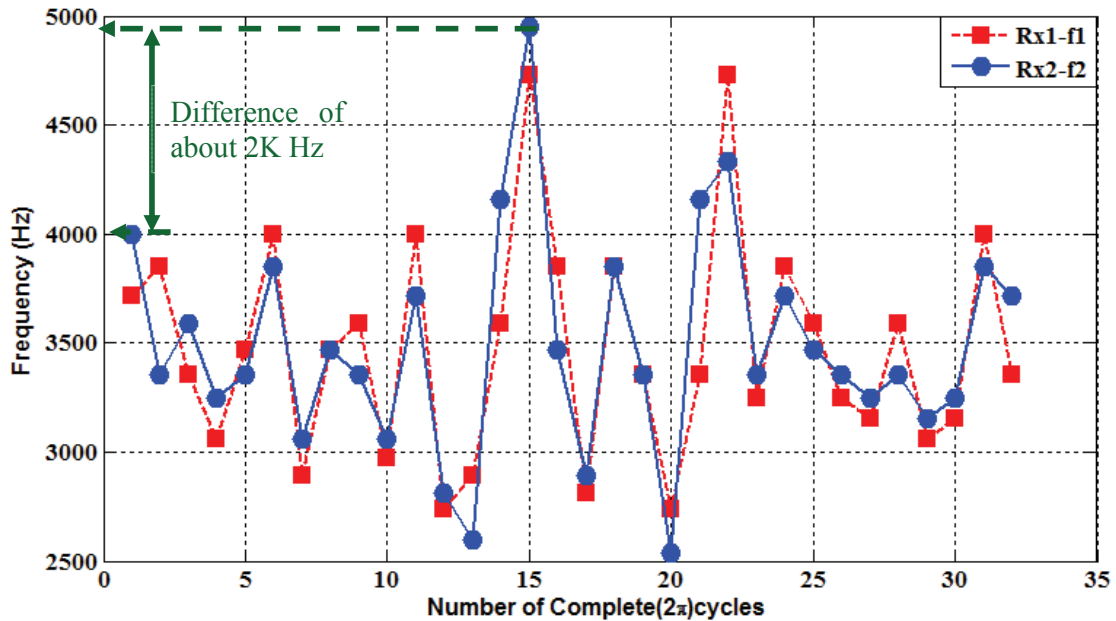


Fig 4.4: Computed frequencies over $T_m=10\text{ms}$.

The X-axis represents the number of complete sinusoidal signals (N) for the two signals whereas Y-axis shows the estimated frequency. The first cycle of the Rx1-f1 has computed frequency 4K Hz whereas its fifteenth cycle has computed frequency 4.9 KHz. These frequencies represent 6 m and 7.35 m in distance according to the relationship 2.12; the difference in distances is 1.35 m. Although, these frequencies are obtained for the same position of the AT but each computed frequency differs from another and it represents different value of distances. The difference in frequencies are perhaps due to the jitter of LO (local oscillator) or of the clock of ADC. Therefore, the average value of all cycles (means all frequencies) will give a more realistic value of the actual distance as explained in Section 2.2.1. Thus, the more number of cycles will help in attaining better estimation of the beat frequency and this will lead to better radial-distance estimate. The expected value of the beat frequency (including the delays in circuits) was 3446 Hz and the estimated ones (Fig 4.4) are obtained close to it.

Further, the radial-distance and angle of azimuth (angle-of-arrival) are computed based on the method presented in Chapter 2. The offline signal processing has been done by triggering the *Prog1.m* [3] from MATLAB which takes the baseband signals collected

through *Prog2.m* [4] as input data for the signal processing. The various parameters and assumption used for the signal during the processing are mentioned below:

- ⌘ Bandwidth of the FMCW Signal: 1GHz
- ⌘ Modulation time/ time-of-sweep: 10 ms
- ⌘ Sampling Frequency (data card): 22.5 MHz
- ⌘ Baseline length, d_{baseline} : 0.30m
- ⌘ Transmitted power: 7dBm
- ⌘ **Assumption:** LBS and Active-Tag are coherently synchronized.

The received baseband data had some jitters problem as marked in Fig 4.3. This problem has been minimized with the successive mean approach which is discussed bellow.

The roughness in curve shows the jittering effects because of the noise. This jitter effects are main drawback in the implementation of counter method during the signal processing, Section 2.2.1. However, based on the simulation performance, this effect can be significantly reduced by computing the mean value between two successive points in order to decrease the jitters as illustrated in Fig 4.5.

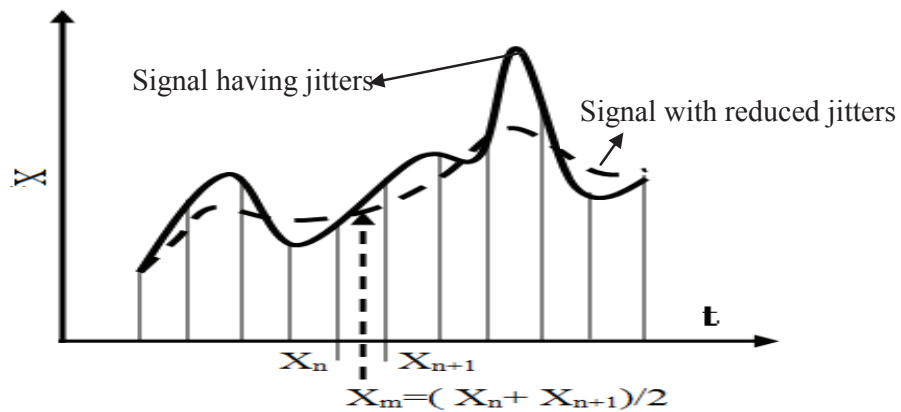


Fig 4.5: Successive Mean Approach Algorithm (SMAA).

The X_n and X_{n+1} are any two consecutive sample points of the signal with jitters. The mean value is marked by the X_m (dashed-curve). The mean value minimizes the jitter as depicted in Fig 4.5. If we repeat/iterate the process of mean computation on the obtained samples ($X_m, X_{m+1}...$) from the previous samples ($X_n, X_{n+1}...$) then the jitters will further

reduce and this will give a smooth curve compared to the previous one. We call this process as Successive Mean Approach Algorithm (SMAA).

Fig 4.6 shows the SMAA output signal after eight iterations. For fast computation, the numbers of samples considered are 1041.

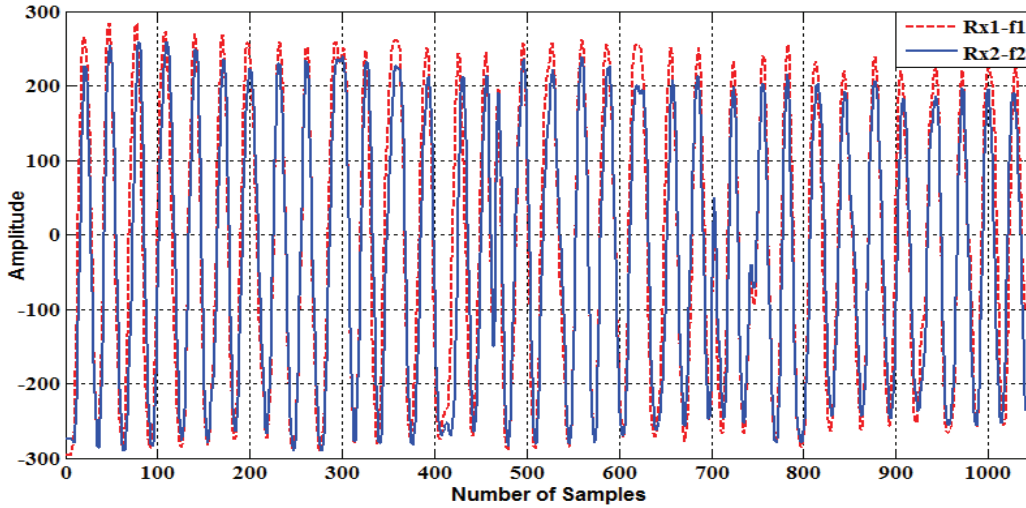


Fig 4.6: Output of the SMA algorithm.

To understand the reduced effects of the jitters around the zero crossing, the beat frequencies are plotted in **Fig 4.7** from the baseband signals presented in **Fig 4.3** (prior to SMAA) and **Fig 4.6** (after SMAA). The x-axis represents the number of complete cycle over T_m and the y-axis represents the beat frequency.

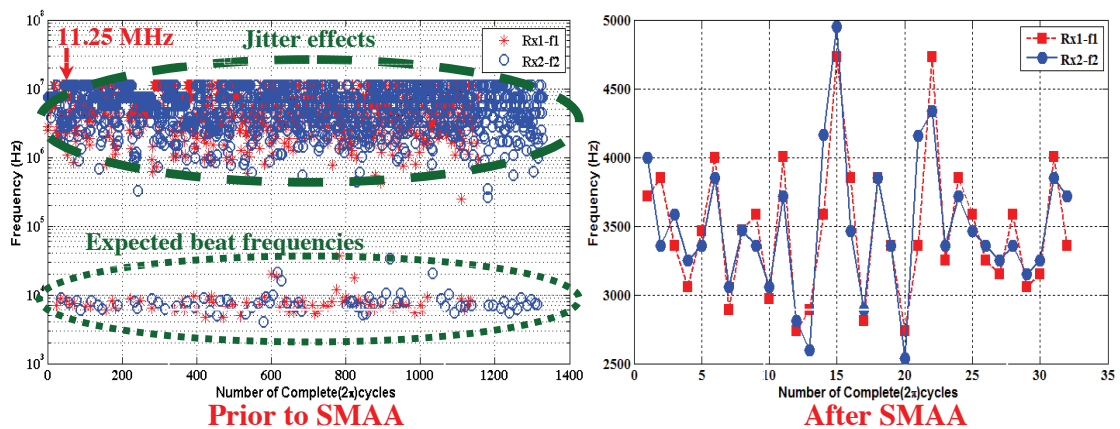


Fig 4.7: Performance analysis of SMAA.

The beat frequencies shown on the left side of the above figure are presented in logarithmic scale. The computed beat frequencies have more than 1300 complete cycles due to multiple times of zero crossing. As an example, a zoomed part of Rx1-f1 at zero crossing is shown in Fig 4.8. This shows the jittering effects (probably due to noise of the data acquisition card) which results in false estimation of the complete cycle from baseband signal and thereafter wrong estimations of beat frequencies.

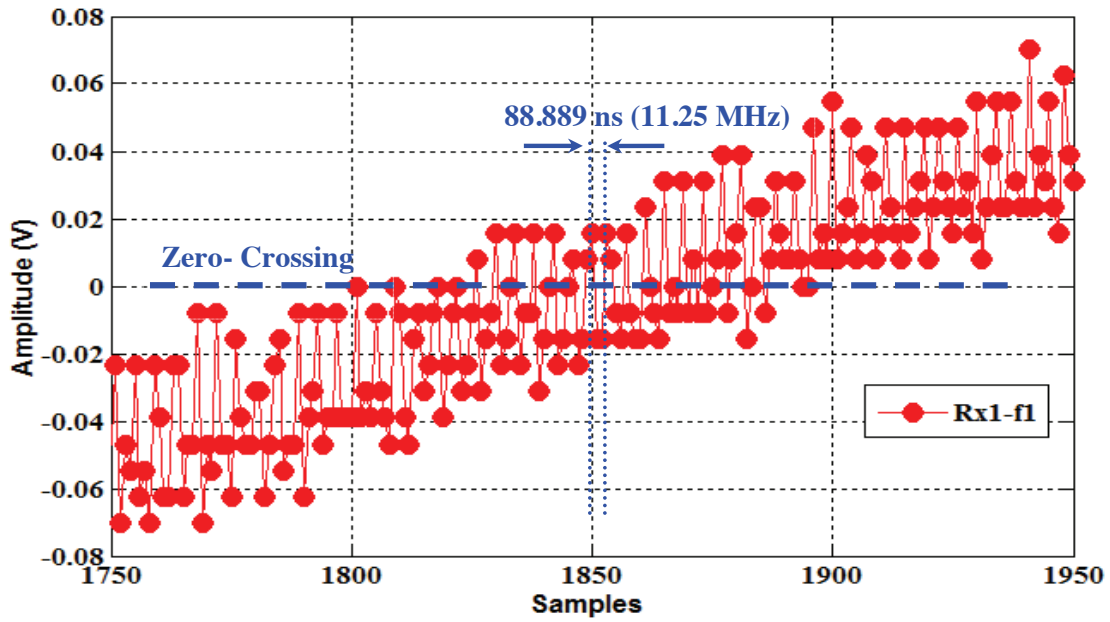


Fig 4.8: Jitters near zero-crossing.

The estimated beat frequencies vary between few KHz to 11.25 MHz which shows the extreme deviation from the expected one (3446 Hz). Since, the sampling frequency (f_{SF}) is 22.5 MHz, therefore, it gives a resolution of 44.44 ns ($T_{sample}=1/f_{SF}$, relationship 4.1) in time. Hence, the maximum observed beat frequency which could be measured is 11.25 MHz ($1/2 \times 44.44$ ns, according to Nyquist principle) as marked in Fig 4.7. However, the jitters are considerably reduced by the SMAA approach and after its use, the computed beat frequencies are plotted on the right side of Fig 4.7. It has same number of cycles (32) as it appears to be in the received baseband signals shown in Fig 4.3. This clearly demonstrates the strength of the SMAA approach in minimizing the jitter effects near zero crossing.

Also, some RF leakage signals have been observed in the system and these are shown in Fig 4.9.

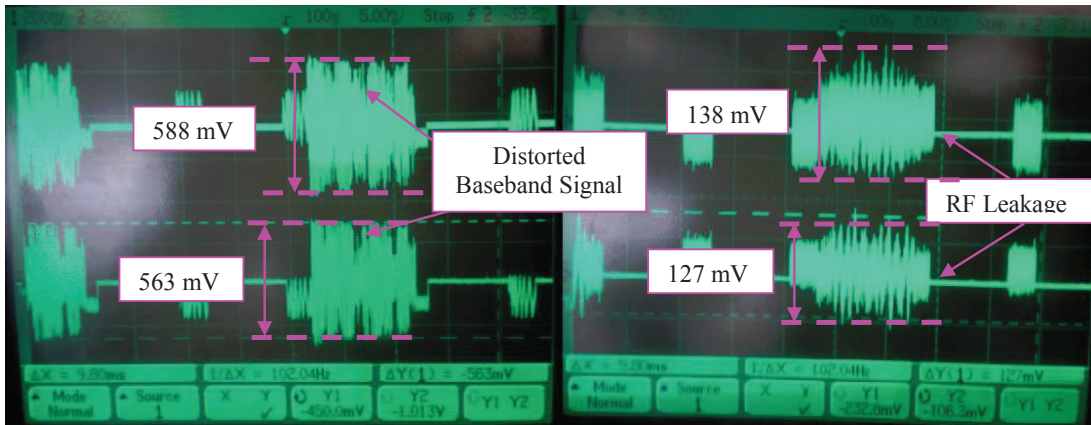


Fig 4.9: Received baseband and RF-leakage signals.

The left side of the above figure shows the obtained baseband signals when the radial distance between the LBS and the Active-Tag is 5.4m where as the right side of the figure shows the RF leakage signals. The received signals have 588 mV and 563 mV peak-to-peak amplitudes and have distortion in amplitude (hole) mostly because of the multipath effects.

These RF leakage signals are observed experimentally by disconnecting the receivers as well as transmitter antennas of the RF circuit. The front ends (transmitter and receivers) of the RF circuits were terminated with a 50Ω load. The amplitude of the leakage signals (receiver 1 and 2) were 138 mV and 127, respectively. However, the distortion is not observed when the Active-Tag remains in close proximity to LBS. **Fig 4.10** shows the received signal at close radial-distance of 0.82m.

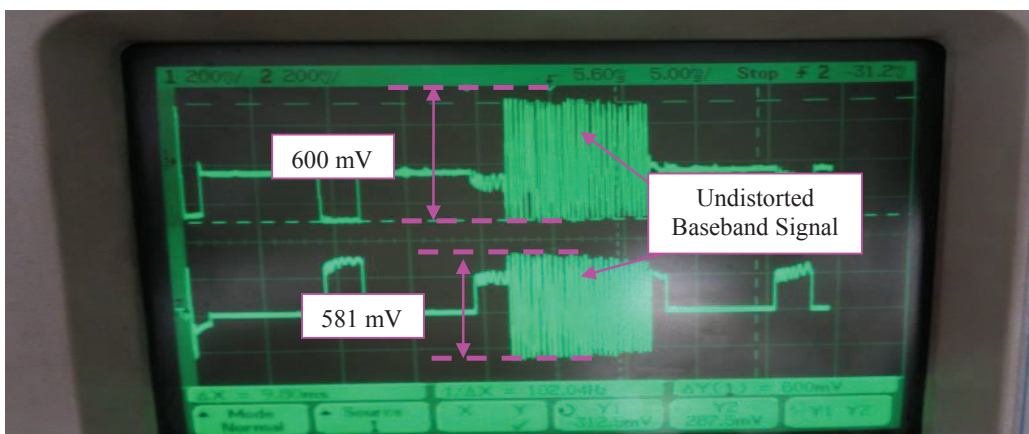


Fig 4.10: Received baseband signals at 0.82 m.

In close distance, the multipath has minimal effects and hence, the signals are robust compared to the baseband signals in [Fig 4.9](#). However, the measured voltages are of same order of magnitude around 600 mV even the AT is close to the emitter. This is perhaps because of the saturation of the receiver amplifier or due to the automatic gain amplifier of the data acquisition card. In fact, our measurements are more concerned about signal's zero-crossing which is independent of received voltage variation. Therefore, this will not affect our measurement technique.

Additionally, the isolators at the input point of antennas were used to see the effects but there was not significant decrease in RF leakages were noticed.

The signal processing has been presented in this section and the same method of processing is also used for the system calibration and for the localization of the Active-Tag in a real indoor environment.

4.2.2 System Calibration

Calibration of the developed Indoor Localization System (ILS) is performed in order to validate the system's measurement performance by compensating the circuit time delays. The distance between Active-Tag and LBS is given by the product of time taken to travel the Euclidian space between them and the signal speed which is equivalent to the speed of light. However, the intended signal also travels within the circuits of LBS and AT apart from the Euclidian space and hence, it introduces extra time delay. These delays need to be shorted out for true determination of the Euclidian space between LBS and AT. The extra delays are shorted out by calibrating the ILS circuits (LBS and AT). The measurements taken by the ILS are compared with the known values of the radial-distance and angle-of-arrival so that the delays due to signal propagations within the circuits can be determined and further it should be compensated. The configuration used for the calibration is depicted in [Fig 4.11](#).

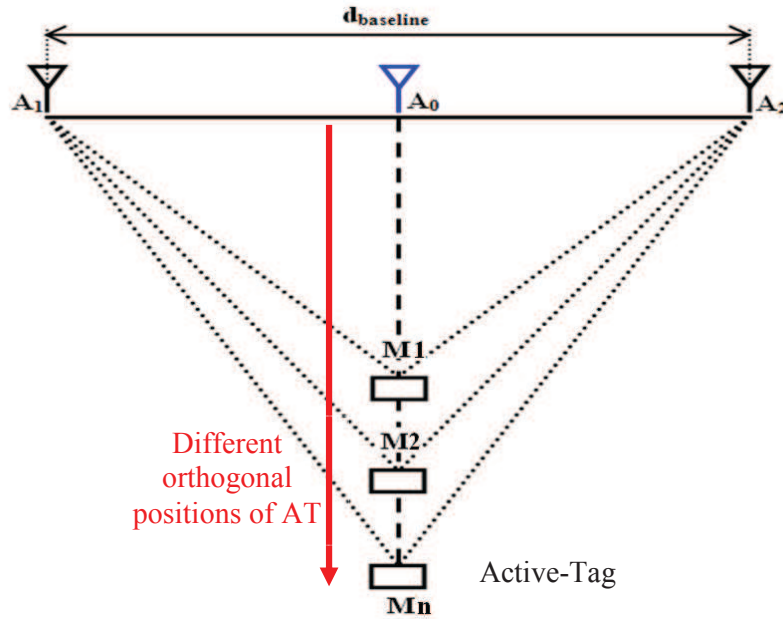


Fig 4.11: Calibration of ILS.

The transmitter antenna (A_0) is kept at the midpoint of the baseline (d_{baseline}) and the two receiver antennas (A_1 and A_2) are placed at the each end of the baseline. All antennas are kept in the same plane and at the same fixed position as shown in **Fig 4.11**. Active-Tag is positioned at equidistance from the two receiver antennas and is orthogonal to the baseline. The calibration is performed for the fixed length of baseline that is $d_{\text{baseline}}=30$ cm.

Active-Tag is moved on the A_0 - M_n line so that it remains at equidistance from the two receiver antennas (A_1 & A_2). Hence, the measured distances through the two receiver antennas (A_1 and A_2) from A_0 via Tag always remain identical. Also, the angle-of-arrival (AoA) measured by the receiver antennas must always remain same, i.e. 90° , with respect to the A_1 - A_0 - A_2 collinear line.

Table 4.1 represents different actual positions (M_1, M_2, \dots , see **Fig 4.11**) of the Active-Tag from the transmitter (Tx-Tag) and the receiver antennas (Tag-Rx1 and Tag-Rx2) of LBS and theirs corresponding beat frequencies are computed with the help of relationship **2.8**. The beat frequencies are named as ‘F1-Act’ and ‘F2-Act’ whereas angle of arrival as ‘Act-AoA’. The Tx-Rx1 and the Tx-Rx2 are the round trip of the wave between LBS and Active-Tag. The radial-distance is varied between 0.89 m to 3.02 m.

Table 4.1
CALIBRATION: ACTUAL POSITION OF ACTIVE-TAG

Sl. No.	Tx-Tag (m)	Tag-Rx1 (m)	Tag-Rx2 (m)	Tx-Rx1 (m)	Tx-Rx2 (m)	F1-Act (Hz)	F2-Act (Hz)	Dif-TxRx1 TxRx2 (m)	Act-AoA
1	0,8900	0,9026	0,9026	1,7926	1,7926	597,52	597,52	0,00	90
2	1,0050	1,0161	1,0161	2,0211	2,0211	673,71	673,71	0,00	90
3	1,1100	1,1201	1,1201	2,2301	2,2301	743,36	743,36	0,00	90
4	1,2850	1,2937	1,2937	2,5787	2,5787	859,58	859,58	0,00	90
5	1,3140	1,3225	1,3225	2,6365	2,6365	878,84	878,84	0,00	90
6	1,3750	1,3832	1,3832	2,7582	2,7582	919,39	919,39	0,00	90
7	1,4900	1,4975	1,4975	2,9875	2,9875	995,84	995,84	0,00	90
8	1,62	1,6239	1,6239	3,2409	3,2409	1080,31	1080,31	0,00	90
9	1,75	1,7604	1,7604	3,5144	3,5144	1171,47	1171,47	0,00	90
10	1,87	1,8710	1,8710	3,7360	3,7360	1245,34	1245,34	0,00	90
11	2,03	2,0335	2,0335	4,0615	4,0615	1353,85	1353,85	0,00	90
12	2,14	2,1472	2,1472	4,2892	4,2892	1429,75	1429,75	0,00	90
13	2,27	2,2710	2,2710	4,5370	4,5370	1512,32	1512,32	0,00	90
14	2,38	2,3847	2,3847	4,7647	4,7647	1588,24	1588,24	0,00	90
15	2,53	2,5344	2,5344	5,0644	5,0644	1688,15	1688,15	0,00	90
16	2,64	2,6433	2,6433	5,2823	5,2823	1760,75	1760,75	0,00	90
17	2,73	2,7331	2,7331	5,4621	5,4621	1820,71	1820,71	0,00	90
18	2,89	2,8889	2,8889	5,7739	5,7739	1924,63	1924,63	0,00	90
19	3,02	3,0247	3,0247	6,0457	6,0457	2015,24	2015,24	0,00	90

Table 4.2 shows the measured data after computations as explained in **Section 4.2.1**. The F_1 .Meas and F_2 .Meas are measured FDoA (frequency difference of arrival) by the two receiver sections of ILS. The corresponding estimated radial-distances are represented by ‘MeaTxRX1’ and ‘MeaTxRX2’ as the round trip of the wave between LBS and Active-Tag. ‘DifMeas’ represents the mismatch between the estimated radial-distances by the two receivers. Since the Active-Tag is placed at equidistance from the receivers, therefore, a zero mismatch was expected. However, the presence of small mismatch can be assumed because of the manual error as the field measurements are carried out in a real indoor environment. The estimated angle is represented by ‘MeaAoA’. Finally, the circuit delays observed by the two receivers are represented by DelayRx1 and DelayRx2.

Table 4.2
CALIBRATION: DELAY DETERMINATIONS

Sl. No.	F1-Meas (Hz)	F2-Meas (Hz)	Mea TXRx1 (m)	Mea TXRx2 (m)	Dif-Mea (m)	Mea AoA (degree)	Delay Rx1 (m)	Delay RX2 (m)
1	1,79E+03	1,79E+03	5,3778	5,373	0,0048	89,10	3,59	3,58
2	1,85E+03	1,85E+03	5,5464	5,5452	0,0012	89,79	3,53	3,52
3	1,93E+03	1,93E+03	5,8002	5,7975	0,0027	89,50	3,57	3,57
4	1,99E+03	2,00E+03	5,9844	5,9904	0,006	88,87	3,41	3,41
5	2,07E+03	2,06E+03	6,2028	6,1899	0,0129	87,55	3,57	3,55
6	2,10E+03	2,10E+03	6,2865	6,3057	0,0192	86,35	3,53	3,55
7	2,18E+03	2,18E+03	6,5346	6,5346	0	90,02	3,55	3,55
8	2,27E+03	2,27E+03	6,7974	6,7995	0,0021	89,62	3,56	3,56
9	2,37E+03	2,37E+03	7,0977	7,0965	0,0012	89,79	3,58	3,58
10	2,44E+03	2,43E+03	7,3077	7,2975	0,0102	88,07	3,57	3,56
11	2,55E+03	2,54E+03	7,6386	7,6332	0,0054	88,99	3,58	3,57
12	2,62E+03	2,62E+03	7,8507	7,8615	0,0108	87,95	3,56	3,57
13	2,66E+03	2,67E+03	7,9911	8,0001	0,009	88,30	3,45	3,46
14	2,79E+03	2,79E+03	8,3583	8,3838	0,0255	85,14	3,59	3,62
15	2,90E+03	2,90E+03	8,712	8,7093	0,0027	89,50	3,65	3,64
16	2,94E+03	2,95E+03	8,8284	8,8551	0,0267	84,91	3,55	3,57
17	3,00E+03	3,01E+03	8,9967	9,033	0,0363	83,07	3,53	3,57
18	3,15E+03	3,14E+03	9,4368	9,4092	0,0276	84,74	3,66	3,64
19	3,19E+03	3,19E+03	9,5838	9,5721	0,0117	87,78	3,54	3,53

The circuit delays are determined by compensating the actual radial-distance from the estimated ones. The estimated delays are plotted in Fig 4.12.

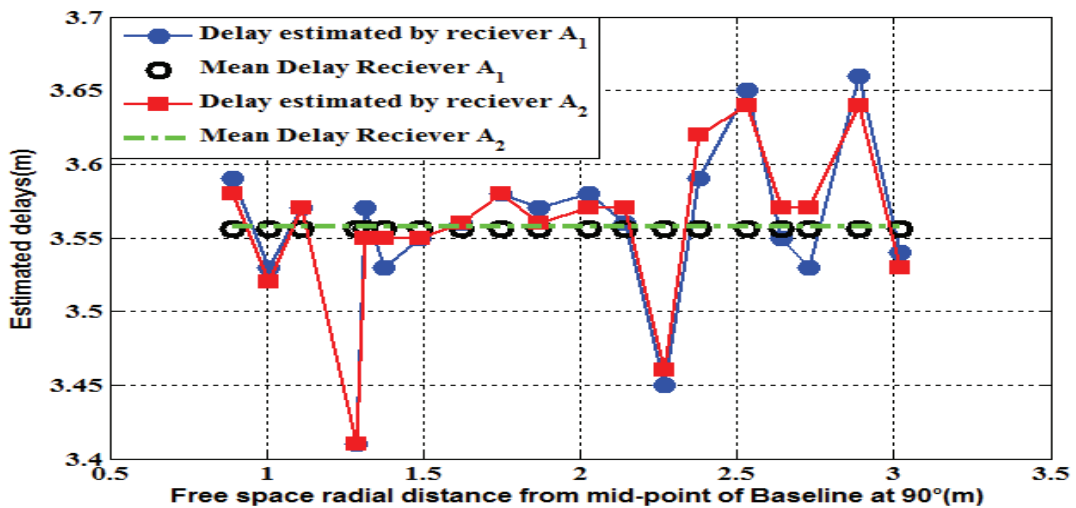


Fig 4.12: Calibration-Observed delays by the receivers.

The red and blue curves shows the delays estimated by the receiver with antenna A_1 and A_2 , respectively. The mean delays are marked by the green and the black markers. The observed mean delays are **3.56 m** for both receivers. The difference in observed mean delays shows the mismatch between the receiver sections which equals to **0.6 cm** that is less than **1 cm**. The fluctuation in the delays curve can be assumed as the influence of real indoor environments. The deep fluctuations observed by the two receivers are at certain radial-distance are close to each other which suggest that the variation is introduced because of the indoor environments otherwise it could have been different.

After performing the calibration, the field-measurements are performed under different conditions, such as line- of-sight, are presented in the following sections.

4.3 Performance in Line-of-Sight Case

In line-of-sight condition, the field-measurements are conducted in two parts. First part presents the 2D position estimations in terms of radial-distance and angle of azimuth whereas second part presents the 3D estimations in terms of radial-distance, angle of azimuth and angle of elevation, respectively. The location of Active-Tag is estimated with respect to the known fixed position of the Localisation Base Station. Only one anchor as LBS is used for 2D and 3D estimations. All field-measurements are performed in a real indoor environment.

4.3.1 2D Field Measurements

General description about the field-measurement is depicted in **Fig 4.13**. The blue coloured signal represents the transmitted signal from the LBS whereas the red coloured signals are the received ones at the LBS which are coming after the frequency-transition from Active-Tag as explained in **Chapter 2**.

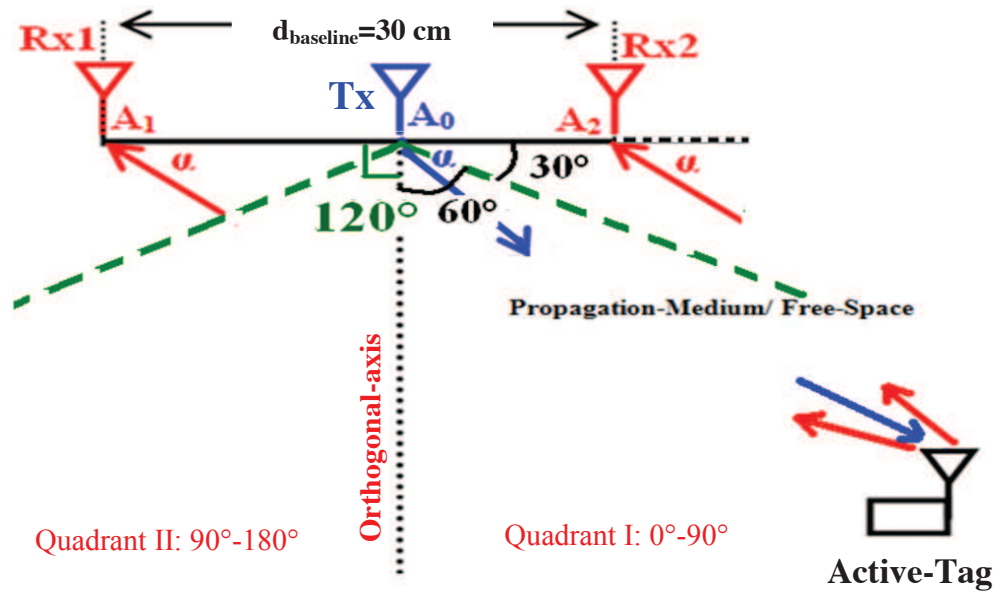


Fig 4.13: 2D-Field measurements in a real indoor environment.

The estimations of radial-distance as well as angle (α) are performed by keeping the active-tag at different angular positions between 30° to 90° and radial-distances between 1.2 m and 1.8 m, with respect to fixed position of the LBS. The estimations are performed for 24 different positions (number of estimated positions). The measurements were performed in Quadrant I from 30° to 90° as marked in Fig 4.13. Since the ILS structure is symmetric about the orthogonal axis to the baseline, therefore, the measurements carried out in Quadrant I will also be valid for the adjacent Quadrant II on the left side of the orthogonal axis defined across the baseline centre.

For the position estimations, the signal processing has followed the same procedures as mentioned in Section 4.2.1, and the estimated positions along with the actual ones are considered for the analysis. The estimated radial-distances are plotted in Fig 4.14.

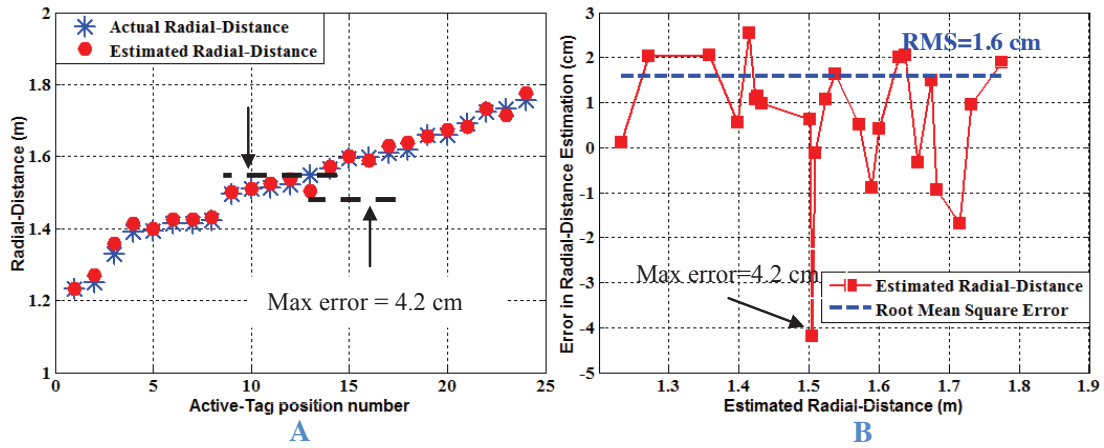


Fig 4.14: A) 2D Radial-distance, B) Root-mean-square error.

The actual radial-distances (y-axis) are marked in blue colour whereas their corresponding estimated ones (y-axis) are in red coloured circle for 24 different radial-distances (x-axis) in **Fig 4.14 (A)**. The positive slope of curves happens to be because of the way of estimated as well as actual radial-distances are presented here, that is, values are sorted and presented in increasing order and it is has nothing to do with the system performance. However, the differences between actual and estimated ones along y-axis represent the error in the position estimates. **Fig 4.14 (B)** illustrates the estimated radial distances (in m on x-axis) and the corresponding errors (in cm on y-axis). The observed estimated rms error is 1.6 cm which is marked by the blue coloured dashed line. The observed maximum error (Max error) is 4.2 cm around 1.5 m (estimated value), therefore, the actual value is equal to 1.54 m (1.5 m+ 4.2 cm, estimated value minus its corresponding error) as marked in the above figure. Although, most of the errors are within 2 cm but the reason behind maximum error could be because of the occurrence of strong jitters around the zero-crossing which leads to wrong estimation of the frequencies during signal processing.

The angles of azimuths are plotted in **Fig 4.15**.

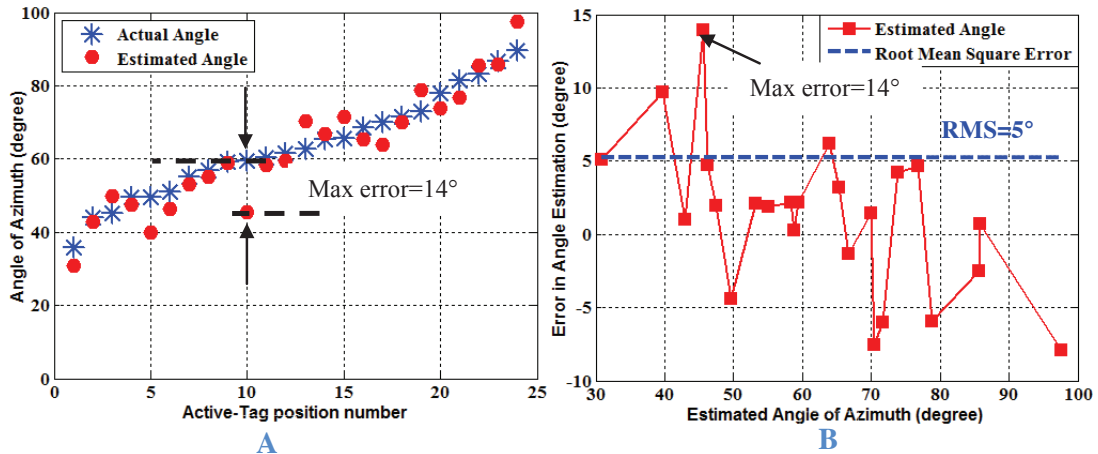


Fig 4.15: A) 2D-Angle of azimuth and, B) Root-mean-square error.

The estimated angles as well as actual ones are plotted in **Fig 4.15 (A)**; the y-axis represents the angle of azimuth whereas the x-axis shows the different measurements, that is, 24 measurements are considered as mentioned in the radial-distance estimates. The estimated angle-of-azimuth is shown with red marker whereas their actual values in blue marker. The estimate at 10th measurement sample equals to 46° , however its actual value is 60° ; this has been marked with ‘Max error’ (14°). Here also, the positive slope of the curves is due to the values are presented in increasing manner, similar to **Fig 4.14**.

In **Fig 4.15 (B)**, the errors versus the estimated angles are plotted. The observed root-mean-square error is equal to 5° and is marked with the blue line. Most of the estimated angles are within the rms values. The observed maximum error (Max error) is equal to 14° which occurred around 60° (actual value) as marked in **Fig 4.15 (A)**. Therefore, the maximum error is observed for the position (1.55 m, 60°) as (4.2 cm, 14°).

The difference in rms values between radial-distance and azimuth are mainly due to the fact that the angle is obtained from the difference in radial-distance information which is actually the path-difference as explained in **Section 2.4.4.2**. As explained in **Chapter 2**, 1 cm is mapped into 3° . Therefore, the observed 1.6 cm rms can be mapped into angle equals to 4.8° and the theoretical mapped value is close to the observed 5° in angle estimations.

Only one anchor as Localization Base Station has been used for 2D measurements and the 3D measurements are presented next.

4.3.2 3D Field Measurements

A general description for the range and the angles estimations has been depicted in Fig 4.16; α and β correspond to angle of arrivals, azimuth and elevation, between the incoming signals received by A_1 - A_2 and A_3 - A_4 as explained in Section 2.4.2.

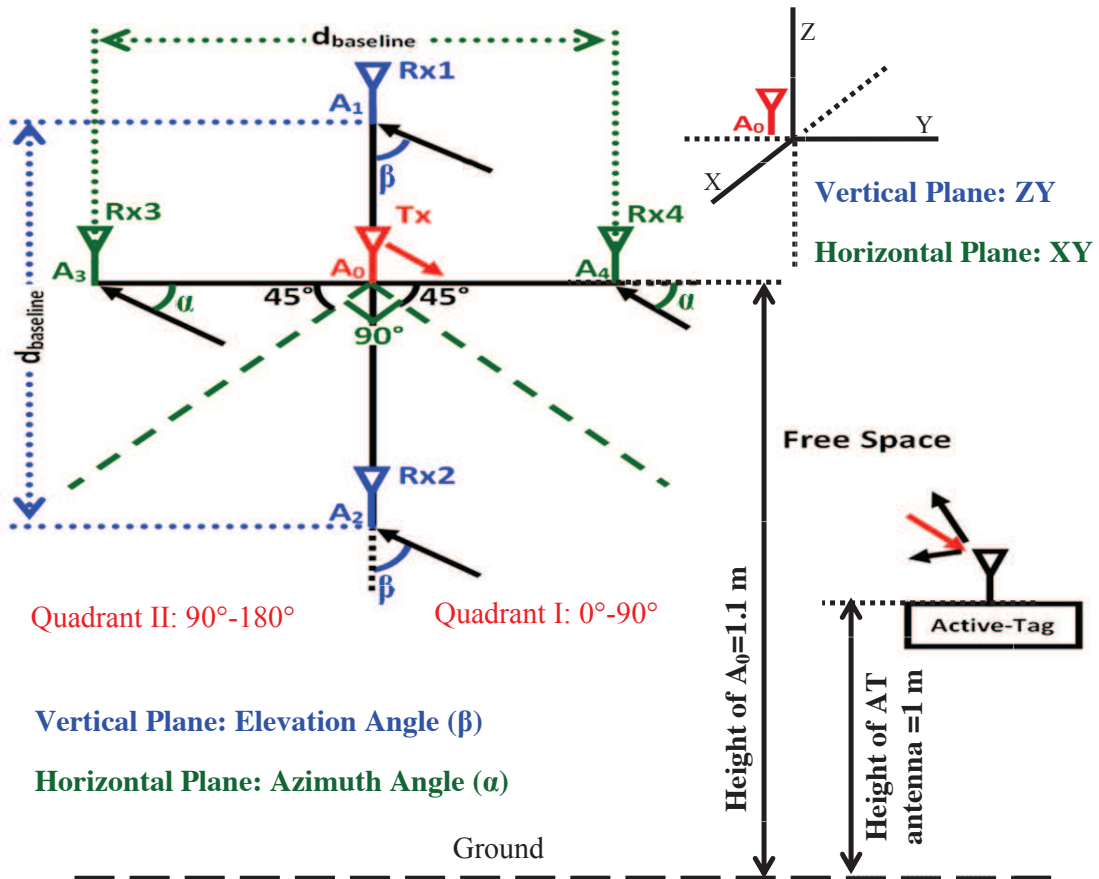


Fig 4.16: 3D-Field measurements in a real indoor environment.

The FMCW signal is transmitted by the LBS towards the Active-Tag (red coloured arrows) and then this signal is transmitted-back towards the LBS (black coloured arrows) as marked in the above figure. Here, same approach is considered as it was in the 2D field-measurements.

The measurements are performed for 19 different random positions of Active-Tag with respect to the fixed position of LBS. Active-Tag is placed between 0.9m to 1.25m as radial-

distance whereas the angle of azimuth is between 45° to 90° . The antennas' height of Active-Tag and LBS (transmitter antenna, A_0) are not kept at the same level from ground that is different from [Section 4.3.1](#). The AT antenna height is kept fixed at 1 m from the ground whereas LBS antenna (A_0) is kept at 1.10 m, respectively. Since the height of Active-Tag and LBS antennas are fixed, therefore, the elevation angle (β) only depends upon the variation of radial-distance. Hence, the elevation angle (β) is varied between 97° to 101° which comes only from the variation in radial-distance between 0.9 m and 1.4 m. The measurements are taken in Quadrant I between 45° and 90° because the designed system is symmetric by structure.

The estimated 3D positions of the remote Active-Tag by the LBS in an indoor environment are presented in two separate planes, Vertical and Horizontal planes. Each plane represents the 2D measurement setup as presented in the previous section and the combined planes present the 3D ILS as explained in [Section 2.4.2 of Chapter 2](#). For better analysis, the each plane is separately presented.

Horizontal Plane: The estimated radial-distance and their corresponding errors are presented in [Fig 4.17](#).

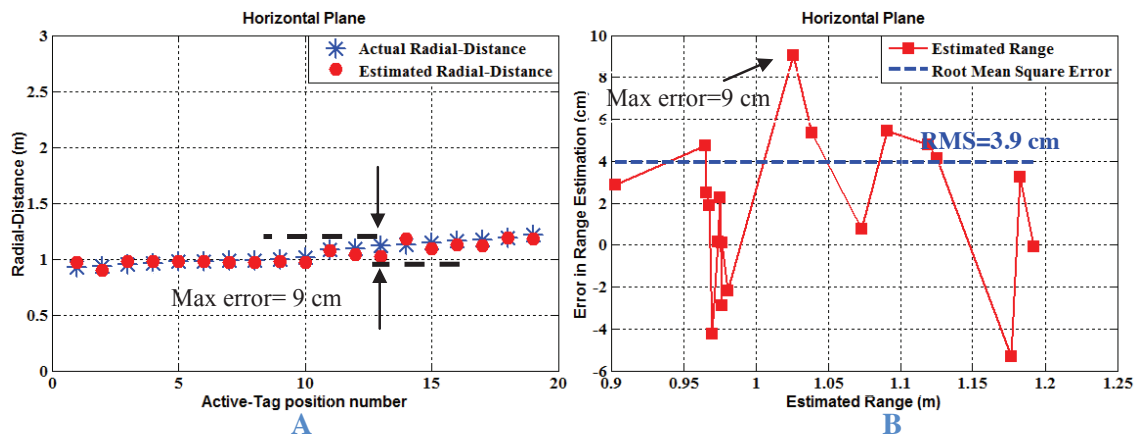


Fig 4.17: 3D-Radial-Distance (A) and root-mean-square error (B) in horizontal plane.

In [Fig 4.17 \(A\)](#), the actual radial-distances (on y-axis) are marked in blue colour whereas the estimated ones (on y-axis) are shown in red coloured circles for different measurements (x-axis). The differences between estimated and actual radial-distances along y-axis represent the errors. [Fig 4.17 \(B\)](#) shows the estimated radial distances (in m, on x-axis)

and the error (in cm, on y-axis). The observed root-mean-square error is 3.9 cm which is marked by the blue coloured dashed line. The observed maximum error is 9 cm around 1.03 m (estimated value), therefore, the actual value is equal to 1.12 m (1.03 m + 9 cm, estimated value minus its corresponding error) as marked on the left figure. The fluctuations show the harsh condition of the indoor environments.

The estimated angles of azimuth (α on y-axis) are plotted in **Fig 4.18 (A)** for different measurements on the x-axis. Here also, the positive slope of the curves is due to the values presented in increasing manner. The blue marked represents the actual angle of azimuths whereas the estimated ones are in red coloured circle. The maximum error (Max error) is 13° for the estimated values of 60° , therefore it represents the 47° of the actual angle of elevation.

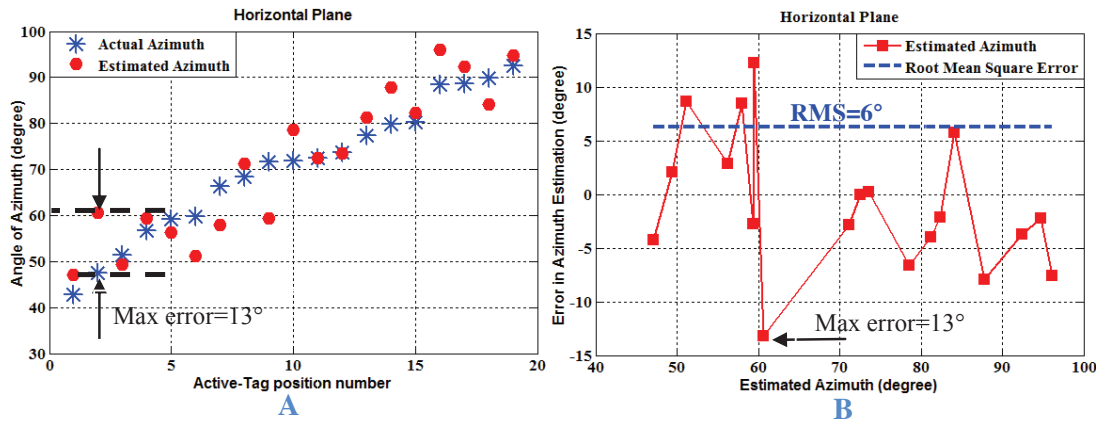


Fig 4.18: 3D-Angle of azimuth (A) and root-mean-square error (B) in horizontal plane.

The error analysis plot is shown in **Fig 4.18 (B)**; the x-axis represents the estimated angle of azimuth whereas the y-axis represents the corresponding errors. The observed root-mean-square error is 6° and is outlined with the blue coloured dashed line. Most of the estimated angles are within 5° which is less than the rms value.

Vertical Plane: The estimated and actual radial-distances and their error analysis are presented in **Fig 4.19**.

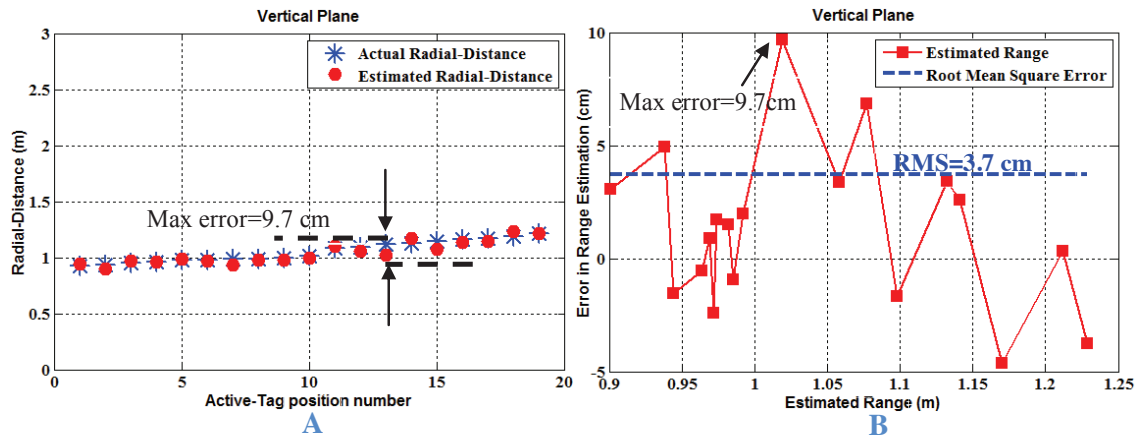


Fig 4.19: 3D-Radial-Distance (A) and root-mean-square error (B) in vertical plane.

The estimated and the actual radial-distances are plotted in **Fig 4.19 (A)** for 19 different measurements on the x-axis. The blue and red markers are used for the actual and the estimated radial-distances. The difference between actual radial-distance and their corresponding estimated values are presented on the y-axis and the maximum error (Max error) is found to be 9.7 cm. The error analysis is plotted in **Fig 4.19 (B)**, the estimated radial-distance and its corresponding errors are represented by the x-axis and the y-axis, respectively. The observed root-mean-square error of the estimated radial-distances is 3.7 cm and is marked by dashed coloured blue line. The maximum error (9.7 cm) is observed for the estimated radial-distance of 1.02 m. Therefore, the actual radial-distance is 1.12 m (1.02 m+9.7 cm) which is shown in the above figure.

The estimated angles of elevation (β on y-axis) are plotted in **Fig 4.20 (A)** for 19 different measurements on the x-axis. The blue and the red markers indicate the actual and the estimated β . The error analysis is presented in **Fig 4.20 (B)**; the estimated β is plotted on the x-axis and the corresponding errors on the y-axis, respectively.

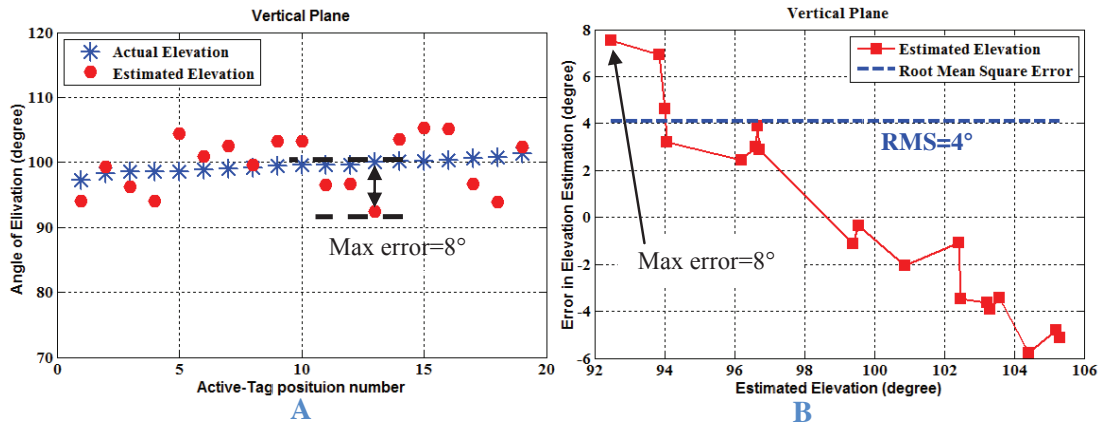


Fig 4.20: 3D-Angle of elevation and root-mean-square error in vertical plane.

The observed root-mean-square error is 4° and is marked with the blue coloured line in Fig 4.20 (B). Here also, the slope of the curves is due to the values presented in decreasing manner that is from 8° to -8° . The maximum observed error is 8° which comes from the 92° as the estimated value, therefore, the 100° is the actual value. The estimated elevation has less fluctuation compared to the azimuth's estimation because in the later case the Active-Tag was placed at different positions in a sector of 45° [over, 45° - 90°] compared to 4° [over, 97° - 101°] of the former case. Hence, the change in position was more profound in azimuth than in elevation because the heights of transmitter (A_0) and AT antenna (from the ground) were kept at a fixed value throughout the measurements.

The observed error analyses for the 3D measurements are summed up in Table 4.3. Different parameters are considered for the presentation such as Absolute Mean (Abs. Mean), Mean, Root-Mean-Square and Absolute Maximum (Abs. Max) errors.

Table 4.3
3D POSITION: ERROR ANALYSES

Parameter (error)	Horizontal Plane		Vertical Plane	
	Range (cm)	AOA(degree)	Range(cm)	AOA(degree)
Abs. Mean	3.6	5	2.9	4
Mean	1.7	-1	1	0 ($\cong 0.01$)
rms	3.9	6	3.7	4
Abs. Max	9	13	9.7	8

The above table shows the good mean errors compared to rms values for both planes which are computed from the same set of estimated values. The mean error, 11 cm as reported in [4], is almost seven and eleven times higher than the mean values observed in horizontal and vertical planes. This shows the robustness of the ILS in a real indoor environment for the LoS case with the use of a single known position.

With this, we demonstrated the 3D localization requires only one anchor as LBS and is given by combining the estimated values from the two planes, vertical and horizontal. Thus, a priori range determination is more precise as the radial-distance is obtained as the average value from two planes.

In comparison with the rms error (1.6 cm) in 2D measurements, the observed rms errors (3.9 cm and 3.7 cm) in both planes are higher than two times. This increase in error may be asserted because of the leakages between the four receiver chains and one transmitter chains. But such error increment in α and β are not observed. Perhaps, these results are concluded from a small set of measured data (19 measurement samples), therefore, a deviation of few centimetres (radial-distance) and degrees (angles) might not be ruled out.

The next section presents the measurements for maximum radial-distance estimations so that the scalability of built ILS prototype can be determined.

4.3.3 Maximum Radial-Distance

The field measurement is also conducted to know the maximum distance that can be estimated with the developed indoor localization system. The same set of parameters and assumption are considered which have been used in the previous two sections.

The field-measurement is conducted upto 6.7 m and the estimated radial-distance is plotted in **Fig 4.21**.

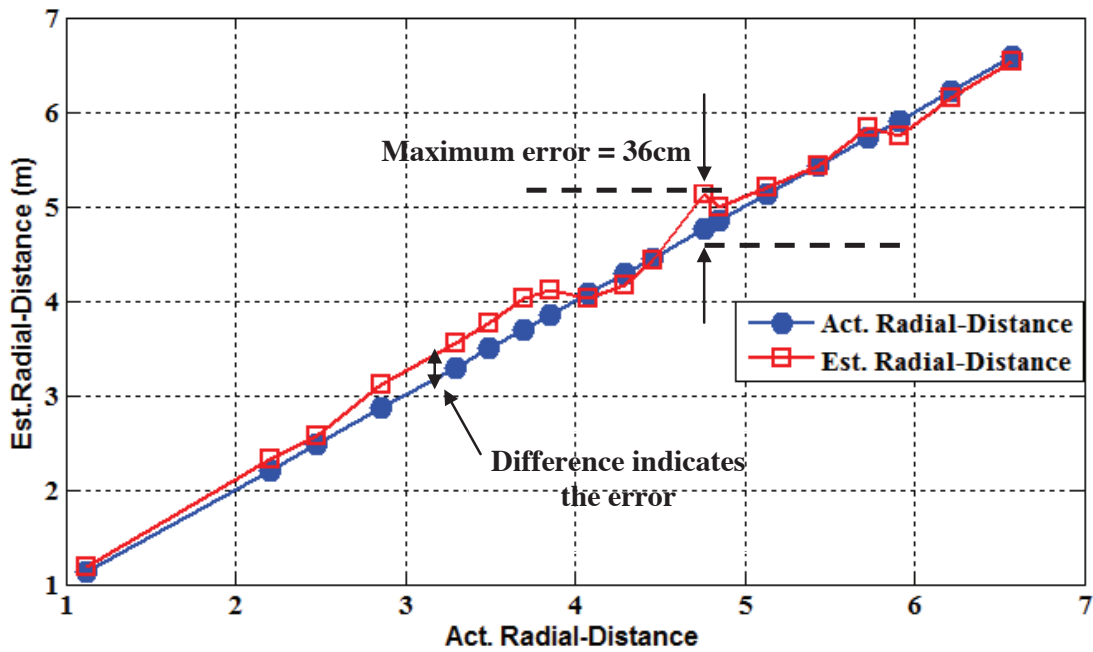


Fig 4.21: Actual and estimated radial-distance for maximum range.

The x-axis represents the actual radial distance (Act.Radial-distance) between LBS and AT whereas the y-axis represents the estimated radial-distance (Est.Radial-Distance). The blue curve represents the actual radial-distance whereas the red curve represents the estimated ones in the above figure. The difference between the actual and the estimated radial-distance indicates the error in estimation.

The estimated radial-distance and their corresponding errors are plotted in **Fig 4.22**. The estimated radial-distance and its corresponding errors are represented by the x-axis and the y-axis, respectively.

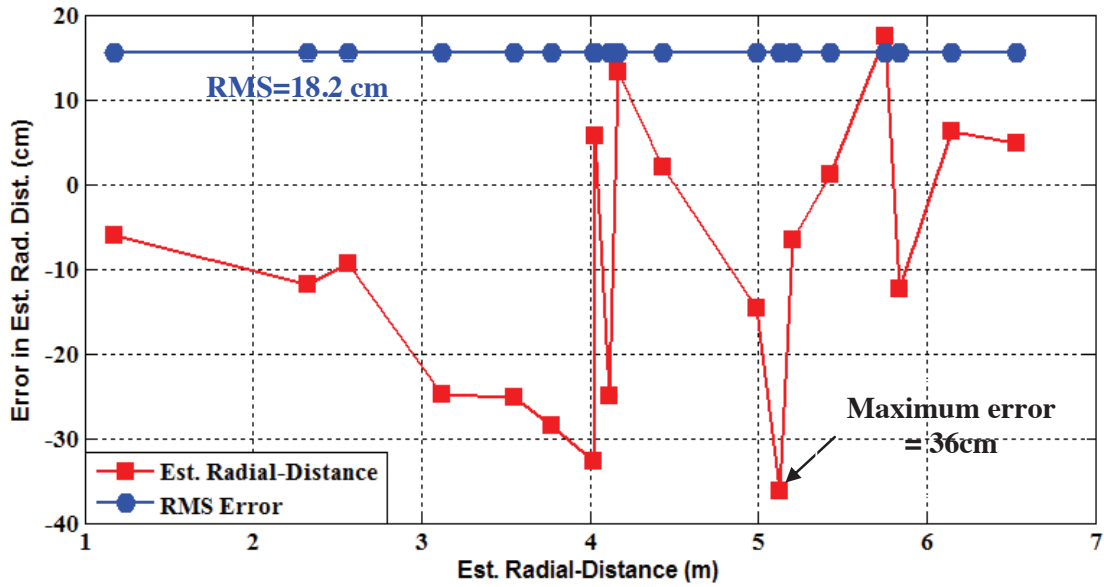


Fig 4.22: Estimated radial-distance and root-mean-square error for maximum range.

The observed root-mean-square error is 18.2 cm upto 6.7 m of radial-distance. The maximum error is observed as 36 cm at 5.1 m (estimated radial-distance) which in fact represents 4.74 m due to the delay time of RF circuit (5.1 m-0.36 m). Th most of the errors are within the 18 cm of the rms values. Hence, the rms error in radial-distance estimation increases from 4 cm (3.8 cm rms-error was observed in 3D measurements) to 18 cm. The increment in radial-distance range from 1 m to 6.7 m (almost 7 times) increases the rms-error by over four times (18/4, from 4 cm to 18 cm).

The measurement was only carried-out upto 6.7 m because of the length of the synchronization-cable (used for synchronizing AT and LBS generators). Therefore, more analysis is done in simulation, to have better understanding about the maximum range which can be attained with the known SNR. Hence, the objective of the simulation is to find the minimum SNR value for which the DMDT technique can have less error (< 4 cm, rms value of the 3D measurement).

The simulation has considered two received baseband signals as

$$S_i(t) = A_i(d_i) \times \sin\{2\pi \times f_i(d_i) \times t\} \tag{4.6}$$

Where, $S_i(t)$ represents the i -th baseband signal with an amplitude A_i and the beat-frequency f_i is a function of the radial-distance d_i based on time evolution ‘ t ’. The beat-frequency is further based on the relationship 2.21

$$f_i = d_i \times \frac{BW}{cT_m} \quad 4.7$$

Where, BW is the FMCW bandwidth (1 GHz), T_m (10 ms) is the modulation-time, and c is the speed of light (3e8 m/s). The amplitude of the signal is expressed as

$$A_i = V_o \times \left(10^{\frac{P_i}{20}} \right) \quad 4.8$$

$$P_i(\text{Path_Loss}) = 32.44 + 20 \times \log_{10}(d_i) - G_{tx} - G_{rx} + R_{gain}$$

Where, V_o is the reference peak-to-peak voltage of 1V (0.707 V rms, thus the input power at the input of emitter antenna is 10 dBm at 50 Ω) and P_i represents the free space path-loss (in dB) and G_{tx} and G_{rx} are the transmitter and the receiver antenna gains, and R_{gain} represents the combined gain of the receiver according to the architecture of ILS, Section 2.3. The power P_i and A_i of the two received RF signals (S_1 and S_2) by each antenna will almost remain same. The small variation in power level between them comes because the path-difference remains low. We will have the difference in beat frequencies between two RF signals. Here, we have not considered the phase change but it can be assumed as in terms of beat frequency because frequency is time derivative of phase change. The G_{tx} and G_{rx} represent the gains of AT and LBS antennas. The schematic of the simulation is illustrated in Fig 4.23.

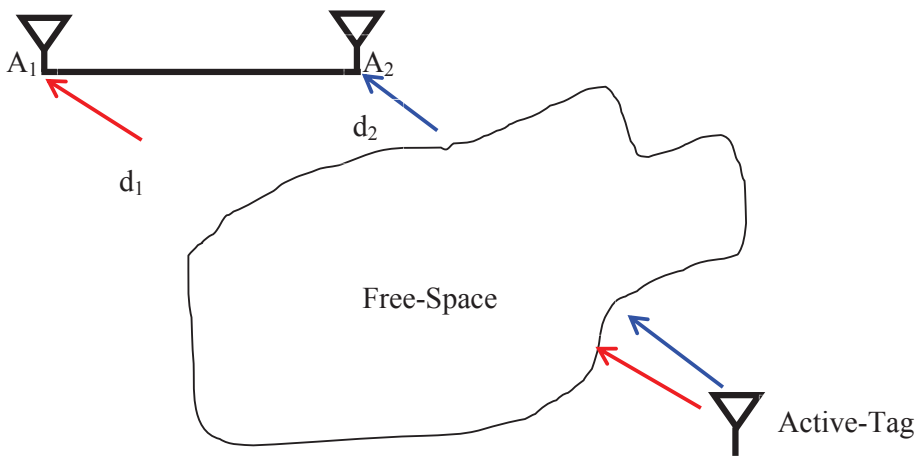


Fig 4.23: Estimated radial-distance and root-mean

Here, one-way path between LBS antennas (A_1 or A_2) and AT is considered, and the d_1 and d_2 represent the distance covered by S_1 - and S_2 -signals and then down converted to the baseband signal ($S_i(T_m)$, $i=1,2$, represented by 4.6) which is finally collected by the data acquisition card. For simplicity, the quantization error because of the data card which is actually Analog-to-Digital Converter is not taken into account.

The signal-to-noise ratio (SNR, in dB) has been added to the baseband signals using MATLAB function-awgn [10] which introduced the effect Gaussian Noise.

$$\text{Baseband_Signal} = \text{awgn}\{S_i(t_i), \text{SNR}\} \quad 4.9$$

Let assume that the SNR represents the value of the received baseband signals just after the down conversion of the received FMCW signal (6-7 GHz) into beat frequency, using relationships 4.7 and 4.8.

The simulation is done for two baseband signals ($S_i(T_m)$ for d_1 and d_2) obtained at the output of the receiver chains over the modulation-time (10 ms). The estimations of the radial-distance are performed according to the DMDT technique discussed in Section 2.2.1 then the errors are computed with the actual distance used for simulation. The simulation has not taken account the multipath effects. The error in radial-distance estimations versus the SNR are plotted in Fig 4.24.

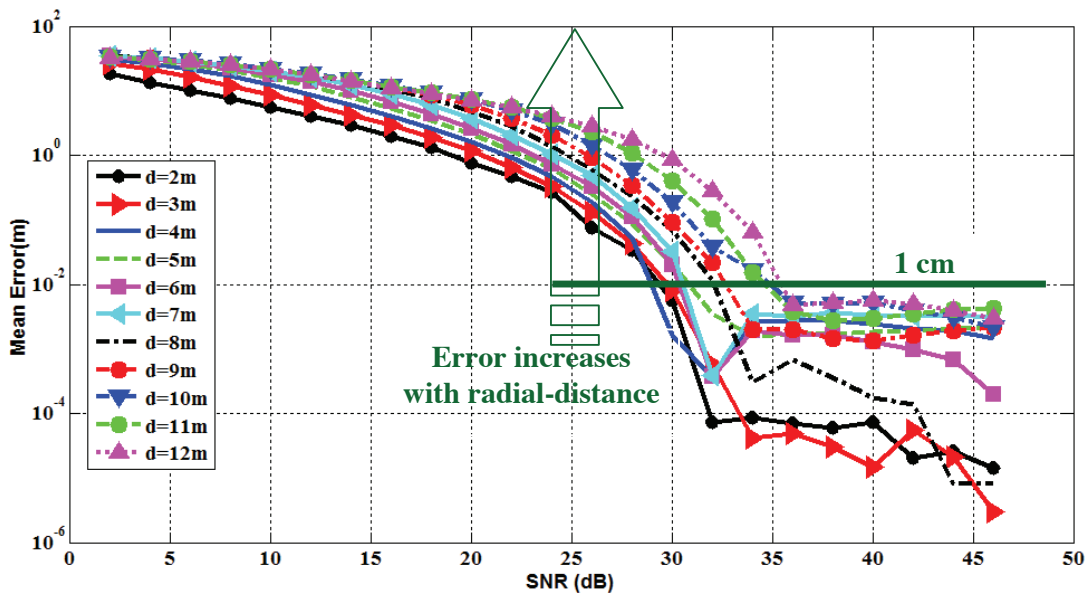


Fig 4.24: RMS-Error in radial-distance estimates vs. SNR.

The SNR is represented on the x-axis in linear scale whereas the y-axis shows the errors in logarithmic scale. The errors in estimated radial-distance between 2 m and 12 m are less than 1 cm for SNR > 35 dB. For 2 m radial distance, the error is found to be more than 1 cm for SNR < 28.5 dB. The error increases with the radial distance for a give SNR value. For lower values of SNR (<20 dB), the errors are typically higher than 1 m between 2 m and 12 m radial-distances. This shows that the DMTD method does not perform well in the presence of low SNR. However, the same method provide less error (< 1cm) for high SNR (> 30dB).

Until now, the performance of the ILS prototype is tested for Line-of-Sight case in a real indoor environment. Additionally, the prototype is also tested in the presence of scatterer in LoS case so that the multipath effects would be demonstrated.

4.3.4 Performance in Presence of strong Scatter (Multipath Effects)

This section presents the comparative performance analysis with and without the presence of a strong scatter (metallic) close to the LBS. A general description about the field measurement setup is presented in Fig 4.25 and the actual system setup is shown in Fig 4.26.

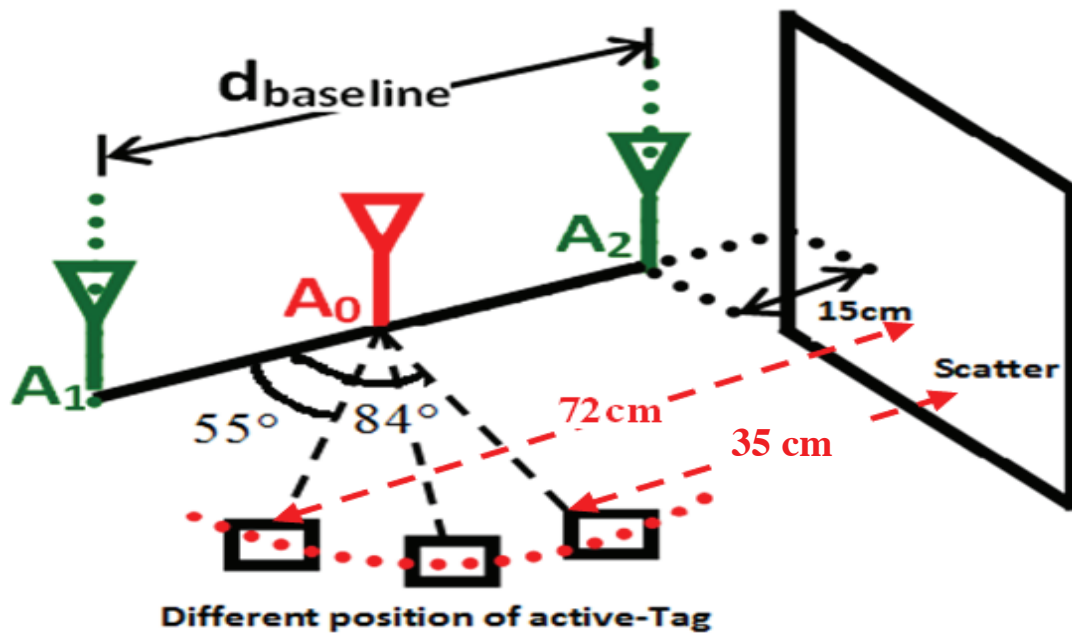


Fig 4.25: Setup for field measurement, a whiteboard used for strong scatter.

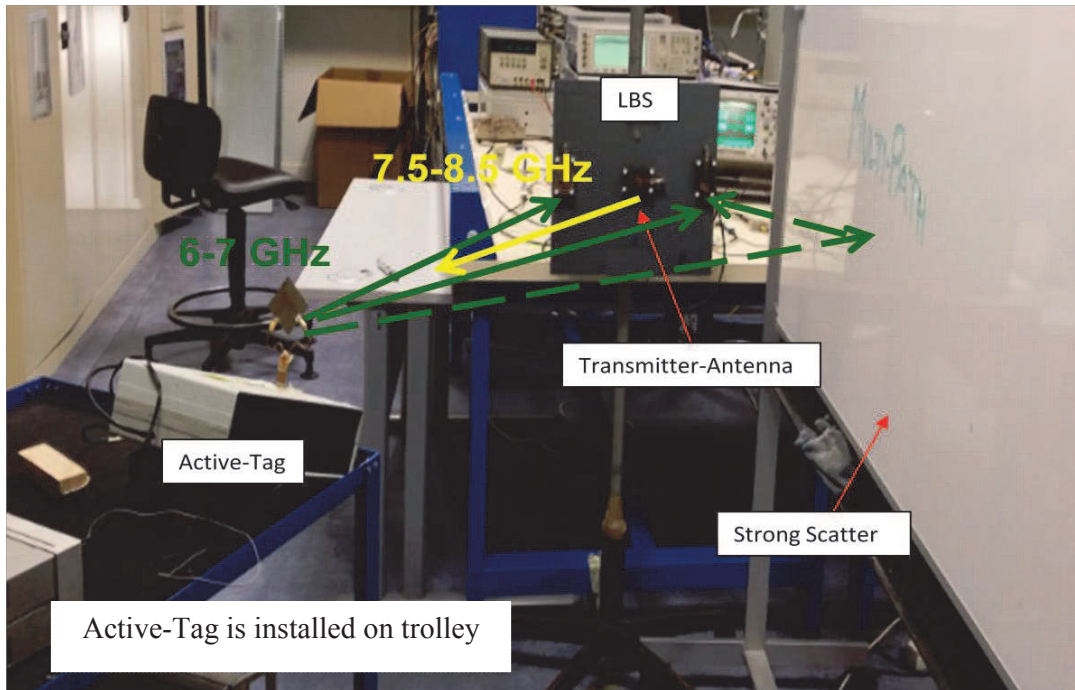


Fig 4.26: System set up in indoor environment.

The estimations are performed for five different positions of Active-Tag, $(1\text{m}, 84^\circ)$, $(0.99\text{m}, 78^\circ)$, $(0.96\text{m}, 68^\circ)$, $(0.99\text{m}, 61^\circ)$ and $(1.02\text{m}, 55^\circ)$. A small deviation in radial-distance around 1 m is due to the placement of heavy trolley as it was difficult to place every time at the same radial distance from the LBS.

For each actual position, the measurements have been done in two steps: in first step, the estimations of positions are done without the presence of scatter and then, in second step, the scatter is kept at 15cm from the LBS-antenna (A_2) as shown in Fig 4.25-4.26 while the active-Tag remains at the same position. These two steps have been repeated for all five different positions. Here, the scatterer is a white-board of dimension 1.5mx1.2m which has metallic surface and is usually coated with polyester [6] as marked in Fig 4.26.

Five measurement-samples (estimated values) have been taken for each position. The estimated positions are shown in Fig 4.27. The x-axis represents the estimated angle of arrival (azimuth) whereas the radial-distance is represented by the y-axis, respectively. Each position of the active-Tag is represented with a specific colour- red, blue, green, magenta, and black for five positions. The bold circle marker represents the actual positions whereas the triangle and the square marker present the estimated positions with and without the scatterer.

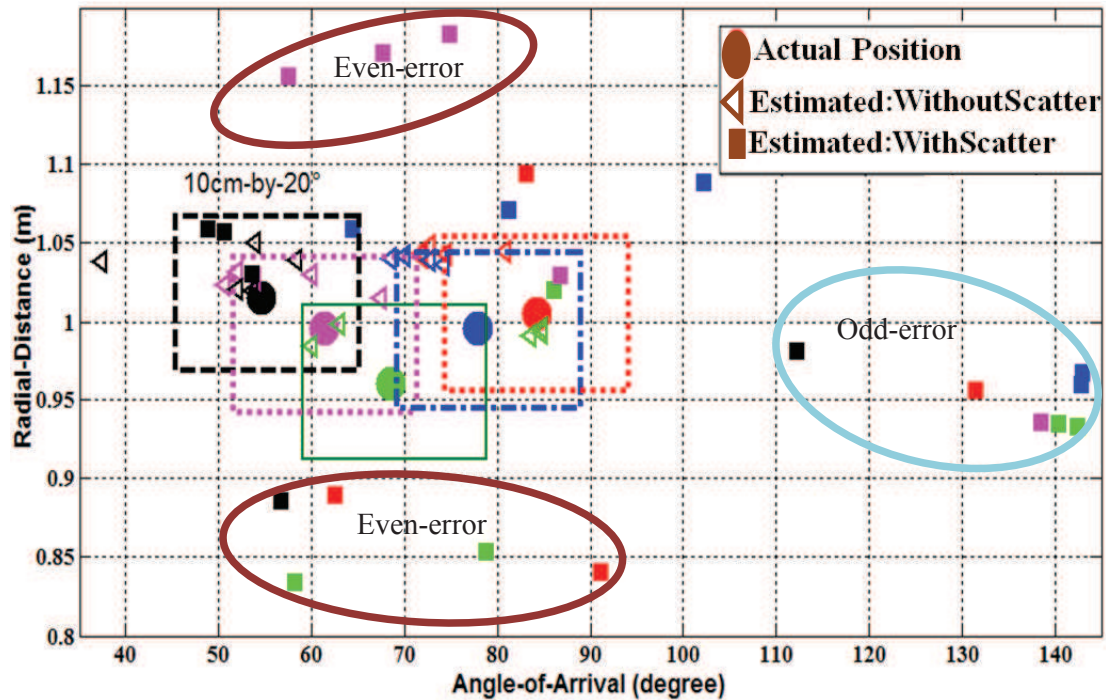


Fig 4.27: Estimated positions with/without the strong scatterer.

In order to understand the influence of scatterer, a window of 10 cm-by-20° size centred at actual position is considered for determining the estimated position as good one if it resides within the window or it is not. The window size is considered about two times of the maximum-values (4.2 cm and 14°) estimated in 2D measurements for better understanding the influence of scatterer.

The numbers of good estimated positions/measurement-samples within the window are tabulated in **Table 4.4**.

Table 4.4
WINDOW: ESTIMATED SAMPLES IN 20°-BY-10CM

STEP	RED-84°	BLUE-78°	GREEN- 68°	MAGENTA-61°	BLACK-56°
WITHOUT SCATTER (TRIANGULAR MARKER)	2	3	2	3	4
WITH SCATTER (SQUARE MARKER)	0	0	0	0	3

When the Active-Tag is positioned at (1m, 84.3°) then it has two good estimations within the window in the absence of scatterer whereas none estimation is observed in the

presence of scatterer. Likewise, the other positions (0.99m, 77.9°), (0.96m, 68.5), and (0.99m, 61.3°) have 3, 2 and 3 as good estimated/measured-samples in the absence of scatterer, but at these positions, none of the estimated values are appeared within window in the presence of scatterer. This shows the influence of scatterer on the estimated values. However, the (1.02m, 55.6°) position has 4 and 3 good estimated with and without the scatterer and this shows the least influence of scatterer as it is positioned at the farthest position from the AT that is 72 cm as compared to 25 cm for (1m, 84.3°) position, see Fig 4.25. Hence, the number of estimated positions (measured-samples) is more if the Active-Tag is kept far from the scatterer as summarised in Table 4.4. This shows the influence of multipath effects created by the scatterer on the estimated positions, and its influence becomes negligible when the Active-Tag is receded from the scatterer. This confirms the presence of strong multipath effects created by the scatterer on the ILS performance.

Also, some of the estimates have good values either in radial-distance or in angle, but not both as marked by the ‘even-error’ and the ‘odd-error’ circles in Fig 4.27.

Even-error: This error has relatively better estimations in angle compared to the radial-distance estimates. This implies that the error is more likely in the radial-distance estimates rather than the angle estimates and this is only possible if same error (of same sign i.e., either negative or positive) occurs in the estimated radial-distance. As it was explained in the Chapter 2, the radial-distance is obtained by taking the average value of the distances estimated by the two receiver sections whereas the angle is estimated from their difference as path-difference, Section 2.4. This can be explained with an example, suppose the radial-distances estimated by the two receiver sections are ‘d₁+e₁’ and ‘d₂+e₂’, where e₁ and e₂ are absolute errors in respective estimates. Based on the relationship 2.22-2.24, the radial-distance and the path-difference are expressed as

$$\begin{aligned} \text{Radial_dist} &= \frac{|d_1 + e_1| + |d_2 + e_2|}{2} = \frac{|d_1 + d_2|}{2} + \frac{|e_1 + e_2|}{2} \\ \text{Path_dif} &= |d_1 + e_1| - |d_2 + e_2| = |d_1 - d_2| + |e_1 - e_2| \end{aligned} \quad 4.10$$

Now, if two errors are close to each other then the above expressions become

$$\left. \begin{aligned} \text{Radial_dist} &= \frac{|d_1 + d_2|}{2} + \frac{|e_1 + e_2|}{2} \cong \frac{|d_1 + d_2|}{2} + |e_1| \\ \text{Path_dif} &= |d_1 - d_2| + |e_1 - e_2| \cong |d_1 - d_2| \end{aligned} \right\} \quad \forall \quad |e_1| \approx |e_2| \quad 4.11$$

This expression can be interpreted in context with the observed even-error as the common error which only affects the radial-distance estimations not the angle.

Odd-error: This error has better estimates in range compared to radial-distance which is contrary to the even-error. This can be expressed as

$$\left. \begin{aligned} \text{Radial_dist} &= \frac{|d_1 + d_2|}{2} + \frac{|e_1 + e_2|}{2} \\ \text{Path_dif} &= |d_1 - d_2| + |e_1 - e_2| \end{aligned} \right\} \forall |e_1| \neq |e_2| \quad 4.12$$

If the estimated values contain errors which are not close to each other then this will not lead to cancellation of error in angle estimation. At the same time, the error in radial-distance becomes maximum if e_1 and e_2 become equal which is the case of even-error, otherwise the error will remain less. Hence, the angle estimations are mostly affected by the odd-error because the difference of 1 cm in path-difference has 3° of change in angle estimation as explained in [Section 2.4.4.2](#). Therefore, the angles are more affected than the radial-distance by this type of error.

Even and Odd errors are not observed when the field measurements were conducted without the scatter as marked in [Fig 4.27](#). Such, even and odd errors are only observed in the presence of strong scatterer which shows the influence of multipath effects created by it.

The estimated radial-distances are also plotted in [Fig 4.28](#).

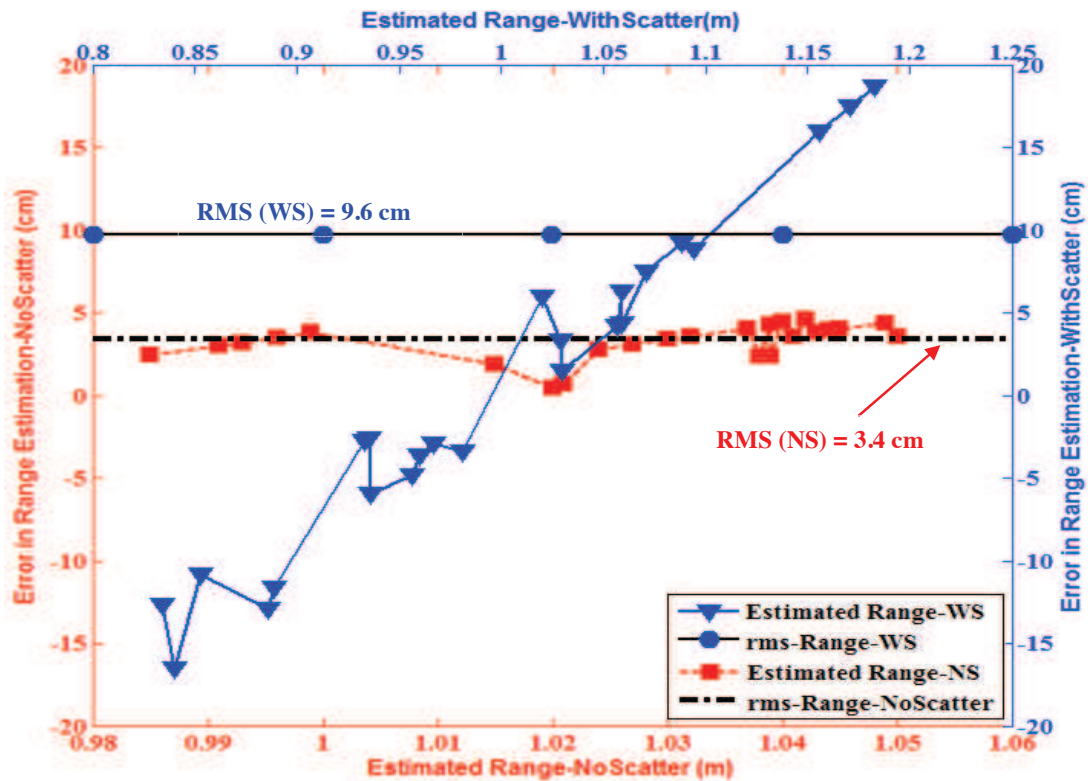


Fig 4.28: Scatterer, estimated radial-distance and its root-mean-square error.

The red-coloured curve represents the estimated radial-distances without the scatter; the bottom x-axis shows the estimated range and the left y-axis represents the error in estimations after comparing with the actual values. The root-mean-square error is 3.4 cm which is marked with the black-dashed line. The observed maximum error is 4.6 cm around 1.04 m (estimated value).

The blue coloured curve shows the case of scatter's presence. The top x-axis shows the estimated range whereas the right y-axis represents the errors in the estimated values. The estimated range is shown as a bold blue curve and its root-mean-square error is 9.6 cm which is shown in black line with blue circle. The observed maximum error is 18.6 cm around 1.05 m (estimated range). The presence of a strong scatterer has influence on the radial-distance estimation. In the absence of scatterer, the performance of ILS is three times better than in the presence of it.

Similarly, the estimated angles (AoA), with and without the scatter, are shown in Fig 4.29 in blue and red colours, respectively.

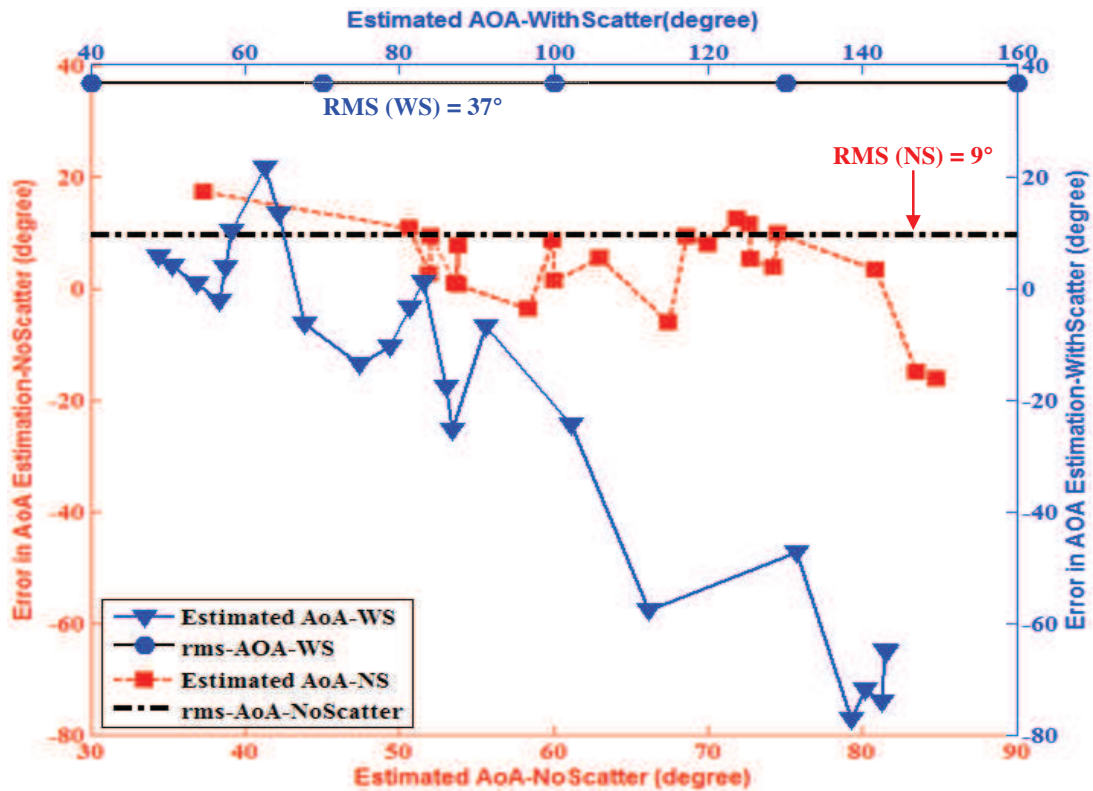


Fig 4.29: Scatterer, estimated AoA and its root-mean-square error.

In the absence of scatterer, the bottom x-axis shows the estimated angles and the left y-axis represents the error in their estimations after comparing with the actual values. The estimated angles are marked with the red colour and its root-mean-square error is 9° which is shown in black-dashed line. The observed maximum error is 17° around 84° & 37° (estimated values) while most of the estimated values are under 10° .

In the presence scatterer, the top x-axis represents the estimated angles, and the right y-axis represents the error in their estimated values. The estimated curve is shown as a bold blue curve in the figure and its root-mean-square error is 37° . The observed maximum error is 77° around 140° (estimated value). The reason for such a deviation from the previous case is due to multipath created by the close scatterer, see Fig 4.26.

More analysis of above condition is performed through simulation in MATLAB. The schematic diagram of the approach is illustrated in Fig 4.30.

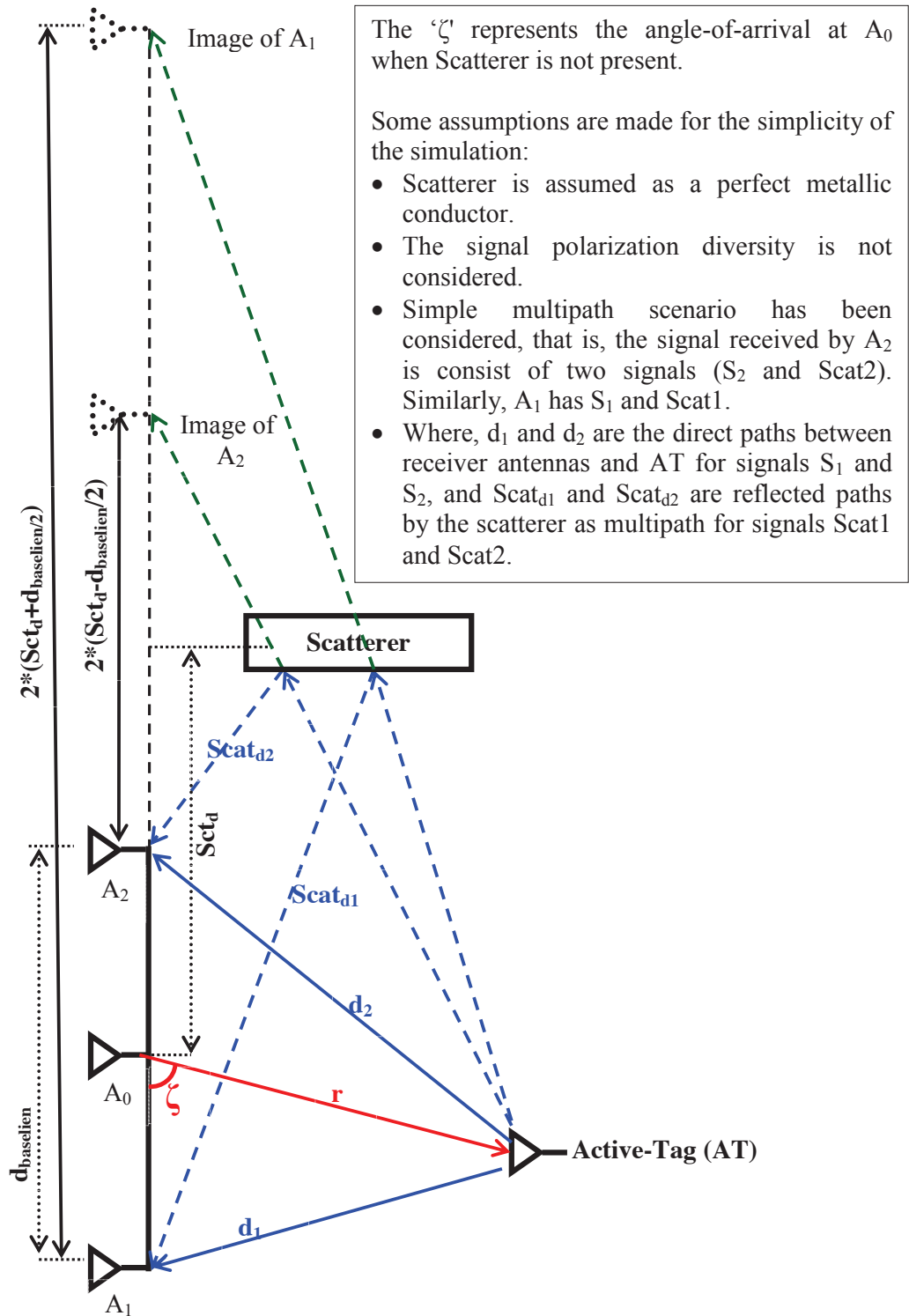


Fig 4.30: Multipaths due to scatterer.

Suppose, a metallic scatterer is positioned at a distance ‘Sct_d’ m from the transmitter antenna A₀. The position of active-antenna is (r, ζ). The simulation has considered two conditions:

1) In the absence of scatterer, and the direct signals (S₁ and S₂) between receiver antennas (A₁ and A₂) and AT will only present and this has been considered as the actual values for the error computations. Therefore, the considered distances (d₁ and d₂) by the signals (S₁ and S₂) are taken as the actual values.

2) The simulation is only performed in the presence of scatterer while considering the multiple signals are received by the receiver antennas (A₁ receives S₁ and S_{cat1} whereas A₂ receives S₂ and S_{cat2}). The signals, S_{cat1} and S_{cat2}, are the reflected from the nearby scatterer to LBS (receivers).

The radial-distance covered by the direct signals (S₁ and S₂) are expressed as

$$\begin{aligned} d_1 &= \sqrt{(0.5 \times d_{baseline} - r \times \cos \zeta)^2 + (r \times \sin \zeta)^2} \\ d_2 &= \sqrt{(0.5 \times d_{baseline} + r \times \cos \zeta)^2 + (r \times \sin \zeta)^2} \end{aligned} \quad 4.13$$

Where, d₁ is the radial-distance covered by the signal S₁, and similarly d₂ is by S₂.

Typically, the multipaths can be assumed as the distance formed by the images of the receiver antennas with respect to the scatterer position as marked with the green arrows. Therefore, the distances covered by the signals (Scat1 and Scat2) are expressed as

$$\begin{aligned} Scat_{d1} &= \sqrt{(2Sct_d + 0.5 \times d_{baseline} + r \times \cos \zeta)^2 + (r \times \sin \zeta)^2} \\ Scat_{d2} &= \sqrt{(2Sct_d - 0.5 \times d_{baseline} + r \times \cos \zeta)^2 + (r \times \sin \zeta)^2} \end{aligned} \quad 4.14$$

Where, Scat_{d1} is the radial-distance covered by the signal Scat1 and similarly Scat_{d2} is by Scat2, and the d_{baseline} is the length of baseline between A₁ and A₂.

These distances (4.13 and 4.14) are used in the simulation which is based on the relationships 4.6-4.9 as explained in Section 4.3.3. The position of the scatterer is varied by the distance ‘Sct_d’. The multipaths are expressed as

$$M(T_m) = \sum_{k=1}^n M_k(t) = \sum_{k=1}^n A_k(d_k) \times \sin\{2\pi \times f_k(d_k) \times t\} \quad 4.15$$

Where, the d_k represents the distance travelled by the k -th signal and the summation of n -signals over $T_m=10$ ms (FMCW modulation-time) is $M(T_m)$. For multipath scenario in presence of the scatterer, we have assumed that the signals received by the antennas (A_1 and A_2) have only two signals that is $n=2$; one from the relationship 4.14 and another from 4.15. While, in the absence of scatterer, only distance from the relationship 4.14 has been considered. The error in radial-distance and angle of arrival estimations in the presence of scatterer are compared with the actual values of the distances (d_1 and d_2) considered during simulation.

The simulation is performed for five different distances of the scatterer (Sct_d , 0.1 m, 0.15 m, 0.3 m, 0.9 m, and 1.2 m) which are plotted in Fig 4.31. The presented results have considered the position of active-tag as (3.5+1 m, 84°); the 3.5 m represents the circuit delay which was computed in Section 4.2.2 and 1 m represents the position of active-tag as marked in Fig 4.24.

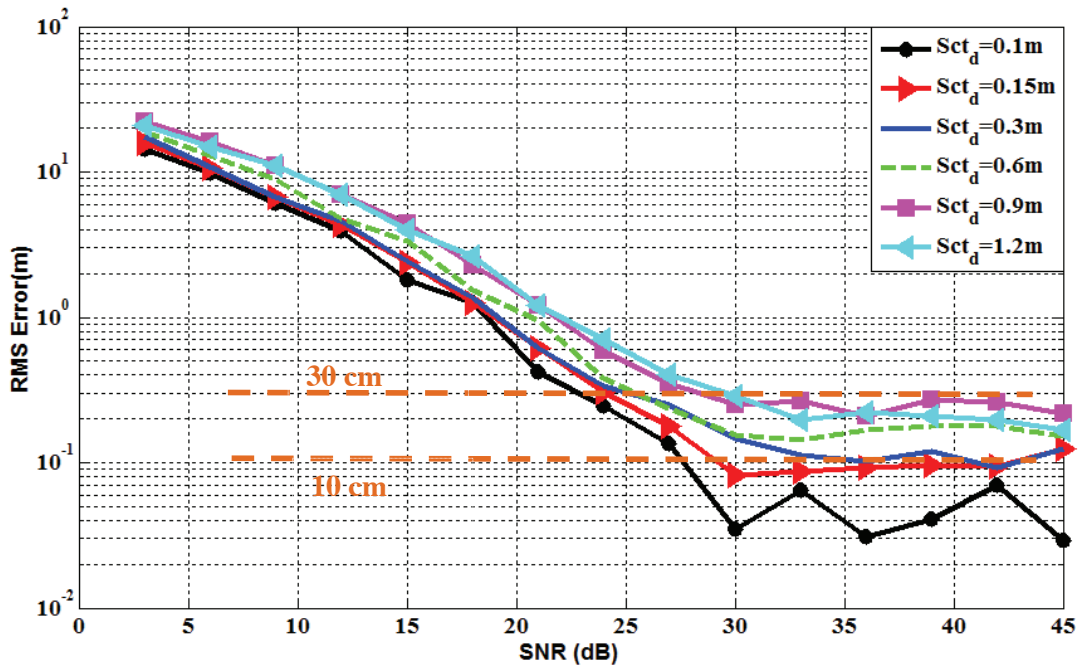


Fig 4.31: Error analysis in radial-distance (multipaths due to scatterer).

The x-axis represents the SNR value whereas the logarithmic y-axis represents the root-mean-square errors. The rms error is less than 30 cm when the scatterer is at 1.2 m (cyan coloured curve) away from the A_0 (Fig 4.31) for $SNR > 30dB$ whereas the rms error is less

than 10 cm (black coloured curve) when the scatterer is at 0.1 m. The rms error in the field-measurement was 10 cm, Fig 4.28 when the active-tag was kept between 35cm and 72 cm. However, the simulated results have rms error between 0.1 m and 0.2 m for scatterer between 0.3 m and 0.6 m. This difference is might be because in simulation the multipath components were always considered whereas in practice this might not be the case. With the increment of distance between the scatterer and the AT, the probability of occurrence of multipath will decrease.

The angle-of-arrival (ζ) is also simulated and the errors in estimated ζ are plotted in Fig 4.32.

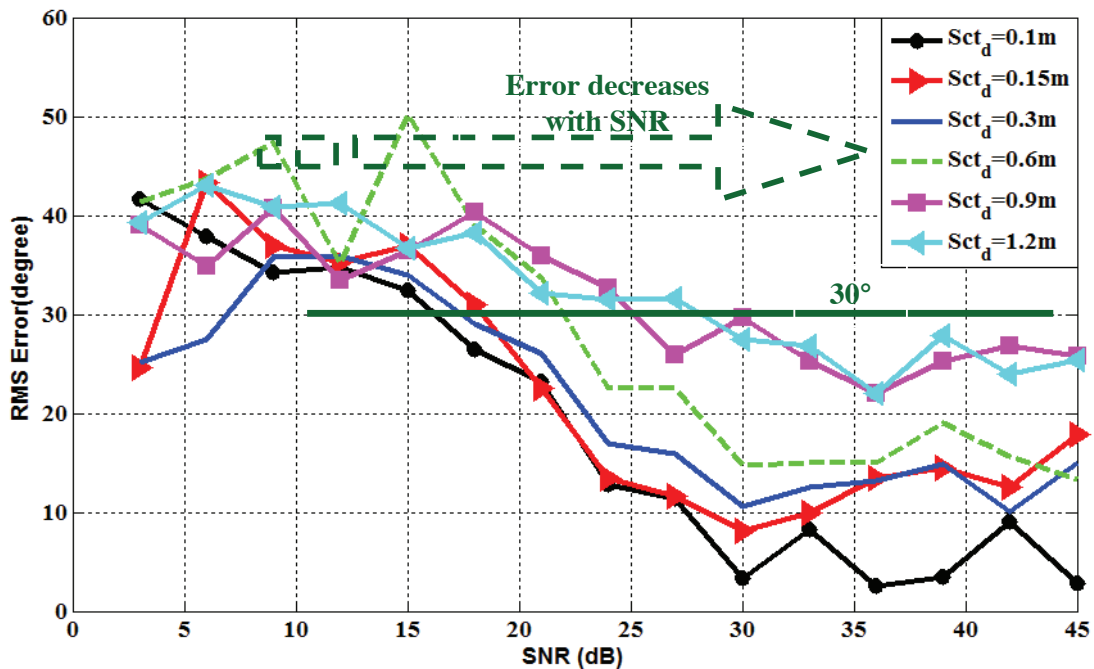


Fig 4.32: Error analysis in angle of arrival (ζ , effect of multipaths due to scatterer).

The SNR and the root-mean-square error is represented on the x-axis and the y-axis in the above figure. The maximum error is 50° at 15 dB SNR when the scatterer (Sct_d) is at 0.6 m from the A_0 . The observed rms error reduces with the increase of SNR, and after 30 dB the rms error is under 30° . The errors are high when the scatterer is at large distance and it decreases when the scatterer is at closer distance. This shows that the scatterer at large distance introduces large error in path-difference because path-difference is difference between radial-distances measured by the receiver antennas (A_1 and A_2). Therefore, the

higher error in the path-difference is derived from the measured values of paths received at A_1 and A_2 , [Section 2.4.1](#). Here, we have not considered the phase change for path-difference computation. However, the path-difference can be assumed as difference between beat frequencies extracted by A_1 and A_2 because frequency is time derivative of phase change.

The simulation has been performed for 1000 times for a given values of SNR and Sct_d . Some simulations were not completed because of the large error at lower SNR. The signal with low SNR (<30 dB) has typically large errors that is more than 1 m, and hence it fails to compute the angle as the path-diff should always remain less than or equal to the $d_{baseline}$. According to the relationship [2.23](#), the angle-of-arrival (ζ) is defined as

$$\zeta = \cos^{-1}\left(\frac{Path_dif}{d_{baseline}}\right) \quad \forall \quad |Path_dif| \leq |d_{baseline}| \quad 4.16$$

Thus, if the error is larger than $d_{baseline}$ then the computation will fail. The numbers of successful computations over varying SNR for different Sct_d are plotted in [Fig 4.33](#).

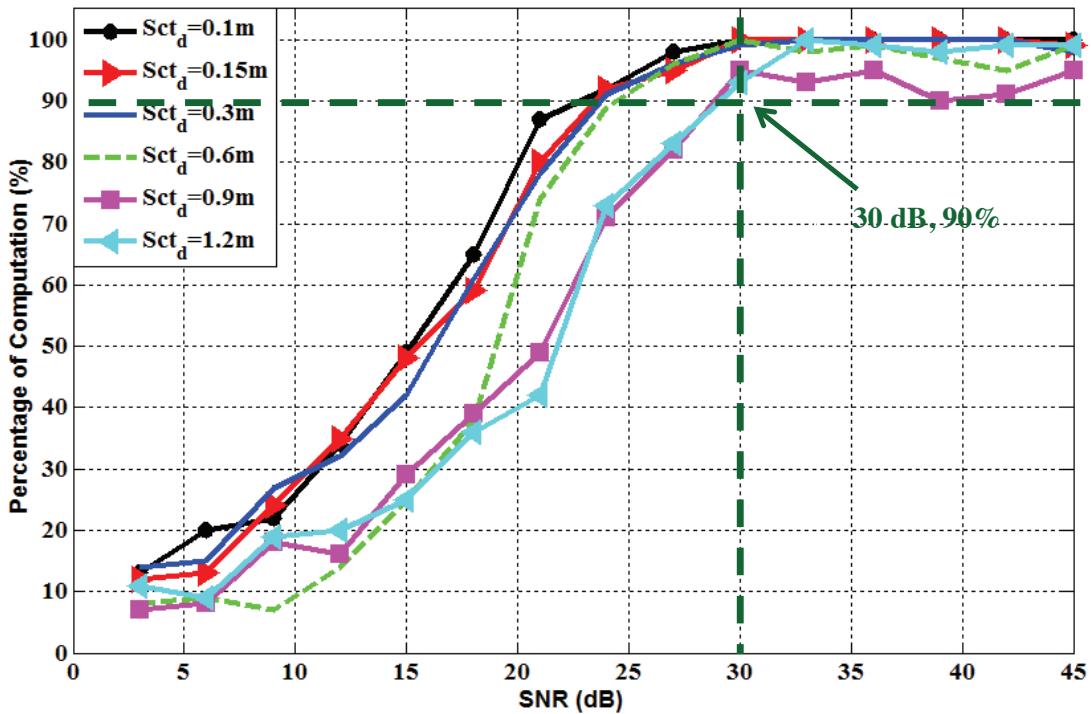


Fig 4.33: SNR versus successful computation.

The successful computations are less than 50% for SNR <15 dB because the signal with lower SNR has more error in radial-distance computation (rms error is > 2 m and 35°, see [Fig](#)

4.31-4.32). With the higher values of the SNR (>30 dB), the computed errors in Fig 4.31 and Fig 4.32 are less than 30 cm and 30° , respectively, and the percentage of successful computation are more than 90% as marked in Fig 4.33.

The performances of ILS prototype are simulated for LoS case and some simulation results are accompanied for which the measurements were not performed such as analysis of SNR during computation. The next section presents the field-measurements performed in the Non-LoS case.

4.4 Performance in Non Line-of-Sight

Non-Line-of-Sight (NLoS) can be defined as the radio transmission line which is partially obstructed by a physical object [5]. Therefore, if direct connection path is not established between transmitter and receiver then we call it NLoS and here by the word “direct connection path” we mean a path without any obstruction. This means the radio transmission mainly established either through the penetration across the obstruction or through the multiple reflections which represent the multipath case. The NLoS is established by keeping the Active-Tag trolley behind the closed-wooden door. Therefore, the radio signal has no direct visual contacts between AT and LBS that is the radio transmission is only established by penetrating the wooden-door. The NLoS setup is depicted in Fig 4.34.

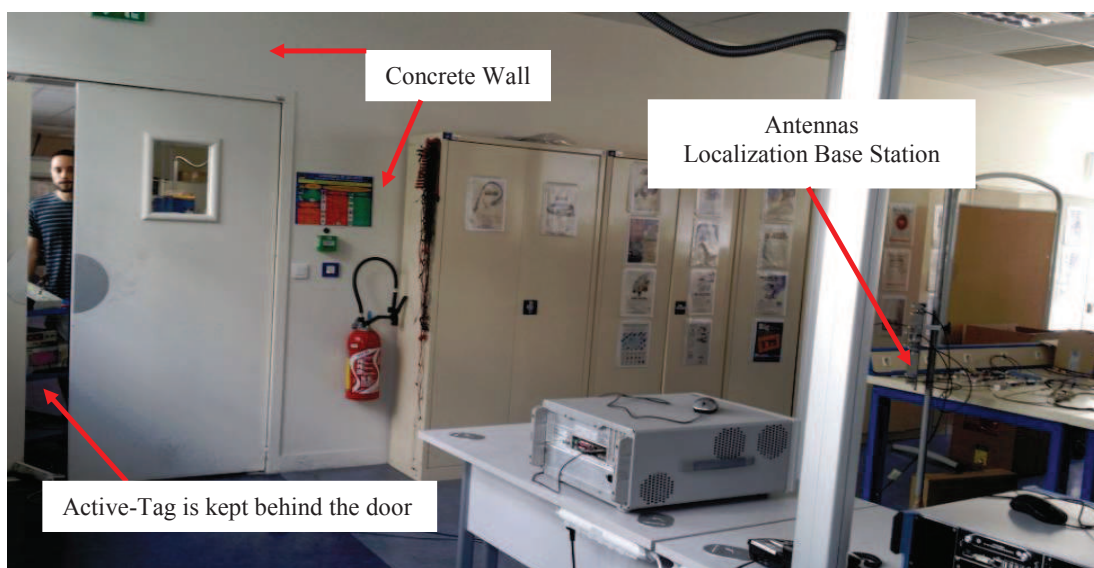


Fig 4.34: Performance in Non-Line-of-Sight case.

The actual radial-distance between the Active-Tag and the LBS is 4.14 m and is not changed throughout the measurement. The radial-distance is estimated for fourteen times by the field-measurements and is plotted in Fig 4.35.

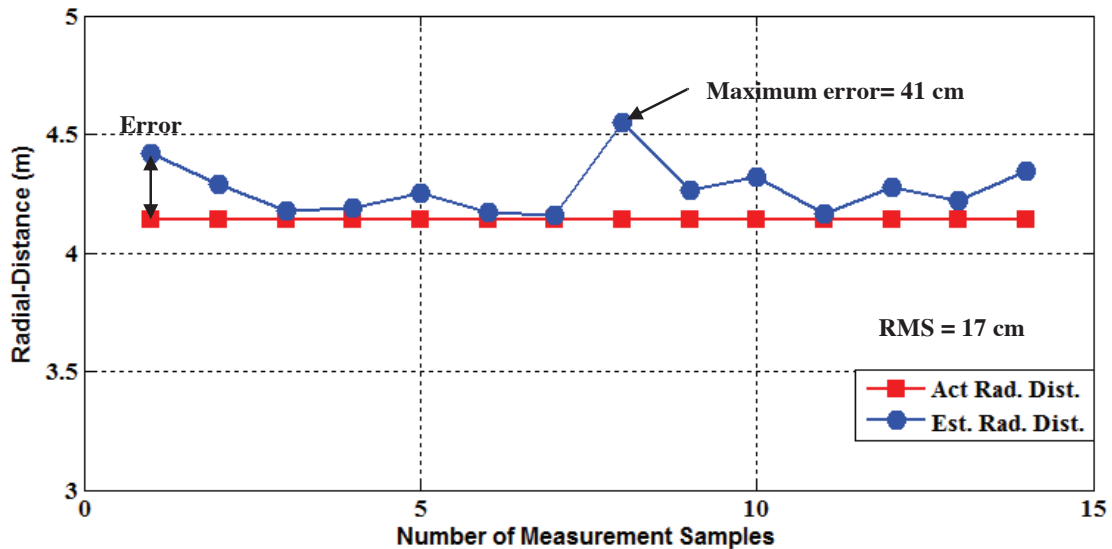


Fig 4.35: Error analysis in NLoS case.

The x-axis represents the number of measurements whereas the y-axis represents the radial-distances. The red line represents the fixed actual radial-distance of Active-Tag and the blue curve represents the estimated values. The difference between these two curves gives the error in radial-distance estimates. The observed rms error is 17 cm and the maximum observed error is 41cm. The most of the estimated values are within the 10 cm which shows the good penetration by the circular polarized radio signals as the Active-Tag was kept behind the wooden closed-door. The estimated radial-distances have positive biased error which represents the larger radial-distance than the actual one because of the extra delay is introduced by the multipath effects [11]. Moreover, the performance of the system would be worst for lower value of SNR (< 15 dB), see Fig 4.31-4.33.

Including this and all previous measurements were done with 1 GHz of bandwidth. In order to understand the impact of the bandwidth on the position estimates are presented in the next section.

4.5 Impact of Bandwidth

To estimate the impact of the frequency bandwidth on the system performance, the position is estimated with the use of two different bandwidths, 1 GHz and 500 MHz. The 500 MHz as testing bandwidth was arbitrary chosen in order to understand the system performance. The measurement is done in a real indoor environment as it was considered in previous all cases. The signal set-ups used for the analysis are mentioned in **Table 4.5**.

Table 4.5
SIGNAL SETUPS

Setup	FMCW Signal	BPF1	BPF2	Bandwidth
1	[6-7]GHz	[6-7]GHz	[7.5-8.5]GHz	1 GHz
2	[6.5-7]GHz	[6.5-7]GHz	[8-8.5]GHz	500 MHz

First, the ILS is calibrated for the above mentioned setups as presented in **Section 4.2.2** for 1 GHz and 500 MHz and the observed corresponding mismatches in delays are tabulated in **Table 4.6**.

Table 4.6
IB: CALIBRATION

Setup	Bandwidth	Mismatch	Tx FMCW Signal
1	1 GHz	1 cm	[6-7]GHz
2	500 MHz	4 cm	[6.5-7]GHz

The field measurements have followed the same basic procedure as mentioned in **Section 4.2**. The estimated positions are compared with the actual values for the performance analysis. Except the bandwidth, all other parameters are kept same as mentioned in **Section 4.2.1**.

Fig 4.36 shows the baseband signals (beat frequencies, without signal processing) acquired for a given position of the active-Tag. The red and blue curves are the signals collected by the data acquisition card with bandwidth equals to 1GHz and 500MHz, respectively.

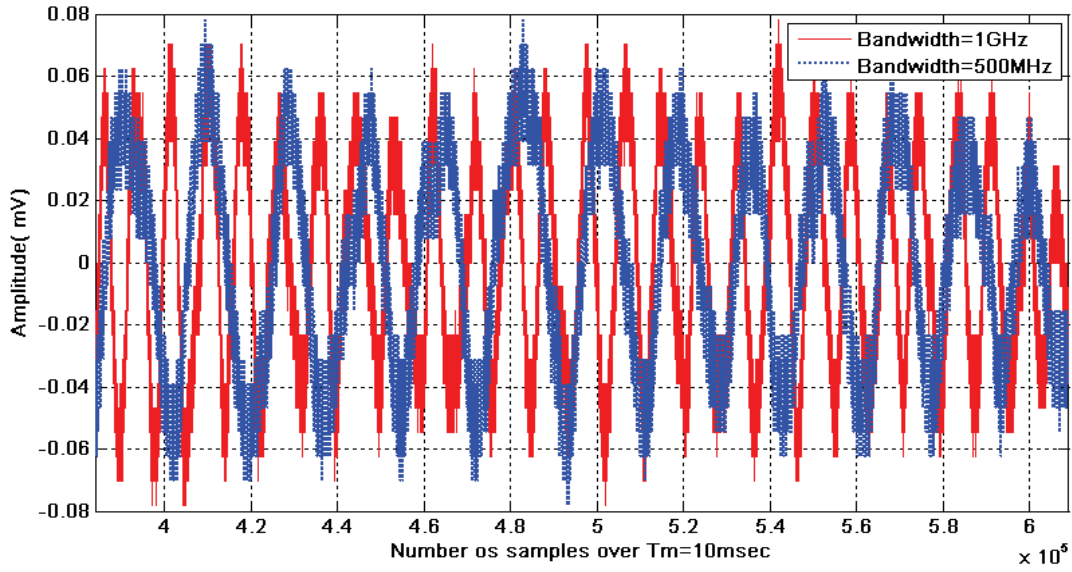


Fig 4.36: Baseband signals acquired by 1 GHz and 500 MHz.

Above figure shows the baseband signals acquired for frequency bandwidths of 1 GHz (red curve) and 500 MHz (blue curve). The numbers of complete cycle of acquired signals for 1GHz and 500 MHz are 27 and 13, respectively. Thus, the position of the remote Active-Tag is estimated with $N=27$ and 13 as explained in [Section 4.2](#). The estimation of position can be made with $N=1$ and its required bandwidth can be derived from the ratio of used bandwidths and their corresponding number of cycles (N). The ratio (bandwidth/ N) remains same and does not vary for a given radial distance which is written as

$$\left. \begin{aligned} \frac{\text{Bandwidth}}{N} &= \frac{1\text{GHz}}{27} = 37\text{MHz}/\text{cycle} \\ \frac{\text{Bandwidth}}{N} &= \frac{500\text{MHz}}{13} = 38\text{MHz}/\text{cycle} \end{aligned} \right\} \text{Constant} = \frac{(37+38)}{2} = 37.5\text{MHz}/\text{cycle} \quad 4.17$$

The ratio for 1 GHz and 500 MHz bandwidths are 37 MHz/Cycle and 38 MHz/Cycle, respectively. The combined value as mean can be considered for better approximation of ratio which is equal to 37.5 MHz/Cycle. Therefore, the minimum bandwidth required by the system for one complete cycle is 37.5 MHz. However, the position estimations from one cycle will not be so reliable if it contains jitter around the zero-crossing. The estimation will be more reliable with more number of complete cycles and this can be attained with the increment of bandwidth. The change in modulation-time (T_m) does not help in obtaining

more number of cycles because the change in T_m only changes the rate of change of frequency as mentioned in 2.3. In fact, the T_m only changes the span of time over which baseband signals (cycles) are obtained.

The estimated radial-distances are plotted in Fig 4.37. The x-axis represents the estimated radial-distances whereas the corresponding errors are represented by the y-axis.

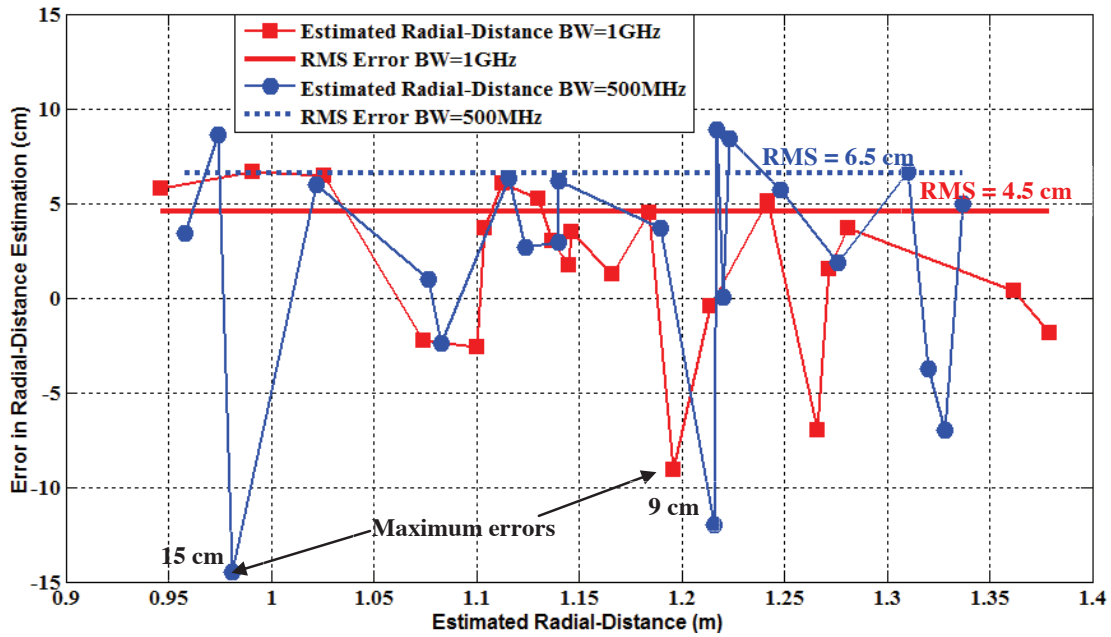


Fig 4.37: Error analysis in radial-distance by 1 GHz and 500 MHz bandwidth.

The estimated radial-distances are plotted in red and blue coloured curves for 1 GHz and 500MHz bandwidth, respectively. The errors are computed by comparison with the actual positions of the remote Active-Tag. The observed root-mean-square (*rms*) errors are shown in red and blue-dash lines which are equal to 4.5 cm and 6.5 cm, respectively. The estimations are better with 1GHz bandwidth compared to 500 MHz. Although, the rms values for the two bandwidths are closed to each other and are differed by 2 cm, only. Additionally, the maximum observed errors are 9 cm and 15 cm by 1 GHz and 500 MHz. The maximum error is higher in the reduced bandwidth.

The estimated angles of arrivals (AoA) are also plotted in Fig 4.38. The measurement is conducted over a sector of 60° that is from 30° to 90° . The estimated AoA is represented by the x-axis and its corresponding error is shown by the y-axis.

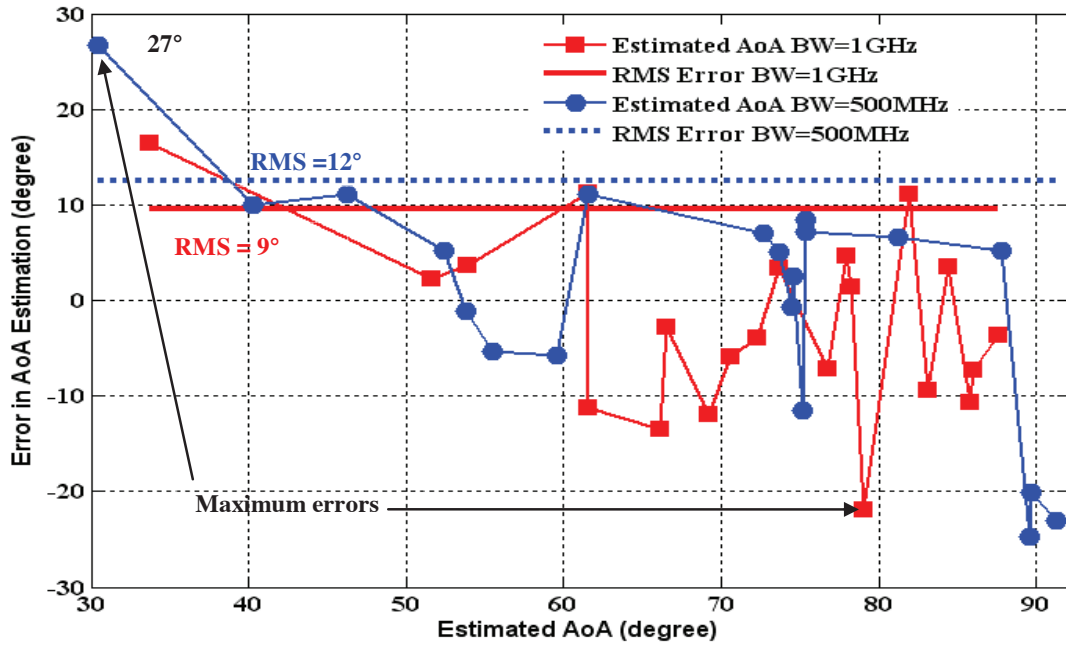


Fig 4.38: Error analysis in estimated AoA by 1 GHz and 500 MHz bandwidth.

The red and the blue curves show the estimated angles for 1 GHz and 500 MHz bandwidths. The observed *rms* errors are 9° (red colour) and 12° (blue colour). Only a difference of 3° in the rms error is observed. The maximum error in AoA is observed for 1 GHz bandwidth which is 22° compared to 27° for the 500 MHz bandwidth.

Table 4.7 summarizes the different parameters observed errors: Absolute Mean (Abs. Mean), Mean, Root-Mean-Square (*rms*), and Maximum-error (Max. Error).

Table 4.7
ESTIMATED ERRORS

Parameter (error)	Bandwidth=1GHz		Bandwidth=500MHz	
	Range(cm)	AOA (degree)	Range(cm)	AOA (degree)
Abs. Mean	3.9	8	5.5	10
Mean	1.6	-2.5	1.8	1
<i>rms</i>	4.5	9	6.5	12
Max. error	9	22	15	27

From the above table, the mean errors become 1.6 cm and 1.8 cm for the two studied frequency bandwidths whereas the mean angle errors are -2.5° and 0.7° . The values from **Table 4.7** can be compared with the results obtained by [4]. The observed mean values for range are quite close to each other and these values are almost ten times lesser than the values reported in [4].

These results also show that the use of 500 MHz (half of the 1 GHz bandwidth) does cause the increase in rms error by a factor of two. It means that the minimum derived bandwidth (37.5 MHz) can be used for the estimations in ideal state that is baseband should be free from noise and should have at least one complete cycle. But as the ratio is close to 26 (1GHz/37.5MHz) the degradation may be too high and it might be practically impossible to obtain any position estimate.

Hence, the reduced bandwidth (compared to 1GHz) can be used for the localization purpose using the developed indoor localization system and its method.

Till now, the designed ILS has been tested under various conditions in a real indoor environment. However, the designed system has some constraints such as Plane Wave Condition as mentioned in **Chapter 2**; those constraints are presented through some measurements in the following section.

4.6 ILS Constraints

The various constraints such as Plane Wave Condition (PWC) are discussed in this section. Along with the PWC, the physical dimensions of the antennas are also investigated for the Near-Field Approximation on the performance of ILS in context with AoA computation. The theoretical concepts mentioned in **Section 2.4.4** of **Chapter 2** are validated with the field-measurements.

4.6.1 Plane Wave Condition

As presented in **Chapter 2**, the Active-Tag acts as a source and the antennas A_{1-2} at LBS represent the points of reception where the condition of plane wave condition between two incoming signals must be satisfied, or a level of tolerance must be defined (in the form of deviation ($\delta\alpha$) in angle of arrival as shown in **Fig 2.5-2.11**) to assume that the incoming signals are PWC.

From **Chapter 2**, the deviation in angle is given by the relationship **2.39**

$$\delta\alpha = \frac{\delta\alpha' + \delta\alpha''}{2} = \frac{1}{2} \left(\tan^{-1} \frac{\tan \alpha}{1 - \left(\frac{1}{B_f} \cos \alpha \right)} - \tan^{-1} \frac{\tan \alpha}{1 + \left(\frac{1}{B_f} \cos \alpha \right)} \right) \quad 4.18$$

Where, B_f is the Baseline Factor (B_f), defined as the ratio of radial-distance from A_0 to the half of the baseline (d_{baseline}) length. The plane wave condition can be approximated for a small value of $\delta\alpha$. This can be achieved by increasing the radial-distance and/or decreasing d_{baseline} . Therefore, the analysis covers the effects of how different values of B_f and d_{baseline} are related to the plane wave condition.

The measurements are performed for two setups:

1. By varying the d_{baseline} for the fixed position (radial-distance and angle) of Active-Tag.
2. By varying the d_{baseline} as well as the angular position (angle) of the active-Tag.

Setup-1: Analysis of deviation by varying the d_{baseline} for the fixed position (radial-distance and angle) of the Active-Tag.

The schematic diagram for the first set-up is shown in **Fig 4.39**. The position of the active-Tag is kept at a fixed position with respect to the transmit-antenna (A_0) of the LBS while receiver antennas (A_1 & A_2) are kept at different positions (M_{1-A1} , M_{2-A1} ... M_{n-A1}). The position of A_0 is always kept at the mid-point of baseline between A_1 & A_2 . Hence, for various baselines we have different values of B_f . As defined by the relationship **2.36**, B_f can be increased by decreasing d_{baseline} for a given value of radial-distance.

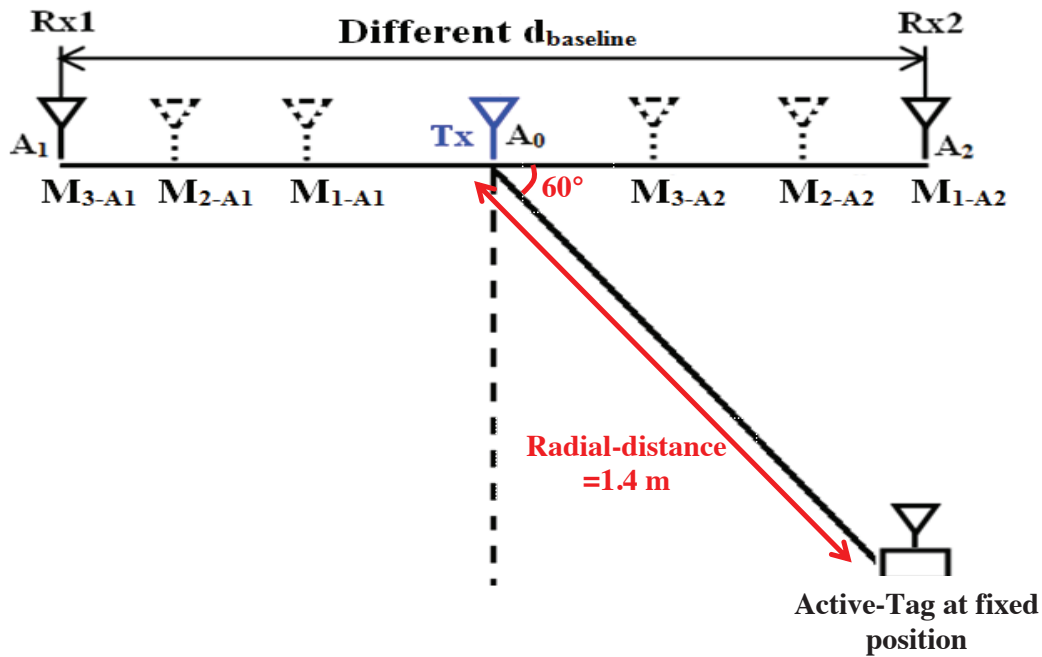


Fig 4.39: Set-up for angle of deviation estimation for a fixed position of active-Tag to varying d_{baseline} .

In this case, relationship 4.18 has been used for the computation of $\delta\alpha$. Here, tag's position is arbitrarily kept at a radial-distance of 1.38 m and at an angle 60° with respect to A_0 . The baseline is varied from 10 cm to 80 cm with a step of 5cm. The simulated (blue-curve) and measured (red circle-curve) results are shown in Fig 4.40. The x-axis represents the baseline-factor where as the y-axis represents the deviation in two incoming signals from the parallel condition.

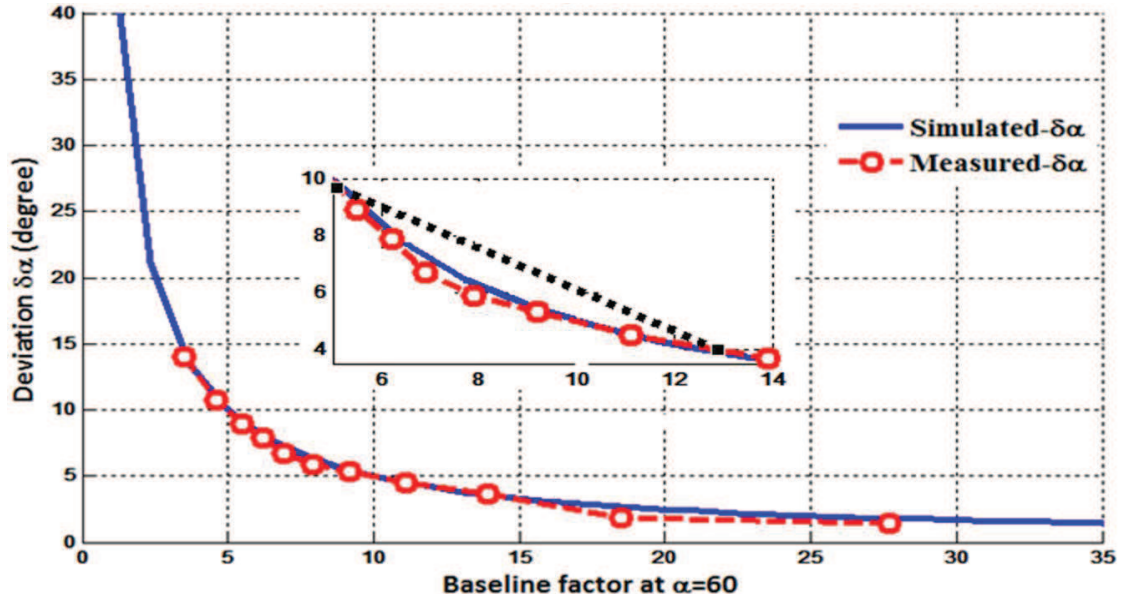


Fig 4.40: PWC-Estimation of deviation for Setup-1.

The estimated deviations are 1° and 13° for B_f between 28 and 3.5 while the relationship 4.18 gives 2° and 14° , respectively. The measured results are close to the simulated results showing a good agreement with the theoretical concept. The small differences between the simulated and the measured results could be due to the manual set-up of the baseline antennas (A_0 , A_1 & A_2). During measurements the minimum value of B_f is considered as 3.5 which was limited by the antenna's dimension and 28 (due to the maximum length of experimental cable) was the maximum considered. This assumes the angle of deviation for a fixed position of the Active-Tag, but in real condition AT will not remain at fixed position and its position will be random in terms of angle and radial-distance. Therefore, the random position of the Active-Tag with respect to A_0 is presented next.

Setup-2: Analysis of different baselines by varying the $d_{baseline}$ as well as the angular position (angle) of the Active-Tag.

The schematic diagram for the second set-up is shown in Fig 4.41. The field-measurement is performed similar to Setup-1, except the position of Active-Tag is not considered at a fixed angle as it was previously. The measurements for deviations in angles ($\delta\alpha$) are taken for four different values of $d_{baseline}$ (20 cm, 30 cm 40 cm and 50 cm) and angles over a sector of 45° from 45° to 90° (Quadrant I) while considering the actual radial-distances randomly between 1.2 m and 1.7 m. The radial-distance is not same because the active-Tag is

installed on a heavy-trolley and it was difficult to place the trolley each time at the same radial-distance from A_0 .

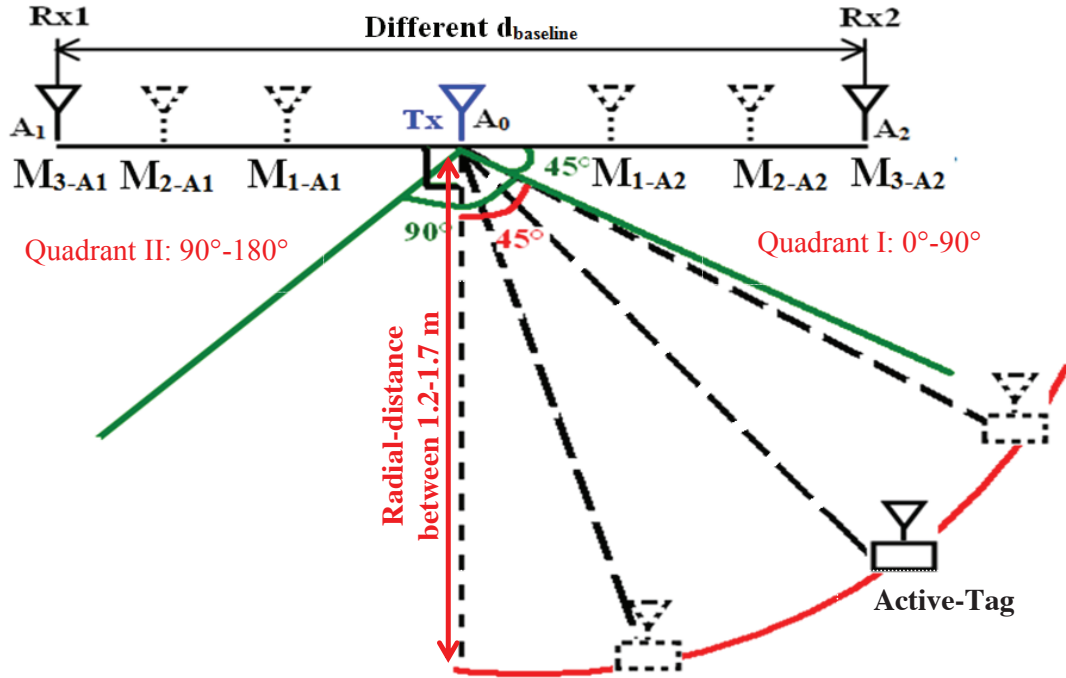


Fig 4.41: PWC-Schematic diagram for the estimation of deviation in AoA at $\alpha=60^\circ$ over 45° -to- 90° while varying the baseline.

The estimated radial-distances are plotted in Fig 4.42. The x-axis represents the estimated radial-distances whereas the errors are represented by the y-axis. The estimated radial-distances are plotted in magenta, green, blue and red curves for 20 cm, 30 cm 40 cm and 50 cm baselines, respectively.

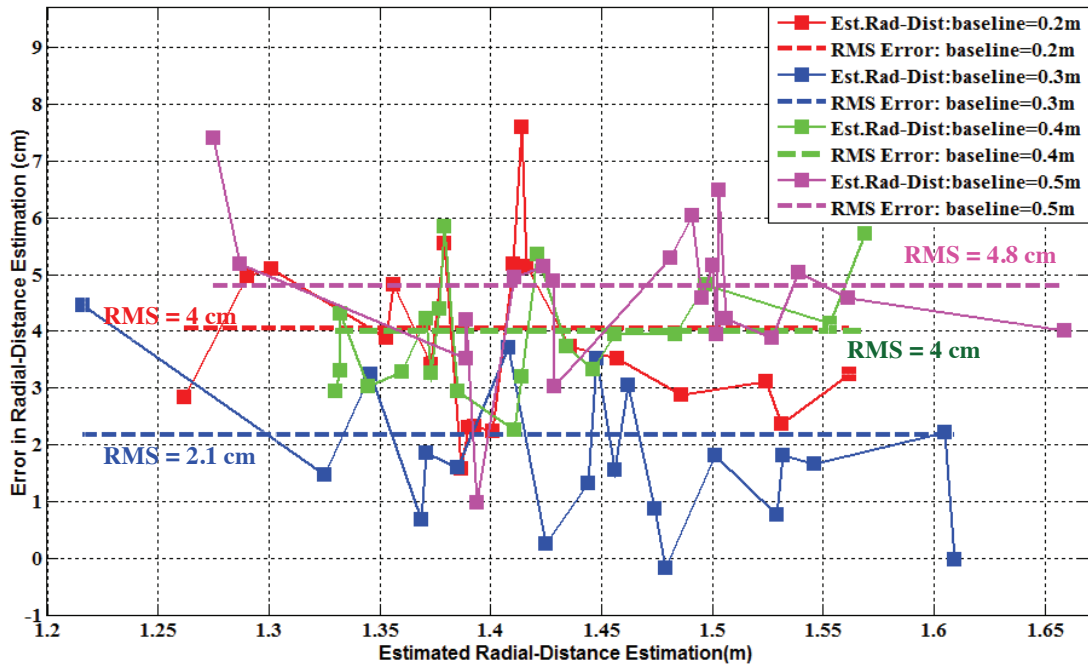


Fig 4.42: PWC-Estimated radial-distance with different baselines.

The root-mean-square (RMS) errors of the estimated radial-distances are 4 cm, 2.1 cm, 4 cm and 4.8 cm for baselines, 20 cm, 30 cm, 40 cm and 50 cm, respectively. The rms values are of about 4 cm except for 30 cm baseline which has minimum RMS error among all. The maximum error among all estimated radial-distances is observed by 20 cm baseline which is equal to 7.7 cm.

Next, the estimated angles of arrivals for all different baselines are plotted in Fig 4.43. The estimated AoA is represented by the x-axis and its corresponding error is shown by the y-axis.

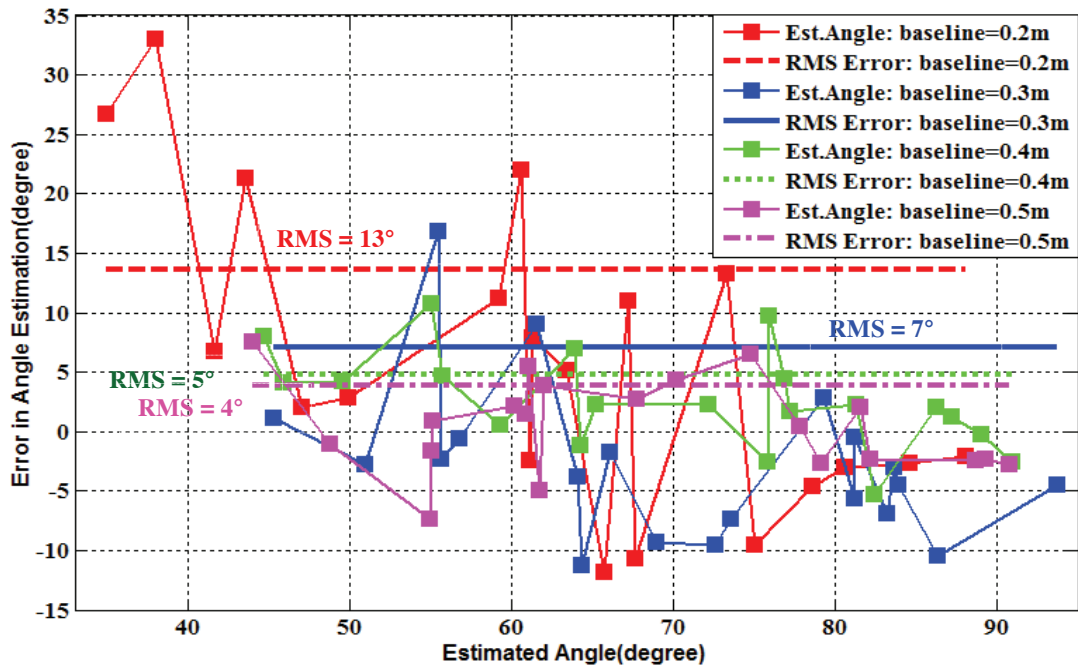


Fig 4.43: PWC-Estimated angle of arrival with different baselines.

The root-mean-square errors of the estimated angles are 13° , 7° , 5° and 4° for baseline equals to 20 cm, 30 cm, 40 cm and 50 cm, respectively. The rms values are decreasing with the use of larger baselines as larger baseline helps in better mapping of path-difference, between two parallel signals, into angle compared to smaller one. Here too, the maximum error in angle is observed for the 0.2m baseline and is equal to 34° . In order to understand the effect of Plane Wave Condition on angle estimates, the deviation ($\delta\alpha$) in angle from the PWC are plotted in Fig 4.44. The x-axis represents the angle of arrival (α) and the y-axis represents the angle of deviation ($\delta\alpha$) from the parallel wave condition. The deviations are plotted from the measurements (obtained from the designed ILS) and the simulated (obtained from the relationship 4.18).

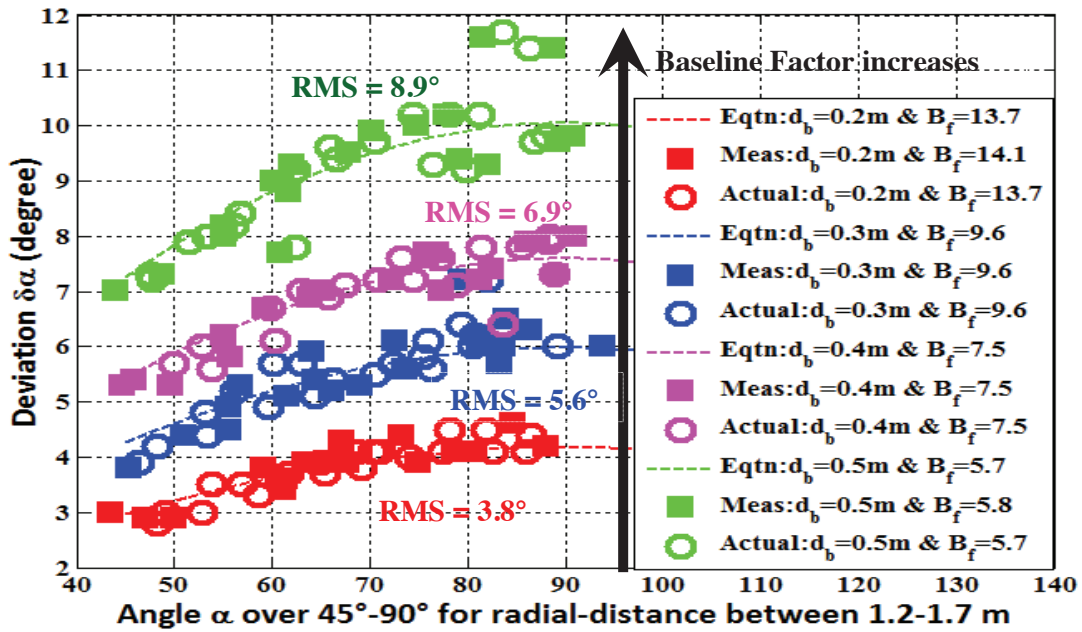


Fig 4.44: Comparison of $\delta\alpha$ between 45° and 90° for radial-distance between 1.2 m & 1.7 m.

The actual deviations are marked by the circular-marker whereas the measured values are marked by square. The dotted curve line (legend-Eqtn) shows the values obtained from the relationship 4.18 and 2.36 for different B_f . The measured values are compared with the actual ones for comparative analysis. It is quite clear from Fig 4.44 that for given values of B_f the deviation increases as angle moves towards 90° and has maximum deviation at the orthogonal position (90°) with respect to the baseline. This behaviour can be asserted in support of the tangential nature of the deviation based on relationship 4.18. The deviation ($\delta\alpha$) increases with the increment in baseline for the same value of radial-distance. The large value of B_f gives the small deviation as 20 cm baseline has relatively small deviation compared to 50 cm baseline which is arguably same as mentioned during the theoretical evolution in Chapter 2.

The root-mean-square values of the deviation for measured and actual values between 45° and 90° are tabulated in Table 4.8.

Table 4.8
PWC DEVIATION: ROOT-MEAN-SQUARE VALUES

Baseline(m)	Actual values			Measured values		
	Bf	Range(m)	$\delta\alpha(\text{degree})$	Bf	Range(m)	$\delta\alpha(\text{degree})$
0.20	13.7	1.37	3.8°	14.1	1.41	3.8°
0.30	9.6	1.43	5.5°	9.6	1.44	5.6°
0.40	7.5	1.50	7.1°	7.7	1.54	6.9°
0.50	5.7	1.41	9.2°	5.8	1.46	8.9°

Although, the smaller baseline has small deviation compared to larger ones but use of smaller baseline will produce more error in angle of arrival estimates because of mapping of smaller length into angle as explained in [Section 2.4.4.2](#) of [Chapter 2](#). In fact, with these deviations in PWC, the observed RMS errors were 13°, 7°, 5° and 4°, as presented in [Fig 4.44](#) and these show the effect on estimated angles. So it is trade off between the PWC and the angle of arrival estimation through considered length of baseline. On one hand, the smaller baseline is good in accordance with the PWC but it will not give good angle estimates. On the other hand, the larger baseline shows complete opposite behaviour that is the larger baseline will not respect the PWC although it will have better angle estimates.

Besides, the estimated root-mean-square errors (radial-distance as well as angle) and deviations are plotted in [Fig 4.45](#). The blue curve represents the root-mean-square values of estimated angle and the red curve represents the root-mean-square errors of radial-distance. The black curve represents the measured root-mean-square values of angle deviation presented in [Table 4.8](#).

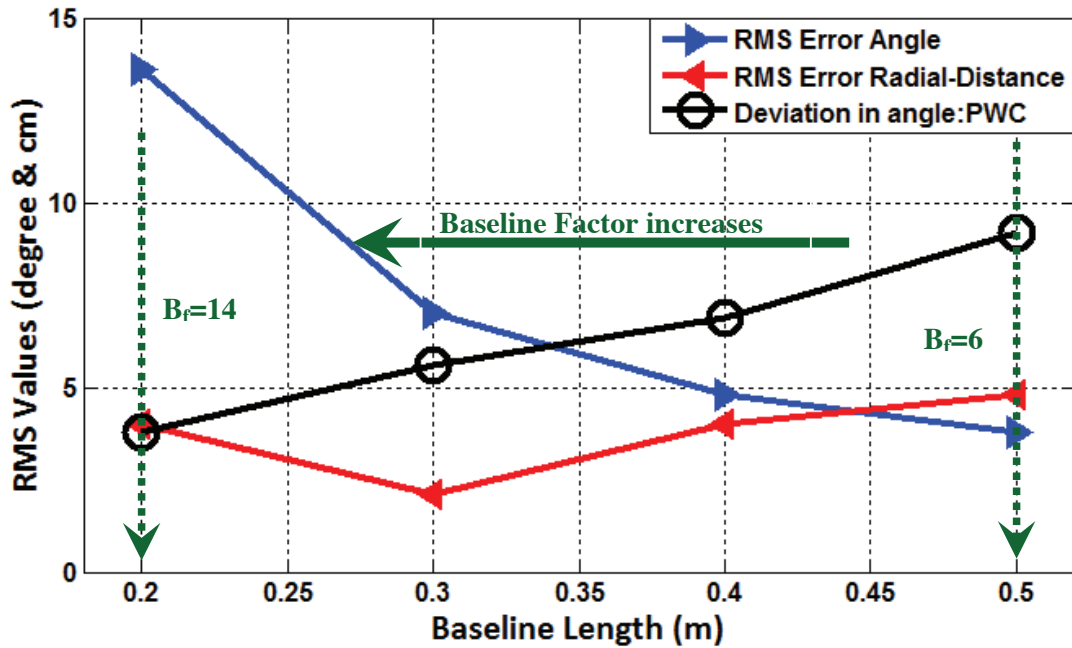


Fig 4.45: Estimated rms values of range, angle and deviation in AoA.

The rms error for radial-distance estimation has almost constant flat curve (red coloured) except for the baseline of length 30 cm. The rms error in angle estimation (blue coloured) have a fall for baseline from 20 cm to 50 cm and further increment in the baseline does not show any significant fall after 40 cm baseline. The measured rms deviation ($\delta\alpha$) has almost linear positive curve with respect to the increment in baseline and this can be explained from the observation made in Fig 4.40. The $\delta\alpha$ -curve in Fig 4.40 between $B_f=6$ and $B_f=14$ can be considered as a linearly increasing curve which is similar to the black curve of Fig 4.45. Although, the smaller baseline has small deviation in angle of arrival but the estimated angle itself has more error because of improper baseline mapping into angle. However, the estimated angle has lower error for larger baseline even the deviation in angles are large and both curves are seemed to converge between 30 cm and 35 cm baselines. In fact, it can be concluded that the 30 cm baseline represents the equilibrium junction between better angles of arrival (rms error 7°) as well as radial-distances (rms error 2 cm) estimates and baseline length for respecting the plane wave condition with deviation equals to 5.5° . Although, the 45 cm baseline, which is 1.5 times greater than 30 cm, has 4° of rms error in angle estimates but the estimated radial-distance has 4 cm rms error, just double in case of 30

cm baseline. Therefore, further increase in baseline has not any significant advantage in angle as well as radial-distance estimates.

4.6.2 Coupling Effects

Coupling between two patches or between two apertures or two wire antennas is a function of the position of one element relative to the other [7]. In general, mutual coupling is primarily attributed to the fields that exist along the air-dielectric medium as outlined in [7]. The work presented by Pozar [8] shows that the measured mutual coupling for E and H planes are $<-25\text{dB}$ and $<-38\text{dB}$ for s/λ equals to 1 where ‘s’ is separation between the two patch elements and ‘ λ ’ is at 1.410 MHz. The mutual coupling further decreases with the separation between two elements. In order to investigate the coupling between two receiver antennas, a part of the received power by A_1 is connected to a spectrum analyzer for power measurement. The schematic diagram for the above mentioned setups is illustrated in Fig 4.46.

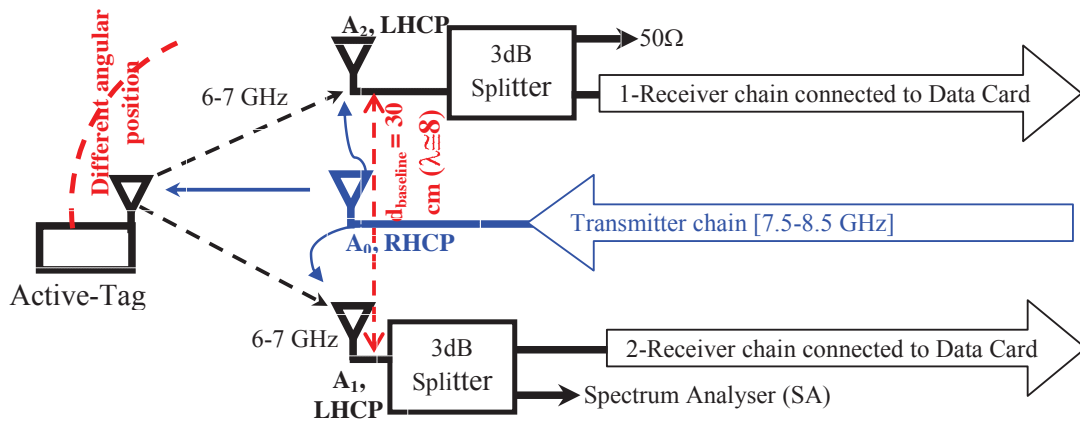


Fig 4.46: Measurement scheme for coupling between receiver antennas (symmetric structure).

Two identical directional couplers (Agilent 87300B, [9]) are connected to the output of receiver antenna A_1 and A_2 to preserve the symmetry. For antenna A_1 , the output of the 3dB coupler is connected to a spectrum analyser (SA) and to the receiver chain. In the case of the coupler of antenna A_2 , the SA is replaced by 50Ω load. For the measurements of received power by A_1 , a RF signal of 6.5 GHz frequency is produced by the signal generator which is then transmitted by the transmitter antenna as per the architecture presented in Section 2.3.

The transmitted signal is retransmitted by the Active-Tag and finally this signal is received by the antenna (A_1) and is measured by spectrum analyser which has noise floor equals to -96 dBm. Active-Tag is kept at different angular positions with respect to the transmitted antenna and the received power is plotted (red curve) in Fig 4.47. The x-axis represents the different angular position of the active-tag with respect to the LBS. The y-axis represents the power level of received RF signal at 6.5 GHz.

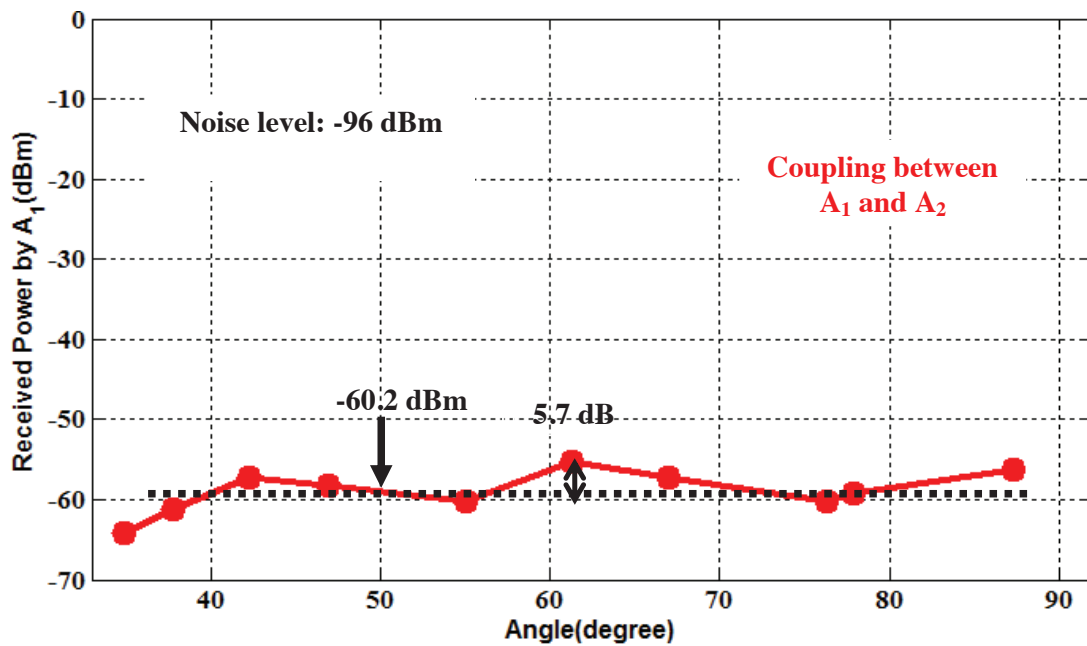


Fig 4.47: Antenna Coupling at LBS

The variation in received power is observed between 90° and 30° . The average received power was -60.2 dBm. The received power does not show any deep fading which might have occurred because of the coupling between antennas. The small variation of 5.7 dB can be accounted because of the indoor environment as well as small variations in radial-distance while placing the Active-Tag. The developed system has used two separate channels for uplink (7.5-8.5 GHz, RHCP) and downlink (6-7 GHz, LHCP) links for circular polarization diversity to minimize the coupling effects. Also, the receiver antennas are separated by more than 8 times of the wavelength at 8.5 GHz. In fact, the received power was equivalent to noise floor (-96 dBm) when the Active-Tag was kept OFF. Therefore, it can be asserted that because of the precautions such as polarization diversity and dedicated channels the

couplings among the LBS antennas are considerably minimized. Hence, the developed ILS architecture helps in reducing the coupling effects among the antennas at LBS.

4.7 Conclusion

In this chapter, the performance of the developed ILS prototype in a real indoor environment is presented. The developed technique is based on the radar interferometry method. The prototype has used single anchor for the 3D position estimates. The performance of the system is rigorously tested under LoS case with different situations such as in presence of Scatterer, impact of baseline, influence of bandwidth, etc. The observed rms errors over 1.15 m distance were less than 4 cm in the radial-distance estimate, and 6° and 4° in angle-of-azimuth and in angle-angle-of-elevation for the 3D localization. The maximum range under LoS condition was also tested so that the scalability of the ILS can be determined. The radial-distance was tested upto 6.7 m in LoS case with 18 cm of rms error. The increase of six times in radial-distance (6.7m/1.15m) coverage only observes four times (18cm /4cm) increment in rms error. The influence of the multipaths on the system performance is demonstrated through the field measurement and the observed rms error was 9.6 cm whereas the 17 cm rms error was observed in NLoS localization. The measurements were also performed with the reduced bandwidth (500 MHz) and the increment of rms error were found less than two times compared to the full bandwidth (1 GHz). These results show the robustness of the designed ILS.

The constraints related to the developed system such as PWC are initially explained through the mathematical expression and then later verified through the field-measurements. Based on the measurement, a most likely acceptable value of the baseline has been estimated which is between 30 cm and 35 cm (d_{baseline}). The estimated parameters (range & angles) demonstrate the reliable performance of system in harsh indoor conditions.

The use of single anchor (LBS) will definitely help in reducing the complexity of the system as well as in lowering the cost of system design dedicated to the indoor localization. The concept of frequency transpose through an Active-Tag has demonstrated a good result in reducing the backscatter signals. Also, the signal processing can be effective one with the use of counter technique along with the use of SMA Algorithm.

The designed ILS based on multistatic FMCW radar systems has a range over 6m and a resolution within 10cm which fits a lot of applications related to indoor localisation.

References

- [1] <http://spectrum-instrumentation.com/en/products/m3i2132>.
- [2] Annexure A
- [3] Annexure B
- [4] Y. Zhang, M. G. Amin, and S. Kaushik, "Localization and Tracking of Passive RFID Tags Based on Direction Estimation," International Journal of Antenna and Propagation Hindwai Publishing Corporation, vol 2007, ID 17426, doi. 10.1155/2007/17426.
- [5] R. H. Lee, C.C Chang, and S.F. Chang. , " A switched-beam FMCW radar for wireless indoor positioning system," European Radar conference, EuRAD, pp. 65-68, 2013.
- [6] http://en.wikipedia.org/wiki/Non-line-of-sight_propagation
- [7] Constantine A. Balanis, "Antenna Theory," Chapter 14, pp. 764.
- [8] D. M. Pozar, "Input Impedance and Mutual coupling of rectangular Microstrip Antennas," IEEE Trans. Antennas Propagat., Vol. AP-30, No, November 1982.
- [9] Annexure F
- [10] <http://www.mathworks.fr/help/comm/ref/awgn.html>
- [11] [A1] S. Marano et. al, "NLOS Identification and Mitigation for Localization Based on UWB Experimental Data", IEEE J. Sel. Areas Commun., Vol. 28, Issue 7, pp. 1026 - 1035, September 2010.

Chapter 5. Conclusions and Perspectives

This chapter is dedicated to the future work related to further optimization of the developed indoor localization system which includes some key issues such as synchronization between Localization Base Station and Active-Tag. First, conclusion of the thesis work is presented. Later, some possible ways of upgrading the ILS are outlined in detailed.

5.1 Conclusions

In this dissertation, the concept of 3D localization of a remote Active-Tag using a single known anchor as a Localization Base station has been presented in details through a working prototype designed for indoor environment. The developed system, Indoor Localization System, is fundamentally based on the principle of monopulse radar system and has utilized the multistatic FMCW Radars for 3D localization. The system architecture and its method have been designed to have 3D position with precision in few centimetres using a single anchor, and the use of ultra wide 1GHz band as system's bandwidth also helps in the achieving higher accuracy. The ILS uses the uniform European 6-8.5 GHz band as two separate uplink and downlink channels, 7.5-8.5 GHz and 6-7 GHz. Furthermore, these channels are used for the circular polarization diversity so that the chances of signal interference with an obstacle would be avoided. In this context, a total six two-dimensional circular polarized antennas are fabricated. Five antennas have been used by the LBS whereas one by the AT. The LBS uses these antennas for forming two planes orthogonal to each other. In fact, the orthogonal antenna structure facilitates the use of single anchor and the especially designed AT antenna implements the circular polarization diversity.

A prototype of the proposed ILS has been built and all field-measurements have been performed with it in a real indoor environment. In line-of-sight, the root-mean-square error in radial-distance estimation is less than 17 cm upto 7 m whereas the angles of arrivals (elevation and azimuth) are less than 10° over a sector of 120° in front of the LBS. Later, the non line of sight was also considered and the observed root mean square was under 20 cm for radial-distance upto 5 m. The field-measurements have been performed under various possible conditions such as under the influence of multipaths. The maximum radial-distance estimated by the prototype is 7m.

Some possible constraints such as Plane Wave Condition are initially evaluated through the mathematical expression, and later it is validated with the measured results. The optimum baseline length has also been proposed which is between 30 cm and 35 cm; the conclusion is given through the field-measurements.

The designed ILS has considered the coherent phase synchronization between the LBS and the AT which needs to be implemented in design. Beside this, some possible works are proposed for further improvement of the designed Indoor Localization System.

5.2 Possible Upgradation and Optimization

5.2.1 Architecture Level: 3D positioning with three antenna structure

The developed ILS has used five antennas at the LBS for 3D position estimates. One of them used as transmitter antenna and the rest are used as receiver antenna. A pair of receiver antenna represents one plane which gives two estimated parameters (radial-distance and angle of arrival). Likewise, another pair also gives the radial-distance and the angle of arrival which is orthogonal to the previous plane. Thus, the two planes in orthogonal position are necessary and compulsory conditions for the computation of position parameters. However, the orthogonal plane condition can be obtained with the use of three antennas as shown in Fig 5.1.

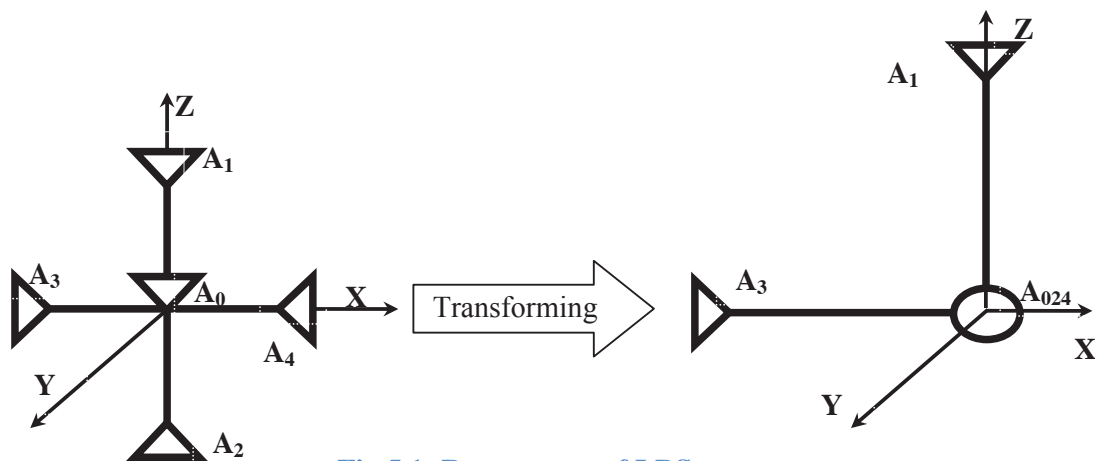


Fig 5.1: Restructure of LBS antennas.

As we know, the signals were interrogated by the four receiver antennas (A_{1-4}) and the transmitter antenna (A_0) was not used for the reception as shown on the right side of the

above figure. However, the two planes can also be formed by the antenna A_3 and A_1 with A_{024} and these two planes remain orthogonal to each other. Where, A_{024} has taken the place of A_0 and it will perform both, transmission and reception, simultaneously. Therefore, the transmitter antenna will be used as duplex communication and this can be achieved by the use of circulator [1] in duplex mode, so that the same antenna can be used for transmitting as well as receiving the signals. However, the circular polarization diversity cannot be achieved with the single port antenna connected to the circulator because one port antenna only supports one sense of circular polarization in a given time and space. But, the transmitter antenna can be replaced by the AT's dual circular polarized antenna which had been used. This will keep the polarization diversity intact with the transformed antenna structure.

The developed ILS has symmetric antenna structure but the proposed modification will no longer hold the symmetric structure. In spite of being unsymmetrical structure, the distance covered by the signal from A_{024} to Active-Tag will remain same for all receivers as it is for the developed ILS. Therefore, it will not affect the developed method much and hence, the proposed modification will lead to a more compact design.

5.2.2 Improvement in Non-Line-of-Sight Condition

The study of various localization systems throws some light on the lack of proper solution in the NLoS condition. The main reason for performance degradation in NLoS arises because of the perturbation of the propagative electromagnetic waves. In other words, a low or zero probability of LoS establishment is the main reason of poor performance. Although increasing the signal bandwidth increases the robustness which implies that ultra wideband (UWB) systems are preferable in indoor environments [2]. However, despite the large bandwidth, NLoS conditions cause positively biased range estimates and inaccurate angle-of-arrival measurements [3].

This issue can only be resolved if the intended area is brought back into the LoS condition. And this can be either done by illuminating the area with the use of more anchors as Anchor-cum-Relay nodes [4] or by exploring dedicated technique such as Fingerprinting method [5] based on the received signal strength indicator (RSSI). An interesting methodology has also been reported by *Arumugam et al* [6-9] that is the use of quasistatic field for the robust wireless connectivity such as magnetoquasistatic field. It will be

interesting to see if my thesis work can be reutilized using magnetoquasistatic fields [7, 9]. I strongly believe if quasistatic field is used, it will give good performance in NLoS condition with a prior knowledge of single anchor. But, the integration of the front-end design with our developed architecture will be a real challenge in this direction.

As mentioned in the previous paragraph about the anchor-cum-relay nodes, the anchors can be deployed for assurance of LoS conditions. In context of our developed ILS, the front end antenna design can be used as the anchor-cum-relay nodes via connecting cable between them and the LBS unit. However, managing a number of such nodes will become both complex in terms of signal management as well as high cost because of connecting cables and compensation of extra signal losses due to it.

Another approach such as RSSI can be integrated with the well known systems for LoS such as radar based system and the signals can be distinguished between LoS and NLoS by observing the received power levels. In chapter 4, the influence of multipath reported in [Section 4.3.4](#) has shown two types of errors which have been named as odd- and even- error. These errors represent the influence of the strong scatterer which creates the strong replica of the intended signal in the form of multipath. In order to make distinguish between them, the RSSI would be a key parameter as it depends on the distance travelled by the signals. Moreover, the linear frequency modulated signal facilitates the way for easy computation related to RSSI [10, 11] that is received signal's amplitude remains constant throughout the signal bandwidth. The phase of the received signals can also be determined by complex demodulation that is I-Q plane of the received baseband voltage [12]. These two information, RSSI and phase, could be further used for the correlating the received signals. As we have seen in [Section 4.3.4](#), the even-error indicates about the common error in two received signals whereas odd-error does not. Therefore, the RSSI and the phase information can helps in deciding the even- and the odd-errors as the closely related travelled paths (having almost same route) will lead to even-error whereas unrelated travelled paths will lead to odd-error. A good correlation between two signals indicates the similar and closed related paths whereas a bad correlation indicates unrelated paths and this helps in choosing good estimation among radial-distance and angle. The correlation between two received signals, in terms of RSSI and signal-phase, can be easily implemented.

Additionally, the fingerprinting method is a well known idea and it is possible to enhance the accuracy of the localization method [13-15] and the knowledge of RSSI simultaneously provides the way for its implementation. Moreover, the fingerprinting can be easily integrated with the developed ILS without any architectural modification as the use of frequency modulation scheme facilitates the FMCW radar interferometry as well as the RSSI computation. Hence, the developed ILS has good potential for becoming a Hybrid System and this will bring the true radical innovation in indoor navigation technology.

5.2.3 Multiple Active-Tag Detection Scheme

At present, the developed ILS has been designed to locate a single remote Active-Tag. However, a number of tags can be used with dedicated ID [16-18]. Traditional ID systems in network protocols embed the destination ID in the packet header. The receiving node breaks the incoming packet and reads the ID in the header to determine the addressee. However, the radio jamming makes this approach unreliable. The radio-triggered technique proposed by *L. Gu et al.* for wireless sensor networks [19] is less vulnerable to spying fact that another people can intercept the RF signal. It deals with multiple-frequency technique for design of an ID system, radio-triggered ID (RTID) and is determined by the combination of a number of frequencies. Fig 5.2 depicts the design of the RTID component with three radio-triggered circuits, RTC0-RTC2 that operates on distinct frequencies and let's denote these frequencies be F0-F2.

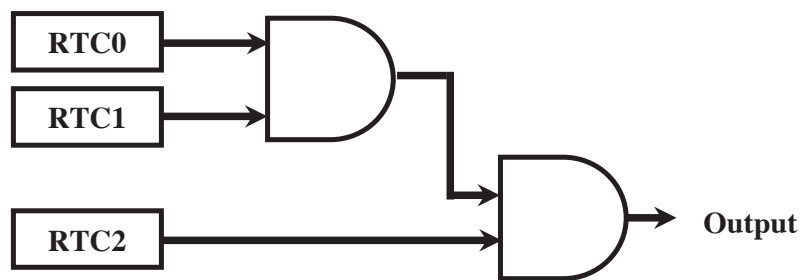


Fig 5.2: Radio-Triggered ID component [19].

The output will be “1” if all the radio-triggered circuits are activated simultaneously otherwise it remains inactive. This facilitates the activation of R TID component by choosing a set of three frequencies. The output of the RTID component can then be connected to the wake-up interrupt input that indicates whether the ID is matched. If it is the case then the

connected node will only awaken if all three frequencies are present. Therefore, it provides a more robust and a secure ID system compared to traditional system.

With this component design, if a set of six different frequencies are used then it can facilitate to excite the twenty distinct ID components, and furthermore, the number of ID can be increased by considering more distinct frequencies. However, it requires as many radio transceivers as the number of distinct frequencies or one radio transceiver capable of transmitting multiple-frequency signal is needed. Besides, it will need extra spectrum for implementation and this can be adjusted between 7-7.5 GHz free available band of the developed ILS, [Section 1.2](#).

The power consumption is also an important issue with the system's design. At this issue, the active-tag can only be excited for the communication when it requires and rest of the time it may remain in stand-by mode. That is, by separating the tag's hardware into two parts, one for wake-up and second for communication. Such circuit for the wake-up has also been mentioned in [\[19\]](#). Hence, this kind of wake-up circuit will certainly help in reducing the power consumption. In fact, the wake-up circuit also helps in reducing the interference at LBS by selecting only the intended tags and not all [\[19\]](#).

5.2.4 Synchronization between Active-Tag and LBS

The thesis work has taken the assumption that the LBS and the Active-Tag are perfectly synchronized, and therefore there will be a coherent detection. The approach towards the avoidance of synchronization problem in active-tag has been reported in [\[20, 21, 22, 23\]](#) and a straight forward implementation of the principle is used in [\[24, 25, 26\]](#). However, the phase synchronization can be achieved based on [\[20\]](#) and it has been utilized in [\[27\]](#) as an application.

The system of [\[27\]](#) is shown in [Fig 5.3](#). The FMCW radar system of [\[27\]](#) has two units: FMCW radar system and active pulsed reflector (APR). This paper says that the APR can be coherently synchronized with the incoming signal from FMCW if every time the APR is turned ON, an oscillation of T_{ON} duration is generated with the initial phase condition imposed by the received signal (S_{rec}). The APR starts oscillating with the phase of S_{rec} .

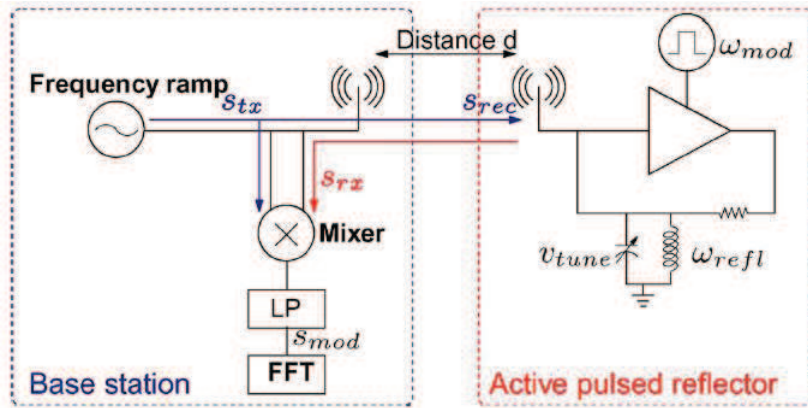


Fig 5.3: FMCW system presented in [27].

In the above figure, S_{tx} , S_{rec} and S_{rx} are marked as RF signals. The ω_{refl} is oscillation frequency (tuned by V_{tune}) of the APR which not necessarily the same frequency as the received signal (S_{rec} , received the S_{tx} transmitted at APR). The synchronization of APR with the incident phase of S_{rec} follows the Brakhausen's criteria as mentioned in [25], and is shown in Fig 5.4.

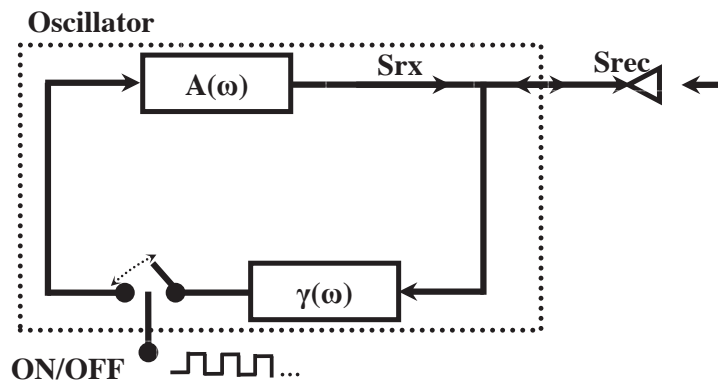


Fig 5.4: Basic principle of APR: Barkhausen's criteria [25].

The open gain is $A(\omega)\gamma(\omega)$, where $\gamma(\omega)$ is a frequency-selective feed-back and $A(\omega)$ is an amplifier transfer function. The oscillator radian centre-frequency ω_{ref} is given by Brakhausen's criteria. The phase delay of $A(\omega)\gamma(\omega)$ must be multiple of 2π with phase of oscillator equals to open gain. The oscillator will only start if $|A(\omega)\gamma(\omega)| > 1$ and if some kind

of stimulus (S_{rec}) is present in the feedback loop. Thus, the phase of the APR is synchronized to the incident phase of S_{rec} .

As our developed system uses a 1.5GHz local oscillator at the Active-Tag while the transmitted signal from the LBS is between 7.5-8.5 GHz that is two different frequencies similar to [27]. Therefore, it gives an idea for solving the synchronization issue which shall be investigated.

5.2.5 Integration of system in MMIC Technology

The presented Indoor Localization System may be integrated into a single circuit using MMIC (Monolithic Microwave Integrated Circuit) technology. Typically, MMIC uses Silicon Germanium (SiGe), Gallium Arsenide (GaAs), Gallium Nitride (GaN) technologies for the integrated circuit design. The SiGe technology has lower cost compared to GaAs technology.

As LBS has distributed orthogonal structure of the antenna for measurement, therefore, except antennas, all RF components such as mixer, amplifier (LNA) and Oscillators can be realized on one chip and then antennas will be connected to the chip via coaxial cable. However, the full circuit of AT can be realized on a single chip. But, the problem is to realize a compact diplexer (using a branch line coupler and two filters). Perhaps, it will be difficult to integrate this part. Some works are reported in [28, 29] which may be the solution for system. For example, the [28] has reported the design of CMOS stacked spiral-coupled (SSC) directional coupler working at the frequency of 900 MHz as notch filter. Also, [29] has mentioned the use of a typical silicon substrate with thick oxide on top (~25 μ m) which made possible to implement the different technologies such as GaAs MMIC and SAW filter on a single substrate.

Using SiGe technology, some works have been reported for different RF components in different technical societies. For example, the 20 dB of gain by SiGe based LNA design has been reported in [30] over 3-10 GHz bandwidth. The mixer performance with 15 dB conversion gain over 6-20 GHz has been reported in [31] using SiGe technology. Also, the [32] reports the 5.725-5.875 GHz FMCW Radar system for localization using SiGe technology and has reported an accuracy of 13 cm in indoor environments. Therefore, the possibility of our ILS implementation using SiGe technology can be achieved. However, the

generation of the frequency ramp over 6-7 GHz will be the most essential part of the system because of the linearity over 1 GHz. Additionally, our ILS has one emitter and four receiver sections, therefore, a good RF isolation will be needed for the better performance.

References

- [1] <http://en.wikipedia.org/wiki/Circulator>
- [2] J.-Y. Lee and R. A. Scholtz, "Ranging in a dense multipath environment using an UWB radio link," *IEEE J. Sel. Areas Commun.*, vol. 20, no. 9, pp. 1677–1683, Dec. 2002.
- [3] Y. Qi, H. Kobayashi, and H. Suda, "Analysis of wireless geolocation in a non-line-of-sight environment," *IEEE Trans. Wireless Commun.*, vol. 5, no. 3, pp. 672–681, Mar. 2006.
- [4] J P Ramirez, and D K Borah, "Anchor-cum-Relay Nodes for Localizing a mobile Source and Relaying Source Signals," Vehicular Technology Conference (VTC Fall), 2013 IEEE 78th DOI:10.1109/VTCFall.2013.6692107.
- [5] C. Stenir, and A. Wittneben, "Low Complexity Location Fingerprinting With Generalized UWB Energy Detection Receivers," *IEEE Trans. Signal. Proc.*, vol. 58, no. 03, pp. 1756–1767, March. 2010
- [6] D.D. Arumugam, J. D. Griffin, D. D. Stancil, and D. S. Ricketts, "Two-dimensional position measurement using magnetoquasistatic fields," *IEEE-APS Tropical Conference on Antenna and Propagation in Wireless Communication 2011*, pp. 1193-1196.
- [7] D.D. Arumugam, D. D. Stancil, and D. S. Ricketts, "Proximity and orientation sensing using magnetoquasistatic fields and complex image theory," *IEEE Vehicular Technology Conference (VTC 2011)*, pp. 1-5.
- [8] D.D. Arumugam, J. D. Griffin, D. D. Stancil, and D. S. Ricketts, "Higher Order Loop Corrections for Short Range Magnetoquasistatic Position Tracking," *IEEE Int. Symp. On Antennas and Propagation (APSURSI)*, pp. 1755-1757.
- [9] D.D. Arumugam, J. D. Griffin, D. D. Stancil, and D. S. Ricketts, "Wireless orientation sensing using magnetoquasistatic fields and complex image theory," *IEEE Radio and Wireless Symposium (RWS 2012)*, pp. 251-254.
- [10] " http://en.wikipedia.org/wiki/Envelope_detector"

-
- [11] V. Moghtadaiee, A. G. Dempster, and S. Lim, "Indoor Localization Using FM Radio Signals: A Fingerprinting Approach," Int. Conf; Indoor Positioning and Indoor Navigation (IPIN 2011), pp. 1-7.
- [12] J P. Nikitin, R. Martinez, S. Ramamurthy, H. Leland, G. Spiess, and K. Rao, "Phase based spatial identification of UHF RFID Tags," Intermec Technol. Corp., Everett, WA, USA, 2010 IEEE International Conference on RFID, 2010.
- [13] Q. Yao, F.-Y. Wang, H. Gao, K. Wang, and H. Zhao, "Location estimation in zigbee network based on fingerprinting," dec. 2007, pp. 1 –6.
- [14] V. Honkavirta, T. Perala, S. Ali-Loytty, and R. Piche, "A comparative survey of wlan location fingerprinting methods," march 2009, pp. 243 –251.
- [15] S. Outemzabet and C. Nerguizian, "Accuracy enhancement of an indoor ann-based fingerprinting location system using particle filtering and a low-cost sensor," may 2008, pp. 2750 –2754.
- [16] J. Ansari, D. Pankin, and P. Mahonen, "Radio-Triggered Wake-ups with addressing Capabilities for Extremely Low Power Sensor Network Applications," Inter. Symp. On Personal, Indoor and Mobile Rad. Comm. 2008, pp. 1-5.
- [17] Demirkol et al., "MAC protocols for wireless sensor networks: a survey," *Communications Magazine, IEEE*, vol. 44, no. 4, pp. 115-121, April 2006.
- [18] J. Polastre, J. Hill, and D. Culler, "Versatile low power media access for wireless sensor networks," in *SenSys*, Nov. 2004.
- [19] L. Gu, and J. A. Stankovic, "Radio-triggered wake-up capability for sensor networks," Real-Time Embedded Technology and Applications Symposium, 2004, pp. 27-26.
- [20] M. Vossiek, R. Roskosch, and P. Heide, "Precise 3-D object position tracking using FMCW radar," in *Proc. 29th Eur. Microw. Conf.*, Oct. 1999, vol. 1, pp. 234–237.
- [21] R. J. King, *Microwave Homodyne Systems*. London, U.K.: Peregrinus, 1978.

-
- [22] M. Kossel, H. R. Benedickter, R. Peter, and W. Bächtold, "Microwave backscatter modulation systems," in *IEEE MTT-S Int. Microw. Symp. Dig.*, Jun. 2000, pp. 1427–1430.
- [23] J. Thornton and D. J. Edwards, "Range measurement using modulated retro-reflectors in FM radar system," *IEEE Microw. GuidedWave Lett.*, vol. 58, no. 2, pp. 267–276, Feb. 2010.
- [24] A. Koelle, S. Depp, and R. Freyman, "Short-range radio-telemetry for electronic identification using modulated backscatter," *Proc. IEEE*, vol. 63, no. 8, pp. 1260–1260, Aug. 1975.
- [25] M. Vossiek and P. Gulden, "The switched injection-locked oscillator: A novel versatile concept for wireless transponder and localization systems," *IEEE Trans. Microw. Theory Tech.*, vol. 56, no. 4, pp. 859–866, Apr. 2008.
- [26] K. Finkenzeller, *RFID Handbook: Fundamentals and Applications in Contactless Smart Cards and Identifications*, 2nd ed. New York: Wiley, 2002.
- [27] S. Wehrli, R. Gierlich, J. Huttner, D. Barras, F. Ellinger, and H. Jackel, "Integrated Active Pulsed Reflector for an Indoor Local Positioning System," *IEEE Trans. Microw. Theory Tech.*, vol. 55, no. 11, pp. 2447–2453, Nov. 2007.
- [28] Y. Zheng, L. Ye, L. Chen, H. Liao, and R. Huang, "SAW-less GNSS front-end amplifier with 80.4-dB GSM blocker suppression using CMOS directional coupler notch filter," *Int. Symp. On Circuits and Systems, ISCAS 2013*, pp. 749-752.
- [29] J. S. Lee, Y. M. Lee, C. M. Jeong, D. W. Kim, and Y. S. Kwon, "System in a package solution for RF receiver with SAW filter integration," *Electronic Components and Technology Conference, 2002*, pp. 1012-1017.
- [30] J. Lee, and J. D. Cressler, "A 3-10 GHz SiGe resistive feedback low noise amplifier for UWB applications," *Radio Frequency Integrated Circuits (RFIC) Symposium, 2005*, pp. 545-548.

-
- [31] P. K. Saha, D. C. Howard, S. Shnakar, R. Diestelhorst, T. England, and J. D. Cressler, “A 6-20 GHz Adaptive SiGe Image reject Mixer for a Self-Healing receiver,” *IEEE Journal of Solid-State*, 2012, pp. 1998-2006.
- [32] R. Eickhoff, F. Ellinger, T. Ussmueller, and S. Spiegel, “A highly-integrated fractional-N synthesizer for FMCW radar,” *IEEE Int. Conf. Microwaves, Communications, Antennas and Electronic Systems, COMCAS 2008*, pp. 1-6.

LIST OF PUBLICATIONS

Book Publication:

Proposed chapter "**Antenna System & Architecture Circular Polarized UWB Antennas for Indoor Positioning Application**" accepted by **IGI GLOBAL Publishing Company** for publication. (Invited for chapter submission)

International Conferences:

- [1] R. Kumar, J. C. Cousin, and B. Huyart, "3D Indoor Localization System using Single Reference/Anchor Position based on Multistatic FMCW Radar System," *European Microwave Week (EuMW2014)*, Rome, Italy, October 2014.
- [2] R. Kumar, J. C. Cousin, and B. Huyart, "2D Indoor Localization System using FMCW Radars and a DMTD Technique," *International Radar Conference (RADAR14)*, Lille, France, October 2014.
- [3] R. Kumar, J. C. Cousin, and B. Huyart, "Performance of Indoor Localization System in Presence of Scatter for Strong Multipath Condition," *International Conference on Ultra-Wideband (ICUWB2014)*, Paris, France, September 2014.
- [4] R. Kumar, J. C. Cousin, B. Huyart, and K. Mabrouk, "Indoor Localization System for 2D Measurement in European UWB Band with One Reference Position," *International Microwave Symposium (IMS2014)*, Tampa, Florida, June 2014.
- [5] R. Kumar, J. C. Cousin, B. Huyart, and K. Mabrouk, "2D Measurement using Interferometry and FMCW Multistatic Radar System for Indoor Localization," *European Microwave Week (EuMW2013)*, Nuremberg, Germany, October 2013.
- [6] R. Kumar, J. C. Cousin, B. Huyart, and K. Mabrouk, "Dual-Circular Polarizes Dumbbell-Shaped Crossed-Dipole Planar Antenna for UWB Application," *European Conference on Antenna & Propagation (EuCAP2013)*, Gothenburg, Sweden, April 2013.

National Conferences:

-
- [7] R. Kumar, J. C. Cousin, B. Huyart, and K. Mabrouk, "2D Measurement with Single Known Reference Position for Indoor Localization in European UWB Band," *Union Radio-Scientifique Internationale, Comité National Français de Radioélectricité Scientifique (URSI-France 2014)*, Paris, France, March 2014.
- [8] R. Kumar, J. C. Cousin, B. Huyart, and K. Mabrouk, "Antenne spirale asymétrique couvrant la bande UWB [6-8.5 GHz] pour une application de localisation indoor," *Journées Nationales Microondes (JNM2013)*, Paris, France, May 2013.
- [9] R. Kumar, J. C. Cousin, B. Huyart, and K. Mabrouk, "Circular Polarized Antennas for Indoor Localization Application in European UWB Band [6-8.5]GHz," *Journée d'Etudes sur la TéléSanté (JETSAN2013)*, Fontainebleau, France, May 2013.
- [10] R. Kumar, **J. C. Cousin**, B. Huyart, and K. Mabrouk, "System de localisation indoor pour aide à la télésurveillance," *Journée d'Etudes sur la TéléSanté (JETSAN2013)*, Fontainebleau, France, May 2013.

ANNEXURE A

MATLAB PROGRAM 1: Used by Data Acquisition Card for collecting baseband frequencies.

```
*****
%
% rec_std_single_rk.m
%
*****
*****

clear; clc;
%%Adding the library path
addpath 'C:\Program Files\Spectrum GmbH\Examples\matlab\LibPackage';
addpath 'C:\Program Files\Spectrum
GmbH\SpcmMatlabDriver\spcm_LibPackage';
addpath 'C:\Program Files\Spectrum
GmbH\SpcmMatlabDriver\spcm_DrvPackage';
load 'filtbb.txt';
load 'filtbb1.txt';
load 'filtbb2.txt';

%%%%%%%%%
% % ***** init card and store infos in cardInfo struct *****
    [success, cardInfo] = spcMInitCardByIdx (0);

Memory_alt= 1e6; %sample number
    [success, cardInfo] = spcMSetupModeRecStdSingle(cardInfo, 0, 3,
Memory_alt, 8 * 1024); %(cardInfo, chMaskH, chMaskL, Memory_alt, 8 *
1024);

Sample_rate=22.5e6;
    [success, cardInfo] = spcMSetupClockPLL (cardInfo, Sample_rate,
1); % clock output : enable = 1, disable = 0

    [success, cardInfo] = spcMSetupTrigSoftware (cardInfo, 0); %
trigger output : enable = 1, disable = 0

% ----- analog acquisition card setup (1 = AnalogIn) -----
% ----- program all input channels to +/-1 V and 50 ohm termination
(if it's available) -----
    for i=0 : cardInfo.maxChannels-1
        [success, cardInfo] = spcMSetupAnalogPathInputCh (cardInfo,
i, 0, 1000, 1, 0, 0, 0);
    end
% ***** start card for acquisition *****
errorCode = spcm_dwSetParam_i32 (cardInfo.hDrv, 100, 16396);
%(cardInfo.hDrv, 100, commandMask); % 100 = SPC_M2CMD

if errorCode == 263 % 263 = ERR_TIMEOUT
    spcMErrorMessageStdOut (cardInfo, ' ... Timeout occurred !!!',
false);
    return;
end
```

```

else
    % ***** transfer data from card to PC memory *****
    fprintf (' Starting the DMA transfer and waiting until data is in
PC memory ...\n');
    % ***** get analog input data *****
    if cardInfo.cardFunction == 1
        dataType = 1;

        switch (cardInfo.setChannels)

            case 1
                % ----- get the whole data for one channel with
offset = 0 -----
                [errorCode, Dat_Ch0] = spcm_dwGetData (cardInfo.hDrv,
0, cardInfo.setMemsize, cardInfo.setChannels, dataType);
            case 2
                % ----- get the whole data for two channels with
offset = 0 -----
                [errorCode, Dat_Ch0, Dat_Ch1] = spcm_dwGetData
(cardInfo.hDrv, 0, cardInfo.setMemsize, cardInfo.setChannels,
dataType);
            end
        end
    end
    grid on;

    fprintf (' ... acquisition ended, data has been transferred to PC
memory.\n');

    t = 0 : cardInfo.setMemsize - 1;
    switch (cardInfo.setChannels)
        case 1
            figure(125);
            plot (t, Dat_Ch0);
        case 2
            d0=conv(Dat_Ch0,filtbb2,'same');
            d1=conv(Dat_Ch1,filtbb2,'same');
            figure(126);plot (t, 10*d0, 'r', t, 10*d1,
'b');grid on;

            legend('Data-Rx1','Data-Rx2');
        end

    spcMCloseCard (cardInfo);
    save Dat_Ch0;
    movefile('Dat_Ch0.mat','Prog1.mat')

```

ANNEXURE B

MATLAB PROGRAM 2: Used for signal processing in MATLAB. The data collected by Annexure A are used.

```
%%% Data Processing File for Distance and Angle-of-Arrival
calculation
%%% Ref file for computation: DMTD_3.m
%%% Advanced algo: Diversity principle is used, more than one ref.
points and the concept of weightage has been included
%%% New algo has been implemented for rejection of notches in
frequencies
clc;
clear;
load Prog1.mat; %Data-File collected in Annexure A

figure(1);clf;
plot(1:1:length(Dat_Ch0),
Dat_Ch0(1,:), 'r*', 'LineWidth', 2, 'MarkerEdgeColor', 'r', 'MarkerFaceColor', 'r', 'MarkerSize', 10);grid on;hold on;
plot(1:1:length(Dat_Ch1),
Dat_Ch1(1,:), 'bs', 'LineWidth', 2, 'MarkerEdgeColor', 'b', 'MarkerFaceColor', 'b', 'MarkerSize', 10);hold on;
legend('Signal-1', 'Signal-2');
xlabel('Number of Samples (Sampling Frequency 22.5MHz, 225000)', 'fontSize', 12, 'fontWeight', 'b');
ylabel('Signal Amplitude (V)', 'fontSize', 12, 'fontWeight', 'b');
set(gcf, 'color', [1 1 1]);
set(gca, 'FontSize', 12, 'fontName', 'Times', 'fontWeight', 'b');
legend('Rx1-f1 (Basenad Signal1)', 'Rx2-f2 (Baseband Signal2)', 32, 'Location', 'SouthEast');

clearvars -except Dat_Ch0 Dat_Ch1;
n_s=(3.52)*(1e5); n_e=n_s + 2.25e5;
c0=Dat_Ch0(1, (n_s+1:1:n_e)); c1=Dat_Ch1(1, (n_s+1:1:n_e));
%clearvars Dat_Ch0 Dat_Ch1;
ref1_pt=[-50 -25 0 25 50];ref2_pt=[-50 -25 0 25 50];
n=size(c0,2);
figure(2);clf;
plot(1:1:n, 200*c0(1,:), 'r. '); hold on; grid on;
plot(1:1:n, 200*c1(1,:), 'b-* '); hold on; grid on;
legend('PrePro-Co', 'PrePro-C1');

legend('PrePro-Co', 'PrePro-C1');
rx1_cali=8.949;
rx2_cali=9.076;

%% Starting of Interjectpolation Approach: rejection of extra
information
```

```

smple=abs(n_e-n_s);
S_dq=smple/0.01;
r_smple=0.1113e6;
w=round(power(S_dq/r_smple,1/3));

p= ones(1,3)*w;    %[20 36 5];    % Rejection factor

%% Loop1
p1=p(1,1);j0=n;j1=1;
c01(1,1)=1000*c0(1,1); c11(1,1)=1000*c1(1,1);
for i=p1:p1:length(c0)
    c01(1,j1)=mean(1000*[c0(1,i) c0(1,i+1-p1)]);
    c11(1,j1)=mean(1000*[c1(1,i) c1(1,i+1-p1)]);
    j1=j1+1;
end
%clearvars c0 c1;
figure(22);clf;
plot(1:1:length(c01), c01(1,:), 'r-'); hold on; grid on;
plot(1:1:length(c11), c11(1,:), 'b-*'); hold on; grid on;
%% Loop2
p2=p(1,2);j2=1;
c02(1,1)=c01(1,1); c12(1,1)=c11(1,1);
for i=p2:p2:length(c01)
    c02(1,j2)=mean([c01(1,i) c01(1,i+1-p2)]);
    c12(1,j2)=mean([c11(1,i) c11(1,i+1-p2)]);
    j2=j2+1;
end
clearvars c01 c11;
%% Loop3
p3=p(1,3);j3=1;
c03(1,1)=c02(1,1); c13(1,1)=c12(1,1);
for i=p3:p3:length(c02)
    c03(1,j3)=mean([c02(1,i) c02(1,i+1-p3)]);
    c13(1,j3)=mean([c12(1,i) c12(1,i+1-p3)]);
    j3=j3+1;
end
clearvars c02 c12;

figure(3);clf;
plot(1:1:length(c03), 10*c03(1,:), 'r-'); hold on; grid on;
plot(1:1:length(c13), 10*c13(1,:), 'b-'); hold on; grid on;
legend('PostProl-C0', 'PostProl-C1');

%% 2nd cycle
%% Curve Smoothing Algo: Successive Mean Approach (SMA)
%% Loop4
p1=1;j4=2;
c04(1,1)=1*c03(1,1); c14(1,1)=1*c13(1,1);
for i=(p1+1):p1:length(c03)
    c04(1,j4)=mean(1*[c03(1,i) c03(1,i-p1)]);
    c14(1,j4)=mean(1*[c13(1,i) c13(1,i-p1)]);
    j4=j4+1;
end
clearvars c03 c13;
%% Loop5
p2=1;j5=2;

```

```

c05(1,1)=c04(1,1); c15(1,1)=c14(1,1);
for i=(p2+1):p2:length(c04)
    c05(1,j5)=mean([c04(1,i) c04(1,i-p2)]);
    c15(1,j5)=mean([c14(1,i) c14(1,i-p2)]);
    j5=j5+1;
end
clearvars c04 c14;
%%Loop6
p3=1;j6=2;
c06(1,1)=c05(1,1); c16(1,1)=c15(1,1);
for i=(p3+1):p3:length(c05)
    c06(1,j6)=mean([c05(1,i) c05(1,i-p3)]);
    c16(1,j6)=mean([c15(1,i) c15(1,i-p3)]);
    j6=j6+1;
end
clearvars c05 c15;

%%Loop7
p4=1;j7=2;
c07(1,1)=c06(1,1); c17(1,1)=c16(1,1);
for i=(p4+1):p4:length(c06)
    c07(1,j7)=mean([c06(1,i) c06(1,i-p4)]);
    c17(1,j7)=mean([c16(1,i) c16(1,i-p4)]);
    j7=j7+1;
end

%%Loop8
p5=1;j8=2;
c08(1,1)=c07(1,1); c18(1,1)=c17(1,1);
for i=(p5+1):p5:length(c07)
    c08(1,j8)=mean([c07(1,i) c07(1,i-p5)]);
    c18(1,j8)=mean([c17(1,i) c17(1,i-p5)]);
    j8=j8+1;
end

%%Loop9
p6=1;j9=2;
c09(1,1)=c08(1,1); c19(1,1)=c18(1,1);
for i=(p6+1):p6:length(c08)
    c09(1,j9)=mean([c08(1,i) c08(1,i-p6)]);
    c19(1,j9)=mean([c18(1,i) c18(1,i-p6)]);
    j9=j9+1;
end

%%Loop10
p7=1;j10=2;
c010(1,1)=c09(1,1); c110(1,1)=c19(1,1);
for i=(p7+1):p7:length(c09)
    c010(1,j10)=mean([c09(1,i) c09(1,i-p7)]);
    c110(1,j10)=mean([c19(1,i) c19(1,i-p7)]);
    j10=j10+1;
end

%%Loop11
p8=1;j11=2;
c011(1,1)=c010(1,1); c111(1,1)=c110(1,1);
for i=(p8+1):p8:length(c010)
    c011(1,j11)=mean([c010(1,i) c010(1,i-p8)]);
    c111(1,j11)=mean([c110(1,i) c110(1,i-p8)]);

```

```

        j11=j11+1;
    end
    %%%Loop12
    p9=1;j12=2;
    c012(1,1)=c011(1,1); c112(1,1)=c111(1,1);
    for i=(p9+1):p9:length(c011)
        c012(1,j12)=mean([c011(1,i) c011(1,i-p9)]);
        c112(1,j12)=mean([c111(1,i) c111(1,i-p9)]);
        j12=j12+1;
    end
    figure(4);clf;
    plot(1:1:length(c012), c012(1,:), 'r-*'); hold on; grid on;
    plot(1:1:length(c112), c112(1,:), 'b-*'); hold on; grid on;
    legend('PostPro2-C0', 'PostPro2-C1');

    %S_dq=400e6;
    fprintf ('\n Sampling rate of data aquisition: %.2fMHz\n',
    S_dq/(1e6));
    S=(S_dq)/round(j0/j3);
    fprintf ('\n Effective Sampling after Interjectpolation: %.2fMHz\n',
    S/(1e6));

    clearvars c06 c16 c07 c17 c08 c18 c09 c19 c010 c110 j0 j1 j2 j3 j4 j5
    j6 j7 j8 j9 j10 j11 j12...
        p1 p2 p3 p4 p5 p6 p7 p8 p9 n_e n_s smple r_smple w;

    %% End of SMA
    %%
    %% Max and Min Wave form

    t0=linspace(0,0.01,length(c012));
    n0_c=[zeros(1,length(ref1_pt))];

    % Number of cycle computation

    for m=1:1:length(ref1_pt) % if more than one reference point is
    considered
        n0_cycle=1;
        for i=2:1:length(c012)
            if ((c012(1,i) >= ref1_pt(1,m) && (c012(1,i-1) <
    ref1_pt(1,m))))
                tc0(m,n0_cycle)=mean([t0(1,i) t0(1,i-1)]); % Time stamp
                n0_cycle=n0_cycle+1;
            end
        end
        %%%
        %t_c0(m,1)=tc0(m,size(tc0,2))-tc0(m,1);
        %f0_i(1,m)=(size(tc0,2)-1)/t_c0(m,1);

        t_c0(m,1)=tc0(m,size(nonzeros(tc0(m,:))',2))-tc0(m,1);% total
    time for 'n' cycle
        f0_i(1,m)=(size(nonzeros(tc0(m,:))',2)-1)/t_c0(m,1); % frequency
    computed from total time and no. of complete cycle

        for k=2:1:length(nonzeros(tc0(m,:)))
            f_0(m,k-1)=1/(tc0(m,k)-tc0(m,k-1)); % frequency from each time
    stamp

```

```

        if ( abs(f_0(m,k-1)-f0_i(1,m)) <= 1000) % Rejecting the next
frequency which has abrupt frequency change
            n0_c(1,m)=n0_c(1,m)+1;
        end
    end
end

%tc0
for m=1:1:length(ref1_pt)

    t_c0(m,1)=tc0(m,size(nonzeros(tc0(m,:))',2))-tc0(m,1);
    f0(1,m)=(n0_c(1,m))/t_c0(m,1); % Frequency computed after
rejecting the abrupt frequencies
end

%tc1
t1=linspace(0,0.01,length(c112));
n1_c=[zeros(1,length(ref2_pt))];

for m=1:1:length(ref2_pt)
    n1_cycle=1;
    for i=2:1:length(c112)
        if ((c112(1,i) >= ref2_pt(1,m) && (c112(1,i-1) <
ref2_pt(1,m))))
            tc1(m,n1_cycle)=mean([t1(1,i) t1(1,i-1)]); % Time stamp
            n1_cycle=n1_cycle+1;
        end
    end
    %%%
    %t_c0(m,1)=tc0(m,size(tc0,2))-tc0(m,1);
    %f0_i(1,m)=(size(tc0,2)-1)/t_c0(m,1);

    t_c1(m,1)=tc1(m,size(nonzeros(tc1(m,:))',2))-tc1(m,1);
    f1_i(1,m)=(size(nonzeros(tc1(m,:))',2)-1)/t_c1(m,1); % frequency
computed from total time and no. of complete cycle

    for k=2:1:length(nonzeros(tc1(m,:)))
        f_1(m,k-1)=1/(tc1(m,k)-tc1(m,k-1) ); % frequency from each time
stamp
        if ( abs(f_1(m,k-1)-f1_i(1,m)) <= 1000)
            n1_c(1,m)=n1_c(1,m)+1;
        end
    end
end
end
%tc1
for m=1:1:length(ref2_pt)

    t_c1(m,1)=tc1(m,size(nonzeros(tc1(m,:))',2))-tc1(m,1);
    f1(1,m)=(n1_c(1,m))/t_c1(m,1);
end

%%%%%%%%%%%%%%%%%%%%%%%%%%%%%%%%%%%%%%%%%%%%%%%%%%%%%%%%%%%%%%%%%%%%%%%%END OF NEW
ALGO%%%%%%%%%%%%%%%%%%%%%%%%%%%%%%%%%%%%%%%%%%%%%%%%%%%%%%%%%%%%%%%%%%%%%%%%
f_d=abs([f0-f1]);
% BW=1e9;
% Tm=10e-3;           %in sec, modulation time
% c=3e8;              %speed of light in m/sec

```

```

% rx1_cali=6.444;
% rx2_cali=6.505;
% d_f0_avg= (f0*c*Tm/BW-rx1_cali)/2;
% d_f1_avg= (f1*c*Tm/BW-rx2_cali)/2;
% d_f_d=(d_f0_avg+d_f1_avg)/2;
%%

%%%%%%%%% Another Algo: REJECTION OF EXTREME FREQUENCY COMPONENTS
%%%%%%%%%
freq_gap=10000; % Frequency Band defined for the rejection

for p=1:1:length(f_d)
    q0=1; %ff0=[];
    for k=2:1:length(nonzeros(tc0(p,:)))
        %size(nonzeros(tc0(p,:))',2)
        fe0(p,k-1)=1/(tc0(p,k)-tc0(p,k-1));% frequency from each time
stamp

        if (fe0(p,k-1) < freq_gap) %( abs(fe0(p,k-1)-f0(1,p)) > 0) &&
(abs(fe0(p,k-1)-f0(1,p)) <= freq_gap) )% comparison with the average
value of frequency
            ff0(p,q0)=fe0(p,k-1);
            q0=q0+1;
        end
    end

    fe0_avg(p,1)=mean(nonzeros(fe0(p,:))); %Avg. from frequency stamps
contains extreme frequency
    ff0_avg(p,1)=mean(nonzeros(ff0(p,:))); %Avg. contains no extreme
frequency

q1=1;%ff1=[];
for k=2:1:length(nonzeros(tc1(p,:)))
    fe1(p,k-1)=1/(tc1(p,k)-tc1(p,k-1) );

    if (fe1(p,k-1) < freq_gap) %( abs(fe1(p,k-1)-f1(1,p)) > 0) &&
(abs(fe1(p,k-1)-f1(1,p)) <= freq_gap) )%comparison with the average
value of frequency
        ff1(p,q1)=fe1(p,k-1);
        q1=q1+1;
    end

end

fe1_avg(p,1)=mean(nonzeros(fe1(p,:))); %Avg. from frequency stamps
contains extreme frequency
ff1_avg(p,1)=mean(nonzeros(ff1(p,:)));

end

ff=[ff0_avg ff1_avg]; ff_d=abs(ff0_avg-ff1_avg);

```

```

for p=1:1:length(f_d)
    freq_gap0=(ff0_avg(p,:));
    q0=1; %ff0=[];
    for k=2:1:length(nonzeros(tc0(p,:)))
        %size(nonzeros(tc0(p,:))',2)
        if ((fe0(p,k-1) > (freq_gap0-2000)) && (fe0(p,k-1) <
(freq_gap0+2000)) ) %( abs(fe0(p,k-1)-f0(1,p)) > 0) && (abs(fe0(p,k-
1)-f0(1,p)) <= freq_gap) )% comparison with the average value of
frequency
            ff0_gap(p,q0)=fe0(p,k-1);
            q0=q0+1;
        end
    end

    ff0gap_avg(p,1)=mean(nonzeros(ff0_gap(p,:))); %Avg. contains no
extreme frequency

    freq_gap1=(ff1_avg(p,:));
    q1=1;%ff1=[];
    for k=2:1:length(nonzeros(tc1(p,:)))

        if ((fel(p,k-1) > (freq_gap1-2000)) && (fel(p,k-1) <
(freq_gap1+2000)) ) %( abs(fel(p,k-1)-f1(1,p)) > 0) &&
(abs(fel(p,k-1)-f1(1,p)) <= freq_gap) )%comparison with the average
value of frequency
            ff1_gap(p,q1)=fel(p,k-1);
            q1=q1+1;
        end
    end

    ff1gap_avg(p,1)=mean(nonzeros(ff1(p,:)));
end

% d_ff0_avg= (ff0_avg*c*Tm/BW-rx1_cali)/2;
% d_ff1_avg= (ff1_avg*c*Tm/BW-rx2_cali)/2;
% d_ff_d=(d_ff0_avg+d_ff1_avg)/2;

figure(5);clf;
plot(1:1:length(nonzeros(fe0(1,:))),nonzeros(fe0(1,:)),'-
rd',1:1:length(nonzeros(fel(1,:))),nonzeros(fel(1,:)),'b-d');grid
on;hold on;
legend('Ref1-PostPro2-C0','Ref1-PostPro2-C1');
plot(1:1:length(nonzeros(fe0(2,:))),nonzeros(fe0(2,:)),'r-
.s',1:1:length(nonzeros(fel(2,:))),nonzeros(fel(2,:)),'b-.s');grid
on;hold on;
%legend('Ref2-PostPro2-C0','Ref2-PostPro2-C1');

plot(1:1:length(nonzeros(fe0(3,:))),nonzeros(fe0(3,:)),'r:o',1:1:leng
th(nonzeros(fel(3,:))),nonzeros(fel(3,:)),'b:o');grid on;
legend('Ref1-PostPro2-C0','Ref1-PostPro2-C1','Ref2-PostPro2-
C0','Ref2-PostPro2-C1','Ref3-PostPro2-C0','Ref3-PostPro2-C1');

```

```

figure(6);clf;
plot(1:1:length(nonzeros(ff0(1,:))),nonzeros(ff0(1,:)),'-
rd',1:1:length(nonzeros(ff1(1,:))),nonzeros(ff1(1,:)),'b-d');grid
on;hold on;
%legend('Ref1-PostPro2-C0','Ref1-PostPro2-C1');
plot(1:1:length(nonzeros(ff0(2,:))),nonzeros(ff0(2,:)),'r-
.s',1:1:length(nonzeros(ff1(2,:))),nonzeros(ff1(2,:)),'b-.s');grid
on;hold on;
plot(1:1:length(nonzeros(ff0(3,:))),nonzeros(ff0(3,:)),'r:o',1:1:leng
th(nonzeros(ff1(3,:))),nonzeros(ff1(3,:)),'b:o');grid on;
legend('Ref1-PostPro2-C0','Ref1-PostPro2-C1','Ref2-PostPro2-
C0','Ref2-PostPro2-C1','Ref3-PostPro2-C0','Ref3-PostPro2-C1');

figure(7);clf;
plot(1:1:length(nonzeros(ff0_gap(1,:))),nonzeros(ff0_gap(1,:)),'-
rd',1:1:length(nonzeros(ff1_gap(1,:))),nonzeros(ff1_gap(1,:)),'b-
d');grid on;hold on;
%legend('Ref1-PostPro2-C0','Ref1-PostPro2-C1');
plot(1:1:length(nonzeros(ff0_gap(2,:))),nonzeros(ff0_gap(2,:)),'r-
.s',1:1:length(nonzeros(ff1_gap(2,:))),nonzeros(ff1_gap(2,:)),'b-
.s');grid on;hold on;
plot(1:1:length(nonzeros(ff0_gap(3,:))),nonzeros(ff0_gap(3,:)),'r:o',
1:1:length(nonzeros(ff1_gap(3,:))),nonzeros(ff1_gap(3,:)),'b:o');grid
on;
legend('Ref1-PostPro2-C0','Ref1-PostPro2-C1','Ref2-PostPro2-
C0','Ref2-PostPro2-C1','Ref3-PostPro2-C0','Ref3-PostPro2-C1');

fe=[fe0_avg fe1_avg]; fe_d=abs(fe0_avg-fe1_avg);
% d_fe0_avg= (fe0_avg*c*Tm/BW-rx1_cali)/2;
% d_fe1_avg= (fe1_avg*c*Tm/BW-rx2_cali)/2;
% d_fe_d=(d_fe0_avg+d_fe1_avg)/2;

f0_avg=f0(1,:); f1_avg=f1(1,:);

fff0_avg=mean([f0_avg fe0_avg ff0_avg ff0gap_avg],2);
fff1_avg=mean([f1_avg fe1_avg ff1_avg ff1gap_avg],2);
%Since Fe effects has been discarded so its better not to consider it
%fff0_avg=mean([f0_avg ff0_avg],2); fff1_avg=mean([f1_avg
fff1_avg],2);

fff=[fff0_avg fff1_avg]; fff_d=abs(fff0_avg - fff1_avg);

F0_m=mean(fff0_avg); F1_m=mean(fff1_avg);
F_md=abs(F0_m-F1_m);

% Selection of good values
g=[f_d' fe_d ff_d]
[r,c]=find(g==min(min(g)))

% F=min([f_d' fe_d ff_d]);
%
```

```

% if F==f_d(1,p)
%   F0=f0_avg; F1=f1_avg;
% end
%
% if F==fe_d
%   F0=fe0_avg; F1=fe1_avg;
% end
%
% if F==ff_d
%   F0=ff0_avg; F1=ff1_avg;
% end

%%
%%%%%%%%%%%%%%%%%%%%%%%%%%%%%%%%%%%%%%%%%%%%%%%%%%%%%%%%%%%%%%%%%%%%%%%%FMCW%%%%%%%%%%%%%%%%%%%%%%%%%%%%%%%%%%%%%%%%%%%%%%%%%%%%%%%%%%%%%%%%%%%%%%%%
BW=1e9;
Tm=10e-3;           %in sec, modulation time
c=3e8;              %speed of light in m/sec
% d= [F0_m F1_m]*(c*Tm)/BW; %targets' distances in m
% bl=0.3;           % baseline length in m
% AoA=(acos((d(1,1)-d(1,2))/bl))*180/pi;

BF=[mean(f0_avg) mean(fe0_avg) mean(ff0_avg) mean(ff0gap_avg)
mean(fff0_avg) ;...
    mean(f1_avg) mean(fe1_avg) mean(ff1_avg) mean(ff1gap_avg)
mean(fff1_avg) ;]

d_0= (BF(1,:)*c*Tm/BW-rx1_cali)/2;
d_1= (BF(2,:)*c*Tm/BW-rx2_cali)/2;

d=(d_0+d_1)/2;

%% Signal processing Graph

figure(11);clf;
plot(1:1:length(c012), c012(1,:), '--
r', 'LineWidth',2, 'MarkerEdgeColor', 'r', 'MarkerFaceColor', 'r', 'MarkerS
ize',10);grid on;hold on;
plot(1:1:length(c112), c112(1,:), '-
b', 'LineWidth',2, 'MarkerEdgeColor', 'b', 'MarkerFaceColor', 'b', 'MarkerS
ize',10);hold on;
xlabel('Number of Samples', 'fontSize',12, 'fontweight', 'b');
ylabel('Amplitude', 'fontSize',12, 'fontweight', 'b');
set(gcf, 'color', [1 1 1]);
set(gca, 'FontSize', 12, 'fontName', 'Times', 'fontweight', 'b');
legend('Rx1-f1', 'Rx2-f2');
axis([0 1050 -300 300])

figure(12);clf;
plot(1:1:length(nonzeros(ff0_gap(3,:))),nonzeros(ff0_gap(3,:)), 's--
r', 'LineWidth',2, 'MarkerEdgeColor', 'r', 'MarkerFaceColor', 'r', 'MarkerS
ize',10);grid on;hold on;

```

```

plot(1:1:length(nonzeros(ff1_gap(3,:))),nonzeros(ff1_gap(3,:)),'o-
b','LineWidth',2,'MarkerEdgeColor','b','MarkerFaceColor','b','MarkerS
ize',10);hold on;
xlabel('Number of Complete(2\pi)cycles
','fontSize',12,'fontWeight','b');
ylabel('Frequency (Hz)','fontSize',12,'fontWeight','b');
set(gcf,'color',[1 1 1]);
set(gca,'FontSize',12,'fontName','Times','fontWeight','b');
legend('Rx1-f1','Rx2-f2');

clearvars g AoA f1_i f0_i f_1 f_0 fe ff fff;

clearvars i k m n n0_cycle n1_cycle Tm bl S S_dq BW p ref_pt c011
c111 t0 t1 t_c0 t_c1 tc0 tc1 r c;
%%

%%
clearvars -except c0 c1;

t0=linspace(0,0.01,length(c0));t1=linspace(0,0.01,length(c1));

n0_c=1;n1_c=1;

% Number of cycle computation

for m=1:1:1 % if more than one reference point is considered
    n0_cycle=1;

    for i=2:1:length(c0)
        if ((c0(1,i) >= 0 && (c0(1,i-1) < 0 )))
            tc0(m,n0_cycle)=mean([t0(1,i) t0(1,i-1)]); % Time stamp
            n0_cycle=n0_cycle+1;
        end
    end

    for k=2:1:length(nonzeros(tc0(m,:)))
        f_0(m,k-1)=1/(tc0(m,k)-tc0(m,k-1)); % frequency from each time
stamp
    end

    %%%
    n1_cycle=1;
    for i=2:1:length(c1)
        if ((c1(1,i) >= 0 && (c1(1,i-1) < 0 )))
            tc1(m,n1_cycle)=mean([t1(1,i) t1(1,i-1)]); % Time stamp
            n1_cycle=n1_cycle+1;
        end
    end

    for k=2:1:length(nonzeros(tc1(m,:)))
        f_1(m,k-1)=1/(tc1(m,k)-tc1(m,k-1)); % frequency from each time
stamp
    end

end

```

```
figure(13);clf;
plot(1:1:length(nonzeros(f_0(1,:))),nonzeros(f_0(1,:)),'r*','LineWidth
h',1,'MarkerEdgeColor','r','MarkerFaceColor','r','MarkerSize',10);gri
d on;hold on;
plot(1:1:length(nonzeros(f_1(1,:))),nonzeros(f_1(1,:)),'bo','LineWidth
h',2,'MarkerEdgeColor','b','MarkerSize',10);hold on;

xlabel('Number of Complete(2\pi)cycles
','fontSize',12,'fontweight','b');
ylabel('Frequency (Hz)','fontSize',12,'fontweight','b');
set(gcf,'color',[1 1 1]);
set(gca,'FontSize',12,'fontName','Times','fontweight','b');
legend('Rx1-f1','Rx2-f2');
```

ANNEXURE C

Data sheet of mixer (MARKI M3-0309)



DOUBLE-BALANCED MIXERS

M3-0309

Features

- LO/RF 3.0 to 9.0 GHz
- IF DC to 4.0 GHz
- 5.5 dB Typical Conversion Loss
- 35 dB Typical LO to RF Isolation
- Carrier and Surface-Mount Outlines
- Multi-Octave Band RF and LO



Electrical Specifications - Specifications guaranteed from -55 to +100°C, measured in a 50-Ohm system.

Parameter	LO (GHz)	RF (GHz)	IF (GHz)	Min	Typ	Max	Diode Option LO drive level (dBm)
Conversion Loss (dB)	3.0-9.0 3.0-9.0	3.0-9.0 3.0-9.0	DC-2.0 2.0-4.0		5.5 6.5	7.5 9.0	
Isolation (dB)				25	32		
LO-RF	3.0-9.0	3.0-9.0			23		
LO-IF	3.0-9.0	3.0-9.0			25		
RF-IF	3.0-9.0	3.0-9.0					
Input 1 dB Compression (dBm)	3.0-9.0	3.0-9.0			+2 +6 +8 +11 +14		L (+7 to +10) M (+10 to +13) N (+13 to +16) H (+16 to +19) S (+19 to +22)
Input Two-Tone Third Order Intercept Point (dBm)	3.0-9.0	3.0-9.0			+12 +15 +18 +21 +24		L (+7 to +10) M (+10 to +13) N (+13 to +16) H (+16 to +19) S (+19 to +22)

Part Number Options

Please specify diode level and package style by adding to model number:	
Package Style(s) ^{1,2}	Example
E , EP , EZ , P	M3-0309 L E

¹Connectorized test fixtures available for most carrier and surface mount packages. Consult factory.

²For non-connectorized packages, specify I-port configuration by adding -1 or -2 suffix to model number. Default is -2 configuration when not specified.

Marki Microwave reserves the right to make changes to the product(s) or information contained herein without notice. Marki Microwave makes no warranty, representation or guarantee regarding the suitability of its products for any particular purpose, nor does Marki Microwave assume any liability whatsoever arising out of the use of or application of any product.

215 Vineyard Court, Morgan Hill, CA 95037 | Ph: 408.778.4200 | Fax 408.778.4300 | info@markimicrowave.com



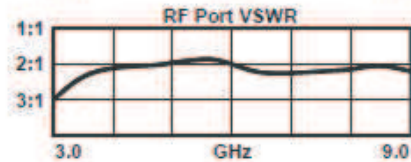
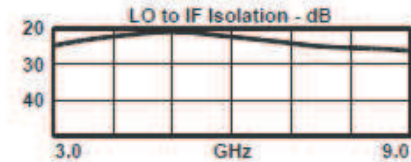
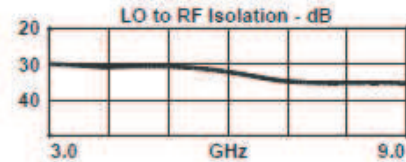
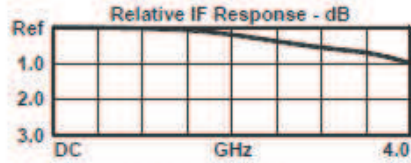
DOUBLE-BALANCED MIXERS

Page 2

M3-0309

LO/RF 3.0 to 9.0 GHz
IF DC to 4.0 GHz

Typical Performance



DATA SHEET NOTES:

1. Mixer Conversion Loss Plot is done with an IF frequency of 100 MHz.
2. Mixer Noise Figure typically measures within +0.5 dB of conversion loss for IF frequencies greater than 5 MHz.
3. Conversion Loss typically degrades less than 0.5 dB for LO drives 2 dB below the lowest and 3 dB above highest nominal LO drive levels.
4. Conversion Loss typically degrades less than 0.5 dB at +100°C and improves less than 0.5 dB at -55°C.
5. Maximum input power is +23 dBm at +25°C, derated linearly to +20 dBm at +100°C.
6. Specifications are subject to change without notice. Contact Marki Microwave for the most recent specifications and data sheets.
7. Catalog mixer circuits are continually improved. Configuration control requires custom mixer model numbers and specifications.

Marki Microwave reserves the right to make changes to the product(s) or information contained herein without notice. Marki Microwave makes no warranty, representation, or guarantee regarding the suitability of its products for any particular purpose, nor does Marki Microwave assume any liability whatsoever arising out of the use or application of any product.

© Marki Microwave, Inc.



215 Vineyard Court, Morgan Hill, CA 95037 | Ph: 408.778.4200 | Fax: 408.778.4300 | info@markimicrowave.com

www.markimicrowave.com

ANNEXURE D

Data sheet of amplifier (HWLF6090-30-10)

Amplifier HWLF6090-30-10

Model	Frequency (GHz)	Gain (dB) min	P-1dB (dBm) min	VSWR max	Gain flatness (dB)	Noise Figure (dB) max	DC (V)	Operation temperature	Storage temperature
0902367A	6-9	31.5	11	1 : 1.8	±0.9	2.6	+12	-40~+85℃	-55~+100℃
0902368A	6-9	33.2	12		±1	2.6	+12		
0902369A	6-9	32.9	12		±1	2.6	+12		
0902370A	6-9	33.5	12		±0.9	2.6	+12		
0902371A	6-9	33.1	12		±0.8	2.6	+12		
0902372A	6-9	32.5	12		±0.9	2.6	+12		
0902373A	6-9	33.6	12		±0.8	2.6	+12		
0902374A	6-9	33.3	12		±0.9	2.6	+12		

Test:

Date:

Inspect:

Date:

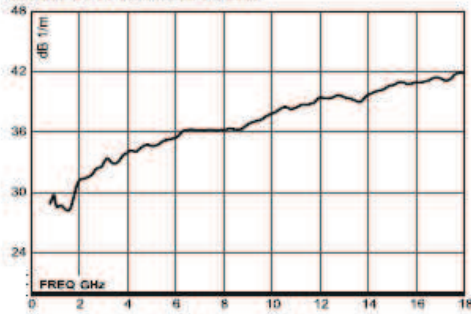
ANNEXURE E

Reference Antenna

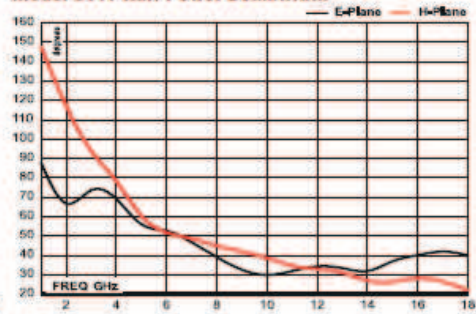


EMC Antennas Double-Ridged Waveguide Horn Model 3117

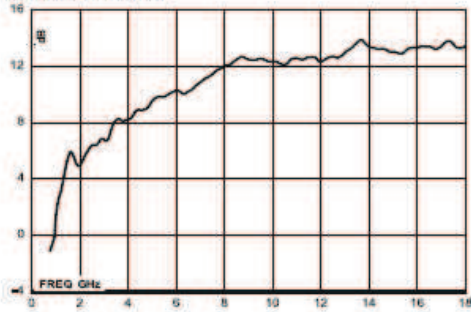
Model 3117 Antenna Factor



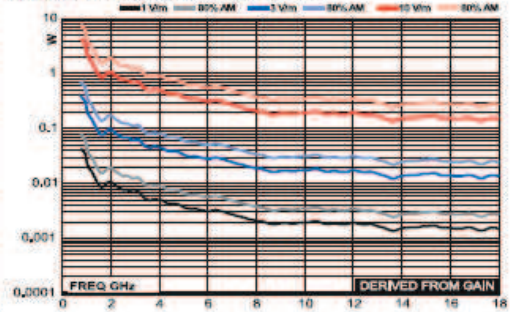
Model 3117 Half Power Beamwidth



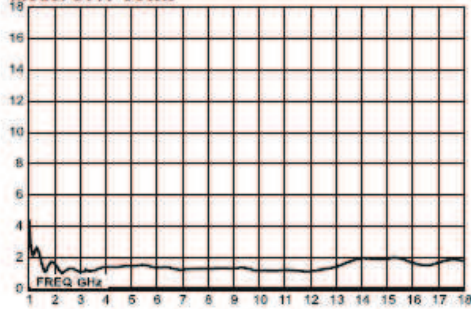
Model 3117 Gain



Model 3117 Forward Power @ 1 m



Model 3117 VSWR



www.ets-lindgren.com

ANNEXURE F

Agilent 87300B: Directional Coupler

Specifications

Model	87300B	87300C	87300D
Frequency range (GHz)	1 to 20 GHz	1 to 26.5 GHz	6 to 26.5 GHz
Nominal coupling and variation with respect to output (or coupling factor over insertion loss)	10 ± 0.5 dB	10 ± 1 dB	10 ± 0.5 dB
Frequency sensitivity	± 0.35 dB, 1 to 20 GHz	± 0.5 dB, 1 to 26.5 GHz	± 0.3 dB
Directivity	> 16 dB	> 14 dB, 1 to 12.4 GHz > 12 dB, 12.4 to 26.5 GHz	> 13 dB
Maximum SWR	1.35	1.35, 1 to 12.4 GHz 1.50, 12.4 to 26.5 GHz	1.40
Insertion loss	< 1.5 dB	< 1.2 dB, 1 to 12.4 GHz < 1.7 dB, 12.4 to 26.5 GHz	< 1.3 dB
Typical insertion loss (dB, f = freq. in GHz)	0.6 + 0.04f	0.6 + 0.04f	0.6 + 0.025f
Power rating			
Average	20 W	20 W	20 W
Peak	3 kW	3 kW	3 kW
Connectors	SMA (f)	3.5 mm (f)	3.5 mm (f)
Weight in grams (oz)	74 (2.6)	60 (2.1)	81.2 (1.1)

Model	87301B	87301C	87301D	87301E
Frequency range (GHz)	10 to 46 GHz	10 to 50 GHz	1 to 40 GHz	2 to 50 GHz
Nominal coupling and variation with respect to output (or coupling factor over insertion loss)	10 ± 0.7 dB	10 ± 0.7 dB	13 ± 1 dB	10 ± 1 dB
Frequency sensitivity	± 0.3 dB	± 0.5 dB	± 1.2 dB, 1 to 40 GHz	± 0.6 dB, 2 to 26.5 GHz ± 0.8 dB, 2 to 50 GHz
Directivity	> 10 dB	> 10 dB	> 14 dB, 1 to 20 GHz > 10 dB, 20 to 40 GHz	> 13 dB, 2 to 26.5 GHz > 10 dB, 26.5 to 50 GHz
Maximum SWR	1.80	1.80	1.5, 1 to 20 GHz 1.7, 20 to 40 GHz	1.5, 2 to 26.5 GHz 1.8, 26.5 to 50 GHz
Insertion loss	< 1.9 dB	< 1.9 dB	< 1.2 dB, 1 to 20 GHz < 1.9 dB, 20 to 40 GHz	< 2 dB
Typical insertion loss	0.8 + 0.022f	0.8 + 0.022f	0.4 + 0.035f	0.55 + 0.025f
Power rating				
Average	20 W	20 W	20 W	20 W
Peak	3 kW	3 kW	3 kW	3 kW
Connectors	2.92 mm (f)	2.4 mm (f)	2.4 mm (f) or 2.92 mm (f) for Option 292	2.4 mm (f)
Weight in grams (oz)	28.4 (1)	28.4 (1)	37 (1.3)	34 (1.2)

LIST OF FIGURES

Figure 1.1: GPS methodology for position estimate [10].....	43
Figure 1.2 : Triangulation algorithm.....	45
Figure 1.3 : Angle-of-Arrival technique	48
Figure 1.4 : Outline of current wireless-base positioning system.....	52
Figure 2.1: FMCW concept: transmitted modulation patters vs. time-delayed received modulation patterns from a remote target.....	72
Figure 2.2: DMDT-Time delay measurement scheme	75
Figure 2.3: Simulated Signals- Signals1 & Signal2.....	75
Figure 2.4: Architecture for the 2D localization.....	78
Figure 2.5: Systematic Configuration for the 2D localization.....	81
Figure 2.6: Scheme for signal measurement: right angle triangle ABC is shown on the left side while whole scenario of the system is depicted on the right side.....	83
Figure 2.7: Orthogonal structure of receiver antennas for 3D measurements	85
Figure 2.8: Representation of LBS for Initial Test	86
Figure 2.9: Representation of AT for Initial Test	87
Figure 2.10: Initial Measurement Setup undar Controlled Environment	88
Figure 2.11: Optics Interferometry Technique	90
Figure 2.12: Deviation in AoA ($\delta\alpha$) at $\alpha=60^\circ$	92
Figure 2.13: Deviation in AoA ($\delta\alpha$) and its mean value over (0° - 180°)	93
Figure 2.14: Mean deviation in AoA ($\delta\alpha$)	94
Figure 3.1: Schematic diagram of complete ILS	104
Figure 3.2: Layout of equal Split-Divider.....	105
Figure 3.3: Measured and Simulated results.....	106
Figure 3.4: Mixer-Marki Microwave.....	107
Figure 3.5: Filters.....	109
Figure 3.6: Filter characterization.....	110
Figure 3.7: Amplifier-HWLF6090-30-10.....	110
Figure 3.8: Amplifier characterization.....	111
Figure 3.9: Sinuous antenna with balun in orthogonal position	113
Figure 3.10: Crossed-dipole with quadratic phase.....	114

Figure 3.11: Circular Polarization diversity scheme	114
Figure 3.12: Circular Polarized Planar Antenna-Single Port.....	117
Figure 3.13: Return loss results	117
Figure 3.14: Ferrite materials used during measurement.....	118
Figure 3.15: Simulated and Measured Axial Ratio.....	119
Figure 3.16: Simulated and Measured Gains (LBS-antenna)	120
Figure 3.17: Left & Right side show the radiation pattern in z-x plane at 6.5 & 8 GHz (LBS-antenna).....	120
Figure 3.18: Left & Right side show the radiation pattern in x-y plane at 6.5 & 8 GHz (LBS-antenna).....	121
Figure 3.19: Connection between 90°-BLC and Antenna	122
Figure 3.20: Return Loss performance of cross diode	123
Figure 3.21: Improved 10 dB Return Loss Bandwidth.....	124
Figure 3.22: Shift in resonance frequency (c_x is in mm).....	124
Figure 3.23: Widening of the bandwidth (r_{at} is in mm)	125
Figure 3.24: Left-antenna configuration; Right-fabricated antenna	126
Figure 3.25: Layout of designed 90°-Hybrid Branch Line Coupler (dimensions are in mm)	127
Figure 3.26: Simulated S-parameters of the designed 90°-Hybrid Branch Line Coupler	128
Figure 3.27: Measured values of the fabricated 90°-Hybrid Branch Line Coupler.....	128
Figure 3.28: Scheme for dual CP by introducing 90° phase shift.....	129
Figure 3.29: Simulated and Measured: Return Loss & Crosstalk (AT-antenna).....	130
Figure 3.30: Simulated and Measured Axial ratio (AT-antenna)	131
Figure 3.31: Simulated and Measured Antenna gains (AT-antenna)	132
Figure 3.32: Left and Right side show the radiation pattern in z-x plane at 6.5 & 8 GHz (AT-antenna).....	133
Figure 3.33: Left and Right side show the radiation pattern in x-y plane at 6.5 & 8 GHz (AT-antenna).....	133
Figure 3.34: Realized Active-Tag (Indoor Localization System).....	134
Figure 3.35: Realized LBS (Indoor Localization System) for 3D Measurements. 1. Agilent E8267D, 2. Agilent E4431B, 3. DC supply, 4. Mixers, 5. Filters, 6. Amplifiers, 7. Transmitter	

Antenna, 8(a-d). Receiver Antennas, 9. Oscilloscope, 10. RF Switches, 11. Data Acquisition Card (Desk-Top), 13. Splitter.....	135
Figure 3.36: Power losses in transmitter section	136
Figure 3.37: Power losses in the Active-Tag	137
Figure 3.38: Power losses in the receiver section	137
Figure 4.1: Flow chart of Indoor Localization System	147
Figure 4.2: Baseband signals acquired by the Data Acquisition Card.....	149
Figure 4.3: Baseband signals over $T_m=10$ ms	151
Figure 4.4: Computed frequencies over $T_m=10$ ms	152
Figure 4.5: Successive Mean Approach Algorithm (SMAA).....	153
Figure 4.6: Output of the SMA algorithm	154
Figure 4.7: Performance analysis of SMAA.....	154
Figure 4.8: Jitters near zero-crossing.....	155
Figure 4.9: Received baseband and RF-leakage signals.....	156
Figure 4.10: Received baseband signals at 0.82 m	156
Figure 4.11: Calibration of ILS.....	158
Figure 4.12: Calibration-Observed delays by the receivers.....	160
Figure 4.13: 2D-field measurements in a real indoor environment.....	162
Figure 4.14: A) 2D radial-distance, B) Root-mean-square error	163
Figure 4.15: A) 2D-Angle of azimuth and, B) Root-mean-square error	164
Figure 4.16: 3D-Field measurements in a real indoor environment	165
Figure 4.17: 3D-Radial-Distance (A) and root-mean-square error (B) in horizontal plane ..	166
Figure 4.18: 3D-Angle of azimuth (a) and root-mean-square error (B) in horizontal plane..	167
Figure 4.19: 3D-Radial-Distance (A) and root-mean-square error (B) in vertical plane.....	168
Figure 4.20: 3D-Angle of elevation (A) and root-mean-square error (B) in vertical plane..	169
Figure 4.21: Actual and estimated radial-distance for maximum range.....	171
Figure 4.22: Estimated radial-distance and root-mean-square error for maximum range.....	172
Figure 4.23: Estimated radial-distance and root-mean.....	173
Figure 4.24: RMS-Error in radial-distance estimates vs. SNR.....	174
Figure 4.25: Setup for field measurement, a whiteboard used for strong scatter	175
Figure 4.26: System set up in indoor environment.....	176
Figure 4.27: Estimated positions with/without the strong scatterer.....	177

Figure 4.28: Scatterer, estimated radial-distance and its root-mean-square error	180
Figure 4.29: Scatterer, estimated AoA and its root-mean-square error	181
Figure 4.30: Multipaths due to scatterer	182
Figure 4.31: Error analysis in radial-distance (multipaths due to scatterer)	184
Figure 4.32: Error analysis in angle of arrival (ζ , effect of multipath due to scatterer).....	185
Figure 4.33: SNR versus successful computation.....	186
Figure 4.34: Performance in Non-Line-of-Sight case.....	187
Figure 4.35: Error analysis in NLoS case	188
Figure 4.36: Baseband signals acquired by 1GHz and 500 MHz.....	190
Figure 4.37: Error analysis in radial-distance by 1 GHz and 500 MHz bandwidth.....	191
Figure 4.38: Error analysis in estimated AoA by 1 GHz and 500 MHz bandwidth.....	192
Figure 4.39: Set-up for angle of deviation estimation for a fixed position of Active-Tag to varying d_{baseline}	195
Figure 4.40: PWC-Estimation of deviation for Setup-1	196
Figure 4.41: PWC-Schematic diagram for the estimation of deviation in AoA at $\alpha=60^\circ$ over 45°-to-90° while varying the baseline	197
Figure 4.42: PWC-Estimated radial-distance with different baselines.....	198
Figure 4.43: PWC-Estimated angle of arrival with different baselines	199
Figure 4.44: Comparison of $\delta\alpha$ between 45° and 90° for radial-distance between 1.2 m & 1.7 m	200
Figure 4.45: Estimated rms values of range, angle and deviation in AoA	202
Figure 4.46: Measurement scheme for coupling between receiver antennas (symmetric structure)	203
Figure 4.47: Antenna coupling at LBS	204
Figure 5.1: Restructure of LBS antennas.....	211
Figure 5.2: Radio-Triggered ID component [19].....	214
Figure 5.3: FMCW system presented in [27].....	216
Figure 5.4: Basic principle of APR: Barkhausen's criteria [25]	216

LIST OF TABLES

Table 1.1: Performance Metrics.....	51
Table 2.1: ILS: LBS and Active-Tag.....	80
Table 2.2: Path-Difference & AoA Computation.....	88
Table 2.3: NFA Computation.....	94
Table 3.1: Equal-Split Divider: Fabricated.....	106
Table 3.2: Mixer: Marki M30309LP.....	107
Table 3.3: Mixer: Conversion Loss.....	108
Table 3.4: Mixer: Leakage Power.....	108
Table 3.5: Passband Filter: REACTEL, INC.....	109
Table 3.6: Amplifier: HWLF6090-30-10.....	111
Table 3.7: Optimized parameters of designed antenna (Active-Tag).....	126
Table 3.8: Received power by receiver antenna.....	138
Table 4.1: Calibration: Actual Position of Active-Tag.....	159
Table 4.2: Calibration: Delay Determinations.....	160
Table 4.3: 3D Position: Error Analysis.....	169
Table 4.4: Window: Estimated Samples in 20°-by-10 cm.....	177
Table 4.5: Signal Setups.....	189
Table 4.6: IB: Calibration.....	189
Table 4.7: Estimated Errors.....	192
Table 4.8: PWC Deviation: Root-mean-square values.....	201

REFERENCES

- [1] S. Buyukcorak, T. Erbas, G. K. Kurt, and A. Yongacoglu, "Indoor localization applications," Signal Processing and Communication Applications Conference, SIU 2014, pp. 1239-1242.
- [2] B. Jensen, R. Kruse, and B. Wendholt, "Application of indoor navigation technologies under practical conditions," Workshop on Positioning, Navigation and Communication, WPNC 2009, pp 267-273.
- [3] D. J. Seo, and J. Kim, "Development of autonomous navigation system for an indoor service robot application," Int. Conf. On Control, Automation and Systems, ICCAS 2013, pp. 204-206.
- [4] J. A. F. Marigal, E. C. Martin, J. Gonzalez, C. Galindo, and J. L. Blanco, "Application of UWB and GPS technologies for vehicle localization in combined indoor-outdoor environments," Int. Conf. On Signal Processing and Its Applications, ISSPA 2007, pp. 1-4.
- [5] E. Lohnert, W. Bar, E. Gohler, and J. Mollmer, "Galileo/GPS indoor navigation & positioning for SAR and tracking applications," Int. Conf. On Indoor Positioning and Indoor Navigation, IPIN 2010, pp. 1-6.
- [6] U. Yayan, B. Akar, F. Inan, and A. Yazici, "Development of indoor navigation software for intelligent wheelchair," IEEE Int. Sympo. On Innovations in Intelligent Systems and Applications, INISTA 2014, pp. 325-329.
- [7] http://www.phonearena.com/phones/Samsung-Galaxy-Note-3_id7984
- [8] http://www.phonearena.com/phones/Apple-iPhone-6-Plus_id8908
- [9] http://www.phonearena.com/phones/Google-Nexus-5_id8148
- [10] <http://copter.ardupilot.com/wiki/common-gps-how-it-works/>
- [11] <http://en.wikipedia.org/wiki/Trilateration>

-
- [12] A. E. C. Redondi, and E. Amaldi, "Optimizing the placement of anchor nodes in RSS-based indoor localization systems," Ann. Mediterranean Ad Hoc netw. Workshop, MED-HOC-Net 2013, pp. 8-13.
- [13] J. N. Ash, and R. L. Moses, "On optimal anchor node placement in sensor localization by optimization of subspace principal angles," in ICASSP, 2008, pp. 2289-2292.
- [14] S. Hara, and T. Fukumura, "Determination of the placement of anchor nodes satisfying a required localization accuracy," in Wireless Communication Systems. 2008. ISWCS '08. IEEE International Symposium on, oct. 2008, pp. 128 -132.
- [15] G. Yanying, A. Lo, L. Niemegeers, "A survey of indoor positioning systems for wireless personal networks", IEEE Communications Surveys & Tutorials, vol. 11, no. 1, 2009, pp. 13 – 32.
- [16] N. Jardak, and N. Semama, "Indoor Positioning Based on GPS-Repeaters: Performance Enhancement using an Open Code Loop Architecture," IEEE Transactions on Aerospace and Electronic Systems, vol. 45, no. 1, 2007, pp. 347 – 359.
- [17] P. Gulden, S. Roehr, M. Christmann, "An overview of wireless local positioning system configurations", IEEE Int. Microwave Workshop on Wireless Sensing, Local Positioning, and RFID, Sept. 2009, pp. 1 – 4.
- [18] K. Pahlavan, L. Xinrong J. P. Makela, "Indoor geolocation science and technology", IEEE Communications Magazine, vol. 40, no. 2, Feb. 2002, pp. 112 – 118.
- [19] H. Yucel, A. Yazici, and R. Edizkan, " A survey of indoor localization systems," Signal Processing and Communication Applications Conference, SIU 2014, pp. 1267-1270.
- [20] F. Li, C. Zhao, G. Ding, J. Gong, C. Liu, and F. Zhao, "A Reliable and Accurate Indoor Localization Method Using Phone inertial Sensors," in ACM UbiComp, 2012, pp. 421-430.

-
- [21] Hui Liu, Houshang Darabi, Pat Banerjee, and Jing Liu, "Survey of Wireless Indoor Positioning Techniques and Systems," in *IEEE Trans. on systems, man, and cybernetics-PartC*, Nov. 2007, vol. 37, pp. 1067–1080.
- [22] I. Lee, G. Yoon, and D. Han, "Nerimi: WiFi-based subway navigation system," IEEE MTT-S Int. Micro. Workshop Series on Intelligent Radio for Future Personal Terminals, IMWS-IRFPT 2011, pp. 1-2.
- [23] A. Flueraşu, A. Vervisch-Picois, G. Boiero, G. Ghinamo, P. Lovisolo, and N. Samama, "Indoor positioning using GPS transmitter: Experimental results," Int. Conf. on Indoor Positioning and Indoor Navigation, IPIN 2010, pp. 1-9.
- [24] F. L; Piccolo, "A new cooperative localization method for UMTS cellular networks," IEEE Global Telecommunications Conference, GLOBECOM 2008, pp. 1-5.
- [25] G. Heinrichs, "Using of Rake receiver architecture for combining GNSS and CDMA cellular wireless location," IEEE 7th Int. Sympo. On Spread Spectrum Techniques and Applications, pp. 787-791, 2002.
- [26] M. Brugger, T. Christ, F. Kemeth, S. Nagy, M. Schaefer, and M. M. Pietrzyk, "The FMCW Technology-Based Indoor Localization System," Ubiquitous Positioning Indoor Navigation and Location Based Service, UPINLBS 2010, pp. 1-6.
- [27] B. Waldmann, R. Weigel, R. Ebel, and M. Vossiek, "An ultra-wideband local positioning system for highly complex indoor environments," Int. Conf. On Localization and GNSS, ICL-GNSS 2012, pp. 1-5.
- [28] T. Ussmueller, M. Jung and R. Weigel, "Synthesizer concepts for FMCW based locatable wireless sensor nodes," IEEE MTT-S International Microwave Workshop on Wireless Sensing , Local Positioning, and RFID, IMWS 2009, pp. 1-4.

-
- [29] N. Obeid, M. Heddebaut, F. Boukour, C Loyez, and N. Rolland, "Millimeter Wave Ultra Wide Band Short range Radar Localization Accuracy," IEEE Vehicular technology Conference, VTC Spring 2009, pp. 1-5.
- [30] N. Patwari, A. O. Hero III, M. Perkins, N. S. Correal, and R. J. O'Dea, "Relative location estimation in wireless sensor networks," IEEE Trans. Signal Process., vol 51, no. 8, pp. 2137-2148, 2003.
- [31] Z. Zheng, J. Hua, Y. W, H. Wen, and L. Meng, "Time of arrival and Time Sum of arrival based NLOS identification and Localization," Int. Conf. Communication Technology, ICCT 2014, pp. 1129-113.
- [32] Seyed A. (Reza) zekavat, and R. Michael Buehrer, "Handbook of positioning Location: Theory, Practice and Advances," John Wiley & Sons, Inc. 2012.
- [33] L. Kumar, A. Tripathy, and R. M. Hegde, "Robust Multi-source Localization Over Planar arrays Using MUSIC-group Delay Spectrum," IEEE Trans. Sig. Pro. 2014.
- [34] B. D. Van Veen and K. M. Buckley, "Beamforming: A versatile approach to spatial filtering," *IEEE ASSP Mag.*, vol. 5, no. 2, pp. 4-24, Apr. 1988.
- [35] P. Stoica and R. L. Moses, *Introduction to Spectral Analysis*. Englewood Cliffs, NJ: Prentice-Hall, 1997.
- [36] B. Ottersten, M. Viberg, P. Stoica, and A. Nehorai, "Exact and large sample ML techniques for parameter estimation and detection in array processing," in *Radar Array Processing*, S. S. Haykin, J. Litva, and T. J. Shepherd, Eds. New York: Springer-Verlag, 1993, pp. 99-151.
- [37] T. Huang, and A. S. Mohan, "Effect of array mutual coupling on near-field DOA estimation," IEEE CCECE 2003 Canadian Conf. On elect; and Computer Engineering, pp. 1881-1884.
- [38] D. S. Yang, J. Shil, and B. S. Liu, "Adaptive trarget tracking for wideband sources in near field," Int; Conf; on Informtion Fusion, FUSION 2009, pp. 315-318.

-
- [39] W. Wang, and S. A. Zekavat, "A novel semi-distributed localization via multi-node TOA-DOA fusion," *IEEE Trans. Veh. Technol*, vol. 58, no; 7, pp. 3426-3435, 2009.
- [40] W. Wang, and S. A. Zekavat, "Comparison of semi-distributed multi-node TOA-DOA fusion localization and GPS-aided TOA (DOA) fusion localization for manets," *EURASIP J; Adv. Signal process.*, vol. 2008, Article ID 439523, 16 pages, 2008. Doi: 10.1155/2008/439523, 2008.
- [41] B. Li, "Terrestrial mobile user positioning using TDOA and fingerprinting techniques," PhD thesis, School of Surveying & Spatial Information Systems, University of New South Wales, Sydney, Australia, 2006.
- [42] V A. Papapostolou, X. Wendong, and H. Chaouchi, "Cooperative fingerprint-based indoor localization using Self-Organizing Maps," *Int. Wireless Communications and Mobile Computing Conference, IWCMC 2011*, p.p. 1814-1819.
- [43] SAP. Kontkanen, P. Myllymäki, T. Roos, H. Tirri, K. Valtonen, and H. Wetzig, "Topics in probabilistic location estimation in wireless networks," in *Proc. 15th IEEE Symp. Pers., Indoor, Mobile Radio Commun.*, Barcelona, Spain, Sep. 2004, vol. 2, pp. 1052–1056.
- [44] P. Torteeka, and Xiu Chundi, "Indoor positioning based on Wi-Fi Fingerprinting Technique using Fuzzy K-Nearest Neighbor," *Int. Burban Conf; on Applied Asciences and Technology, IBCAST 2014*, pp. 461-465.
- [45] B; Kachimeczyk, D. Dzaik, and J. W. Kulesza, "RFID-Hybrid Scene Analysis-Neural Network system for 3D Indoor Positioning optimal system arrangement approach," *IEEE Int. Instrument and Measurement Technology Conf. Proc., I2MTC 2014*, pp. 191-196.
- [46] V. Vapnik, *The Nature of Statistical Learning Theory*. New York: Springer, 1995.
- [47] P. Prasithsangaree, P. Krishnamurthi, and P. K. Chrysanthis, "On indoor position with wireless LANs," in *Proc. IEEE Int. Symp. Pers. Indoor, Mobile Radio Commun.*, Sep. 2002, vol. 2, pp. 720–724.

-
- [48] D. Macii, F. Trenti, and P. Pivato, "A robust wireless proximity detection technique based on RSS and ToF measurements," *IEEE Int. Workshop on Measurements and Networking Proc. M&N 2011*, pp. 31-36.
- [49] J. Hightower, R. Want, and G. Borriello, "SpotON: An indoor 3D location sensing technology based on RF signal strength," Univ. Washington, Seattle, Tech. Rep. UW CSE 2000-02-02, Feb. 2000.
- [50] M. Vossiek, M. Wiebking, L. Gulden, P. Weighardt, and J. Hoffmann, "Wireless local positioning—Concepts, solutions, applications," in *Proc. IEEE Wireless Commun. Netw. Conf.*, Aug. 2003, pp. 219–224.
- [51] UbiSense Company. <http://www.ubisense.net>
- [52] P. K. Enge, "The global positioning system: Signals, measurements and performance," *Int. J. Wireless Inf. Netw.*, vol. 1, no. 2, pp. 83–105, 1994.
- [53] S. Manapure, H. Darabi, V. Patel, and P. Banerjee, "A comparative study of radio frequency-based indoor location systems," in *Proc. IEEE Int. Conf. Netw., Sens. Control*, 2004, vol. 2, pp. 1265–1270.
- [54] P. Krishnan, A. S. Krishnakumar, W.-H. Ju, C. Mallows, and S. Ganu, "A system for LEASE: Location estimation assisted by stationary emitters for indoor RF wireless networks," in *Proc. IEEE INFOCOM*, Mar. 2004, pp. 21–32.
- [55] M. Eallbaum, "Wheremops: An indoor geolocation system," in *Proc. IEEE Int. Symp. Pers., Indoor, Mobile Radio Commun.*, Sep. 2002, vol. 4, pp. 1967–1971.
- [56] A. Smailagic, D. P. Siewiorek, J. Anhalt, D. Kogan, and Y. Wang, "Location sensing and privacy in a context aware computing environment," in *Proc. Int. Conf. Pervasive Comput.*, May 2001, pp. 10–17.
- [57] A. Kotanen, M. Hannikainen, H. Leppakoski, and T. D. Hamalainen, "Experiments on local positioning with Bluetooth," in *Proc. IEEE Int. Conf. Inf. Technol.: Comput. Commun.*, Apr. 2003, pp. 297–303.

-
- [58] J. J. Caffery and G. L. Stuber, "Overview of radiolocation in CDMA cellular system," *IEEE Commun. Mag.*, vol. 36, no. 4, pp. 38–45, Apr. 1998.
- [59] P. Cherntanomwong, and D. J. Suroso, "Indoor Localization System using Wireless Sensor Networks for Stationary and Moving Target," *Inte. Conf. On Information, Communication and Signal Processing, ICICS 2011*, pp. 1-5.
- [60] Y. Gwon and R. Jain, "Error characteristic and calibration-free techniques for wireless LAN-based location estimation," in *Proc. Mobi- Wac'04*, Philadelphia, PA, Oct. 1, 2004, pp. 2–9.
- [61] J. Kwon, B. Dundar, and P. Varaiya, "Hybrid algorithm for indoor positioning using wireless LAN," *IEEE Veh. Technol. Conf.*, vol. 7, pp. 4625–4629, Sep. 2004.
- [62] Y. Gwon, R. Jain, and T. Kawahara, "Robust indoor location estimation of stationary and mobile users," in *Proc. IEEE INFOCOM*, Mar. 2004, vol. 2, pp. 1032–1043.
- [63] V. Otsason, A. Varshavsky, A. LaMarca, and E. de Lara, "Accurate GSM indoor localization," *UbiComp 2005, Lecture Notes Computer Science, Springer-Verlag*, vol. 3660, pp. 141–158, 2005.
- [64] Y. Cho, J. Kim, M. J. Y. Lee, and S. Park, "GPRS based Wi-Fi radio map construction from real/virtual indoor dynamic surveying data," *Int. Conf. on Control, Automation and Systems, ICCAS 2013*, pp. 712-714.
- [65] A. B-Delai, J. C. Cousin, R. Ringot, Ahmed Mamouni, and Y. Leroy, "Microwave Short Baseline Interferometers for Localization Systems," *IEEE Trans. On Instrumentation and Measurement*, vol; 50, no; 1, pp. 32-39, Feb 2001.
- [66] A. Bocquet, C. Loyez, and A. B-Delai, "Using Enhanced-TDOA Measurement for Indoor Positioning," *IEEE Microwave and Wireless Components Letters*, vol; 15, no; 10, pp; 612-614, Oct 2005.
- [67] V. Y. Vu, and A. B. Delai, "A New Digital Receiver Architecture for Direction Finding Systems," *Int. Conf. on Communication and Electronics (ICC 2006)*, pp; 430-433, 2006.

-
- [68] V. Y. Vu, and A. B. Delai, "Digital Solution for inter-vehicle localization system by means of Direction-Of-Arrival," Int. Symp. on Intelligent Signal Processing and Communication Systems (ISPACS 2006), pp; 875-878, 2006.
- [69] S. Galler, W. Geork, J. Schroeder, K. Kyamakya, and T. Kaiser, "Combined AOA/TOA UWB localization," Int. Symp. On Communications and information Technologies, ISCIT 2007, pp. 1049-1053.
- [70] I. B. Shirokov, G. V. Jandieri, D. V. Sinitsyn, and D. I. Martynjuk, " Multipath Angle-Of-Arrival And Phase Progression Measurements On Microwave Line-Of-Sight links," Ant. and Prog. Proc, EuCAP 2006, pp. 1-6.
- [71] M. Vossiek, and P. Guldenl, "The Switched Injection-Locked Oscillator: A Novel Versatile Concept for Wireless Transponder and Localization Systems", IEEE Transactions on Microwave Theory & Technique, vol. 56, no. 4, 2008, pp. 859-866.
- [72] D. Boontrai, T. Jingwangsa, and P. Cherntanomwong, "Indoor Localization Technique using Passive RFID Tags," ISCIT 2009, pp. 922-926.
- [73] S. Wehrli, R. Gierlich, J. Huttner, D. Barras, F. Ellinger, and H. Jackel, "Integrated Active Pulsed Reflector for an Indoor Local Positioning System", IEEE Transactions on Microwave Theory & Technique, vol. 58, no. 2, 2010, pp. 267-276.
- [74] Y. Qi, H. Kobayashi, and H. Suda, "Analysis of wireless geolocation in a non-line-of-sight environment," IEEE Trans. Wireless Commun., vol. 5, no. 3, pp; pp. 672-681, 2006.
- [75] I. Guvenc, C. C. Chong, and F. Watanable, "NLOS identification and mitigation for UWB localization systems," Proc. Of Wireless Communication and Networking Conf., pp. 1571-1576, 2007.
- [76] J. Khodjaev, Y. Park, and A. S. Malik, "Survey of NLoS identification and error mitigation problems in UWB-based positioning algorithms for dense environments," Ann. Telecommun., vol. 65, no. 5-6, pp. 301-311, 2010.

-
- [77] C. P. Vega, and G. Garcia, "Polarisation behaviour in the indoor propagation channel," IEE, electronics Letters, pp. 898-899, March 1997.
- [78] R. Szumny, K. Kurek, S. Kozlowski, and J. Modelski, "Influence of antennas characteristics on accuracy of TOA indoor positioning systems," Microwave, Radar and Wireless Communications, MIKON 2008, pp. 1-4.
- [79] J P Ramirez, and D K Borah, "Anchor-cum-Relay Nodes for Localizing a mobile Source and Relaying Source Signals," Vehicular Technology Conference (VTC Fall), 2013 IEEE 78th DOI:10.1109/VTCFall.2013.6692107.
- [80] C. Stenir, and A. Wittneben, "Low Complexity Location Fingerprinting With Generalized UWB Energy Detection Receivers," IEEE Trans. Signal. Proc., vol. 58, no. 03, pp. 1756–1767, March. 2010.
- [81] D.D. Arumugam, J. D. Griffin, D. D. Stancil, and D. S. Ricketts, "Two-dimensional position measurement using magnetoquasistatic fields," IEEE-APS Tropical Conference on Antenna and Propagation in Wireless Communication 2011, pp. 1193-1196.
- [82] D.D. Arumugam, D. D. Stancil, and D. S. Ricketts, "Proximity and orientation sensing using magnetoquasistatic fields and complex image theory," IEEE Vehicular Technology Conference (VTC 2011), pp. 1-5.
- [83] J P. Nikitin, R. Martinez, S. Ramamurthy, H. Leland, G. Spiess, and K. Rao, "Phase based spatial identification of UHF RFID Tags," Intermec Technol. Corp., Everett, WA, USA, 2010 IEEE International Conference on RFID, 2010.
- [84] H. Griffiths, "New ideas in FM radar", Electronics & Communication Engineering Journal, vol. 2, no. 5, Oct. 1990, pp. 185 – 194.
- [85] M.Vossiek at al., "Inverse Synthetic Aperture Secondary Radar Concept for Precise Wireless Positioning", IEEE Transactions on Microwave Theory and Techniques, vol. 55, no. 11, Nov. 2007, pp. 2447 – 2453.
- [86] J. Shefer, R. Klensch, "Harmonic radar helps autos avoid collisions", IEEE Spectrum, vol. 10, no. 5, May 1973, pp. 38 – 45.

-
- [87] B. Colpitts, G. Boiteau, “Harmonic radar transceiver design: miniature tags for insect tracking”, *IEEE Transactions on Antennas and Propagation*, vol. 52, no. 11, Nov. 2004, pp. 2825 – 2832.
- [88] D. Psychoudakis et al., “A Portable Low-Power Harmonic Radar System and Conformal Tag for Insect Tracking”, *IEEE Antennas and Wireless Propagation Letters*, vol. 7, 2008, pp. 444 – 447.
- [89] E. de Moura Presa, et al., “A new microwave harmonic direction-finding system for localization of small mobile targets using passive tags”, *Microw. and Opt. Techn. Letters*, vol. 47, no. 2, Oct. 2005, pp. 134-137.
- [90] J. Cousin, “Radar multistatique d’aide la conduite pour le positionnement 2D de cible à courtes distances par la technique FMCW associe l’interférométrie”, 15^{mes} Journées Nationales Microondes, 2007.
- [91] M. Vossiek at al., “Inverse Synthetic Aperture Secondary Radar Concept for Precise Wireless Positioning”, *IEEE Transactions on Microwave Theory and Techniques*, vol. 55, no. 11, Nov. 2007, pp. 2447 – 2453.
- [92] R. Al Alwai, “RSSI based location estimation in wireless sensors networks,” *IEEE International Conference on Networks (ICON) 2011*, pp. 118-122.
- [93] X. Xiao, X. Jing, S. You, and J. Zeng, “An environmental-adaptive RSSI based indoor positioning approach using RFID,” *International Conference on Advanced Intelligence and Awareness Internet (AIAI 2010)*, pp. 127-130.
- [94] U. Grossmann, M. Schauch, and, S. Hakobyan, “RSSI based WLAN Indoor Positioning with Personal Digital Assistants,” *Intelligent Data Acquisition and Advanced Computing Systems: Technology and Applications, IDAACS 2007*, pp. 653-656.
- [95] K. Wen-Hsing, C. Yun-Shen, J. Gwei-Tai, and L. Tai-Wei, “An intelligent position approach: RSSI-based indoor and outdoor localization scheme in Zigbee networks,” *International Conference on Machine Learning and Cybernetics (ICMLC 2010)*, pp. 2754-2759.

-
- [96] A. Narzullaev, P. YongWang, and J. Hoyoul, "Accurate signal strength prediction based positioning for indoor WLAN systems," Position, Location and Navigation Symposium 2008, Monterey pp. 127-130.
- [97] Widawan, M. Klepal, and D. Pesch, "Influence of Predicted and Measured Fingerprint on the Accuracy of RSSI-based Indoor Location Systems," Position, Navigation and Communication 2007, Hannover, pp. 145-151.
- [98] L. Ruey-Hsuan, W. Jen-Chieh, C. Shao-Hsuan Chang, and C. Sheng-Fuh, "Radar design for wireless indoor positioning applications," European Microwave Conference (2013), Nuremberg, pp. 846-849.
- [99] F. Tappero, B. Merminod, and M. Ciurana, "IEEE 802.11 ranging and multi-lateration for software-defined positioning receiver," in Indoor positioning and Indoor Navigation (IPIN), 2010, pp. 1-6.
- [100] W. Vinicchayakul, and S. Promwong, "Improvement of fingerprinting technique for UWB indoor localization," Information and Communication Technology, Electronic and Electrical Engineering (JICTEE), 2014, pp. 1-5.
- [101] M. Vuckovic, I. Petrovic, D. Vidovic, Z. Kostovic, S. Pletl, and D. Kukolj, "Space grid resolution impact on accuracy of the indoor localization fingerprinting," Telecommunications Forum (TELEFOR), 2011 19th, pp. 321-324.
- [102] S. el Khediri. A. Kachouri, and N. Nasri, "Diverse synchronization issues in wireless sensor networks," International Conference on Microelectronics, ICM 2011, pp. 1-6.
- [103] Bassem R.Mahafza, Introduction to RADAR ANALYSIS, Chapter-5, "Continuous Wave and Pulsed Radar", Page-117.
- [104] B. Lathi, "Modern digital and analog communication systems," The Oxford series in electrical and computer engineering, Oxford University Press, 1998.
- [105] R. Barillet, J. Y. Richard, J. Cermak, and L. Sojdr, "Application of dual-mixer-time-difference multiplication in accurate time-delay measurements," Frequency Control Symposium and Exposition, 2004, pp. 729-733.

-
- [106] Y. Zhang, M. G. Amin, and S. Kaushik, "Localization and Tracking of Passive RFID Tags Based on Direction Estimation," *International Journal of Antenna and Propagation* Hindwai Publishing Corporation, vol 2007, ID 17426, doi. 10.1155/2007/17426.
- [107] R. Szumny, K. Kurek, and J. Modelski, "Attenuation of multipath components using directional antennas and circular polarization for indoor wireless positioning systems," *Radar Conference, EuRAD*, pp. 401-404, 2007.
- [108] S. Wehrli, R. Gierlich, J. Huttner, D. Barras, F. Ellinger, and H. Jackel, "Integrated Active Pulsed Reflector for an Indoor Local Positioning System", *IEEE Transactions on Microwave Theory & Technique*, vol. 58, no. 2, 2010, pp. 267-276.
- [109] M. Vossiek, and P. Guldenl, "The Switched Injection-Locked Oscillator: A Novel Versatile Concept for Wireless Transponder and Localization Systems", *IEEE Transactions on Microwave Theory & Technique*, vol. 56, no. 4, 2008, pp. 859-866.
- [110] "<http://spectrum-instrumentation.com/en/products/m3i2132>".
- [111] Z. Ma, Y. Qiao, B. Lee, and E. Fallon, "Experimental Evaluation of Mobile Phone Sensors," *Signals and Systems Conference (ISSSC 2013)*, LYIT Letterkenny, pp. 1-8.
- [112] J. Cousin, "Radar multistatique d'aide la conduite pour le positionnement 2D de cible à courtes distances par la technique FMCW associé l'interférométrie," *15`mes Journées Nationales Microondes*, 2007 (in french).
- [113] Constantine A. Balanis, "Antenna Theory: Analysis and Design," 3rd ed (2005), Ch. 2, USA Wiley, pp. 32-34.
- [114] http://en.wikipedia.org/wiki/Analog-to-digital_converter
- [115] <http://spectrum-instrumentation.com/en/products/m3i2132>.

-
- [116] Daniel D. Harty, "Novel Design of a wideband Ribcage-Dipole Array and its feeding," Master's Degree Thesis, Worcester Polytechnic Institute. ECE Dept. 2010.
- [117] Annexure C
- [118] Annexure D
- [119] Warren L. Stutzman, "Polarization in Electromagnetic Systems," Ch. 4 & 8, Artech House Boston-London, pp. 96-98 & 183-216.
- [120] <http://www.astronwireless.com/topic-archives-antennas-polarization.asp>.
- [121] J. E. Hill, "Antenna Polarization," Watkins-Johnson Tech-notes, Aug. 1979.
- [122] Constantine A. Balanis. Antenna theory analysis and design, 3rd ed., USA: A John Wiley & Sons, INC, 2005.
- [123] Z. Chen, and Q. Cao, "Study of a two-arm sinuous antenna and the relevant wideband balun," International Conference on Microwave and Millimeter Wave Technology, ICMMT2008, pp. 1837-1840.
- [124] J. R. James and P. S. Hall, "Handbook of Microstrip Antennas, London, U.K," Peter Peregrinus, 1989.
- [125] R. Moini, M. Samiee. A Tavakoli, and G.Z. Rafi, "A dual-feed dual-excitation mode circularly-polarized crossed-slot antenna," Antennas and Propagation Society International Symposium, APS Digest 1996, pp. 58-61.
- [126] J. Huang, "A technique for an array to generate circular polarization with linearly polarized elements," IEEE Transaction on Antennas and Propagation, 1986, pp. 1113-1124.
- [127] A. Manna, P. Baldonero, and F. Trotta, "Novel UWB Low-Profile Sinuous Slot Antenna," Proceedings of 5th European Conference on Antennas and Propagation, EuCAP 2011.

-
- [128] J. Edwards, and G. Rebeiz, "Dual-Polarized Sinuous Antennas on Silicon Dielectric Lenses," Antennas and Propagation Society International Symposium, APSURSI 2010, pp. 1-4.
- [129] L. Liu, H. Xu, R. R. Percy, D. L. Herald, a. W. Lichtenberger, J. L. Hesler, and R. M. Weikle, "Development of Integrated Terahertz Broadband Detectors Utilizing Superconducting Hot-Electron Bolometers," IEEE Transaction on Applied Superconductivity, 2009, pp. 282-286.
- [130] M. C. Buck, and D. S. Filipović, "Split-Beam Mode Four-Arm Slot Sinuous Antenna," IEEE Antennas And Wireless Propagation Letter, 2004, pp. 83-87.
- [131] Y. Shen, C.L. Law, "A microstrip-fed quasi spiral circularly polarized ultra-wideband antenna," Antennas and Propagation Society International Symposium, APSURSI 2011.
- [132] M. Vahdani, and X. Begaud, "Sinuous Antenna fed by a Microstrip to CPS Balun," Proceedings of 3rd European Conference on Antennas and Propagation, EuCAP 2009, pp. 1622-1626.
- [133] S. G. Mao, J. C. Yeh, and S. L. Chen, "Ultra wideband circularly polarized spiral antenna using integrated balun with application to time domain target detection," IEEE Trans. Antennas Propag., vol. 57, no. 7, pp. 1914-1919, Jul. 2009.
- [134] K. M. Mak, K. M. Luk, "A Circularly Polarized Antenna With Wide Axial Ratio Beamwidth", IEEE Trans. on Ant. And Prop., vol. 57, No. 10, Oct 2009.
- [135] X. L. Bao, and M. J. Ammann, "A printed dipole antenna for wideband circular polarization operation," Antennas and Propagation, EuCAP, pp.2367-2370, 2009.
- [136] Y. H. Suh, and K. Chang, "A wideband coplanar stripline to microstrip transition," Microwave and Wireless Components Letters, IEEE, vol. 11, pp. 28-29, 2001.
- [137] Per-Simon Kildal, Foundation of Antenna- A Unified Approach, 1st ed., Studentlitteratur AB, 2000, Chapter 2, pp. 30.

-
- [138] Annexure E
- [139] K. M. Mac, and K. M. Luk, "A shorted cross bowtie patch antenna with a cross dipole for circular polarization," *Antennas and Propagation Society International Symposium 2007*, pp. 2702-2705.
- [140] C. C. Chiaw, and M. R. Kamarudin, "Novel Design of Circular UWB Antenna," *Asia Pacific Microwave Conference, APMC 2009*, pp. 1977-1979.
- [141] X. Chen, J. Liang, P. Li, L. Guo and C. C. Chiau, "Planar UWB Monopole Antennas," *IEEE Transaction on Asia-Pacific Conference Proceedings 2005*, pp. 1-4.
- [142] L. Guo, S. Wang, Y. Gao, X. Chen, and C. Parini, "Miniaturization of Printed Disc UWB Monopoles," *IEEE Transaction on Antenna Technology: Smart Antennas and Novel Metamaterials 2008*, pp. 95-98.
- [143] C. L. Hsu, "Design of quadrature hybrid with closely separated dual passband using three-branch line coupler," *Microwave proceedings (AMC)*, pp. 1232-1235, 2010.
- [144] I. Glover and P. Grant, *Digital Communications*. Prentice Hall, 2009.
- [145] A. Afuah, *Innovation Management: Strategies, Implementation and Profits*, Oxford Univ. Press, 2003.
- [146] <http://spectrum-instrumentation.com/en/products/m3i2132>.
- [147] Annexure A
- [148] Annexure B
- [149] Y. Zhang, M. G. Amin, and S. Kaushik, "Localization and Tracking of Passive RFID Tags Based on Direction Estimation," *International Journal of Antenna and Propagation Hindwai Publishing Corporation*, vol 2007, ID 17426, doi. 10.1155/2007/17426.

-
- [150] R. H. Lee, C.C Chang, and S.F. Chang. , “ A switched-beam FMCW radar for wireless indoor positioning system,” European Radar conference, EuRAD, pp. 65-68, 2013.
- [151] http://en.wikipedia.org/wiki/Non-line-of-sight_propagation
- [152] Constantine A. Balanis,“Antenna Theory,” Chapter 14, pp. 764.
- [153] D. M. Pozar, “Input Impedance and Mutual coupling of rectangular Microstrip Antennas,” IEEE Trans. Antennas Propagat., Vol. AP-30, No, November 1982.
- [154] Annexure F
- [155] <http://www.mathworks.fr/help/comm/ref/awgn.html>
- [156] S. Marano et. al, "NLOS Identification and Mitigation for Localization Based on UWB Experimental Data", IEEE J. Sel. Areas Commun., Vol. 28, Issue 7, pp. 1026 - 1035, September 2010.
- [157] <http://en.wikipedia.org/wiki/Circulator>
- [158] J.-Y. Lee and R. A. Scholtz, “Ranging in a dense multipath environment using an UWB radio link,” *IEEE J. Sel. Areas Commun.*, vol. 20, no. 9, pp. 1677–1683, Dec. 2002.
- [159] C. Stenir, and A. Wittneben, “Low Complexity Location Fingerprinting With Generalized UWB Energy Detection Receivers,” IEEE Trans. Signal. Proc., vol. 58, no. 03, pp. 1756–1767, March. 2010
- [160] D.D. Arumugam, J. D. Griffin, D. D. Stancil, and D. S. Ricketts, “Higher Order Loop Corrections for Short Range Magnetoquasistatic Position Tracking,” IEEE Int. Symp. On Antennas and Propagation (APSURSI), pp. 1755-1757.
- [161] D.D. Arumugam, J. D. Griffin, D. D. Stancil, and D. S. Ricketts, “Wireless orientation sensing using magnetoquasistatic fields and complex image theory,” IEEE Radio and Wireless Symposium (RWS 2012), pp. 251-254.

-
- [162] V. Moghtadaiee, A. G. Dempster, and S. Lim, "Indoor Localization Using FM Radio Signals: A Fingerprinting Approach," *Int. Conf; Indoor Positioning and Indoor Navigation (IPIN 2011)*, pp. 1-7.
- [163] J P. Nikitin, R. Martinez, S. Ramamurthy, H. Leland, G. Spiess, and K. Rao, "Phase based spatial identification of UHF RFID Tags," *Intermec Technol. Corp., Everett, WA, USA, 2010 IEEE International Conference on RFID, 2010*.
- [164] Q. Yao, F.-Y. Wang, H. Gao, K. Wang, and H. Zhao, "Location estimation in zigbee network based on fingerprinting," *dec. 2007*, pp. 1 –6.
- [165] V. Honkavirta, T. Perala, S. Ali-Loytty, and R. Piche, "A comparative survey of wlan location fingerprinting methods," *march 2009*, pp. 243 –251.
- [166] S. Outemzabet and C. Nerguizian, "Accuracy enhancement of an indoor ann-based fingerprinting location system using particle filtering and a low-cost sensor," *may 2008*, pp. 2750 –2754.
- [167] J. Ansari, D. Pankin, and P. Mahonen, "Radio-Triggered Wake-ups with addressing Capabilities for Extremely Low Power Sensor Network Applications," *Inter. Symp. On Personal, Indoor and Mobile Rad. Comm. 2008*, pp. 1-5.
- [168] Demirkol et al., "MAC protocols for wireless sensor networks: asurvey," *Communications Magazine, IEEE*, vol. 44, no. 4, pp. 115-121, April 2006.
- [169] J. Polastre, J. Hill, and D. Culler, "Versatile low power media accessfor wireless sensor networks," in *SenSys*, Nov. 2004.
- [170] L. Gu, and J. A. Stankovic, "Radio-triggered wake-up capability for sensor networks," *Real-Time Embedded Technology and Appllications Symposium, 2004*, pp. 27-26.
- [171] M. Vossiek, R. Roskosch, and P. Heide, "Precise 3-D object position tracking using FMCW radar," in *Proc. 29th Eur. Microw. Conf.*, Oct. 1999, vol. 1, pp. 234–237.
- [172] R. J. King, *Microwave Homodyne Systems*. London, U.K.: Peregrinus, 1978.

-
- [173] M. Kossel, H. R. Benedickter, R. Peter, and W. Bächtold, "Microwave backscatter modulation systems," in *IEEE MTT-S Int. Microw. Symp. Dig.*, Jun. 2000, pp. 1427–1430.
- [174] J. Thornton and D. J. Edwards, "Range measurement using modulated retro-reflectors in FM radar system," *IEEE Microw. GuidedWave Lett.*, vol. 58, no. 2, pp. 267–276, Feb. 2010.
- [175] A. Koelle, S. Depp, and R. Freyman, "Short-range radio-telemetry for electronic identification using modulated backscatter," *Proc. IEEE*, vol. 63, no. 8, pp. 1260–1260, Aug. 1975.
- [176] M. Vossiek and P. Gulden, "The switched injection-locked oscillator: A novel versatile concept for wireless transponder and localization systems," *IEEE Trans. Microw. Theory Tech.*, vol. 56, no. 4, pp. 859–866, Apr. 2008.
- [177] K. Finkenzeller, *RFID Handbook: Fundamentals and Applications in Contactless Smart Cards and Identifications*, 2nd ed. New York: Wiley, 2002.
- [178] Y. Zheng, L. Ye, L. Chen, H. Liao, and R. Huang, "SAW-less GNSS front-end amplifier with 80.4-dB GSM blocker suppression using CMOS directional coupler notch filter," *Int. Symp. On Circuits and Systems, ISCAS 2013*, pp. 749-752.
- [179] J. S. Lee, Y. M. Lee, C. M. Jeong, D. W. Kim, and Y. S. Kwon, "System in a package solution for RF receiver with SAW filter integration," *Electronic Components and Technology Conference*, 2002, pp. 1012-1017.
- [180] J. Lee, and J. D. Cressler, "A 3-10 GHz SiGe resistive feedback low noise amplifier for UWB applications," *Radio Frequency Integrated Circuits (RFIC) Symposium*, 2005, pp. 545-548.
- [181] P. K. Saha, D. C. Howard, S. Shnakar, R. Diestelhorst, T. England, and J. D. Cressler, "A 6-20 GHz Adaptive SiGe Image reject Mixer for a Self-Healing receiver," *IEEE Journal of Solid-State*, 2012, pp. 1998-2006.

-
- [182] R. Eickhoff, F. Ellinger, T. Ussmueller, and S. Spiegel, "A highly-integrated fractional-N synthesizer for FMCW radar," IEEE Int. Conf. Microwaves, Communications, Antennas and Electronic Systems, COMCAS 2008, pp. 1-6.

Système de localisation indoor pour l'aide à la télésurveillance

RESUME :

Dans le cadre d'un suivi régulier de patients âgés pouvant souffrir de maladie d'Alzheimer, de nombreuses applications, dont leur localisation, s'avèrent utiles. Un système de localisation compact dédié à un environnement en intérieure est nécessaire. Cette thèse est dédiée à la réalisation d'un système de localisation pouvant répondre à cette attente.

Le système développé (Indoor Localization System, ILS) permet la localisation en trois dimensions d'un badge actif (Active Tag, AT) relativement à une ancre unique (Localization Base Station, LBS). Le système utilise le principe de radar monopulse multistatique FMCW (Frequency Modulation Continuous Wave) et exploite la bande de fréquence Européenne ULB (6-8.5 GHz). La méthode employée pour l'ILS est une méthode goniométrique se basant sur la mesure conjointe de la différence de fréquence d'arrivée (FDoA) et la différence de phase d'arrivée (PDoA) pour l'estimation de la distance radiale et des angles de direction (azimut et élévation) de l'AT relativement au plan formé par l'ILS. Afin de valider ce système, un prototype d'ILS a été réalisé à Télécom ParisTech.

L'objectif de cette thèse est d'obtenir un système de localisation compact permettant de localiser un badge actif avec une précision submétrique dédié pour les environnements en intérieurs exposés aux problèmes de multi-trajets.

Mots clés : L'angle d'arrivée, Localisation intérieure, radar FMCW, Distance-radiale, Mesuré en 3D

Indoor Localization System for Telemonitoring

ABSTRACT :

Regular and accurate position monitoring of elderly suffering from dementia related problems (Alzheimer) may be required. To assist their monitoring a compact and a less complex indoor localization system is compulsory. This thesis is dedicated to design a Line-of-Sight (LoS) system to allow the indoor localization.

The thesis aims to develop an Indoor Localization System (ILS) for three-dimension position estimates with respect to single Localization Base Station as an anchor. The designed ILS uses an Active-Tag (AT) as remote target. The system uses the monopulse multistatic FMCW radar principle and covers the European UWB (6-8.5 GHz) frequency band. The designed ILS is based on the frequency-difference of arrival (FDoA) and the phase-difference-of-arrival (PDoA) techniques for the radial-distance and the angles (azimuth and elevation) estimates. In order to validate this system, a prototype of the ILS is designed at Telecom ParisTech, France.

The objective of the designed ILS is to have a localization system with an accuracy in few centimeters in Line-of-Sight condition. The system is designed to need a single anchor, and simultaneously addressing the indoor challenges such as multipaths, strong signal attenuations, reflections, etc.

Keywords : Angle-of-Arrival, FMCW Radar, Indoor Localization, Radial-Distance, 3D Measurement

